Cementitious materials subjected to mechanical and environmental stressors: A computational framework

by

Shahin Hajilar

A dissertation submitted to the graduate faculty

in partial fulfillment of the requirements for the degree of

DOCTOR OF PHILOSOPHY

Major: Civil Engineering (Structural Engineering)

Program of Study Committee:
Behrouz Shafei, Major Professor
Alice Alipour
In Ho Cho
Kejin Wang
Richard Alan LeSar

The student author, whose presentation of the scholarship herein was approved by the program of study committee, is solely responsible for the content of this dissertation. The Graduate College will ensure this dissertation is globally accessible and will not permit alterations after a degree is conferred.

Iowa State University

Ames, Iowa

2018

DEDICATION

To my beloved parents, Masoud and Farideh,

my dearest twin brother, Shayan,

and

my sweet little sister, Shima

TABLE OF CONTENTS

LIST OF FIGURES

LIST OF TABLES

ACKNOWLEDGMENTS

My deepest gratitude goes to my advisor, Professor Behrouz Shafei, not only for his invaluable technical advice in this study, but also for his unwavering support, passion, and encouragement throughout my doctoral journey.

I would like to express my sincerest gratitude to Professors Alice Alipour, In Ho Cho, Kejin Wang, and Richard LeSar, the members of my Ph.D. committee, for their valuable guidance, perspective, and commentary throughout my research project.

Also, I would like to acknowledge Drs. Tao Cheng and Andres Jaramillo-Botero (California Institute of Technology), Dr. Adri van Duin (Pennsylvania State University), and Dr. Andrey Kalinichev (Université de Nantes, France) for their feedback and discussions which greatly helped part of the research presented in this dissertation.

The support from the Extreme Science and Engineering Discovery Environment (XSEDE), sponsored by National Science Foundation grant number ACI-1548562, which was used for part of the atomistic simulations conducted in this study, is gratefully appreciated.

For their friendship, support, and collaborative spirit, I am thankful to my fellow graduate students working in the Department of Civil, Construction, and Environmental Engineering at Iowa State University.

Last but not least, I would like to thank my beloved parents and siblings for their endless love and support throughout my Ph.D. work. Although I have not had the chance to visit them since the beginning of my graduate studies, they have always been in my heart and mind. Knowing that they are proud of my academic accomplishments is of my greatest inspirations.

ABSTRACT

Despite the significant amount of concrete produced worldwide, there are long-standing issues with the long-term performance of concrete structures and facilities subjected to the mechanical and environmental stressors. To settle these issues, it is first imperative to understand the structural hierarchies and heterogeneous characteristics of concrete. While the structure of concrete at large length scales have been widely investigated in the literature, little knowledge is available about the structure, composition, and properties of the smallest building blocks of concrete, i.e., hydrated cement paste (HCP). This is mainly due to the complexities involved in the atomic structure of HCP phases that are often difficult to be characterized using conventional experimental methods. Atomistic simulations, however, can offer a promising solution, which not only plays a critical role to further interpret the experimental test results, but also advances the fundamental knowledge that is not accessible otherwise.

In this dissertation, a robust bottom-up computational framework supported with experimental test data is established to address three categories of research needs. These research needs seamlessly connect the atomic structure of cement-based systems to the long-term performance of concrete structures at the macroscale. The first category of research needs attempts to understand the interplay between the structure and properties of the crystalline HCP phases, including portlandite, and the AFt and AFm phases. The second category of research needs deals with the characterization of the magnitude, sign, and directionality of the mechanical stresses produced as a result of the formation of the secondary sulfate-bearing minerals during the chemical sulfate attack reactions. Lastly, the third category of research needs is associated with the identification of the atomistic processes underlying the diffusion of water molecules and chloride ions at the interfaces of the main aluminum-rich phases in HCP.

The outcome of this study (1) will extend the fundamental knowledge about the structure, dynamics, and properties of the HCP phases at the nanoscale, (2) will offer an invaluable addition to the existing experimental test data, and (3) can directly contribute to understanding and controlling the long-standing issues due to the deterioration of concrete structures subjected to the mechanical and environmental stressors.

CHAPTER 1: INTRODUCTION

1.1 Overview

Concrete, the structural backbone of our infrastructure, is the most versatile and commonly used construction material in the world. In the United States and considering only the amount of the ready-mixed concrete sold annually, concrete production is estimated to contribute up to $35 billion to the economic cycle (NRMCA, 2017). Despite the rising size of the concrete industry, there are serious challenges in the *long-term performance* of the structures and facilities made of concrete.

Depending on the application, concrete structures and facilities might be exposed to a broad spectrum of external environments such as soil, groundwater, wastewater, and seawater, many of which cause the material to undergo detrimental physical and/or chemical processes that can adversely affect the long-term strength and durability of concrete. The durability of concrete is defined as its ability to resist mechanical and environmental stressors while maintaining its desired engineering properties. The environmental stressors include, but are not limited to, chemical attacks, biological processes, elevated temperatures, and weathering actions that can lead to the deterioration of concrete structures. Among the environmental factors, the attack of chemical compounds such as acids, carbonates, chlorides, and sulfates are the most destructive processes that can degrade the physical and/or chemical properties of concrete, leading to costly repair, maintenance, and replacement. The annual repair, protection, and retrofitting costs for the concrete structures in the U.S. are estimated to be between $18 and $21 billion (ACI 562-16). Development of durable concrete reduces its environmental impact by both decreasing the amount of cement used and prolonging the service life of concrete structures, which saves on energy and resources associated with their maintenance repair, and replacement.

1.2 Research Needs and Motivations

The existing issues concerning the long-term performance of concrete structures have been translated into a number of research needs and questions. In this section, three categories of research needs are elaborated that together represent the main motivations of this dissertation. These research needs stand at the interface of a number of disciplines from structural engineering and solid mechanics to materials science and engineering.

The first category of the research needs attempts to enhance the sustainability of cementitious materials with the aim of reducing their carbon footprint. One of the main hypothesis of this research is that improving the physical and chemical properties of concrete can lead to a major increase in the durability of concrete structures, which helps save energy and reduce cement production. Nonetheless, to develop a high-performance concrete with enhanced engineering properties, it is first imperative to understand the mechanical, thermal, and chemical characteristics of hydrated cement paste (HCP). HCP binds the fine and coarse aggregates together and directly contributes to the stiffness, strength, and durability properties of concrete.

HCP is composed of several phases formed as a result of a number of chemical reactions between cement clinker and mixing water. The HCP phases are often categorized into four major groups: poorly crystalline calcium silicate hydrates (C-S-H gel), crystalline phases of calcium hydroxide (portlandite), calcium aluminate monosulfate hydrates (AFm), and calcium aluminate trisulfate hydrates (AFt). The C-S-H gel constitutes 50-60% of the total volume of the solid HCP. This percentage changes to 20-25% for portlandite and 15-20% for the AFm and AFt phases combined. Among the hydration products, the structure and properties of the C-S-H gel, a mesoporous amorphous phase with unfixed stoichiometry, have been widely investigated in the literature (e.g., Allen et al., 2007; Jennings, 2008; Richardson, 2008; Pellenq et al., 2009; Dolado

et al., 2011; Qomi et al., 2014). Nevertheless, the mechanical, thermal, and chemical characteristics of the other HCP phases, such as portlandite, as well as the AFt and AFm phases, are still not fully known. It is worth noting that although the AFt and AFm phases, i.e., the most abundant aluminum-rich species in HCP, contribute only up to 15-20% of the total volume of the OPC paste, they are the dominant hydrated products of the calcium sulfoaluminate (CSA) cement. The CSA cement is considered as an environmentally-friendly alternative to the OPC cement because the firing temperature to produce the former is 200 °C lower than the latter one's (Ali et al., 1994; Winnefeld and Lothenbach, 2010; Telesca et al., 2014).

This dissertation provides the first-known effort to *characterize the relation between the structure and properties of portlandite and the aluminum-rich phases present in OPC and CSA cement pastes*. This research offers an invaluable fundamental knowledge essential to introduce strategies to enhance the intrinsic properties of concrete made with OPC and CSA types of cement. Furthermore, the mechanical, thermal, and chemical properties determined in this study can be directly utilized in the available finite element and phase field models of cementitious materials at the macro- and micro-level, respectively.

The second category of the research needs deals with the understanding of deterioration mechanisms in concrete structures and facilities subjected to sulfate-rich service environments. Sulfate ions can be possibly present in the concrete mixing materials, such as cement, aggregate, mixing water, and chemical/mineral admixtures. In this case, the attack is often defined as "Internal Sulfate Attack" (ISA). It is also possible that the sulfate ions are originated from the external environment in which the concrete structure is exposed to, such as contaminated groundwater, soils, atmospheric pollution, and sewage systems, to name a few. This type of attack is often classified as "External Sulfate Attack" (ESA).

It has been documented that the external sulfate ions can attack concrete structures through a number of chemical and/or physical processes (Chabrelie, 2010; Whittaker and Black, 2015; Batilov, 2016). While the former generally involves chemical reactions between sulfate ions and the HCP phases (Chabrelie, 2010), the latter is attributed to the phase change processes in the penetrating sulfate compounds (Suleiman, 2014). As a result of chemical sulfate attack (CSA), which is one of the primary focuses of this dissertation, a number of secondary sulfate-bearing minerals such as ettringite and thaumasite are formed. Despite decades of research, however, the mechanism of deterioration is still under debate (Mehta and Monteiro, 1993; Taylor et al., 2001; Santhanam et al., 2002 and 2003; Collepardi, 2003; Neville, 2004; Whittaker and Black, 2015). This triggers the second set of research needs to be addressed in this dissertation. To this end, *the structural, thermal, and mechanical properties of these secondary sulfate-bearing minerals are fully characterized*. Moreover, *the magnitude, sign, and directionality of the mechanical stresses* induced as a result of the formation of ettringite and thaumasite are investigated in detail. Lastly, the *full plane-stress yield surface* fitted to the mechanical responses of these minerals are identified. The fundamental knowledge obtained from this study can be ultimately used to control the expansion, spalling, and loss of strength caused by the formation of ettringite and thaumasite during chemical sulfate attack.

The third category of the research needs is associated with the durability of concrete structures subjected to chloride attack. It is known that the corrosion of steel bars in reinforced concrete structures attacked by chloride compounds is the most long-standing issue in, particularly, the structures and facilities exposed to seawater, deicing compounds, and saline environments such as underground, highway, and marine structures (Alipour et al., 2011 and 2013; Shafei et al., 2012 and 2013; Shafei and Alipour, 2015a,b). The chloride ions can also have internal sources including

contaminated aggregates, mixing water, and admixtures that contain chloride (e.g., calcium chloride). In chloride contaminated concrete structures, a substantial amount of free chloride ions in the cement pore solution diffuses toward the reinforcing steel embedded in the concrete matrix to resist tensile stresses. Once the chloride ions reach the steel reinforcing bars, the pH decreases, the protective film is disrupted, and the pitting corrosion is initiated. Such chemical reactions produce a layer of porous materials around the reinforcing steel with less strength and larger volume compared to those of the original steel. This decreases the bond between concrete and steel (Fang et al., 2006), reduces strength (Du et al., 2005) and forms microcracks (Andrade et al., 1993; Vidal et al., 2004) that all together lead to the deterioration of the concrete structures.

While the corrosion of reinforcing steel bars, and the consequent degradation of concrete caused by chloride attack, are well documented in the literature, there are still several research questions that have remained unanswered. It is widely accepted that the aluminum-rich phases of HCP play a substantial role in controlling the chloride attack processes, however, *the mobility and transport properties of chloride ions and water molecules in contact with those phases have been poorly understood.* Thus, it is necessary to investigate the extent to which the chloride ions are free to diffuse within the pore spaces in comparison to the ones bounded to the surfaces of the aluminum-rich phases of HCP. Furthermore, the current literature falls short in explaining *the physico-chemical processes underlying the adsorption of chloride ions and water molecules to the basal surfaces of the aluminum-rich species in HCP*. To address the standing research questions raised above, this dissertation aims to obtain a fundamental understanding of the physical and/or chemical interactions between chloride ions and the reactive surfaces of the aluminum-rich phases of HCP. The outcome of this study helps unravel the atomistic origins of the chloride binding capacity of different cementitious phases. This, together with the structural and dynamics

properties, such as diffusion coefficients and chloride binding isotherms, determined in this study can be used by the cement industry to refine the microstructure of cement products with the aim of eliminating (or minimizing) the deteriorations due to chloride attack.

1.3 Research Approach and Objectives

The identified research needs can be pursued at various length scales, spanning from the scale of the atomic structures of cementitious materials all the way to the macroscale level that includes the structural elements made of concrete. The smallest length scale features a few atoms or below and the Schrödinger equation is employed to describe the evolution of a quantum state with time. At the mesoscale, the dynamic of a system composed of thousands of atoms and molecules is investigated by time integration of Newton's equations of motion. This approach is based on the detailed description of the chemical bonding between various atoms, and the interactions of different chemical compounds and molecules. At the large length scales, the theories of continuum mechanics are applied to develop constitutive relationships used to describe the system behavior. This dissertation aims to obtain and sieve the fundamental information at the nanoscale to explain the response of concrete structures and facilities subjected to the mechanical and environmental stressors. To this end, it is first imperative to understand the hierarchical structure of concrete across various length scales.

In concrete, the structural features differ substantially across different length scales (Figure 1-1). At the macroscale ($\geq 10^{-3}$ m), concrete can be taken as a material containing mainly fine and coarse aggregates, as well as the cement matrix. At the microscale ($\sim 10^{-6}$ - 10^{-3} m), the heterogeneous material is composed of various HCP phases (mix of water and cement), unhydrated clinker, and pore spaces. Concrete at the nanometer length scale ($\sim 10^{-9}$ - 10^{-6} m) is mostly composed of the HCP phases and some nanopores. For instance, the layered structure of a

synthesized C-S-H gel is clearly observed with an inconceivable resolution of 5 nm from the latest transmission electron microscope (TEM) image (Figure 1.1). Finally, the basic building blocks, i.e. the distribution and arrangement of atoms, water, and ions existing in the nanopores, and chemical bonds present in the atomic structures of the HCP phases fall within the atomic length scale (~10^{-10} - 10^{-9} m).

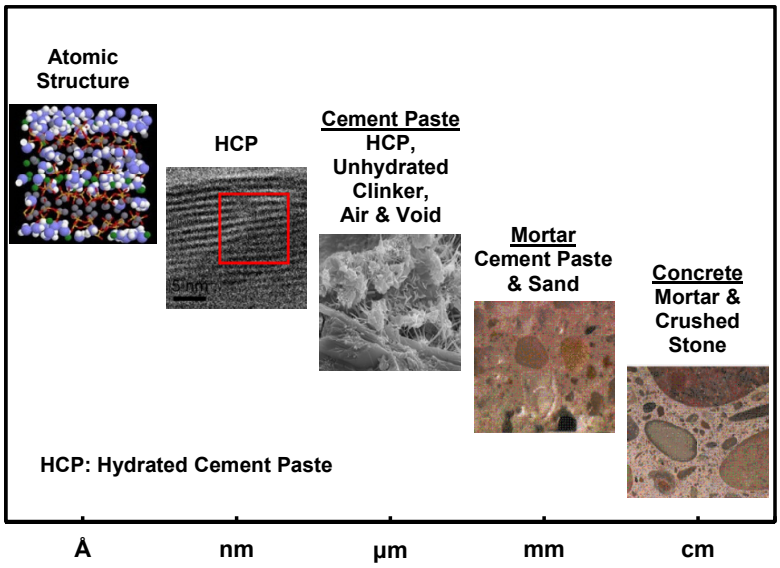

Figure 1-1. Hierarchical structure of concrete across various length scales. Image Credits: Level *Å* from Pellenq et al. (2009); Level *nm* from Taylor et al. (2015); Level *μm* from Stutzman (2001), Levels *mm* and *cm* from Garboczi and Bentz (1996).

While a detailed information about the atomic structure of the cement paste is not needed for an engineering design process, the macroscopic mechanical, thermal, and chemical characteristics of concrete are truly the consequences of the atomic arrangements and interatomic interactions in the structure of the HCP phases at the nanoscale. Despite decades of continuous research, the interplay between the structure and properties of concrete have not been fully understood. This is mainly due to the complexities involved in the structure of concrete at the small length scales that are often difficult to be characterized using conventional laboratory facilities. Atomistic simulations, however, can offer a promising solution, which not only plays a critical role to further

interpret the experimental test results, but also advances the fundamental knowledge that is not accessible otherwise.

This dissertation aims to develop a robust atomic-scale computational framework supported by experimental tests to address three main research needs and questions: (1) understanding the interplay between the structure and properties of the crystalline HCP phases including portlandite, and the AFt and AFm phases, (2) characterizing the magnitude, sign, and directionality of the mechanical stresses produced as a result of the formation of the secondary sulfate-bearing minerals (i.e., ettringite and thaumasite) during the chemical sulfate attack reactions, and (3) identifying the atomistic processes underlying the diffusion of water molecules and chloride ions at the interfaces of the main aluminum-rich phases in HCP.

In this work, a systematic approach is established to benefit from a variety of atomistic simulation methods, which are employed based on their individual capabilities to solve the research problems highlighted above. The atomistic simulation results are validated with the available experimental test data in the literature obtained from nuclear magnetic resonance, small angle neutron scattering, and X-ray diffraction methods. It is believed that the fundamental knowledge obtained in this dissertation could ultimately pave the way to design a more sustainable cementitious material with improved engineering properties.

1.4 Dissertation Outline

The theme of this dissertation is paper-based, in which each chapter contains all the necessary components of a research article including introduction, literature review, computational methodology, results, discussions, conclusions, and bibliography.

Following the introductory chapter, Chapter 2 presents the mechanical failure mechanisms of the aluminum-rich species in HCP such as hydrogarnet (a stable calcium hydroaluminate phase),

ettringite (AFt or calcium aluminate trisulfate) and monosulfoaluminate (AFm or calcium aluminate monosulfate). The aluminum-rich species are formed as a result of a number chemical reactions between tricalcium aluminate and water. Through an extensive set of reactive molecular dynamics (RMD) simulations, the mechanical response of these crystalline structures is examined under uniaxial tensile strains. The mechanical properties of the aluminum-rich species are fully characterized by the obtained stress-strain curves. Through performing chemical bond and structural damage analysis, the atomistic origins of failure mechanisms under high tensile strains are determined.

In Chapter 3, the structural, thermal, and mechanical properties of portlandite (calcium hydroxide) are characterized using the classical molecular dynamics (MD) method. The properties obtained by the MD simulations are validated with those available from the experimental tests. The mechanism of mechanical failure for different crystallographic directions is identified. The energy of the fractured surfaces and that of the ideal surfaces are determined to predict the plastic energy necessary to cause the fracture in the atomic structure of portlandite. The effect of temperature and strain rate on the stress-strain response of portlandite under tensile strains is investigated. A constitutive relationship is then derived to couple the strain rate and temperature with the fracture strength of portlandite.

Chapter 4 aims at investigating the mechanical response of thaumasite (calcium silicate carbonate sulfate hydrate) under various temperatures and strain rates using RMD simulations. Thaumasite is one of the main sulfate-bearing species formed as a result of the chemical reactions taking place during sulfate attack. With employing a first-principles based reactive force field, the RMD simulations enable the description of bond dissociation and formation under realistic conditions. A comprehensive chemical bond analysis is performed to reveal the bonds responsible

for the mechanical strength of thaumasite. Moreover, the stress-strain curves of thaumasite are generated in different crystallographic directions and the tensile strength, Young's modulus, and fracture strain are determined.

Chapter 5 discusses the atomistic origins of strength anisotropy and tension-compression asymmetry in ettringite and thaumasite, which are the main secondary sulfate-bearing phases formed during the attack of sulfate compounds to concrete structures. Through a set of RMD simulations, the effect of strain directionality is fully captured in this study for the first time by subjecting the atomic structures of ettringite and thaumasite to various multiaxial strain conditions. The atomistic processes underlying the mechanical response of these sulfate-bearing phases in different straining conditions are determined. A yield criterion is introduced to captures the intrinsic features observed from the constitutive responses of ettringite and thaumasite under plane stress biaxial straining conditions.

Chapters 6 and 7 present the structure, orientation, and dynamics of water molecules and chloride anions at the basal surfaces of ettringite and monosulfoaluminate, which are the main crystalline minerals representing the AFt and AFm phases in HCP, respectively. An aqueous layer containing various concentrations of sodium chloride solution is sandwiched between the basal surfaces of these aluminum-rich phases. The MD simulations at constant temperature and volume provide an in-depth insight into the mechanisms of adsorption of water and ions at the inner- and outer-sphere distances from the basal surfaces of ettringite and monosulfoaluminate. Moreover, the physical adsorption, binding capacity, and self-diffusion coefficient of water molecules and chloride ions are determined.

In the end, Chapter 8 presents a summary of the research outcome and contributions. Moreover, future research and development directions are suggested to close the dissertation.

CHAPTER 2: MECHANICAL FAILURE MECHANISMS OF HYDRATED PRODUCTS OF TRICALCIUM ALUMINATE: A REACTIVE MOLECULAR DYNAMICS STUDY

The hydrogarnet, ettringite, and monosulfoaluminate crystals are known as the most important hydrated products of tricalcium aluminate, a major phase of ordinary cement with applications as a sustainable binder material. To understand the mechanical strength and performance of this important category of materials under external loads, the atomic structures of them are investigated at the nano-scale in the current study. Through an extensive set of reactive molecular dynamics simulations, the mechanical behavior of the representative crystalline structures is examined under uniaxial tensile strains and the corresponding stress-strain curves are obtained. The effects of strain direction and rate on the stress-strain behavior are particularly investigated. From the stress-strain curves, both elastic and plastic response of the hydrated phases of tricalcium aluminate are determined. A comprehensive chemical bond and structural damage analysis is also performed to characterize the failure mechanisms under high tensile strains.

2.1 Introduction

Tricalcium aluminate ($Ca_3Al_2O_6$), which is also referred to as C_3A according to the cement chemistry notation (where $C = CaO$ and $A = Al_2O_3$), constitutes up to 15 wt. % of Portland cement clinkers. It is also a major phase of cements commonly used for dental root filling. During the hydration process, C_3A rapidly reacts with water, and as a result, the calcium hydroaluminate phase, which is known as hydrogarnet (C_3AH_6 where $H = H_2O$), is formed (Lea and Hewlett, 1998). This reaction, however, is not desired because the formation of hydrogarnet increases the stiffness and adversely affects the workability of cement paste. To avoid this situation, retardants such as Gypsum ($C\bar{S}H_2$ where $\bar{S} = SO_3$) are added to cement clinkers to reduce the rate of the reaction of C_3A with water. Gypsum is highly soluble and releases calcium and sulfate ions into the pore solution. The presence of sulfate ions causes C_3A to undergo a different chemical reaction

that produces the calcium trisulfoaluminate phase, which is referred to as mineral ettringite ($C_6A\bar{S}_3H_{32}$). If gypsum is completely consumed before C_3A, the concentration of sulfate ions decreases drastically, C_3A starts consuming ettringite, and solid phases containing fewer sulfate ions are formed. As a result of such reactions, monosulfoaluminate ($C_4A\bar{S}H_{12}$) is produced (Taylor, 1997). However, if a new source of sulfate ions becomes available (e.g., from ground water, sea water, or soil), it will be thermodynamically favorable to form ettringite again, just as it was initially, through the consumption of the existing monosulfoaluminate (Taylor et al., 2001). In this case, since the replacing ettringite occupies a volume larger than the original monosulfoaluminate, expansive stresses are created, which may cause undesirable cracking and deterioration of cementitious materials (Mehta and Monteiro, 1993). This highlights the importance of the current study as C_3A and its reactions with other chemical species during cement hydration can result in the formation of the products that directly affect the structural evolution and mechanical properties of the hydrated cement paste.

Tricalcium aluminate also exists in calcium sulfoaluminate (CSA) cements, an environmentally friendly alternative to ordinary cement (Pera and Ambroise, 2004). The firing temperature to produce the CSA cements is 200 °C lower than that for ordinary Portland cement. This results in more sustainable cements as a substantial reduction in the emissions of CO_2 is achieved (Ali et al., 1994). Ettringite is the most important binding phase of CSA cements and depending on the other phases available, a range of hydration products, such as calcium-silicate-hydrates, monosulfate, monocarboaluminate, and hydrogarnet are formed (Winnefeld and Lothenbach, 2010). Another potential application of the CSA cements is their use as a binder for hazardous waste encapsulation (Chrysochoou and Dermatas, 2006). In this application, the divalent and trivalent metals, such as Cu, Cr, Cd, Pb, Zn, and Fe can be stabilized by occupying the positions of the calcium and

aluminum atoms present in the hydration products of the CSA cements (Albino et al., 1996). Moreover, oxyanions, such as $B(OH)^{4-}$, CrO_4^{2-}, MoO_4^{2-}, and SeO_4^{2-}, can be removed from wastewater through the channels that exist between the C_3A columns of ettringite (Zhang et al., 2003).

To address the structural response issues from one side and requirements for the efficient stabilization of heavy ions from the other side, it is essential to investigate the C_3A hydrated phases when they are subjected to an external mechanical force. A review of the existing literature indicates that the past efforts have been mainly focused on the other phases of hydrated cement paste, especially calcium silicate hydrates (C-S-H). For example, Pellenq et al. (2009) proposed a detailed model for the atomic structure of the C-S-H gel and obtained the corresponding shear stress-strain relationship through Molecular Dynamics (MD) simulations. This study identified the hydrolytic weakening effect from the interlayer water molecules as one of the main causes of failure under large strains. The tensile stress-strain relationship of the C-S-H gel was later reported by Hou et al. (2014a and 2015) using both classical and Reactive Molecular Dynamics (RMD) simulations. The latter studies examined the mechanical response and chemical reactions of the C-S-H gel with different compositions expressed in terms of Ca/Si ratio. It was found that the breakage of silicate chains together with the penetration of water molecules adversely affect the stiffness and cohesive energy of the C-S-H gel. Moreover, the effect of water content on the structure, dynamics, and mechanical properties of the C-S-H gel was investigated. Through MD simulations, it was revealed that the structural water molecules weakens the stiffness and cohesive energy of the C-S-H gel as they replace the strong ionic-covalent bonds with unstable H-bond connections.

The current study presents one of the first-known efforts to understand the mechanical response and failure mechanisms of hydrogarnet, ettringite, and monosulfoaluminate. Contrary to the case of C-S-H gel, only few studies have been conducted to characterize the mechanical properties of the aluminum-rich species of hydrated cement paste: Speziale et al. (2008) estimated the elastic properties of single-crystal ettringite, including all the adiabatic elastic constants and acoustic velocities, using the Brillouin spectroscopy in the ambient conditions. Through separate efforts, Manzano (2009) and Hajilar and Shafei (2014 and 2015) employed Molecular Mechanics and Molecular Dynamics methods to characterize the elastic properties of a range of cement phases, including hydrogarnet, ettringite, and monosulfoaluminate. While the listed studies contributed to understand the mechanical properties of the C_3A hydrated phases in the elastic regime, where deformations are small and reversible, very limited information on the mechanical properties of these three phases beyond the elastic regime is available. At this time, Liu et al. (2012) is the only study in the literature that utilized a reactive force field (ReaxFF) to evaluate the elastic, plastic, and failure response of ettringite at the nano scale. The study reported that the Ca-O bonds are responsible for the failure of the calcium sulfate and tricalcium aluminate columns in ettringite under external strains. Liu et al. (2012), however, was only focused on ettringite and did not investigate the other important aluminum-rich phases, such as hydrogarnet and monosulfoaluminate. Furthermore, the sensitivity of response predictions to the strain rate was not examined by Liu et al. (2012).

In this study, the RMD simulation method is used to evaluate the mechanical behavior of all the hydrated phases of C_3A under tensile strains. For this purpose, the crystalline structures of hydrogarnet, ettringite, and monosulfoaluminate are constructed at the atomic scale. The hydrated phases of C_3A crystals are subjected to tensile strains to generate the stress-strain curves, which

can be immediately employed to interpret both elastic and plastic behavior of the materials of choice. The effect of the direction of straining on the stress-strain behavior is also evaluated to understand the corresponding anisotropic properties. Since the obtained results depend on the strain rate, a wide range of strain rates from 0.0005/ps to 0.01/ps are evaluated in this study. From the generated stress-strain curves, the mechanical properties of the hydrated phases of C_3A are characterized under three strain directions and four strain rates. Subsequently, a comprehensive bond analysis is performed to find the correlation between the formation and/or breakage of the chemical bonds and the stress-strain curves. A separate structural damage analysis is also conducted to investigate the extent of damage to the crystalline structures of the hydrated phases of C_3A under axial strains. The failure mechanisms for each crystalline structure stretched in three main directions are identified and discussed in detail. The presented results are expected to directly contribute to understand how the strength and stiffness of the C_3A hydrated phases can be improved based on the fundamental mechanical behavior captured at the atomic scale.

2.2 Hydrated Products of Tricalcium Aluminate

2.2.1 Hydrogarnet

Hydrogrossular is a calcium-aluminum garnet, $Ca_3Al_2(SiO_4)_{3-X}(OH)_{4X}$, with variable stoichiometry where $0 \leq X \leq 3$. In the hydrogrossular series, hydrogarnet is the Si-free end member with $X = 3$. This means that the Si^{4+} is missing from the tetrahedral sites of the atomic structure of hydrogarnet. The charge balance, however, is maintained by bonding a H^+ to each of the four oxygen atoms surrounding the vacant site. In other words, the hydrogarnet crystal is obtained from the isomorphic replacement of $(SiO_4)^{4-}$ by $(OH)_4^{4-}$. As discussed earlier, hydrogarnet is formed as a result of the reaction of C_3A with water. This reaction is very fast and known as flash setting, during which a large amount of heat is released causing the paste to set

within few minutes after mixing. The flash setting is not desired as it adversely affects the rheology of the paste at early ages, reduces the workability of the paste, and prevents the homogeneity of the mix. The hydration reaction of tricalcium aluminate can be expressed as:

$$2C_3A + 21H \rightarrow C_4AH_{19} + C_2AH_8 \rightarrow 2C_3AH_6 + 9H \quad (2\text{-}1)$$

The first products, i.e., C_4AH_{19} and C_2AH_8 are unstable calcium hydroaluminates, which rapidly evolve to hydrogarnet (Lea and Hewlett, 1998). To prevent flash setting, retardants such as gypsum are added to Portland cement. Thus, the contribution of hydrogarnet is typically less than 2% of the total weight of the cement paste and it can be mainly found in the older pastes made of calcium aluminate cements or warm cured Portland cements (Taylor, 1997; Paul and Glasser, 2000). The crystalline structure of synthetic hydrogarnet has been characterized by Lager et al. (1987) using Neutron and X-ray diffraction tests. The characterization data show two different cation environments in the atomic structure of hydrogarnet. The calcium atoms are each eight-coordinated and have triangular dodecahedra sites. On the other hand, the aluminum atoms are each six-fold octahedrally coordinated to six hydroxyl groups. The chemical constitution of hydrogarnet is $Ca_3Al_2(OH)_{12}$ and its cubic unit cell has a space group of $Ia\bar{3}d$. Figure 2-1 shows the cubic unit cell of hydrogarnet.

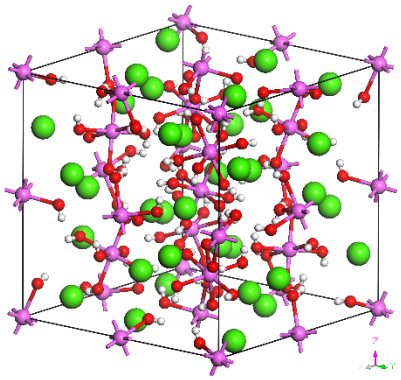

Figure 2-1. The unit cell of hydrogarnet.
(Green: Ca; Pink: Al; Red: O; White: H)

2.2.2 Ettringite

During the early stages of hydration of Portland cement, ettringite is formed as a result of the reaction of water and tricalcium aluminate in the presence of a calcium sulfate source like gypsum. Gypsum is typically added to Portland cement to prevent rapid setting while improving strength. This reaction is called early ettringite formation (EEF) as shown below:

$$C_3A + 3C\bar{S}H_2 + 26H \rightarrow C_6A\bar{S}_3H_{32} \quad (2\text{-}2)$$

After all the available gypsum clinker is depleted, the reaction of water and C_3A consumes ettringite and forms a secondary product called monosulfoaluminate with a lower sulfate content compared to ettringite. Despite the formation of monosulfoaluminate, it should be noted that a considerable amount of ettringite crystals still exists in the mature cement paste and contributes to its mechanical characteristics (Taylor et al., 2001). Ettringite may also be formed in the mature cement paste through two other processes known as sulfate attack and delayed ettringite formation (DEF). Sulfate ions penetrating into the concrete from the outside environment (e.g., sulfate-rich water and soil) react with calcium hydroxide and monosulfoaluminate, two other phases of the hydrated cement paste, to form new ettringite crystals. Furthermore, if the cement paste is exposed to a temperature higher than 70˚ C, monosulfoaluminate releases aluminum and sulfate ions. The aluminum ions are likely to enter into the structure of the C-S-H gel. Therefore, when the temperature decreases again, the Al^{3+}/SO_4^{2-} ratio decreases and the ettringite is formed. The latter process of the ettringite formation can cause expansion and consequently cracking of the cement paste (Mehta and Monteiro, 1993). This reaction can be represented as follows:

$$C_4A\bar{S}H_{12} + 2C\bar{S}H_2 + 16H \rightarrow C_6A\bar{S}_3H_{32} \quad (2\text{-}3)$$

Ettringite has rod-like or needle-shape morphology with the chemical composition of $Ca_6[Al(OH)_6]_2(SO_4)_3.26H_2O$. The structure of the ettringite crystal has been fully characterized in the literature (Moore and Taylor, 1968; Hartman and Berliner, 2006). A distinct aspect of this crystal is the existence of an extensive network of hydrogen bonds along a central column of aluminum and calcium polyhedra. The aluminum atoms are each six-fold, octahedrally coordinated with six hydroxyl groups. The calcium atoms, on the other hand, are each eight-fold coordinated with four hydroxyl groups and four water molecules. The excess charge of the columns is neutralized with the sulfate ions that exist in the channels between them. Ettringite has a trigonal unit cell with a space group of $P31c$ and a density of 1.8 g/cm^3 (Figure 2-2).

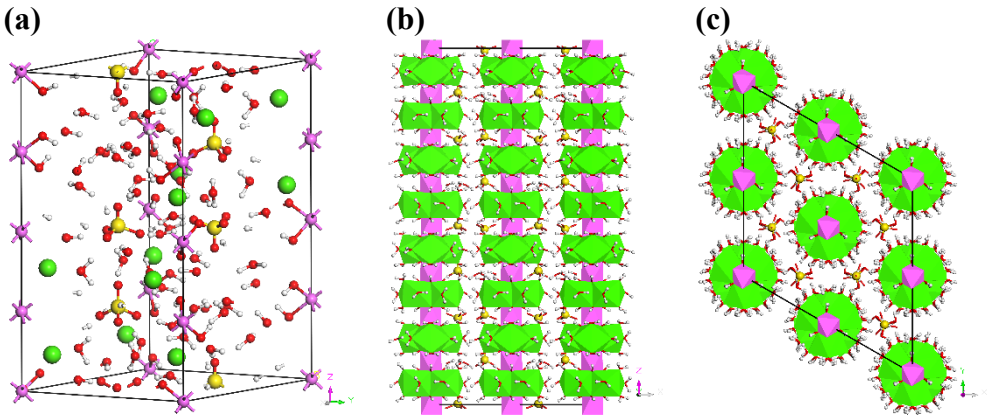

Figure 2-2. (a) Unit cell of ettringite, (b) configuration of the C_3A columns parallel to the z axis, and (c) arrangement of the SO_4^{2-} groups and water molecules in the intercolumn channels. (Green: Ca; Pink: Al; Yellow: S; Red: O; White: H)

2.2.3 Monosulfoaluminate

Monosulfoaluminate has a higher ratio of aluminum to calcium atoms in comparison with ettringite. In the early stages of the hydration process of Portland cement, when the sulfate source is consumed and the alumina content decreases, ettringite is dissolved and monosulfoaluminate is formed as:

$$2C_3A + C_6A\bar{S}_3H_{32} + 4H \rightarrow 3C_4A\bar{S}H_{12} \quad (2\text{-}4)$$

On the other hand, by the sulfate attack, when the alumina content increases, monosulfoaluminate is dissolved and new ettringite is formed. Therefore, the monosulfoaluminate phase in the cement paste is highly linked to the ettringite content. The layered structure of monosulfoaluminate is derived from that of calcium hydroxide, but with one-third of the calcium ions replaced by Al^{3+}. The water content in monosulfoaluminate ranges from 12 to 18 (Taylor, 1997). While the atomic structure of monosulfoaluminate with low water content has not been characterized yet, the structure of monosulfoaluminate with 18 water molecules in the interlayer space has been found to have a natural analogue called kuzelite. The crystalline structure of kuzelite has been fully characterized by Allmann (1997). The main layer of kuzelite consists of the brucite-like cations of $[Ca_2Al(OH)_6]^+$. The calcium ions approach the H_2O molecule of the interlayer and become seven-coordinated. Furthermore, two possible positions of $SO_4{}^{2-}$ are replaced by two molecules of water in every other cell, which makes the remaining part of the interlayer disordered (Figure 2-3). Kuzelite with the chemical composition of $[Ca_2Al(OH)_6]^+.[0.5SO_4.3H_2O]^-$ has a trigonal unit cell, a space group of $R\bar{3}$, and a density of 2.0 g/cm^3.

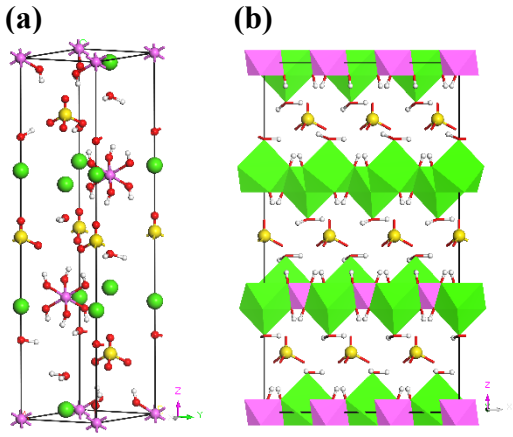

Figure 2-3. (a) Unit cell of kuzelite and (b) the configuration of the $[Ca_2Al(OH)_6]^+$ layers perpendicular to the z axis as well as the SO_4^{2-} groups and water molecules in the interlayer. (Green: Ca; Pink: Al; Yellow: S; Red: O; White: H)

2.3 Computational Methodology

2.3.1 Reactive Force Field

Since the MD method is based on the calculation of particle motions, it is found well-suited to study the dynamics of deformation, crack growth, and eventually fracture (e.g., Liu and Wang, 1999; Wunderlich and Awaji, 2001; Tsai and Tu, 2010; Xiao et al., 2015; Zhang et al., 2015). Nevertheless, the classical force fields are not capable of describing the chemical reactions that will be initiated due to large deformations. This issue has been addressed in the current study through RMD simulations using ReaxFF developed by van Duin et al. (2001). In ReaxFF, the harmonic bonds of classical MD is replaced by the bond orders and energies that depend on interatomic distances. This approach can capture the bond breakage and formation as the bonded interactions are allowed to decay smoothly to zero. The non-bonded Columbic and van der Waals interactions are calculated for all the atoms in the system using a screened taper function. The atomic charges are determined by the charge equilibrium (QEq) method (Mortier et al., 1986) and must be updated at each time step. The parameters of ReaxFF used in the current study can be directly obtained from Liu et al. (2012).

2.3.2 Model Construction

RMD simulations are conducted in the current study using the large-scale atomic/molecular massively parallel simulator (LAMMPS) package (Plimpton, 1995). Atomic models of the C_3A hydrated products are constructed in LAMMPS according to the latest crystallographic data. The lattice constants of the phases under consideration are presented in Table 2-1. While hydrogarnet crystalizes in a cubic crystal system, the ettringite and kuzelite crystals have a trigonal lattice (*a*, *b* and *c* axes). For the study of mechanical behavior, the trigonal unit cells of ettringite and kuzelite are transformed into orthorhombic cells (*x*, *y* and *z* axes) with the *z* axis parallel to the primitive *c*

axis. To maintain the periodicity of the new orthorhombic lattice, it is necessary to double the size in the *a*-axis direction. This results in a pseudo orthorhombic unit cell twice as large as the initial trigonal unit cell. The unit cell of each phase is then expanded in the three orthogonal directions to obtain larger simulation cells known as supercells. The supercell of hydrogarnet, ettringite, and kuzelite contain 3712, 2048, and 2544 atoms, respectively. A three-dimensional periodic boundary condition is applied to each of the supercells before the simulation begins (Allen and Tildesley, 1987). The potential energy of the supercells is minimized at zero temperature to reduce residual stresses. To capture the chemical reactions and update the bond orders, all the simulations are performed with a time step equal to 0.25 fs (10^{-15} s). The supercells are equilibrated in the isobaric-isothermal (*NPT*) ensemble for 50 ps (10^{-12} s) to reach the target equilibrium temperature and pressure of 300 K and zero atmosphere, respectively. The equations of motion are integrated via the Velocity-Verlet algorithm. During the equilibration stage, the convergence of a variety of parameters (e.g., total energy and its components, temperature, and pressure) is closely monitored.

Table 2-1. Lattice parameters of hydrated products of C_3A

	a **(nm)**	***b*** **(nm)**	***c*** **(nm)**	***α*** **(deg.)**	***β*** **(deg.)**	***γ*** **(deg.)**
Hydrogarnet [a]	1.2565	1.2565	1.2565	90	90	90
Ettringite [b]	1.1167	1.1167	2.1354	90	90	120
Kuzelite [c]	0.57586	0.57586	2.67946	90	90	120

[a] Lager et al. (1987)
[b] Hartman and Berliner (2006)
[c] Allmann (1997)

2.3.3 Uniaxial Tension Testing

Contrary to conventional macro-scale experiments, it is often found more convenient to control strain rather than stress in atomistic simulations. To determine the uniaxial stress-strain relationships, the relaxed supercell of each of the three crystals is strained along one of the three orthogonal directions (*x*, *y*, and *z*). The effect of strain rate on the mechanical properties of hydrogarnet, ettringite, and kuzelite is explored as well. To this end, the tensile strain rate applied

in this study ranges from 0.0005/ps to 0.01/ps. Under tensile strains, the positions of atoms in the straining direction are remapped to fit within the new dimension. To ensure capturing the Poisson's effect, the directions perpendicular to the one under external strain are allowed to relax anisotropically. This can be achieved by using the *NPT* equations of motion at zero pressure in the lateral directions. Along the straining direction, the pressure evolution is considered as an internal stress. The application of tensile strain, which is repeated for all the three axes (*x*, *y*, and *z*), continues each time until the target strain of 0.50 is reached. By applying large strains, i.e., beyond the elastic limit, the full structural response of the C_3A hydrated products to tensile strains is captured. This makes it possible to analyze the mechanical failure mechanisms of hydrogarnet, ettringite, and kuzelite in different straining directions. The stress and strain in the straining direction are recorded to generate the stress-strain curves, which are used to characterize the mechanical properties of the crystalline structures under consideration. The changes in the size of supercells perpendicular to the straining direction are also monitored to calculate the corresponding Poisson's ratios. For further chemical bond and structural damage analyses, 1,000 strained structural configurations are recorded. The Open Visualization Tool (OVITO) package is utilized to demonstrate the simulation results (Stukowski, 2010).

2.4 Stress-Strain Relationships

2.4.1 Hydrogarnet

Hydrogarnet has a cubic unit cell with the structural features identical in all the three orthogonal directions. Because of the high symmetry present in the structure of hydrogarnet, the octahedral chains of $[Al(OH)_6]^{3-}$ and divalent Ca^{2+} are uniformly distributed in the *x*, *y*, and *z* directions. This indicates that the mechanical behavior of hydrogarnet does not depend on the direction of applied strain. The stress-strain behavior of hydrogarnet in response to uniaxial tensile strain

applied at two strain rates of 0.001/ps and 0.0005/ps is shown in Figure 2-4. From the stress-train curves, it is found that stress increases with strain until it reaches a maximum value at which it abruptly drops to zero showing a brittle behavior. The stress-strain relationship, however, is found not reliable if a higher strain rate is employed. This is mainly because simulations with high strain rates will not allow the atoms to overcome the energy barriers that will result in bond breakage.

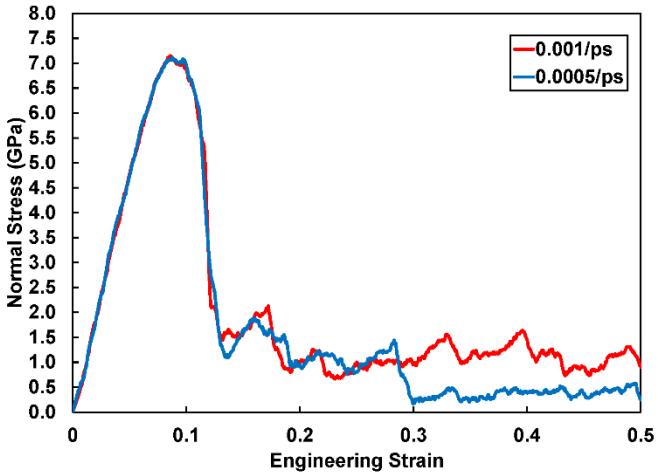

Figure 2-4. Stress-strain behavior of hydrogarnet under uniaxial tensile strain in the *x*, *y*, and *z* directions.

The changes in the number of bonds during the dynamics of tensile straining have been monitored in the current study to obtain a detailed insight into the failure mechanism of hydrogarnet. Figure 2-5 shows the normalized number of Ca-O, Al-O, and H-O bonds as a function of the tensile strain applied to the crystalline structure of hydrogarnet. It is observed that the number of Ca-O bonds undergoes a significant change as strain increases while the number of H-O bonds remain unchanged during the entire process. As for Al-O bonds, it is seen that the number of bonds does not change under small tensile strains. However, after the strain of 0.11 is reached, the number of Al-O as well as Ca-O bonds decreases and a fracture in the structure of hydrogarnet is initiated.

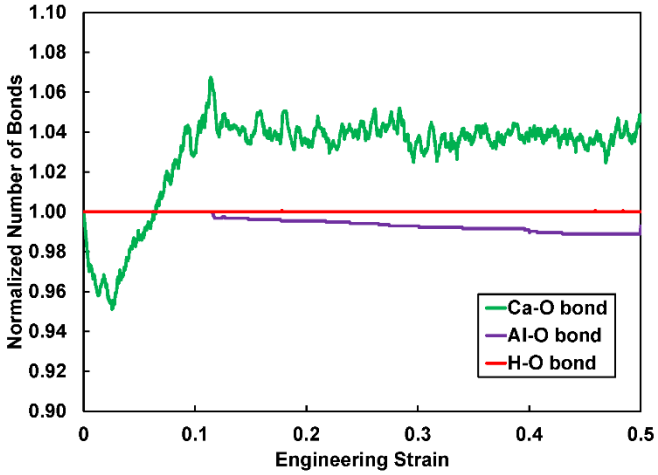

Figure 2-5. Changes in the number of bonds during the dynamics of mechanical straining of hydrogarnet.

A detailed structural damage analysis confirms that the breakage of Al-O and Ca-O bonds is primarily responsible for the mechanical failure of hydrogarnet under large tensile strains. Figure 2-6 displays the formation of damage in the structure of hydrogarnet subjected to uniaxial tensile strains in the *x* direction. In the initial stage of straining, i.e., up to 0.11, there is no observable change in the crystalline structure of hydrogarnet. As tensile strain increases, two voids appear due to the breakage of Al-O and Ca-O bonds. By further increasing the tensile strain, the voids grow and then coalesce forming a large crack perpendicular to the direction of applied tensile strain. It is interesting to note that even when the structure of hydrogarnet undergoes a large tensile strain, a long tricalcium aluminate chain remains unbroken and links the two fractured surfaces. Similar behavior was observed in the C-S-H gel subjected to tensile strains in the *y* direction when a long calcium silicate chain remained even after the target strain of 0.8 was reached (Hou et al., 2014b).

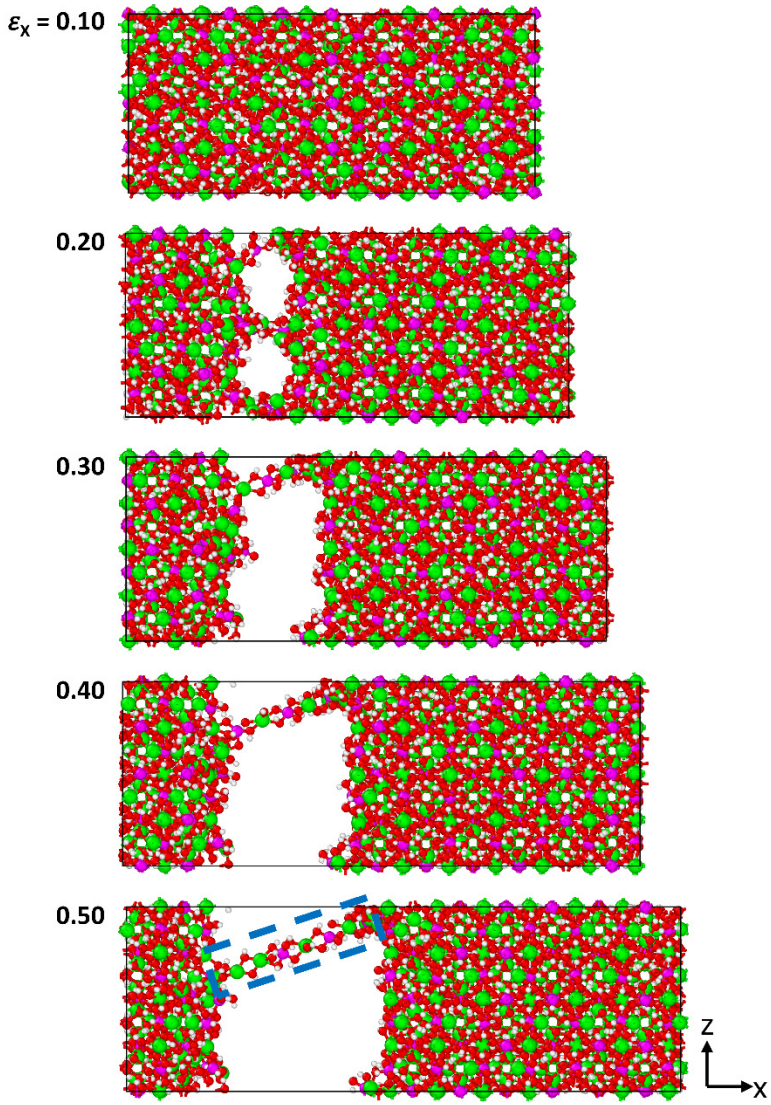

Figure 2-6. Damage to the atomic structure of hydrogarnet under tensile strains in the *x* direction. The dashed line displays the stretched tricalcium aluminate chain that links the two fractured surfaces. Initial cell parameters: a = 5.026 nm, $b = c$ = 2.513 nm, and $\alpha = \beta = \gamma = 90^{o}$. (Green: Ca; Pink: Al; Red: O; White: H)

2.4.2 Ettringite

Unlike hydrogarnet, the mechanical behavior of ettringite is noticeably dependent on the direction of applied tensile strain. This is due to the fact that the structural features of ettringite in the *x* and *y* directions are different from those in the *z* direction. The stress-strain behavior of ettringite subjected to tensile strain in the three main directions is presented in Figure 2-7. In the *x*

and *y* directions, after the ultimate stress is reached, stress gradually decreases with increasing the applied tensile strain. In the *z* direction, however, stress drops abruptly after the ultimate stress is reached, reflecting a brittle mechanical behavior. Further to the mode of failure, the magnitude of the ultimate stress in the *z* direction is found greatly different from the magnitude obtained in the *x* and *y* directions. To evaluate the effect of strain rate on the stress-strain relationship, four different strain rates of 0.01/ps, 0.005/ps, 0.001/ps, and 0.0005/ps are examined and the results are reported in Figure 2-7. The outcome indicates that reliable predictions for the stress-strain relationship in ettringite can be still achieved even with increasing the strain rate to 0.01/ps.

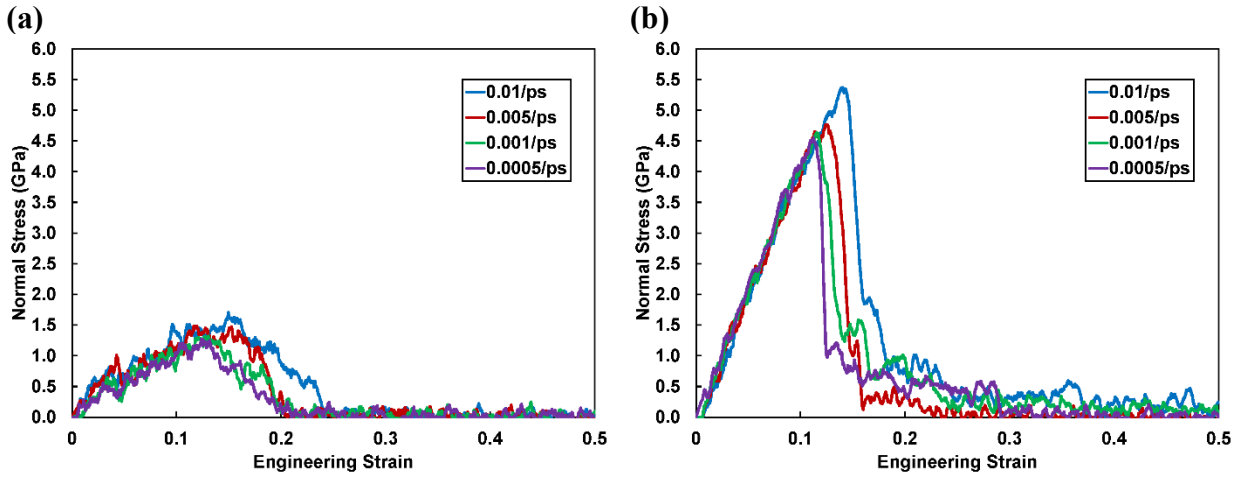

Figure 2-7. Stress-strain curves obtained for ettringite under uniaxial tensile strain in the (a) *x* and *y*, and (b) *z* direction.

The stress-strain relationship observed in different directions can be further understood using chemical bond analysis. The normalized number of Ca-O, Al-O, S-O, and H-O bonds at different tensile strains is presented in Figure 2-8. It can be seen that the number of Ca-O bonds changes significantly during the dynamics of tensile straining in all the three orthogonal directions. While the number of Al-O bonds in the *x* and *y* directions remains unchanged, this number experiences a sudden drop in the *z* direction when a strain level of 0.12 is reached. This observation can be supported by the fact that the covalent Ca-O bonds and high-energy Al-O bonds are expected to

contribute to resist the applied tensile strains as also reported by Liu et al. (2012). Contrary to Ca-O and Al-O bonds, the number of S-O and H-O bonds do not undergo observable changes in any strain direction. This indicates the minimal contribution of these chemical bonds to resist the external tensile strain.

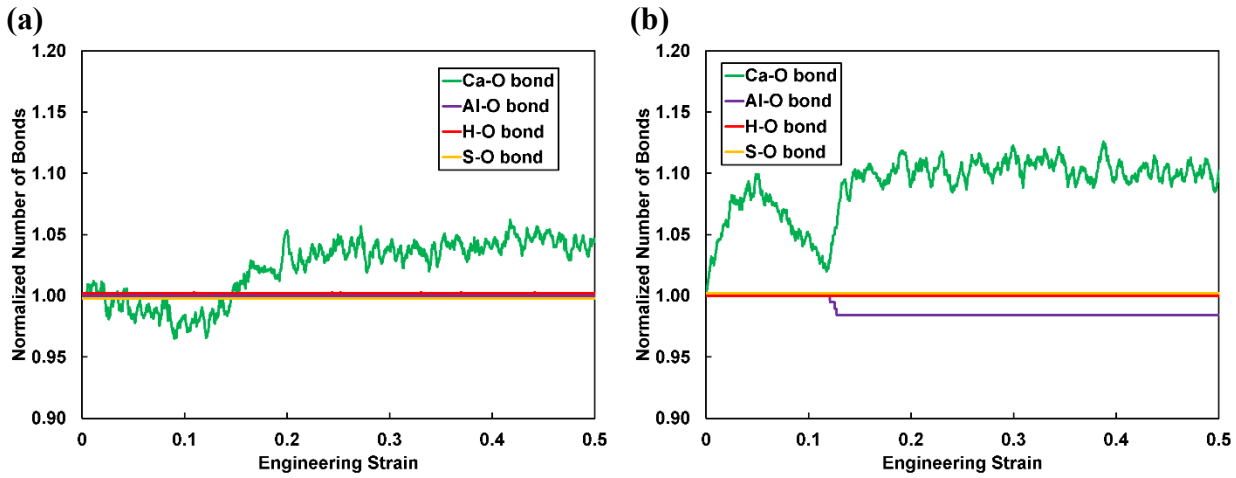

Figure 2-8. Changes in the number of bonds during the dynamics of mechanical straining of ettringite in the (a) *x* and *y*, and (b) *z* direction.

To understand the failure mechanism in different directions, the process of formation of damage in the atomic structure of ettringite is monitored. Figure 2-9 shows this process under tensile strains in the *z* direction. At lower strains, there are no noticeable changes in the atomic structure of ettringite and an elastic response is recorded. However, when strain increases, particularly after the yield stress is reached, there are major changes in the position of divalent Ca^{2+} and trivalent Al^{3-} ions. This is mainly due to the breakage of the Ca-O and Al-O bonds, which creates local voids inside the atomic structure. By further increasing the applied strain, the local voids propagate and coalesce. This eventually leads to the breakage of the C_3A columns into two halves and the loss of the entire structural capacity.

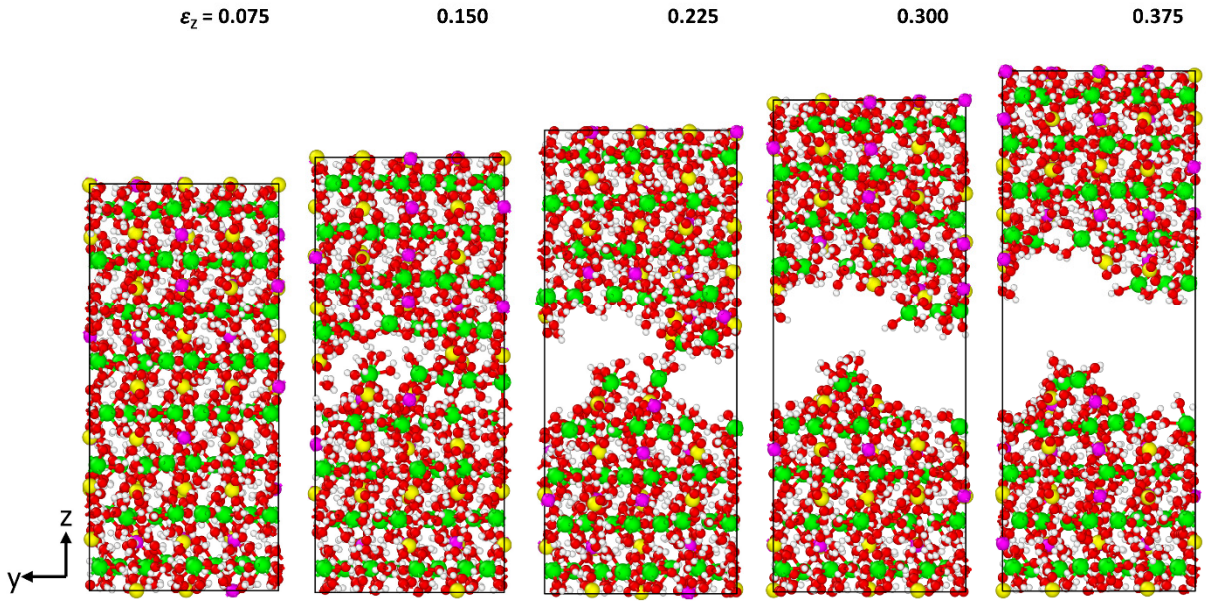

Figure 2-9. Damage to the atomic structure of ettringite under tensile strains in the *z* direction. Initial cell parameters: *a* = 1.934 nm, *b* = 2.233 nm, *c* = 4.271 nm, and *α* = *β* = *γ* = 90º. (Green: Ca; Pink: Al; Yellow: S; Red: O; White: H)

In the *x* and *y* directions, however, the failure mechanism is different. The SO_4^{2-} groups and water molecules that are located at the interstices between the C_3A columns provide structural stability to columnar conformation. Considering the similarities in the structural response of ettringite in the *x* and *y* directions, Figure 2-10 shows the progress of formation of damage to the atomic structure of ettringite under tensile strains in the *y* direction. As can be seen in this figure, after the $Ca - H_2O$ interactions are lost, the C_3A columns move apart from one another forming a large crack perpendicular to the strain direction. This results in a complete failure in the atomic structure of ettringite when the tensile strain is beyond 0.20.

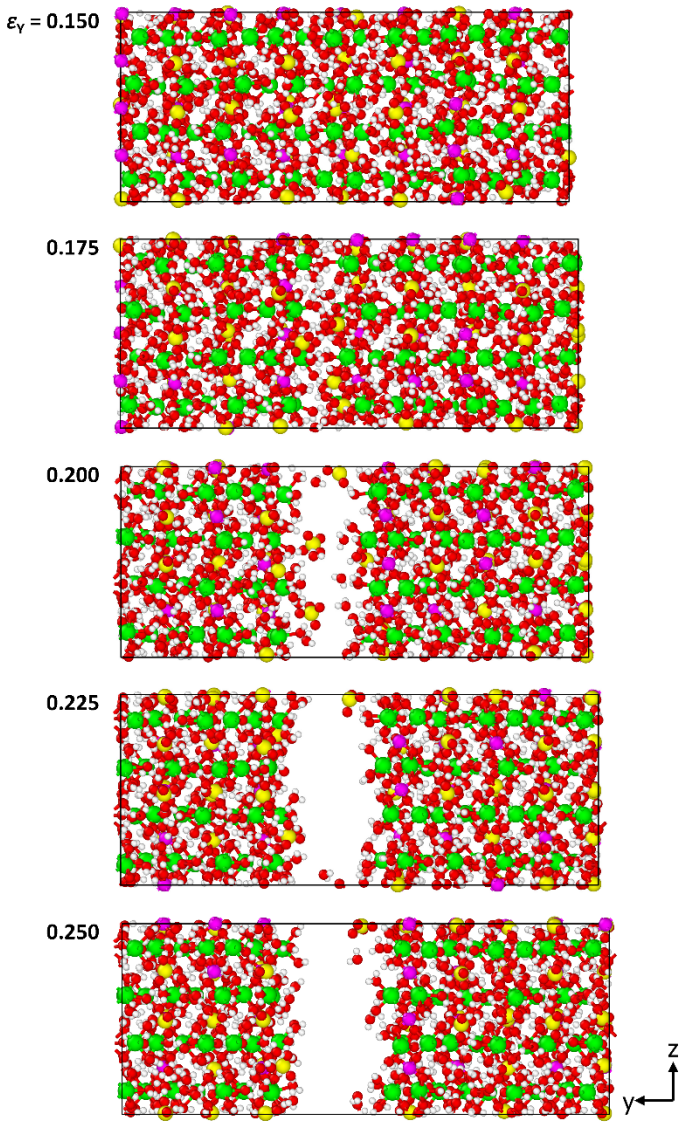

Figure 2-10. Damage to the atomic structure of ettringite under tensile strains in the *y* direction. Initial cell parameters: a = 1.934 nm, b = 4.467 nm, c = 2.135 nm, and $\alpha = \beta = \gamma =$ 90º. (Green: Ca; Pink: Al; Yellow: S; Red: O; White: H)

2.4.3 Kuzelite

Similar to ettringite, the mechanical behavior of kuzelite greatly depends on the direction of straining. Figure 2-11 shows the stress-strain curves for kuzelite under tensile strain in the three main directions. It can be observed that the stress-strain curves of kuzelite follow a similar shape in a sense that stress increases with strain and drops rapidly after the ultimate stress is reached.

The difference, however, is in the magnitude of recorded stress and strain values. The ultimate stress in the *x* and *y* directions is three to four times larger than that in the *z* direction.

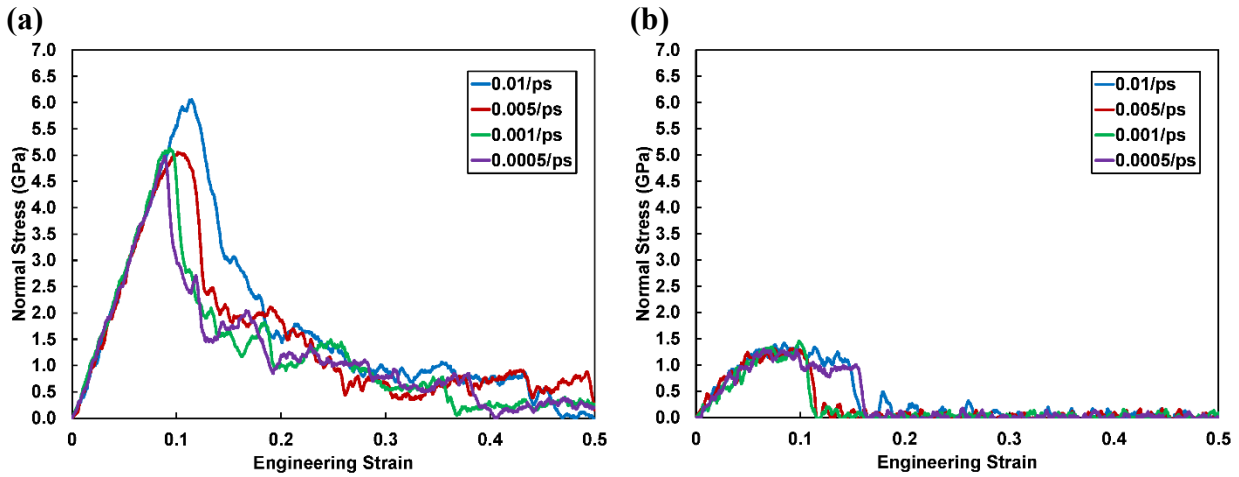

Figure 2-11. Stress-strain behavior of kuzelite under uniaxial tensile strain in the (a) *x* and *y*, and (b) *z* direction.

This significant difference is originated from the breakage and formation of Ca-O and Al-O bonds during the dynamics of tensile straining as reflected in Figure 2-12. This figure shows that the number of S-O and H-O bonds do not change under the applied tensile strain indicating that they have no major contribution to tensile resistance. A similar behavior has also been observed for ettringite as discussed earlier. Contrary to S-O and H-O bonds, the number of Ca-O bonds changes with strain highlighting the key role of the covalent Ca-O bonds in providing the tensile capacity of kuzelite. On the other hand, while the number of Al-O bonds remains constant in the *z* direction, the strong covalent-ionic Al-O bonds are stretched broken beyond 0.10 in the *x* and *y* directions. The improved tensile strength of kuzelite in the *x* and *y* directions can be attributed to the participation of both Ca-O and Al-O bonds when the tensile strain is applied.

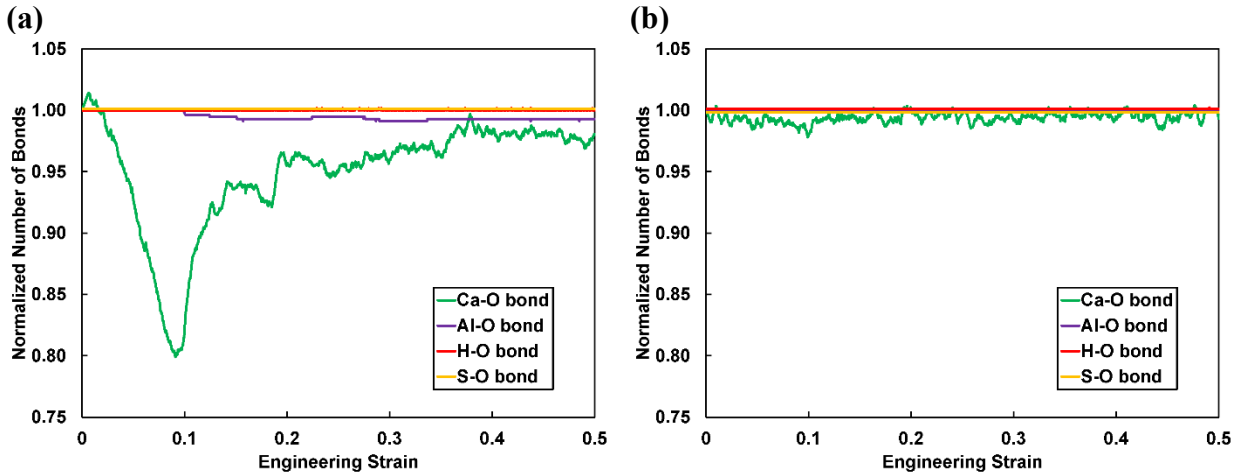

Figure 2-12. Changes in the number of bonds during the dynamics of mechanical straining of kuzelite in the (a) *x* and *y*, and (b) *z* direction.

Kuzelite has a brucite-like layered structure, which consists of $[Ca_2Al(OH)_6]^+$ cations. The space between the layers is filled with the $0.5SO_4^{2-}.3H_2O$ groups that neutralize the charge of the system. As highlighted in the bond analysis, the S-O bonds in none of the three directions contribute to resist tensile strain. Therefore, the strong $[Ca_2Al(OH)_6]^+$ layers remain responsible for the mechanical behavior of kuzelite. Figure 2-13 shows the damage formation process in the structure of kuzelite in the *x* and *y* directions. The sequential breakage of the Ca-O and Al-O bonds results in the formation of local low-density regions in the $[Ca_2Al(OH)_6]^+$ layers. As the tensile strain increases, the low-density regions grow, coalesce, and large voids are formed. In the *z* direction, the $Ca-H_2O$ bonds are stretched broken as the tensile strain increases. This situation causes the $[Ca_2Al(OH)_6]^+$ layers to move apart from one another, which creates a large crack in a plane perpendicular to the *z* direction (Figure 2-14). By further increasing the applied strain, the crack grows and significantly reduces the resistance against tensile strains. Therefore, the segregation of the $[Ca_2Al(OH)_6]^+$ layers can be considered as the cause of failure in the *z* direction.

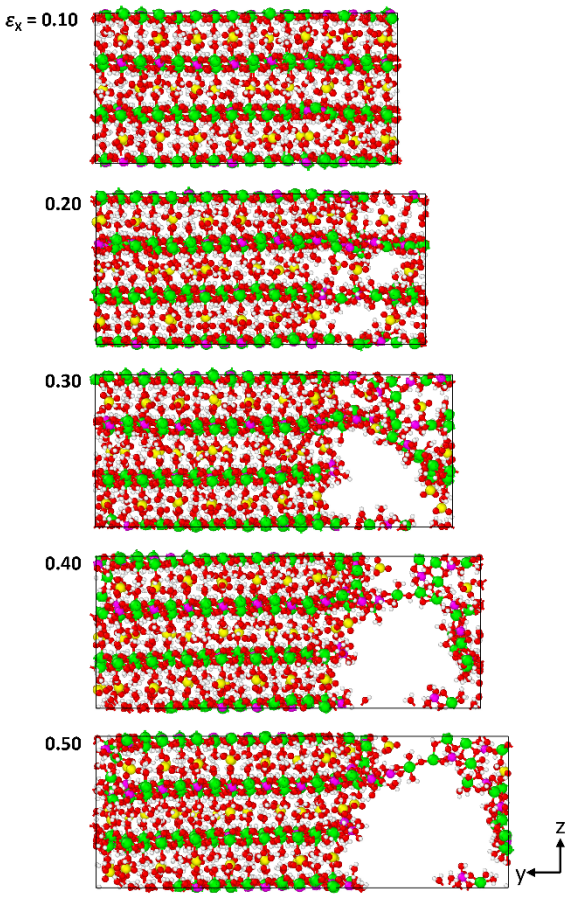

Figure 2-13. Damage to the atomic structure of kuzelite under tensile strains in the *y* direction. Initial cell parameters: *a* = 1.995 nm, *b* = 4.607 nm, *c* = 2.679 nm, and *α* = *β* = *γ* = 90º. (Green: Ca; Pink: Al; Yellow: S; Red: O; White: H)

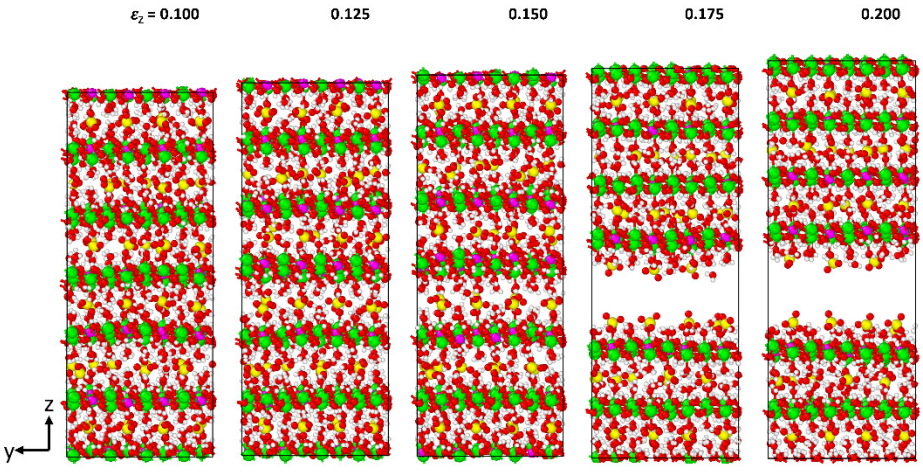

Figure 2-14. Damage to the atomic structure of kuzelite under tensile strains in the *z* direction. Initial cell parameters: *a* = 1.995 nm, *b* = 2.303 nm, *c* = 5.359 nm, and *α* = *β* = *γ* = 90º. (Green: Ca; Pink: Al; Yellow: S; Red: O; White: H)

2.5 Mechanical Properties

The stress-strain data obtained from RMD simulations provide invaluable information to fully characterize the mechanical properties of the hydrated phases of C_3A, in terms of Young's modulus, ultimate strength, and Poisson's ratio. The first two quantities can be directly extracted from the stress-strain curves presented in the previous section. Young's modulus (E) is a measure of material's stiffness, which can be quantified by the ratio of stress to strain along a specific axis as long as the Hooke's law holds. On the other hand, ultimate strength (σ_U) is defined as the maximum stress that a given material can withstand before it fails. Tables 2-2 to 2-4 summarize the Young's modulus and ultimate strength of the hydrated phases of C_3A obtained from the stress-strain curves for four strain rates. This is the first effort in the literature to quantify the sensitivity of the mechanical properties to the applied strain rate in the aluminum-rich species of hydrated cement paste. As expected, the Young's modulus and ultimate strength increase under high strain rates, mainly due to the fact that atoms have no sufficient time to make the necessary moves that accommodate the applied strain.

Table 2-2. Mechanical properties of hydrogarnet calculated from the response to strain in the *x*, *y*, and *z* directions at the strain rates of 0.0005, 0.001, 0.005, and 0.01/ps

	x/*y*/*z*				Others
Strain Rate (/ps)	**0.01**	**0.005**	**0.001**	**0.0005**	
***E* (GPa)**	94.54	94.89	92.87	93.03	54.9[a], 55.5[b]
σ_U (GPa)	7.33	7.19	7.15	7.11	NA

[a] Hajilar and Shafei (2015)
[b] Manzano (2009)

Table 2-3. Mechanical properties of ettringite calculated from the response to strain in the *x*, *y*, and *z* directions at the strain rates of 0.0005, 0.001, 0.005, and 0.01/ps

	x/*y*				*z*				Others
Strain Rate (/ps)	**0.01**	**0.005**	**0.001**	**0.0005**	**0.01**	**0.005**	**0.001**	**0.0005**	
***E* (GPa)**	10.00	9.24	9.96	9.05	43.63	40.97	42.93	41.98	29.7[a], 18.6[c], 25.0±2[d]
σ_U (GPa)	1.71	1.49	1.32	1.27	5.37	4.77	4.63	4.55	1.1-5.0[b]

[a] Hajilar and Shafei (2015)
[b] Liu et al. (2012)
[c] Manzano (2009)
[d] Speziale et al. (2008)

Table 2-4. Mechanical properties of kuzelite calculated from the response to strain in the *x*, *y*, and *z* directions at the strain rates of 0.0005, 0.001, 0.005, and 0.01/ps

	x/*y*				*z*				Others
Strain Rate (/ps)	**0.01**	**0.005**	**0.001**	**0.0005**	**0.01**	**0.005**	**0.001**	**0.0005**	
***E* (GPa)**	57.35	56.17	57.82	56.71	17.41	14.98	18.58	17.00	32.1[a], 29.1[b]
σ_U (GPa)	6.06	5.05	5.12	4.97	1.42	1.31	1.45	1.31	NA

[a] Hajilar and Shafei (2015)
[b] Manzano (2009)

The direction of straining is investigated in the current study to evaluate how the mechanical properties obtained for the hydrated phases of C_3A change in different directions. As for hydrogarnet, the Young's modulus does not depend on the direction of strain and is 93.03 GPa. The same quantity for ettringite and kuzelite ranges from 9.05 to 41.98 GPa and from 17.00 to 56.71 GPa, respectively. To verify the accuracy of predictions, the values obtained for Young's modulus are compared with the values reported in the literature based on the Brillouin spectroscopy, classical energy minimization, and molecular dynamics studies (Speziale et al., 2008; Manzano, 2009; Hajilar and Shafei, 2015). While none of the previous studies has investigated the stress-strain behavior of this category of materials, their estimates of the Young's modulus are consistent with the values calculated here based on the slope of the stress-strain curves. This is an important step forward as all the previous predictions of the Young's modulus are based on averaging the elastic constants without taking into account the dependency of the elastic properties of the hydrated phases of C_3A to the direction of straining.

The ultimate strength of the hydrated phases of C_3A under uniaxial tensile strains is determined from the stress-strain curves. While the ultimate strength of hydrogarnet is independent of straining direction, it is observed that ettringite and kuzelite have their highest tensile strengths along the *z* and *x*/*y* direction, respectively. The ultimate strengths of ettringite obtained through this study are in complete agreement with the values presented by Liu et al. (2012) in all the three orthogonal directions. For hydrogarnet and kuzelite, however, there is no experimental or simulation study

available in the literature to compare the obtained results with. In the absence of such studies, the physico-chemistry properties of the hydrated phases of C_3A are examined to evaluate the values predicted for the Young's modulus and ultimate strength. Since the nature of bonds in all the crystals under consideration is similar, it is expected that the crystalline structures with a higher density provide a higher mechanical strength. This fact can be verified from Figure 2-15. Moreover, it is known that as the ratio of the number of aluminum to calcium atoms (also known as Al/Ca ratio) increases in a unit cell, the mechanical properties of the crystalline structure is expected to improve (as can be seen in Figure 2-15). This is due to the fact that the aluminum atoms approach the oxygen atoms in the unit cell and high-energy covalent-ionic Al-O bonds are formed.

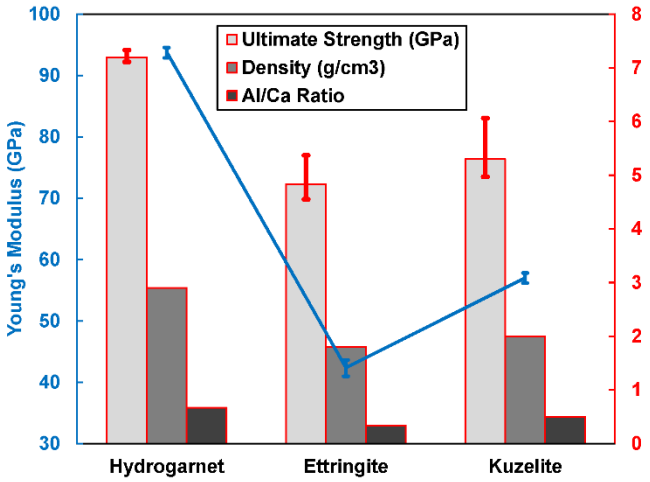

Figure 2-15. An overview of the relations identified between the mechanical properties obtained from the RMD simulations and the atomic structural characteristics reported for the hydrated products of C_3A.

When a material is stretched in one direction, it tends to shrink in the other two directions perpendicular to the direction of elongation. Poisson's ratio (v) is the measure of this effect and can be defined by the negative gradient of the transverse to axial strain in the elastic regime. The Poisson's effect is captured in the current study by allowing the supercells to relax anisotropically

in lateral directions. The Poisson's ratios of the hydrated phases of C_3A under different strain directions are listed in Table 2-5. The Poisson's ratios extracted from the transverse-axial strain curves are compared well with the available literature (Speziale et al., 2008; Manzano, 2009; Hajilar and Shafei, 2015). The Poisson's ratio of hydrogarnet is 0.32, while the same quantity for ettringite and kuzelite fall in the range of 0.10-0.69 and 0.13-0.37, respectively. Such a variation indicates the existence of a strong anisotropy in the mechanical properties of ettringite and kuzelite. It is interesting to note that the Poisson's ratio for ettringite and kuzelite may even reach 0.69 in the *x*/*y* directions and 0.37 in the *z* direction, respectively. The strongest elements in the structure of both crystals are the positively charged components, i.e., C_3A columns in ettringite stretched along the *z* axis and $[Ca_2Al(OH)_6]^+$ layers in kuzelite lying in the *x*-*y* plane. This is why the simulation cell is expanded/contracted easier in the directions perpendicular to the direction of these positively charged components.

Table 2-5. Poisson's ratio of hydrated products of C_3A

		Hydrogarnet		Ettringite		Kuzelite	
		y*/*x	***z***	***y*/*x***	***z***	***y*/*x***	***z***
Straining Direction	***x*/*y***	0.32	0.32	0.69	0.10	0.27	0.37
	z	0.32	-	0.35	-	0.13	-
Others		0.22[a], 0.35[b]		0.34[a], 0.39[b], 0.34±0.02[c]		0.36[a], 0.27[b]	

[a] Hajilar and Shafei (2015)
[b] Manzano (2009)
[c] Speziale et al. (2008)

2.6 Conclusions

In cementitious materials, tricalcium aluminate reacts with water and produces various hydrated products. While the concentration of such products depends on a number of factors ranging from the chemical composition of cement to the environment that it is exposed to, it is believed that a considerable amount of hydrogarnet, ettringite, and monosulfoaluminate crystals constantly exists in cementitious materials. The listed products have different structural and mechanical

characteristics, which can directly affect the properties of hydrated cement paste. Except very few studies limited to estimate the elastic properties of hydrogarnet, ettringite and monosulfoaluminate, there was no comprehensive simulation effort or experimental study in the literature to characterize the mechanical behavior of these three aluminum-rich crystals. This was the motivation of the present study to evaluate the stress-strain behavior of the hydrated phases of tricalcium aluminate under uniaxial tensile strains. For this purpose, the atomic structures of hydrogarnet, ettringite, and monosulfoaluminate were modeled at the nano-scale. The stress-strain curves of each crystal were then generated using RMD simulations that allows the breakage and formation of chemical bonds. For this purpose, a wide range of tensile strain rates was utilized to quantify the sensitivity of the mechanical properties to the strain rate as well. The effect of the direction of straining on the stress-strain behavior was particularly investigated by applying tensile strains in the three orthogonal directions. Chemical bond and structural damage analysis were conducted to reveal the correlation between the chemical bond characteristics and damaged atomic structures. It was found that the stress-strain relationship of hydrogarnet does not depend on the direction of applied tensile strain. The sequential breakage of the Ca-O and Al-O bonds was found to result in a significant reduction in the tensile strength after the yield stress is reached. Unlike hydrogarnet, the stress-strain relationship of ettringite and monosulfoaluminate is substantially dependent to the direction of applied tensile strains. The tricalcium aluminate columns in ettringite and $[Ca_2Al(OH)_6]^+$ layers in monosulfoaluminate are found mainly responsible for resisting tensile strains. The separation and sequential breakage of the tricalcium aluminate columns are the main causes of failure identified for ettringite in the *x*/*y* and *z* directions, respectively. As for monosulfoaluminate, the sequential breakage of the Ca-O and Al-O bonds of the $[Ca_2Al(OH)_6]^+$ layers results in the failure

of the atomic structure in the *x* and *y* directions. In the *z* direction, however, the segregation of the positively charged layers is identified as the main cause of failure under large strains.

2.7 References

1- Albino V., Cioffi R., Marroccoli M., and Santoro L., 1996. "*Potential application of ettringite generating systems for hazardous waste stabilization*", Journal of Hazardous Materials 51: 241-252.

2- Ali M.M., Gopal S., and Handoo S.K., 1994. "*Studies on the formation kinetics of calcium sulphoaluminate*", Cement and Concrete Research 24 (4): 715-720.

3- Allen M., and Tildesley D., 1987. "*Computer simulation of liquids*", New York: Oxford University Press.

4- Allmann R., 1997. "*Refinement of the hybrid layer structure* $[Ca_2Al(OH)_6]^+.[1/2SO_4.3H_2O]^-$ ". Neus Jahrbuch fur Mineralogie Monatshefte 4: 136-144.

5- Chrysochoou M., and Dermatas D., 2006. "*Evaluation of eetringite and hydrocalumite formation for heavy metal immobilization: Literature review and experimental study*", Journal of Hazardous Materials 136: 20-33.

6- Hartman M., and Berliner R., 2006. "*Investigation of the structure of ettringite by time-of-flight neutron powder diffraction techniques*". Cement and Concrete Research 36(2): 364-370.

7- Hajilar S., and Shafei B., 2014. "*Nano-scale characterization of elastic properties of AFt and AFm phases of hydrated cement paste*". Computational Modeling of Concrete Structures 1: 299-306.

8- Hajilar S., and Shafei B., 2015. "*Nano-scale investigation of elastic properties of hydrated cement paste constituents using molecular dynamics simulations*". Computational Materials Science 101: 216-226.

9- Hou D., Zhao T., Ma H., Li Z., 2015. "*Reactive molecular simulation of water confined in the nanopores of the calcium silicate hydrate gel: structure, reactivity, and mechanical properties*", The Journal of Physical Chemistry C 119(3): 1346-1358.

10- Hou D., Ma H., Yu Z., Li Z., 2014a. "*Calcium silicate hydrate from dry to saturated state: Structure, dynamics and mechanical properties*". Acta Materialia 67: 81-94.

11- Hou D., Youyuan Y., and Li Z., 2014b. "*Mechanical properties of calcium silicate hydrate (C-S-H) at nano-scale: A molecular dynamics study*", Materials Chemistry and Physics 146: 503-511.

12- Lager G., Armbruster T., and Faber J., 1987. "*Neutron and X-ray diffraction of hydrogarnet $Ca_3Al_2(O_4H_4)_3$*". American Mineralogist 72: 756-765.

13- Lea F.M., and Hewlett P.C., 1998. "*Lea's chemistry of cement and concerte*". 4th edition, Oxford: Elsevier Butterworth-Heinemann.

14- Liu P., and Wang Y., 1999. "*Tight-binding molecular-dynamics study of a copper oxide Cu_4O*", Materials and Design 20: 291-295.

15- Liu L., Jaramillo-Botero A., Goddard III W.A., and Sun H., 2012. "*Development of a ReaxFF reactive force field for ettringite and study of its mechanical failure modes from reactive molecular dynamics*", Journal of Physical Chemistry A 116(5): 3918-3925.

16- Manzano H., 2009. "*Atomistic simulation studies of the cement paste components*", Guipúzcoa, Spain: PhD dissertation, Universidad del Pais Vasco.

17- Mehta P.K., and Monteiro P., 1993. "*Concrete: structure, properties, and materials*". 2nd edition, Englewood Cliffs, N.J.: Prentice Hall.

18- Moore A., and Taylor H., 1968. "*Crystal structure of ettringite*", Nature 218(5146): 1048-1049.

19- Mortier W., Ghosh S.K., and Shankar S., 1986. "*Electronegativity equalization method fo the calculation of atomic charges in molecules*", Journal of American Chemical Society 108: 4315-4320.

20- Paul M., and Glasser F.P., 2000. "*Impact of prolonged warm (85˚C) moist cure on Portland cement paste*". Cement and Concrete Research 30(12): 1869-1877.

21- Pellenq R.J.M., Kushima A., Shahsavari R., Van Vliet K.J., Buehler M.J., Yip S., and Ulm F.J., 2009. "*A realistic molecular model of cement hydrates*", Proceedings of the National Academy of Sciences of the United States of America 106(38): 16102-16107.

22- Pera J., and Ambroise J., 2004. "*New application of calcium sulfoaluminate cement*", Cement and Concrete Research 34: 671-676.

23- Plimpton S., 1995. "*Fast Parallel Algorithms for Short-Range Molecular Dynamics*". Journal of Computational Physics 117 (1): 1-19.

24- Speziale S., Jiang F., Mao Z., Monteiro P.J.M., Wenk H.R., Duffy T.S., and Schilling F.R., 2008. "*Single-crystal elastic constants of natural ettringite*". Cement and Concrete Research 38(7): 885-889.

25- Stukowski A., 2010. "*Visulization and analysis of atomistic simulation data with OVITO- the open visulization tool*". Modeling and Simulation in Materials Science and Engineering 18, 015012.

26- Taylor H.F.W., 1997. "*Cement Chemistry*", 2nd edition, London: Thomas Telford Publishing.

27- Taylor H.F.W., Famy C., and Scrivener K.L., 2001. "Delayed ettringite formation". Cement and Concrete Research 31(5): 683-693.

28- Tsai J.L., and Tu J.F., 2010. "*Characterizating mechanical properties of graphite using molecular dynamics simulations*", Materials and Design 31: 194-199.

29- van Duin A.C.T., Dasgupta S., Lorant F., and Goddard III W.A., 2001. "*ReaxFF: A reactive force field fo hydrocarbons*", Journal of Physical Chemistry A 105: 9396-9409.

30- Winnefeld F., and Lothenbach B., 2010. "*Hydration of calcium sulfoaluminate cements - Experimental findings and thermodynamic modeling*", Cement and Concrete Research 40: 1239-1247.

31- Wunderlich W., and Awaji H., 2001. "*Molecular dynamics – Simulations of the fracture toughness of sapphire*", Materials and Design 22: 53-59.

32- Xiao H., Long C., Tian X., and Li S., 2015. "*Atomistic simulations of the small xenon bubble behavior in U-Mo alloy*", Materials and Design 74: 55-60.

33- Zhang M., and Reardon E.J., 2003. "*Removal of B, Cr, Mo, and Se from wastewater by incorporation into hydrocalumite and ettringite*", Environmental Science and Technology 37: 2947-2952.

34- Zhang J.C., Chen C., Pei Q.X., Wan Q., Zhang W.X., and Sha Z.D., 2015. "*Ab initio molecular dynamics study of the local atomic structures in monatomic metallic liquid and glass*", Materials and Design 77: 1-5.

CHAPTER 3: ASSESSMENT OF STRUCTURAL, THERMAL, AND MECHANICAL PROPERTIES OF PORTLANDITE THROUGH MOLECULAR DYNAMICS SIMULATIONS

The structural, thermal, and mechanical properties of portlandite, the primary solid phase of ordinary hydrated cement paste, are investigated using molecular dynamics method. To understand the effects of temperature on the structural properties of portlandite, the coefficients of thermal expansion of portlandite are determined in the current study and validated with what reported from the experimental tests. The atomic structure of portlandite equilibrated at various temperatures is then subjected to uniaxial tensile strains in the three orthogonal directions and the stress-strain curves are developed. Based on the obtained results, the effect of the direction of straining on the mechanical properties of portlandite is investigated in detail. Structural damage analysis is performed to reveal the failure mechanisms in different directions. The energy of the fractured surfaces are calculated in different directions and compared to those of the ideal surfaces available in the literature. The key mechanical properties, including tensile strength, Young's modulus, and fracture strain, are extracted from the stress-strain curves. The sensitivity of the obtained mechanical properties to temperature and strain rate is then explored in a systematic way. This leads to valuable information on how the structural and mechanical properties of portlandite are affected under various exposure conditions and loading rates.

3.1 Introduction

To improve the available models of cement-based materials at macro-, micro-, and nano-scale, it is necessary to determine the intrinsic properties of the ordinary hydrated cement paste (HCP) products. Among the HCP products, portlandite is known as the primary solid phase, which constitutes 20-25% of the volume of ordinary cement paste (Mehta and Monteiro, 2006). In cement-based materials, such as concrete and mortar, portlandite is formed as a result of reactions

between water and cement clinkers, i.e., tricalcium silicate (alite) and dicalcium silicate (belite). During the exothermic hydration reactions, thermal stresses are generated, which can cause early-age cracking and structural damage. This highlights how critical it is to determine the temperature-dependent structural and mechanical properties of the HCP products, particularly portlandite. The thermo-elastic properties of portlandite were investigated first by Fukui et al. (2003) using in-situ X-ray diffraction. Xu et al. (2007) studied the anisotropic thermal expansion and hydrogen bonding behavior of portlandite via high-temperature neutron diffraction tests. There was a substantial difference between the coefficients of thermal expansion (CTEs) calculated by Xu et al. (2007) compared to those obtained by Fukui et al. (2003). This was attributed to the fact that Fukui et al. (2003) calculated the lattice parameters using the conventional least-squares analysis of selected individual reflection lines, whereas Xu et al. (2007) employed the more accurate whole-pattern Rietveld method to calculate the same quantities. Beyond these two studies, no other investigation on the thermal properties of portlandite was found in the literature. This was one of the main motivations of the current study to characterize the changes in the structural and mechanical properties of portlandite as a function of temperature.

A number of experimental and theoretical studies have been conducted to determine the elastic properties of portlandite. The initial experimental studies include Brillouin interferometry (Holuj et al., 1985), tests of compacted powder samples with different porosities (Beaudoin, 1983, and Wittmann, 1986), and compression tests (Maede and Jeanloz, 1990). Based on the experimental test results, Monteiro and Chang (1995) calculated the elastic properties of portlandite from the mathematical morphology of concrete. Later on, Laugesen (2005) calculated the elastic constants of portlandite using density functional theory (DFT); Constantinides and Ulm (2007) performed nano-indentation experiments to directly find the indentation and Young's moduli and Poisson's

ratio of portlandite; and Speziale et al. (2008) estimated the elastic properties of natural calcium hydroxide, including all the adiabatic elastic constants and acoustic velocities using the Brillouin spectroscopy. In the most recent studies, Manzano et al. (2009) and Qomi et al. (2015) estimated the elastic properties of the portlandite using molecular mechanics (MM) method. Despite the contribution of the listed studies, there is a gap in the literature on the mechanical behavior of portlandite beyond the elastic range. Considering that this is critical to capture the onset of permanent deformations and fracture, the current study provides the first-known effort to address this research gap. The outcome of this effort also contributes to estimate the tensile strength and failure strain of portlandite subjected to extreme external loads.

The structure, energetics, and reactivity of the portlandite's surfaces have been investigated in the literature. Kalinichev and Kirkpatrick (2002) performed molecular dynamics (MD) simulations to study the binding of chloride ions to the surfaces of various HCP phases, including portlandite. It was observed that the chloride binding capacity of portlandite is significantly higher than that of tobermorite and ettringite, the other two abundant phases of the HCP. Through a set of MD simulations, Wang et al. (2006) reported that for water at the portlandite's (001) surface, the $Ca_3{}^{VI}OH$ surface functional groups serve as both H-bond donors and acceptors. Galmarini et al. (2011) performed systematic experimental tests and atomistic simulations to study the change in the morphology of portlandite in the environments where various ions, such as chlorides, nitrates, sulfates, and silicates exist. It was revealed that the portlandite particles have a regular facetted shape in the presence of chloride and nitrate ions, whereas the sulfate groups result in the formation of portlandite particles with a hexagonal platelet shape. Moreover, it was found that the addition of silicates leads to the formation of large agglomerated particles that are irregularly shaped. The hydration of CaO was investigated using reactive MD simulations by Manzano et al. (2012a). It

was reported that the CaO {001} surface is highly reactive toward water and maintains its structure only up to 0.75 water monolayer content. For a higher water content, however, the surface is altered drastically, which results in the formation of disordered calcium hydroxide. The listed studies contribute to provide a more detailed insight on how the properties of the fractured surfaces of portlandite identified in the current study are compared with those of the ideal surfaces available in the literature.

In this study, the Molecular Dynamics (MD) method is utilized to investigate the structural, thermal, and mechanical properties of portlandite. To this end, the crystalline structure of portlandite is constructed at the nano-scale. The effect of temperature on the lattice parameters and unit cell volume of portlandite is investigated. The CTEs are then determined and compared to those available to the literature. Subsequently, uniaxial tensile strains are applied in the x, y and z axis of the equilibrated super cells and the stress-strain data are recorded. A separate structural damage analysis is performed to reveal the correlation between the structural damages and the stress-strain curves obtained from MD simulations. The failure mechanism for portlandite elongated in the three orthogonal directions is identified and discussed in detail. To understand the plastic energy required for fracture, the energy of the fractured surfaces are calculated and compared with those for the ideal surfaces. From the stress-strain curves, the tensile strength, Young's modulus, and fracture strain of portlandite are fully characterized as well. As the algorithm used in this study allows for anisotropic relaxation in the directions perpendicular to the direction of straining, the Poisson's effect can be simulated without imposing any artificial constraints. To investigate the sensitivity of the mechanical properties of portlandite to temperature and strain rate effects, an extensive set of MD simulations are conducted under different temperatures and strain rates. From the obtained results, the relationship between the fracture stress

of portlandite and strain rate is determined at various temperatures. The outcome of this study provides the information needed to understand the key mechanical properties of portlandite at both elastic and plastic ranges. This directly contributes to improve the models available for cement-based materials at different length scales.

3.2 Computational Methodology

3.2.1 Crystalline Structure

Portlandite is the mineral name of crystalline calcium hydroxide, $Ca(OH)_2$, and is the calcium analogue of brucite ($Mg(OH)_2$). In cement-based materials, portlandite is produced through the hydration of tricalcium silicate (Ca_3SiO_5) and dicalcium silicate (Ca_2SiO_4) as shown in Equations (3-1) and (3-2), respectively:

$$2Ca_3SiO_5 + 6H_2O \rightarrow 3CaO.2SiO_2.3H_2O + 3Ca(OH)_2 \quad (3\text{-}1)$$

$$2Ca_2SiO_4 + 4H_2O \rightarrow 3CaO.2SiO_2.3H_2O + Ca(OH)_2 \quad (3\text{-}2)$$

where the first product in both reactions ($3CaO.2SiO_2.3H_2O$) is the calcium-silicate-hydrates (C-S-H) gel, which is another important component of the HCP. While the two chemical reactions are similar in terms of the compounds produced (i.e., C-S-H gel and portlandite), they demonstrate different reaction rates. This is why the first reaction is known to be responsible for early-age strength, while the second one, which has a lower reactivity, contributes to the strength of the HCP in later stages. Portlandite is expected to decompose into calcium oxide and water when it is heated to 500 °C (Halstead and Moore, 1957):

$$Ca(OH)_2 \xrightarrow{\Delta} CaO + H_2O \quad (3\text{-}3)$$

The crystalline structure of portlandite is well known and has been identified by both X-ray spectroscopy (Bernal and Megaw, 1935; Petch and Megaw, 1954) and neutron diffraction (Busing and Levy, 1957). The position of hydrogen atoms in the crystalline structure of portlandite has

been determined using X-ray diffraction and Fourier synthesis techniques (Petch, 1961) and ^{1}H nuclear magnetic resonance (NMR) (Henderson and Gutowsky, 1962). While portlandite has a hexagonal morphology, the crystalline structure is trigonal with space group of $P\bar{3}m1$. The crystallographic parameters of the unit cell of portlandite is $a = b = 3.5925$ Å, $c = 4.905$ Å, $\alpha = \beta = 90°$, and $\gamma = 120°$. Figure 3-1 illustrates the unit cell of portlandite, which contains a total of five atoms. The calcium atoms are octahedrally coordinated with six oxygen atoms. The oxygen atoms are tetrahedrally coordinated with three calcium atoms and one hydrogen atom. The structure of portlandite consists of layers lying in the (001) plane and interacting mainly by weak *H*-mediated dispersive forces. The oxygen and hydrogen atoms form hydroxyl groups running along the *c*-axis. In this study, the crystalline structure of portlandite is adopted based on the experimental data by Henderson and Gutowsky (1962).

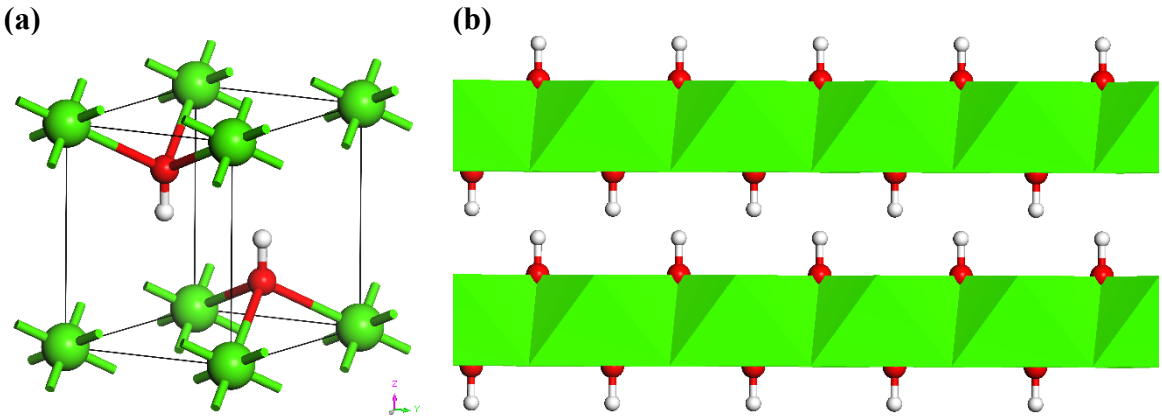

Figure 3-1. (a) The trigonal unit cell and (b) the layered structure of portlandite. (Green: Calcium; Red: Oxygen; White: Hydrogen)

3.2.2 Molecular Dynamics Method

The MD simulations are conducted using the large-scale atomic/molecular massively parallel simulator (LAMMPS) package (Plimpton, 1995). As mentioned earlier, portlandite crystallizes in a trigonal lattice (*a*, *b*, and *c* axes). To generate the simulation cell, the unit cell of portlandite is periodically extended 12, 12, and 9 times in the *a*, *b*, and *c* directions, respectively. This generates

the super cell of portlandite, which contains 6,480 atoms. It is notable that the large number of atoms used in this study ensures reliable simulation results from a statistical point of view. The modified CSH-FF force-field (Qomi et al., 2015) is chosen for the current study to describe the atomic interactions. The CSH-FF force-field was originally developed to reproduce the structural and elastic properties of various CSH crystals comparable to those obtained using first principle calculations (Shahsavari et al., 2011). Recently, Qomi et al. (2015) modified the CSH-FF force-field to predict the structure and mechanical properties of other crystals, such as calcium hydroxide (portlandite), tricalcium silicate (alite), and dicalcium silicate (belite). To ensure the structural stability and conformity of portlandite in the ambient conditions, the 12×12×9 super cell of portlandite is equilibrated using the modified CSH-FF for 100 ps in an isobaric-isothermal (*NPT*) ensemble at 300 K and 0 atm with a time step of 0.10 fs. The last 50 ps trajectories are used for computing the unit cell parameters. During the equilibration stage, the convergence of a variety of parameters (e.g., total energy and its components, lattice parameters, temperature, and pressure) is closely monitored. During the equilibration stage, the long-range Coulombic interactions are calculated using the Wolf method (Wolf et al., 1999) with a cutoff radius of 12 Å and damping parameter of 0.25 (1/ Å). Since the Wolf summation method scales with O(N) compared to the Ewald summation method that scales with O($N^{3/2}$), the former reduces the computational time significantly compared to the later method. This is also another feature incorporated to the modified CSH-FF force-field. The equilibrated atomic structure of portlandite is employed for the characterization of the stress-strain behavior at both elastic and plastic regimes.

3.2.3 Elastic Properties Calculation

The elastic constants of portlandite are calculated from the linear relation between the stress and strain tensors within the limit of infinitesimal deformation. In this study, the elastic constants

are calculated at the finite temperature. For this purpose, the simulations start with the super cell of portlandite equilibrated to the ambient conditions (300 K and 0 atm). The equilibrated super cell is then subjected to twelve strain configurations, including three uniaxial tension/compression pairs and three pure shear pairs, in such a way that only one component of the strain tensor is non-zero. In this study, the target strain in each of the strain configurations has been set equal to a value that ensures the deformations will remain in the elastic range. During the course of elastic straining, the position of atoms in the super cell is equilibrated in a microcanonical (*NVE*) ensemble coupled with a Langevin thermostat, which keeps the temperature at 300 K. It should be noted that although the calculation of elastic constants at ambient temperature requires obtaining the time averages of stress components, it provides the opportunity of capturing the thermal expansion of the unit cell at finite temperatures. This could not be achieved if the elastic constants had been calculated at zero temperature. Once the elastic constants are determined, the Voigt-Reuss-Hill (VRH) elastic properties of portlandite are estimated according to the method described in Hajilar and Shafei (2014, 2015(a) and 2015(b), 2016). The obtained elastic properties are then compared with the theoretical and experimental ones available in the literature.

3.2.4 Uniaxial Tensile Straining

The equilibrated super cell of portlandite is subjected to a range of uniaxial strains along each of the three orthogonal *x*, *y*, and *z* directions. For this purpose, a constant strain rate is applied to the super cell. In the current study, four different strain rates of 0.0005, 0.001, 0.005, and 0.01 ps^{-1} are used. During the continuous straining, the positions of atoms in the super cell are fully relaxed to fit within new dimensions. It should be noted that the directions perpendicular to the one under external strain are allowed to relax anisotropically. This makes it possible to capture the Poisson's effect for the stress-strain calculations. To achieve this goal, the *NPT* equations of motion at zero

pressure are used in the directions perpendicular to the direction of straining. The stress evolution in the atomic structures is recorded while the super cells are strained. To mitigate the stress changes induced by thermal fluctuations, the atomic stresses are averaged over a small time interval of 100 time steps. The straining procedure is repeated for all the three *x*, *y*, and *z* directions with the maximum target strain of 0.25 Å/Å. The full set of stress and strain data of the portlandite structure are used to generate the stress-strain curves for each straining direction. To examine the stress-strain behavior, the strained structural configurations are recorded for further structural damage analysis. The structural damage analysis is carried out by visualizing the atomic structures and tracking the changes in the position and orientation of atoms at each time step. The permanent changes in the atomic structure of portlandite are identified and used to understand the damage formation process. The outcome of the structural damage analysis can be used to fully characterize the structural response and failure mechanisms of portlandite under uniaxial tensile strains. The Open Visualization Tool (OVITO) package is utilized to demonstrate the simulation results (Stukowski, 2010).

3.3 Results and Discussions

3.3.1 Structural and Thermal Properties of Portlandite

The cell parameters of portlandite equilibrated over the course of 100 ps *NPT*-MD at ambient temperature and pressure are reported in Table 3-1. It can be seen that the calculated unit cell parameters are in a close agreement with the experimental data and the percentage of difference is always less than 2.5%. In addition to the equilibration at ambient temperature (300 K), the cell parameters of portlandite are further investigated at various temperatures ranging from 300 to 500 K with 50 K intervals. Figure 3-2 illustrates the normalized volume and unit cell parameters of portlandite at various temperatures.

Table 3-1. Comparison between portlandite cell parameters calculated by *NPT*-MD and those obtained from the experiments by Henderson and Gutowsky (1962)

Cell Parameter	*NPT*-MD	Experiment	Difference (%)
***a*/*b* (Å)**	3.5037	3.5925	2.47
***c* (Å)**	4.8045	4.9050	2.05

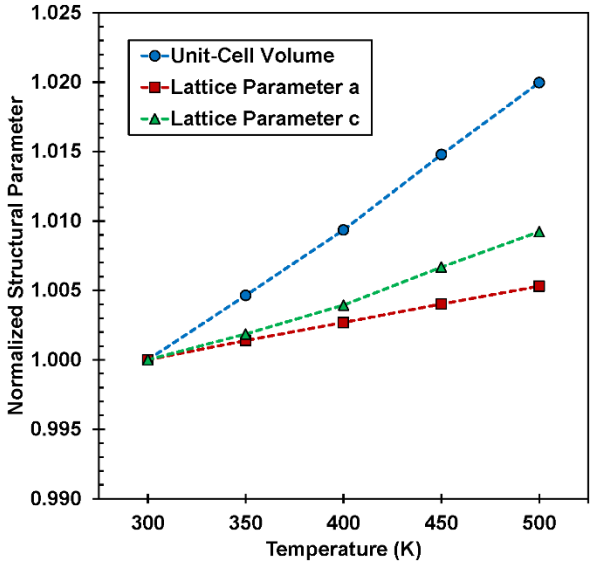

Figure 3-2. Thermal expansion of portlandite between 300 and 500 K.

This figure shows that the volume of the unit cell expands by 2% as the temperature increases from 300 to 500 K. It can be observed that the *c*-axis expands twice as the *a*-axis within the temperature range considered in this study. This is attributed to the major difference in the structural features of portlandite in the direction parallel (*a*-axis direction) and perpendicular (*c*-axis direction) to the strong (001) [CaO_6] octahedral layers: In the *a*-axis direction, the Ca-O bonds resist the expansion due to temperature. In the *c*-axis direction, however, the interlayer only relies on the hydroxyl groups and expands significantly by increasing the temperature. This highlights the fact that the forces between neighboring [CaO_6] sheets are much weaker than those within the sheets. Table 3-2 reports the coefficients of thermal expansion (CTEs) of portlandite at various temperature ranges considered in this study.

Table 3-2. Coefficients of thermal expansion (CTEs) calculated for the structural parameters of portlandite under four temperature ranges.

	NPT-MD				
	300-350 K	**350-400 K**	**400-450 K**	**450-500 K**	**Mean**
α_V **(×10^{-5} K^{-1})**	9.27	9.37	10.77	10.21	9.91
α_a **(×10^{-5} K^{-1})**	2.77	2.60	2.65	2.56	2.65
α_c **(×10^{-5} K^{-1})**	3.71	4.15	5.46	5.06	4.60

The mean volume, *a*-axis, and *c*-axis CTEs of portlandite in the temperature range of 300-500 K are found to be $\alpha_V = 9.91 \times 10^{-5}$ K^{-1}, $\alpha_a = 2.65 \times 10^{-5}$ K^{-1}, and $\alpha_c = 4.60 \times 10^{-5}$ K^{-1}, respectively. The range and magnitude of the values obtained from MD simulations are consistent with the ones obtained through the high-temperature neutron diffraction experiments (Xu et al., 2007). To estimate the unit cell volume and lattice parameters of portlandite at any desired temperature in the range of 300-500 K, a polynomial equation is fitted to the thermal expansion data obtained from MD simulations:

$$V(T) = V_0 \, exp[\int \alpha(T) dT] \tag{3-4}$$

where V_0 and V denote the reference and current unit cell volume, respectively. $\alpha(T)$ is the CTE at temperature *T* and is derived from the linear equation below:

$$\alpha(T) = \alpha_0 + \alpha_1 T \tag{3-5}$$

Table 3-3 summarizes the fitting parameters, i.e., α_0 and α_1, of portlandite together with those available in the literature. The values obtained from MD simulations are found closer to those calculated by the latest neutron diffraction experiments (Xu et al., 2007) than those estimated by the conventional X-ray diffraction tests (Fukui et al., 2003). This outcome proves the prediction capabilities of the conducted MD simulations as Xu et al. (2007) is believed to provide more reliable predictions due to the reasons discussed earlier.

Table 3-3. Comparison of thermal expansion parameters fitted to *NPT*-MD simulation results with those available in the literature.

	***NPT*-MD**	**Fukui et al. (2003)**	**Xu et al. (2007)**
α_0 (× 10^{-5} K^{-1})	8.392	0.0342	5.966
α_1 (× 10^{-8} K^{-2})	6.759	12.736	3.333

3.3.2 Elastic Properties of Portlandite

Elastic properties of portlandite are presented and discussed in this section. Portlandite crystallizes in the trigonal system with a space group of $P\bar{3}m1$. Therefore, portlandite has 6 independent non-zero elastic constants: C_{11}, C_{12}, C_{13}, C_{14}, C_{33}, and C_{44}. From C_{11} and C_{12}, C_{66} can be calculated as below:

$$C_{66} = 0.5(C_{11} - C_{12}) \tag{3-6}$$

Table 3-4 summarizes the elastic constants of portlandite obtained from MD simulations together with those determined from Brillouin spectroscopy tests (Holuj et al., 1985; Speziale et al., 2008) as well as density functional theory (DFT) calculations (Laugesen, 2005). The elastic constants obtained in the current study are in a reasonable agreement with the values reported in the literature. It is observed that the axial and transverse elastic constants in the (001) plane are 2.5 times larger than those that include the *c*-axis component. This is consistent with the literature as well. For example, Table 3-4 shows that C_{11} is about three times larger than C_{33}. This indicates that portlandite is much stiffer in the direction parallel to the (001) [CaO_6] octahedral sheets than the directions perpendicular to them. Similar behavior was also observed in the previous section for the thermal expansion of portlandite. The direction sensitivity of the mechanical properties of portlandite can be further investigated by analyzing the full stress-strain curves in different directions. As mentioned earlier, a number of experimental and theoretical studies have been performed to determine the elastic properties of portlandite (i.e., Beaudoin, 1983; Holuj et al., 1985; Wittmann, 1986; Maede and Jeanloz, 1990; Monteiro and Chang, 1995; Laugesen, 2005;

Constantinides and Ulm, 2007; Speziale et al., 2008; Manzano et al., 2009; Qomi et al., 2015). It can be seen that the MD Voigt, Reuss and Voigt-Reuss-Hill elastic properties are in a good agreement with those reported in the literature. This highlights that the modified CSH-FF parameters are capable of capturing the mechanical properties of portlandite.

Table 3-4. Elastic properties of portlandite obtained from MD simulations, Brillouin spectroscopy tests, density functional theory (DFT), and other methods

	MD	Brillouin[k]	DFT [g]	Brillouin [e]	Others
C_{11} (GPa)	96.78	99.28	99.39	102.0	
C_{12} (GPa)	37.06	36.21	30.78	32.0	
C_{13} (GPa)	15.70	29.65	7.36	8.4	
C_{14} (GPa)	3.13	$\approx 0^{*}$	$\approx 0^{*}$	4.5	
C_{33} (GPa)	33.86	32.60	36.29	33.6	
C_{44} (GPa)	3.18	9.85	7.88	12.0	
C_{66} (GPa)	29.87	31.55^{**}	34.31^{**}	35.0^{**}	
K^{V} (GPa)	40.48	46.9	36.46	37.3	40.1[b]
K^{R} (GPa)	29.11	32.4	26.63	26.0	19.7[b]
K^{VRH} (GPa)	34.79		31.54	31.6	28.8[a], 55.5[c], 31.1[d], 39.65[h], 37.8[i]
G^{V} (GPa)	17.85	19.3	22.7	24.4	23.0[b]
G^{R} (GPa)	6.61	13.4	13.9	17.5	5.3[b]
G^{VRH} (GPa)	12.23	16.3	18.3	20.9	12.4[a], 25[c], 13.4[d], 16.36[h]
E^{V} (GPa)	46.68			60.0	
E^{R} (GPa)	18.44			42.8	
E^{VRH} (GPa)	32.84			51.4	65.2[c], 35.2[d], 40.3[f], 39.77-44.22[h], 48[j], 35.2[l]
ν^{V}	0.31			0.23	
ν^{R}	0.39			0.23	
ν^{VRH}	0.34			0.23	0.31[a,d], 0.30[c], 0.305-0.325[h]

[*] Assumed zero

[**] $C_{66} = (C_{11} - C_{12})/2$

V, *R*, and *VRH* superscripts denote the Voigt bound, Reuss bound, and Voigt-Reuss-Hill average, respectively.

[a] Qomi et al. (2015); [b] Galmarini et al. (2011); [c] Al-Ostaz et al. (2010); [d] Manzano et al. (2009); [e] Speziale et al. (2008); [f] Constantinides and Ulm (2007); [g] Laugesen (2005); [h] Monteiro and Chang (1995); [i] Maede and Jeanloz (1990); [j] Wittmann (1986); [k] Holuj et al. (1985); [l] Beaudoin (1983)

3.3.3 Stress-Strain Relationships

The stress-strain curves of portlandite generated from MD simulations under uniaxial tensile strains in the *x*/*y* and *z* directions at ambient temperature and pressure are shown in Figure 3-3. In the *x* and *y* directions, after the ultimate stress is reached, stress decreases slowly with strain, which reflects a strain-softening behavior. The stress-strain curve in the *z* direction, however, shows that stress increases linearly with strain until it reaches the peak, after which the stress drops abruptly

to zero. This indicates that portlandite has a brittle behavior under tensile strains in the *z* direction. In addition to difference observed in failure mechanisms, the tensile strength of portlandite is found to be substantially direction dependent, such that the tensile strength in the *x*/*y* directions is more than 3.5 times larger than that in the *z* direction. In the *x*/*y* directions, the ultimate stress of 6.75 GPa occurs at a strain of 0.095 Å/Å. In the *z* direction, however, the ultimate stress reaches 1.91 GPa at the strain of 0.078 Å/Å. This clearly shows a lower mechanical strength in the *z* direction compared to the *x*/*y* directions. In the absence of experimental/simulation results in the literature, the mechanical properties of crystalline portlandite can be compared with those of the hypothetic portlandite nanotube reported by Manzano et al. (2012b). The tensile stress of a (9,9) portlandite nanotube reaches the maximum strength of 8.4 GPa at a strain level of 27%. This indicates that the fracture strain of portlandite nanotube is significantly larger than that of the crystalline portlandite, while the tensile strength for both materials is consistent.

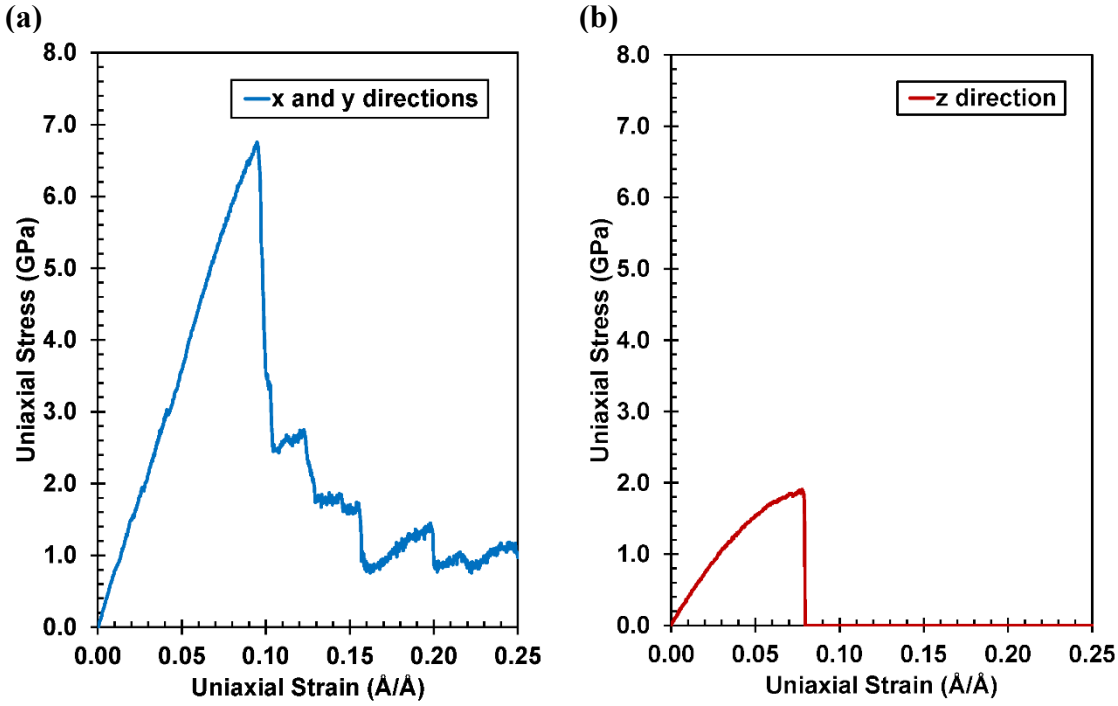

Figure 3-3. Stress-strain curves of portlandite under tensile strains in the (a) *x*/*y* and (b) *z* directions at ambient temperature and pressure conditions.

Figure 3-4 shows the progress of the formation of damage to the structure of portlandite under tensile strains in the *z* direction. As can be observed in this figure, the Ca-Ca and O-O interactions are lost and the [CaO_6] layers are stretched away from each other. This forms a large crack perpendicular to the *z* direction and significantly reduces the capacity of portlandite to accommodate the tensile strains. It is worth noting that the crack has been formed at a strain level of 0.08 Å/Å consistent with the stress-strain curve obtained in the *z* direction. The physical origin of the failure mechanism in the *z* direction can be attributed to the disruption of the weak dispersive cohesive forces between the [CaO_6] layers. As the applied tensile strain in the *z* direction increases, particularly after the yield point is reached, the weak van der Waals bonds tend to break. This causes a segregation between the (001) [CaO_6] layers, which eventually leads the structure to break into two halves.

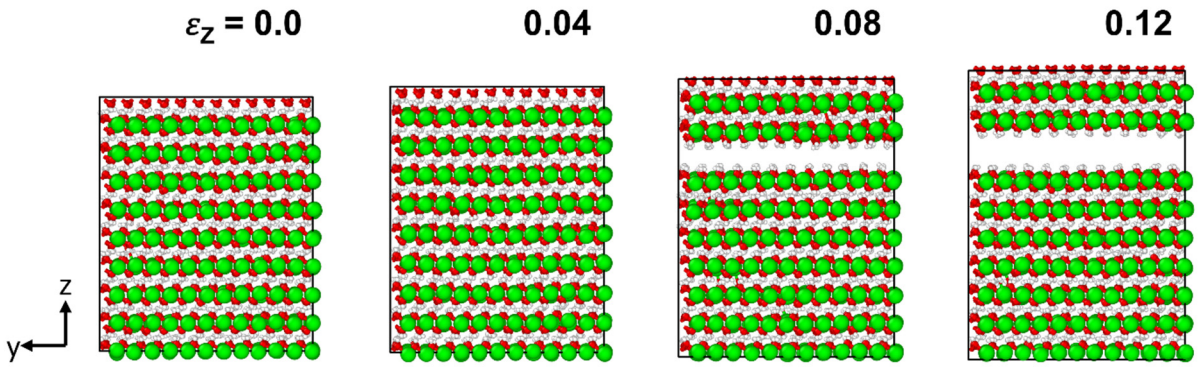

Figure 3-4. Progress of damage to the atomic structure of portlandite under tensile strains in the *z* direction. (Green: Ca; Red: O; White: H)

Figure 3-5 shows the evolution of damage to the structure of portlandite under tensile strains in the *y* direction. At lower strains, there are no noticeable changes in the portlandite's atomic structure and an elastic response is recorded. However, when strain increases, low-density regions are formed and stretched perpendicular to the direction of straining. This can be attributed to the breakage of the ionic-covalant Ca-O bonds. It should be noted that the deformed structure still

resists the applied strain even after the target strain of 0.25 Å/Å is reached. This residual capacity can be confirmed through the strain-softening plasticity observed in the stress-strain curve of portlandite in the *x*/*y* directions (Figure 3-3).

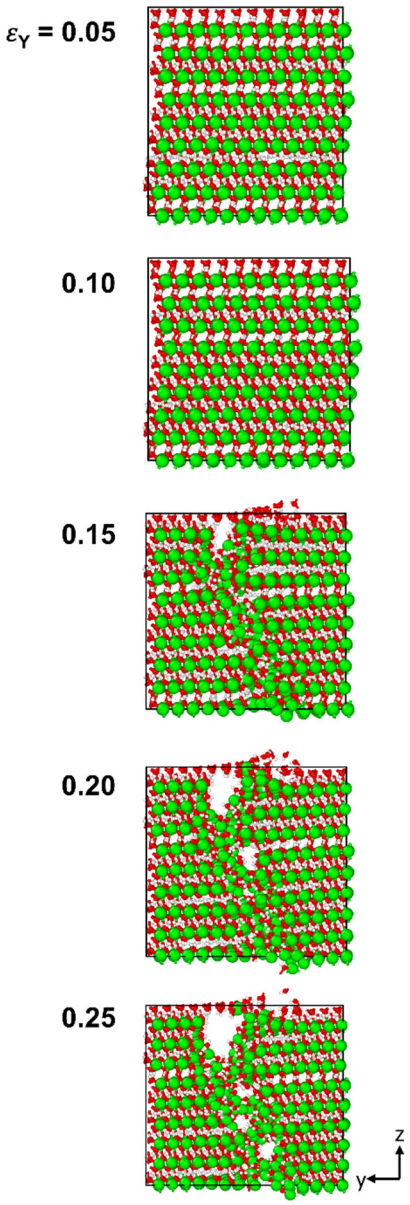

Figure 3-5. Progress of damage to the atomic structure of portlandite under tensile strains in the *y* direction. (Green: Ca; Red: O; White: H)

The results of the structural damage analysis can be further discussed by comparing the energies of the fractured surfaces of portlandite with those of the known ideal surfaces (Galmarini et al.,

2011). This can contribute to understand the plastic energy for different surfaces of portlandite before fracture. Table 3-5 presents the surface energies of portlandite obtained from MD calculations in comparison with the literature. It can be seen that the energy of the (001) surface is lower than that of the (010) surface, which is expected for minerals with a hexagonal platelet morphology, as is the case for portlandite. In the *z* direction, fracture takes place by the perfect cleavage of the (001) [CaO_6] layers (Figure 3-4). Hence, the energy difference before and after fracture can be corresponded to the surface energy. From Table 3-5, it is observed that the energy of the fractured surface (001) is 0.101 J/m^2, which is comparable with 0.073 J/m^2 from Galmarini et al. (2011). In the *y* direction, the energy of the fractured surface (0.409 J/m^2) is lower than the ideal surface energy (0.551 J/m^2). This can be attributed to the fact the fractured surface (010) is rough and far from regular (Figure 3-5). The difference between the energies for the fractured and ideal surfaces highlights the plastic energy required for a perfect fracture in the (010) direction. From MD calculations, the relative surface energy of (010) with respect to (001) is 4.049. This falls in the range obtained from experimental tests (i.e., 0.499-4.050).

Table 3-5. Surface energies of fractured surfaces of portlandite calculated from MD simulations compared with those of the ideal cleaved surfaces obtained from MM simulations and experimental tests

	Present MD	Galmarini et al. (2011)	
		MM	Experiment
(010) J/m^2	0.409	0.551	N.A.
(001) J/m^2	0.101	0.073	N.A.
(010)/(001)	4.049	7.548	0.499-4.050

3.3.4 Poisson's Ratio

If a material is stretched in one direction, it tends to shrink in the other two directions perpendicular to the direction of elongation. Poisson's ratio (v) is the measure of this effect and can be defined by the negative gradient of the transverse to axial strain in the elastic regime. As

mentioned earlier, the directions perpendicular to the direction of uniaxial tensile strain are allowed to relax anisotropically. This makes it possible to characterize the Poisson's ratio of portlandite in different directions with respect to the direction of the applied strain. Table 3-6 lists the Poisson's ratios of portlandite for different strain and response directions. It can be observed that in response to uniaxial tensile strains in the *x*/*y* direction, the contraction in the *z* direction (ν = 0.63) is three times larger than that in the *y*/*x* direction (ν = 0.21). This can be mostly attributed to the fact that the Ca-O bonds present in the (001) plane can substantially resist the contraction forces, while the dispersive forces cause a significant contraction in the *z* direction. Furthermore, it is observed that the Poisson's ratios of portlandite have a very large direction dependency, ranging from 0.08 to 0.63. This is due to the fact that portlandite has an anisotropic structure formed by the Ca-O bonds in the (001) plane and weak cohesive forces along the *c*-axis. A review of the existing literature shows that the Poisson's ratio of portlandite falls in the range of 0.23-0.31 (Monteiro and Chang, 1995; Speziale et al., 2008; Manzano et al., 2009; Al-Ostaz et al., 2010; Qomi et al., 2015). The reported values, however, have been obtained by averaging over elastic constants and with the assumption of an isotropic media. This issue has been addressed in this current study as the Poisson's ratios are directly calculated from the strain data obtained from the MD simulations.

Table 3-6. Poisson's ratio of portlandite in different directions at strain rate of 0.0005 ps^{-1}.

		Response direction	
		y*/*x	***z***
Straining direction	***x*/*y***	0.21	0.63
	z	0.08	-
Others		0.31[a,c], 0.30[b], 0.23[d], 0.305-0.325[e]	

[a] Qomi et al. (2015)
[b] Al-Ostaz et al. (2010)
[c] Manzano et al. (2009)
[d] Speziale et al. (2008)
[e] Monteiro and Chang (1995)

3.3.5 Effect of Temperature on Mechanical Properties

At any non-zero temperature, atoms in a solid move around the equilibrium positions due to thermal oscillations. To evaluate the mechanical properties of materials when the external forces are applied, temperature is an important factor as it can alter the atomic structure and bond lengths. In this study, further to the simulations in the ambient temperature (300 K), systematic MD simulations are performed to capture the sensitivity of the mechanical properties of portlandite to temperature changes. The stress-strain curves of portlandite under uniaxial tensile strains, with a constant rate of 0.0005 ps^{-1}, at various temperatures ranging from 300 to 500 K are shown in Figure 3-6.

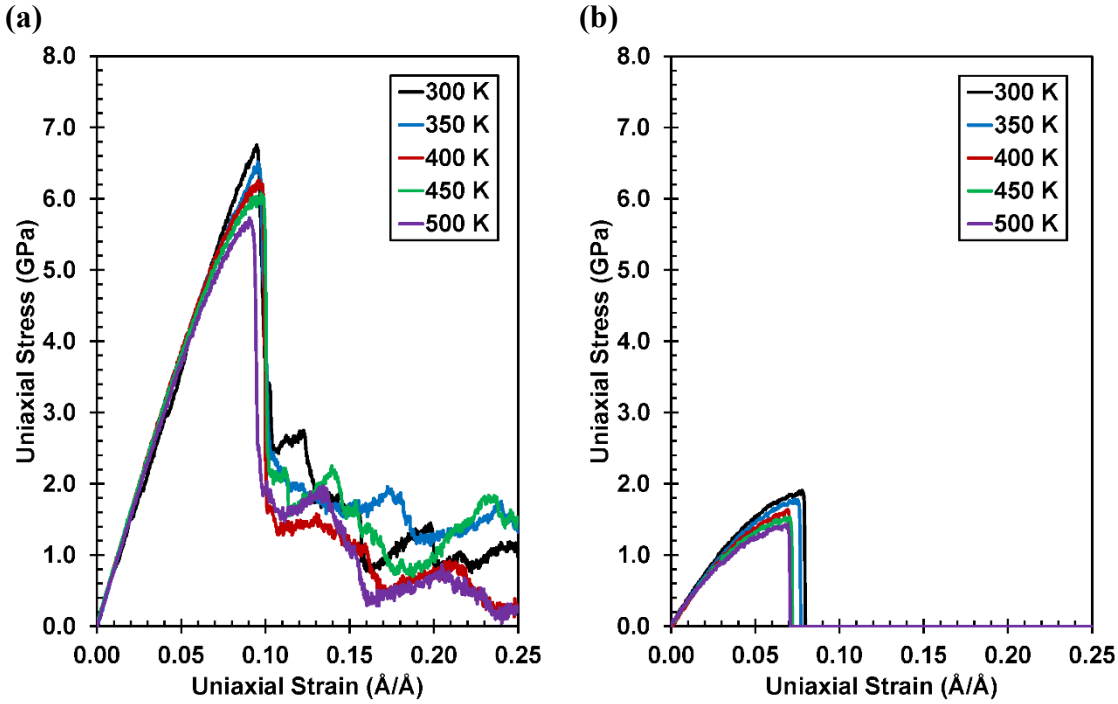

Figure 3-6. Stress-strain curves of portlandite at various temperatures under uniaxial tensile strains in the (a) *x*/*y* and (b) *z* directions.

It can be observed that temperature exerts a substantial effect on the mechanical properties of portlandite. With the increase of temperature, the tensile strength, Young's modulus, and fracture strain of portlandite decrease significantly (Figure 3-7).

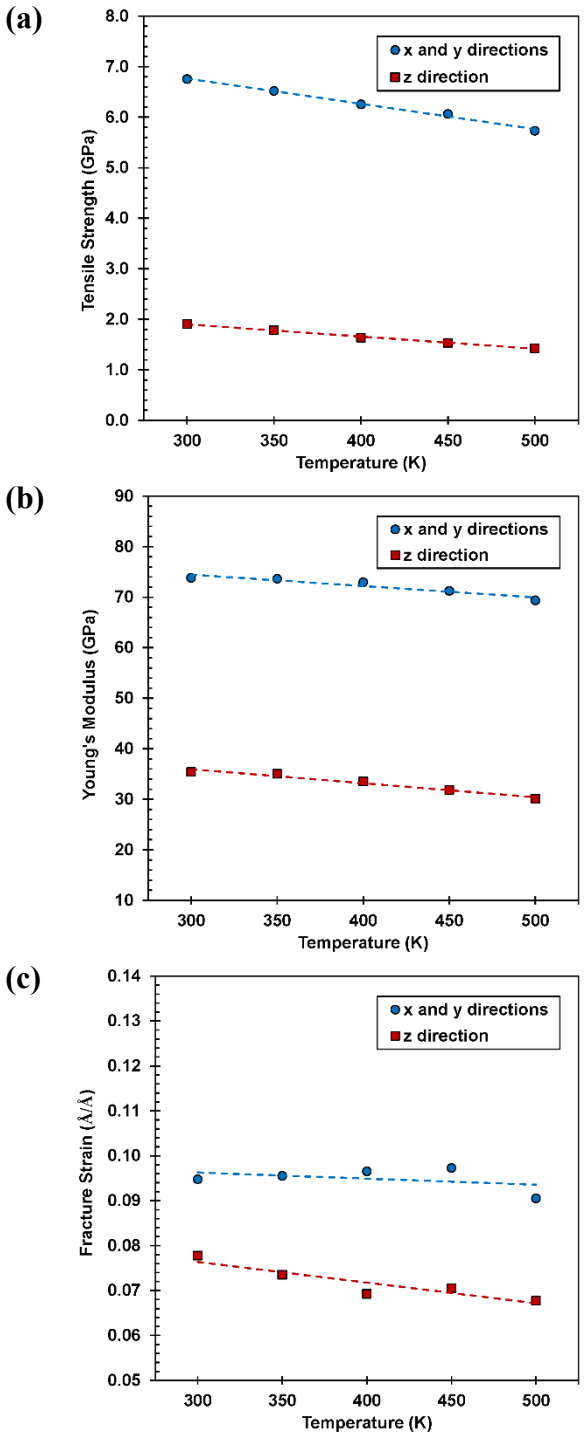

Figure 3-7. Mechanical Properties of portlandite at various temperatures under uniaxial tensile strains in the *x*/*y* and *z* directions: (a) Tensile strength, (b) Young's modulus, and (c) Fracture strain.

This behavior, which is referred to as thermal-softening effect, has been captured for a variety of other materials, such as platinum nanowire (Koh et al., 2005), silica glass (Pedone et al., 2008),

polymer (Li and Strachan, 2011), and silicene (Pei et al., 2014) to name a few. By increasing the temperature from 300 to 500 K, the tensile strength, Young's modulus, and fracture strain of portlandite decreases by ~ 15.2, 4.5, and 6.0% in the *x* and *y* directions, and by 25.1, 12.9 and 15.1 % in the *z* direction, respectively. The fact that the increase of temperature results in a significant reduction in the tensile strength, Young's modulus, and fracture strain can be attributed to three reasons: First, since the equilibrium lengths of bonds are larger at higher temperatures, the bonds can sooner reach their breaking lengths during the tensile straining process. Second, the lengths of chemical bonds experience larger fluctuations at higher temperatures, which may cause them to extend to their critical lengths and break. Third, the disordered movements of atoms are intensified due to higher temperatures, which leads to weaker interatomic bond forces. It is worth noting that the mechanical properties of portlandite in the *z* direction are more sensitive to the temperature changes than those in the *x*/*y* directions. Such behavior has also been captured for the structural properties of portlandite primarily because α_c is larger than α_a.

3.3.6 Effect of Strain Rate on Mechanical Properties

According to the kinetic theory of solid fracture, strain rate affects the mechanical properties of solids. To capture the effect of strain rate on the mechanical properties of portlandite, a wide range of strain rates from 0.0005 to 0.01 ps^{-1} is chosen. This range has been widely used in the previous atomistic simulation efforts (e.g., Koh et al., 2005; Pedone et al., 2008; Pei et al., 2014; Wu et al., 2014). It should be noted that the listed strain rates are approximately three orders of magnitude faster than the ones induced by dynamic or shock loading (Zhuang et al., 2002). Nonetheless, since the time scale of molecular dynamics is set by the atomic motion, a high strain rate is required to induce the expected deformation within the reasonable simulation time. Figure 3-8 shows the

stress-strain curves of portlandite at different strain rates under uniaxial tensile strains at ambient temperature (300 K).

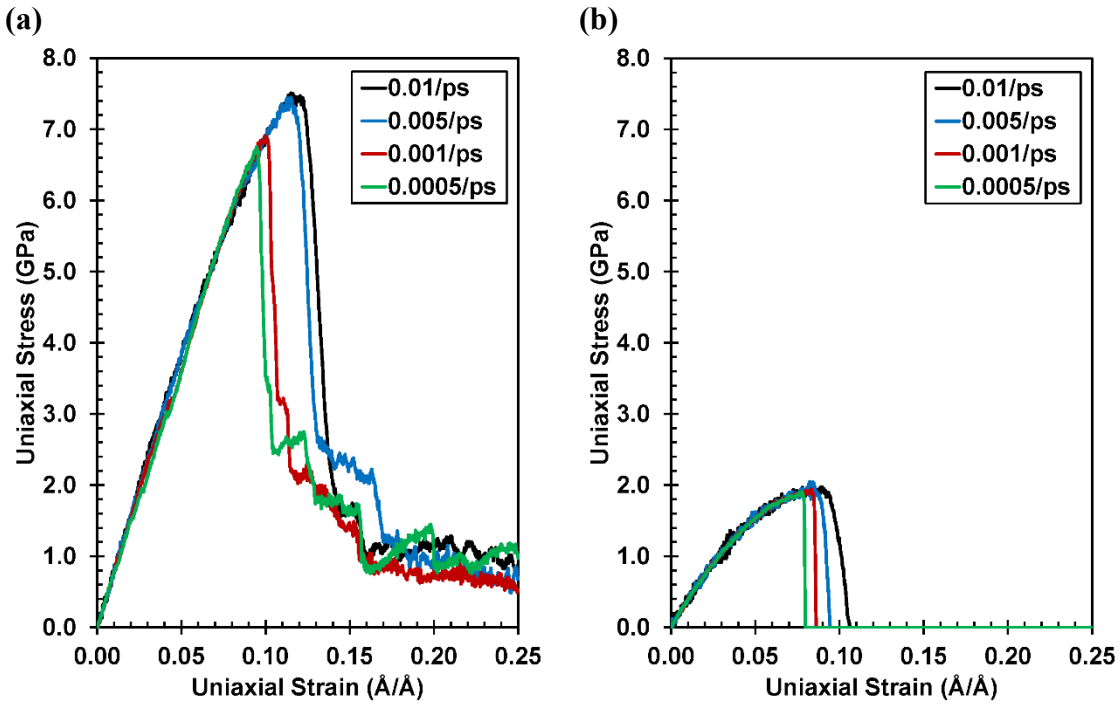

Figure 3-8. Stress-strain curves of portlandite at various strain rates under uniaxial tensile strains in the (a) *x*/*y* and (b) *z* directions.

It can be observed that compared to the temperature effect on stress-strain curves, the strain rate effect is less significant. It is seen that the tensile strength and fracture strain of portlandite slightly increases with increasing the strain rate. On the other hand, the elastic region seems to be least influenced by the strain rate as reflected in Figure 3-9(b). This figure shows that the Young's modulus of portlandite remains relatively unchanged even after the strain rate decreases from 0.01 to 0.0005 ps^{-1}.

By changing the strain rate from 0.01 to 0.0005 ps^{-1}, the tensile strength of portlandite drops from 7.51 to 6.75 GPa in the *z* direction and from 1.98 to 1.91 GPa in the *x*/*y* directions (Figure 3-9(a)). A similar trend is captured for the fracture strain of portlandite as shown in Figure 3-9(c).

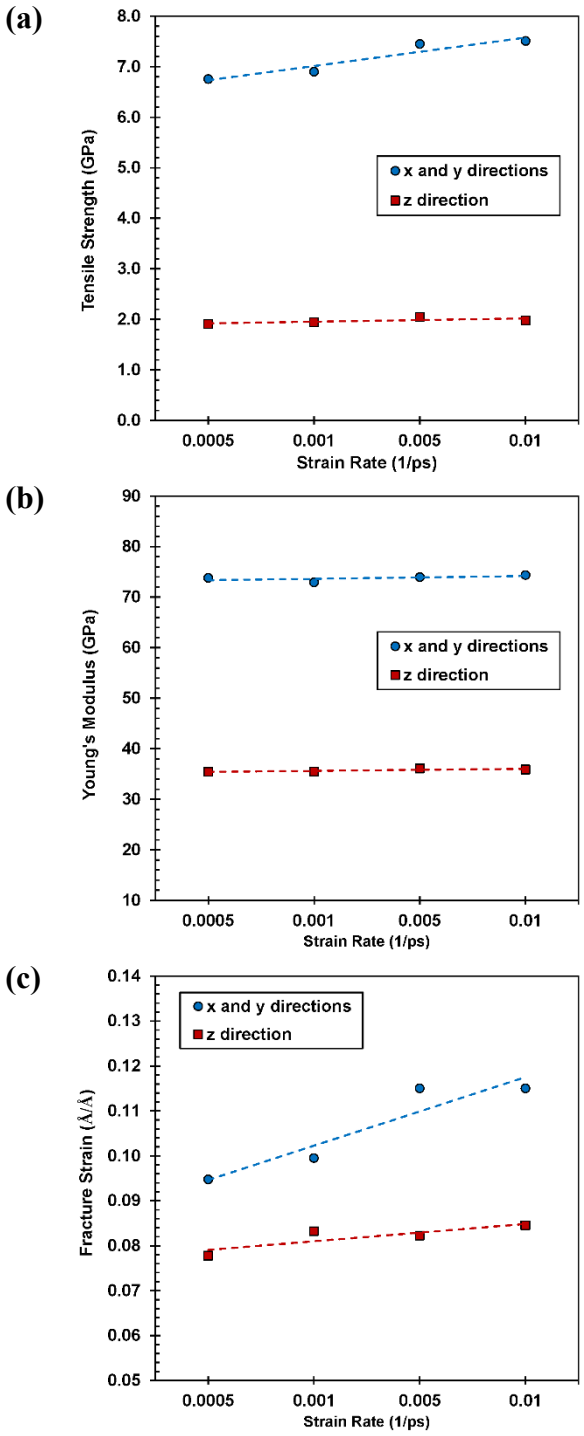

Figure 3-9. Mechanical properties of portlandite at various strain rates under uniaxial tensile strains in the *x*/*y* and *z* directions: (a) Tensile strength, (b) Young's modulus, and (c) Fracture strain.

The fact that a lower strain rate results in a lower tensile strength has been also confirmed via macroscopic experiments for cementitious materials (Rossi, 1997). A lower strain rate allows more

time for the thermal fluctuation of atoms, which helps them to overcome the energy barriers and break bonds. On the other hand, it is observed that while the overall structural behavior remains unchanged under different strain rates, the plastic deformation improves with increasing the strain rate. This will decelerate the fracture, mainly due to the rearrangement of atoms. While straining, the strain flows from high to low density regions, leading to coalescence of voids.

3.3.7 Combined Effect of Strain Rate and Temperature

In the previous section, it was shown that the stress-strain curves of portlandite at the ambient temperature are not greatly influenced by changes in the rate of straining. In this section, the effect of strain rate on the mechanical properties of portlandite is investigated at various temperatures. At a constant temperature and strain, the relationship between the fracture stress and strain rate can be represented by (Zener and Hollomon, 1944; Dieter, 1961):

$$\sigma = C(\dot{\varepsilon})^m|_{\varepsilon,T} \tag{3-7}$$

where σ and $\dot{\varepsilon}$ are fracture stress and strain rate, respectively. C is a constant and m is a coefficient known as the strain-rate sensitivity. This coefficient is defined as the ratio of the incremental change in $\log(\sigma)$ to the resultant change in $\log(\dot{\varepsilon})$, at a given strain and temperature. To obtain the strain-rate sensitivity coefficient, the below equation shall be solved for m:

$$\log(\sigma) = m\ \log(\dot{\varepsilon}) + \log(C) \tag{3-8}$$

Figure 3-10 represents the $\log(\sigma)$ vs. $\log(\dot{\varepsilon})$ plots of portlandite under uniaxial tensile strains in the x/y and z directions for various strain rates and temperatures. It can be observed that temperature has a major contribution to strain-rate sensitivity. At the temperatures of 300 K and above, the strain-rate sensitivity coefficient increases significantly with temperature and strain rate in the z direction. The slope of the $\log(\sigma)$ vs. $\log(\dot{\varepsilon})$ plots of portlandite at 500 K in the z direction, i.e. strain-rate sensitivity coefficient, is as twice as the same quantity at the ambient temperature.

This reflects the dependency of the fracture stress of portlandite on the strain rate at temperatures above the ambient temperature in the *z* direction. On the other hand, in the *x*/*y* directions, the $\log(\sigma)$ vs. $\log(\dot{\varepsilon})$ plots are relatively flat indicating the fact that the fracture stress of portlandite is less sensitive to the strain rate in the *x*/*y* directions. This behavior is expected because as discussed earlier, the CTE of portlandite in the *x*/*y* directions is smaller than that in the *z* direction. The smaller CTE results in less sensitivity of the stress-strain curves to the temperature.

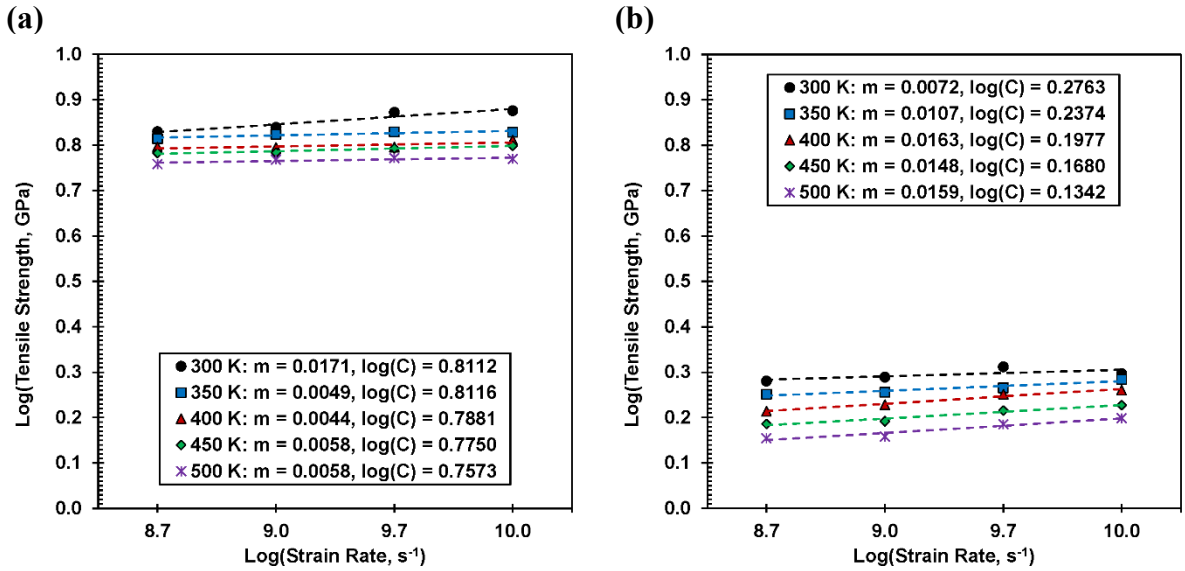

Figure 3-10. Relationship between $\log(\sigma)$ and $\log(\dot{\varepsilon})$ at various temperatures for portlandite under uniaxial tensile strains in the (a) *x*/*y* and (b) *z* directions.

3.4 Conclusions

The crystalline structure of portlandite was simulated at the nano-scale using the MD method. Based on the unit cell volume and lattice parameters monitored at various temperatures ranging from 300 to 500 K, the CTEs were calculated and compared to the experimental test results available in the literature. The thermal expansion parameters fitted to the MD simulation results were found in a reasonable agreement with the conventional X-ray diffraction as well as the latest neutron diffraction test data. The atomic structure of portlandite equilibrated at different temperatures was then subjected to a set of uniaxial tensile strains in the three orthogonal directions

and the stress-strain curves were generated. It was observed that the stress-strain curves of portlandite substantially depend on the direction of straining. It was shown that portlandite has a higher mechanical strength and stiffness in the *x* and *y* directions compared to those in the *z* direction. This was attributed to the presence of strong [CaO_6] layers running in the (001) plane of the portlandite's atomic structure. In the *z* direction, however, the structural damage analysis indicated that the breakage of weak dispersive forces causes the segregation of the layers. This resulted in the structure to break into two halves and collapse. The surface energies were calculated based on the energies before and after fracture in different directions. The perfect cleavage of the (001) plane resulted in a lower energy in the surface (001) compared to the surface (010).

All the key mechanical properties were also extracted from the stress-strain curves. This was the first-known effort to understand the mechanical behavior of portlandite beyond the elastic range. Since the algorithm used in this study allowed for anisotropic relaxation in the lateral directions, it became possible to also capture the Poisson's effect in the directions perpendicular to the direction of the applied strain. The developed models provided a unique opportunity to investigate the effect of temperature and strain rate on the mechanical properties of portlandite for the first time. It was observed that the tensile strength, Young's modulus, and fracture strain of portlandite decrease with temperature and increase with strain rate. However, the strain rate has less significant effect on the magnitudes of the mechanical properties compared to temperature. The sensitivity of mechanical properties of portlandite to different strain rates at different temperatures were also investigated. It was found that in the *z* direction, the mechanical properties are substantially dependent on the rate of straining. Nevertheless, in the *x* and *y* directions, the mechanical properties of portlandite do not vary much with the strain rate. The outcome of this study provides detailed information about the nonlinear behavior, plastic deformation, and

structural failure of portlandite and similar atomic structures. The intrinsic structural, thermal, and mechanical properties of portlandite determined in this study can be directly implemented in the available models for cement-based materials at different length scales.

3.5 References

1- Al-Ostaz A., Wu W., Cheng A.H.-D., and Song C.R., 2010. "*A molecular dynamics and microporomechanics study on the mechanical properties of major constituents of hydrated cement*". Composites: Part B 41: 543- 459.

2- Beaudoin J.J., 1983. "*Comparison of mechanical properties of compacted calcium hydroxide and Portland cement paste systems*". Cement and Concrete Research, 13(3): 319-324.

3- Bernal J.D., and Megaw H.D., 1935. "*The function of hydrogen in intermolecular forces*". Proceedings of Royal Society of London, Series A, Mathematical and Physical Sciences.

4- Busing W.R., and Levy H.A., 1957. "*Neutron Diffraction Study of Calcium Hydroxide*". The Journal of Chemical Physics 26: 563-568.

5- Constantinides G., and Ulm F.J., 2007. "*The nanogranular nature of C-S-H*", Journal of the Mechanics and Physics of Solids 55(1): 64-90.

6- Dieter G.E., 1961. "*Mechanical Metallurgy*". McGraw-Hill, New York.

7- Fukui H., Ohtaka O., Fujisawa T.F., Kunisada T., Suzuki T., and Kikegawa T., 2003. "*Thermo-elastic property of $Ca(OH)_2$ portlandite*", High Pressure Research 23(1-2): 55-61.

8- Galmarini S., Aimable A., Ruffray N., and Bowen P., 2011. "*Changes in portlandite morphology with solvent composition: Atomistic simulations and experiment*", Cement and Concrete Research 41: 1330-1338.

9- Halstead P.E., and moore A.E., 1957. "*The thermal dissociation of calcium hydroxide*". Journal of the Chemical Society 769: 3873-3875.

10- Hajilar S., and Shafei B., 2014. "*Nano-scale characterization of elastic properties of AFt and AFm phases of hydrated cement paste*". Computational Modeling of Concrete Structures 1: 299-306.

11- Hajilar S., and Shafei B., 2015(a). "*Molecular dynamics simulation of elastic properties of ordered CSH gel: Case study of tobermorite and jennite*", Proceedings of the 5th International Symposium on Nanotechnology in Construction (NICOM-5).

12- Hajilar S., and Shafei B., 2015(b). "*Nano-scale investigation of elastic properties of hydrated cement paste constituents using molecular dynamics simulations*", Computational Materials Science 101: 216-226.

13- Hajilar S., and Shafei B., 2016. "*Mechanical failure mechanisms of hydrated products of tricalcium aluminate: A reactive molecular dynamics study*", Materials and Design 90 (15): 165-176.

14- Henderson D.M., and Gutowsky H.S., 1962. "*A nuclear magnetic resonance determination of the hydrogen positions in $Ca(OH)_2$*", American Mineralogist 47 (11 and 12): 1231.

15- Holuj F., Drozdowski M., and Czajkowski M., 1985. "*Brillouin spectrum of $Ca(OH)_2$*". Solid State Communications, 56(12): 1019-1021.

16- Kalinichev A.G., and Kirkpatrick R.J., 2002. "*Molecular dynamics modeling of chloride binding to the surfaces of calcium hydroxide, hydrated calcium aluminate, and calcium silicate phases*", Chemistry of Materials 14: 3539-3549.

17- Koh S.J.A., Lee H.P., and Cheng Q.H., 2005. "*Molecular dynamics simulation of a solid platinum nanowire under uniaxial tensile strain: Temperature and strain-rate effects*". Physical Review B 72: 085414.

18- Laugesen J.L., 2005. "*Density functional calculations of elastic properties of portlandite, $Ca(OH)_2$*". Cement and Concrete Research, 35(2): 199-202.

19- Li C., and Strachan A., 2011. "*Molecular dynamics predictions of thermal and mechanical properties of thermoset polymer EPON862/DETDA*". Polymer 52: 2920-2928.

20- Maede C., and Jeanloz R., 1990. "*Static compression of $Ca(OH)_2$ at room temperature; observation of amorphization and equation of state measurements to 10.7 GPa*". Geophysical Research Letters, 17(8): 1157-1160.

21- Manzano H., Dolado J.S., Ayuela A., 2009. "*Elastic properties of the main species present in Portland cement pastes*". Acta Materialia 57(5): 1666-1674.

22- Manzano H., Pellenq R.J.M., Ulm F.J., Buehler M.J., and van Duin A.C.T., 2012(a). "*Hydration of calcium oxide surface predicted by reactive force field molecular dynamics*". Langmuir 28: 4187-4197.

23- Manzano H., Enyashin A.N., Dolado J.S., Ayuela A., Frenzel J., and Seifert G., 2012(b). "*Do cement nanotubes exist?*", Advanced Materials 24: 3239-3245.

24- Mehta P.K., Monteiro P.J.M., 2006. "*Concrete: microstructure, properties and materials*". McGraw-Hill, New York.

25- Monteiro P.J.M., and Chang C.T., 1995. "*The elastic moduli of calcium hydroxide*", Cement and Concrete Research 25(9): 1605-1609.

26- Pedone A., Malavasi G., Menziani M.C., Segre U., and Cormack A.N., 2008. "*Molecular dynamics studies of stress-strain behavior of silica glass under a tensile load*". Chemistry of Materials 20: 4356-4366.

27- Pei Q.X., Sha Z.D., Zhang Y.Y., and Zhang Y.W., 2014. "*Effects of temperature and strain rate on the mechanical properties of silicene*". Journal of Applied Physics 115: 023519.

28- Petch H.E., and Megaw H.E., 1954. "*Crystal structure of brucite $Mg(OH)_2$ and portlandite $Ca(OH)_2$ in relation to infrared absorption: Errata*". Journal of the Optical Society of America 44: 744-745.

29- Petch H.E., 1961. "*The hydrogen positions in portlandite, $Ca(OH)_2$, as indicated by electron distribution*". Acta Crystallographica 14: 950-957.

30- Plimpton S., 1995. "*Fast Parallel Algorithms for Short-Range Molecular Dynamics*". Journal of Computational Physics 117: 1-19.

31- Qomi M.J.A., Ulm F.J., and Pellenq R.J.M., 2015. "*Physical origins of thermal properties of cement paste*", Physical Review Applied 3: 064010.

32- Rossi P., 1997. "*Strain rate effects in concrete structures: the LCPC experience*". Materials and Structures 30(1): 54-62.

33- Shahsavari R., Pellenq R.J.M., and Ulm F.J., 2001. "*Empirical force fields for complex hydrated calico-silicate layered minerals*", Physical Chemistry Chemical Physics 13: 1002-1011.

34- Speziale S., Richmann H.J., Schilling F.R., Wenk H.R., and Monteiro P.J.M., 2008. "*Determination of the elastic constants of portlandite by Brillouin spectroscopy*". Cement and Concrete Research, 38(10): 1148-1153.

35- Stukowski A., 2010. "*Visulization and analysis of atomistic simulation data with OVITO- the open visualization tool*", Modeling and Simulation in Materials Science and Engineering 18: 015012.

36- Wang J., Kalinichev A.G., Kirkpatrick R.J., 2006. "*Effects of substrate and composition on the structure, dynamics, and energetics of water at mineral surfaces: A molecular dynamics modeling study*". Geochimica et Cosmochimica Acta 70: 562-582.

37- Wittmann F.H., 1986. "*Estimation of the modulus of the elasticity of calcium hydroxide*". Cement and Concrete Research, 16(6): 971-972.

38- Wolf D., Keblinski P., Phillpot S.R., and Eggebrecht J., 1999. "*Exact method for the simulation of coulombic systems by spherically truncated, pairwise r^{-1} summation*", The Journal of Chemical Physics 110: 8254–8282.

39- Wu X., Moon R.J., and Martini A., 2014. "*Tensile strength of Iβ crystalline cellulose predicted by molecular dynamics simulation*". Cellulose 21(4): 2233-2245.

40- Xu H., Zhao Y., Vogel S.C., Daemen L.L., and Hickmott D.D., 2007. "*Anisotropic thermal expansion and hydrogen bonding behavior of portlandite: A high-temperature neutron diffraction study*", Journal of Solid State Chemistry 180: 1519-1525.

41- Zener C., and Hollomon J.H., 1944. "*Effect of strain rate upon plastic flow of steel*". Journal of Applied Physics 15(1): 22-32.

42- Zhuang S., Lu J., and Ravichandran G., 2002. "*Shock wave response of a zirconium-based bulk metallic glass and its composite*". Journal of Applied Physics Letters 80: 4522.

CHAPTER 4: REACTIVE MOLECULAR DYNAMICS SIMULATIONS TO UNDERSTAND MECHANICAL RESPONSE OF THAUMASITE UNDER TEMPERATURE AND STRAIN RATE EFFECTS

Understanding the structural, thermal, and mechanical properties of thaumasite is of great interest to the cement industry, mainly because it is the phase responsible for the aging and deterioration of civil infrastructures made of cementitious materials attacked by external sources of sulfate. Despite the importance, effects of temperature and strain rate on the mechanical response of thaumasite had remained unexplored prior to the current study, in which the mechanical properties of thaumasite are fully characterized using the reactive molecular dynamics (RMD) method. With employing a first-principles based reactive force field, the RMD simulations enable the description of bond dissociation and formation under realistic conditions. From the stress-strain curves of thaumasite generated in the x, y, and z directions, the tensile strength, Young's modulus, and fracture strain are determined for the three orthogonal directions. During the course of each simulation, the chemical bonds undergoing tensile deformations are monitored to reveal the bonds responsible for the mechanical strength of thaumasite. The temperature increase is found to accelerate the bond breaking rate and consequently the degradation of mechanical properties of thaumasite, while the strain rate only leads to a slight enhancement of them for the ranges considered in this study.

4.1 Introduction

Thaumasite is a calcium silicate carbonate sulfate hydrate phase, known as the main product and indicator of thaumasite sulfate attack (TSA) in cementitious materials (Crammond, 1985; Santhanam et al., 2002 and 2003; Neville, 2004). Cementitious materials exposed to sulfate bearing solutions from the outside environment, such as soil and water, show significant deterioration over time. This occurs through the attack of external sulfate ions to the calcium

silicate hydrates (CSH), which are the main binding agents in ordinary and sulfate-resisting Portland cements. As a result of such chemical reactions, thaumasite is precipitated. The formation of thaumasite substantially reduces the binding capacity of the cement paste, transforming it into a mushy and incohesive mass (Crammond, 2002). In addition, the replacement of CSH with thaumasite can cause significant stresses and strains, leading to the expansion of the paste, formation of cracks, and eventually spalling and degradation of civil infrastructures made of concrete (Glasser et al., 2008). While TSA can be destructive at any finite temperature, it has been observed it is greatly accelerated at temperatures below 0 °C (Bensted, 1999; Bickley, 1999). To address the long-standing deterioration issues associated with TSA to cementitious materials, an in-depth understanding of the structural, thermal, and mechanical properties of thaumasite is essential.

Jacobsen et al. (2003) studied the thermal expansion of thaumasite between 130 and 298 K using single-crystal X-ray diffraction. Over this temperature range, no phase transition was observed and most structural units demonstrated positive thermal expansion coefficients. Moreover, it was revealed that, contrary to the carbonate groups with zero thermal expansions, the sulfate tetrahedra and the silicate octahedra exhibit negative thermal expansions. A high-temperature study of thaumasite was conducted by Martucci and Cruciani (2006). In situ, time resolved synchrotron power diffraction between 303 and 1098 K was used for this purpose. It was observed that the cell parameters of thaumasite increased linearly with temperature up to 393 K. As a result of the complete removal of the crystallization water molecules, however, the crystalline structure of thaumasite collapsed at close to 417 K, turning it into an amorphous structure. By a further increase of temperature, anhydrite and cristobalite crystallized at 953 K. In a separate effort, the structure of thaumasite was characterized in detail using single-crystal neutron diffraction and

Raman spectroscopy by Gatta et al. (2012). The stability of the structure of thaumasite was attributed to the geometry of hydrogen bonds that connect the main structural units. This study found that by decreasing the temperature, although the hydrogen bonds became shorter, the sulfate tetrahedra expanded, indicating negative thermal expansion at the molecular level driven by shrinkage of the hydrogen bonds between the $[Ca_3Si(OH)_6.12H_2O]^{4+}$ columns. Most recently, Scholtzováet al. (2015) performed Brillouin spectroscopy experiments and ab initio simulations to generate the full elasticity tensor of thaumasite. From the calculated elastic constants, the bulk, shear, and Young's moduli, as well as Poisson's ratio, of thaumasite were estimated. This was the only study, to our knowledge, that characterized the mechanical properties of thaumasite in the elastic range. There is, however, no evidence to understand the expansion, loss of strength, and crack formation observed in thaumasite during the experiments due to TSA. The current study primarily focuses on addressing this critical research gap.

Prior studies have demonstrated the capabilities of the reactive molecular dynamics (RMD) method to calculate the mechanical properties of cementitious crystalline materials (e.g., Liu et al., 2012; Hajilar and Shafei, 2016a). In this study, first-principles based ReaxFF RMD (van Duin et al., 2011) simulations are performed to investigate the mechanical characteristics of thaumasite. The ReaxFF force field is used from Liu et al. (2012), albeit complemented with C-Ca bond interactions (Jaramillo-Botero et al, 2014) prepared using the GARFfield parameter optimization framework (Jaramillo-Botero et al., 2012). To this end, the crystalline atomistic structure of thaumasite is built and then deformed uniaxially in the *x*, *y* and *z* directions of the simulation cell. In addition to recording the stress-strain data, a chemical bond analysis is performed on the resulting atomistic trajectories to correlate the stretching of chemical bonds with the stresses obtained by the RMD simulations. From the stress-strain curves, the tensile strength, Young's

modulus, and fracture strain of thaumasite are determined. In the next step, an extensive set of RMD simulations are performed to investigate the sensitivity of the mechanical properties of thaumasite to temperature and strain rate effects. From the results generated at a wide range of temperatures and strain rates, the relationships between the tensile strength of thaumasite and these two important factors are identified. The outcome of this study contributes to enhance the understanding of the key mechanical properties of thaumasite under different thermal and loading conditions, which can be further used to develop constitutive models for cementitious materials at various length scales.

4.2 Computational Details

4.2.1 Crystalline Structure of Thaumasite

Thaumasite ($Ca_3Si(OH)_6(CO_3)(SO_4)\cdot 12H_2O$) is a rare mineral that has a hexagonal structure with 122 atoms in the unit cell and a space group of $P6_3$. Because more than half of the weight of this crystalline structure is from water and hydroxyl, thaumasite has a relatively low density of 1.88 g/cm^3. The crystalline structure of thaumasite (Figure 4-1) was first determined by Edge and Tylor (1971) and later refined by other studies, such as Effenberger et al. (1983) and Gatta et al. (2012). Thaumasite is the only known mineral that possesses silicon atoms coordinated by six hydroxyl groups stable at (or close to) ambient pressure-temperature conditions. Using infrared spectra, Moenke (1964) was the first study that recognized that thaumasite contains octahedral silicon atoms. It was later confirmed by 29Si NMR spectroscopy that the silicon atoms in thaumasite are six-coordinated (Grimmer et al., 1980; Stebbins and Kankazi, 1991). This is a unique feature as other silicate minerals that make up most of the earth's crust contain silicon atoms coordinated to four oxygen atoms. The other two silica compounds that contain fully hydrated, six-fold coordinated silicon atoms, however, have been found in the synthetic high-

pressure phase D, $MgSi(OH)_2O_4$ (Yang et al., 1997; Frost and Fei, 1998) and $MgSi(OH)_6$ (Wunder et al., 2012).

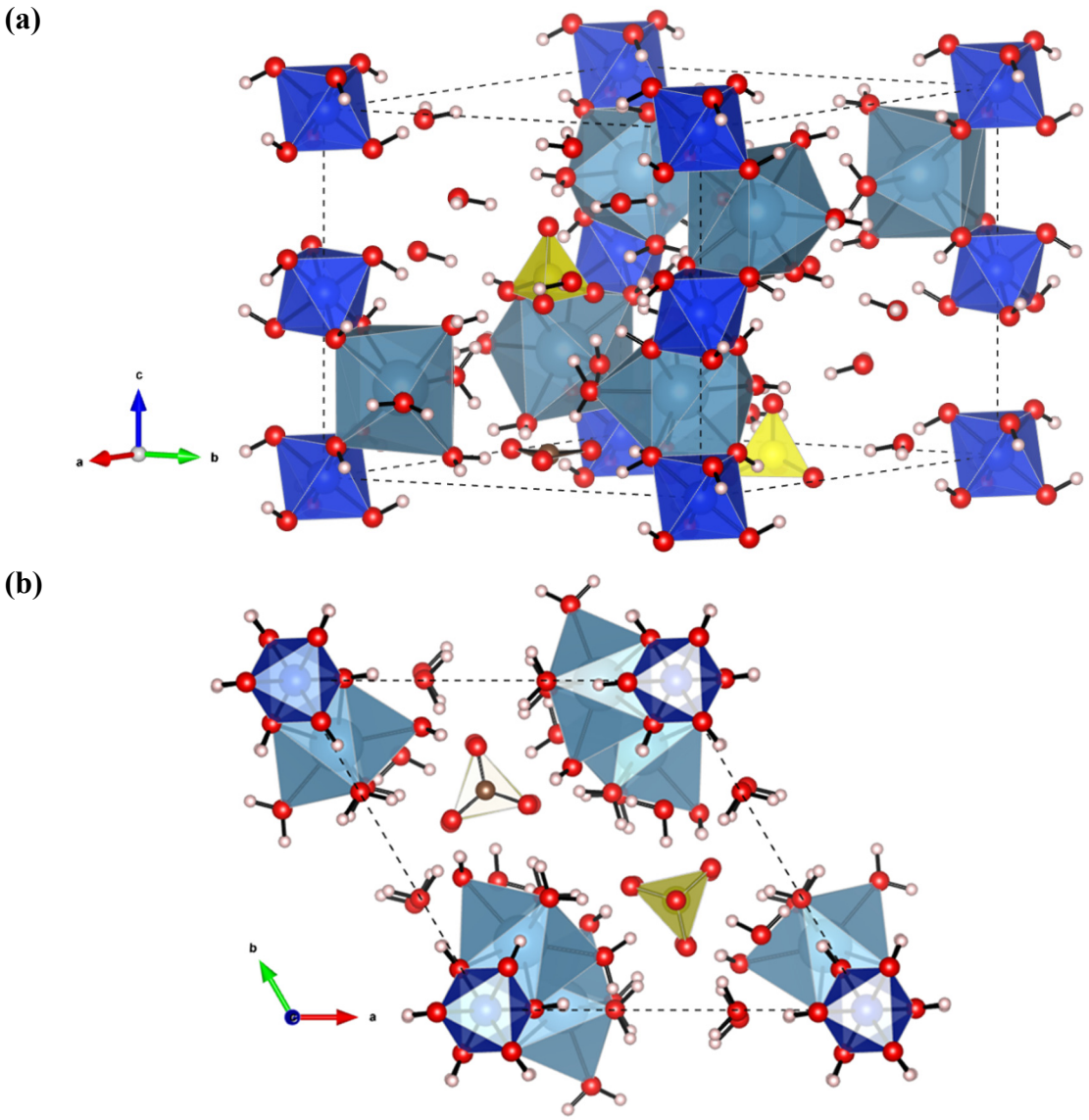

Figure 4-1. (a) Unit cell of thaumasite; (b) The crystal structure of Thaumasite viewed from (001). The color scheme is as follows: Blue: Silicon; Cyan: Calcium; Yellow: Sulfur, Brown: Carbon; Red: Oxygen; White: Hydrogen

In thaumasite, six hydroxyl groups are coordinated to Si^{4+}, resulting in $Si(OH)_6^{2-}$ anions, which are balanced by Ca^{2+} cations. These anions and cations are surrounded by 12 water molecules that form columns of $[Ca_3Si(OH)_6.12H_2O]^{4+}$, which lay parallel to the *c* axis of the unit cell. These

columns are interconnected only through hydrogen bonding with the SO_4^{2-} and CO_3^{2-} groups located in the interstitial positions in the channels between the columns. The sulfate and carbonate groups that neutralize the excess charge of the system alternate along the *c* axis of the unit cell and are fully ordered.

4.2.2 Mechanical properties from RMD Simulations

The RMD simulations are conducted using the large-scale atomic/molecular massively parallel simulator (LAMMPS) package (Plimpton, 1995).The triclinic unit cell of thaumasite is built in the LAMMPS input format using the latest crystallographic data available in the literature (Gatta et al., 2012). Because thaumasite crystallizes in a trigonal lattice (*a*, *b*, and *c* axes), the simulation cell is generated by extending the unit cell of thaumasite three times in the *a*, *b*, and *c* directions. The simulation cell of thaumasite contains a total of 3294 atoms. The interatomic interactions are described using the ReaxFF force field developed by van Duin et al. (2001). ReaxFF partitions the total energy of interactions similar to those found in classical nonreactive force fields, that is, in valence, nonbonded, and H-bond terms, but it introduces bond order dependencies on valence terms and additional potential energy corrections in the form of penalties or contributions to properly describe bond dissociation and formation under different environmental conditions. By using a bond length/order relationship, smooth transitions from nonbonded to single, double, and triple bonded systems, and vice versa, are obtained. Furthermore, charges are allowed to change as bonds are broken or formed. The van der Waals (vdW) interactions are included between all atoms, not just nonbonded ones, which allows the valence bonding interaction to be monotonically attractive. Because the vdW inner wall balances the bond attraction, all valence interactions depend on the bond order and go to zero as the bonds are broken. All parameters are obtained directly and systematically from quantum mechanics. The atomic charges calculated by the charge equilibrium

(QEq) method (Rappe and Goddard, 1991) are updated at each time step. The ReaxFF parameters used in this study have been derived from Liu et al. (2012) and then extended and reoptimized to include all sulfur interactions using GARFfield (Jaramillo-Botero et al., 2014). To ensure the structural stability and conformity of the thaumasite model in ambient conditions, its 3×3×3 super cell is equilibrated for 100 ps using an isobaric-isothermal (*NPT*) ensemble at 298 K and 0 atm at a time step of 0.25 fs. The final 50 ps of the equilibrated trajectories are used to compute the cell parameters. Convergence of a variety of parameters, including total energy and its components, lattice parameters, and volume, are particularly monitored and ensured. The equilibrated molecular structure of thaumasite is then used as the initial configuration for characterization of the stress-strain behavior at both elastic and plastic ranges.

4.2.3 Calculating Elastic Properties at Finite Temperature

The elastic constants of thaumasite are calculated from the linear relation between the stress and strain tensors within the limit of infinitesimal deformation. In this study, the elastic constants are calculated from the 3×3×3 super cell of thaumasite equilibrated at room temperature (298 K). The simulation cell is then subjected to 12 strain configurations, including three uniaxial tension/compression pairs and three shear pairs. Small deformations for each configuration have been applied to ensure that the strains remain in the elastic range. Each separate straining simulation is performed for 30 ps with a time step of 0.25 fs. The pressure of the system for the last 10 ps dynamics is recorded to obtain the elastic constants. During the course of straining, the positions of the atoms in the simulation cell are equilibrated in a microcanonical (*NVE*) ensemble coupled with a Langevin thermostat, which keeps the temperature at 298 K. Once the elastic constants are determined, the Voigt-Reuss-Hill (VRH) elastic properties of thaumasite are estimated following the method described in our previous studies (Hajilar and Shafei, 2014 and

2015). The ReaxFF calculated elastic properties are then compared with those available in the literature.

4.2.4 Calculating Stress-Strain Response

The equilibrated simulation cell of thaumasite is subjected to a range of uniaxial tensile strains along each of the three orthogonal *x*, *y* and *z* directions. During the infinitesimal deformation, a constant strain rate (i.e., 0.0005, 0.001, 0.005, and 0.01 ps^{-1}) is applied to the simulation cell. The atoms in the simulation cell are then fully relaxed to fit within new dimensions. It must be noted that the directions perpendicular to the one under external strain are allowed to relax anisotropically in order to capture the material's Poisson ratio. This can be achieved by using the *NPT* ensemble equations of motion with NULL pressure in the deformation direction and 1.0 atm pressure in the other two directions. The evolution of atomic stress in the molecular structure is recorded as a function of strain. The cell stress fluctuations induced by kinetic contributions are smeared by averaging the atomic stresses over a short time interval of 100 time steps. The straining procedure is repeated for all three Cartesian axes (*x*, *y*, and *z*) and continues until the maximum target strain of 25% is reached. The full set of stress and strain data are then used to generate the stress-strain curves for each strain direction. To examine the stress-strain behavior, 1000 strained conformers are recorded at equal intervals of the full strain range for further chemical bond and structural damage analyses. The chemical bond analysis is used to fully characterize the structural response of thaumasite under uniaxial strain.

4.3 Results and Discussions

4.3.1 Structural Properties of Thaumasite

The cell parameters of thaumasite equilibrated over the course of 100 ps *NPT*-RMD at ambient temperature and pressure are reported in Table 4-1. The calculated unit cell parameters accurately reproduce the experimental values with a difference less than 4% for all cases.

Table 4-1. Thaumasite cell parameters calculated using ReaxFF and obtained by Gatta et al.'s (2012) experimental tests.

Cell Parameters	ReaxFF *NPT*-RMD	Experiment	Difference (%)
a*/*b **(Å)**	11.4048	11.0545	3.20
c **(Å)**	10.8245	10.4131	3.95

In addition to ambient temperature (298 K) equilibration, the cell parameters of thaumasite are further investigated at different temperatures. Because thaumasite dehydrates at temperatures above 380 K (Brough and Atkinson, 2001), the range of temperature considered in this study is 100-380 K. Figure 4-2 illustrates the volume and unit cell parameters of thaumasite at different temperatures within the established range.

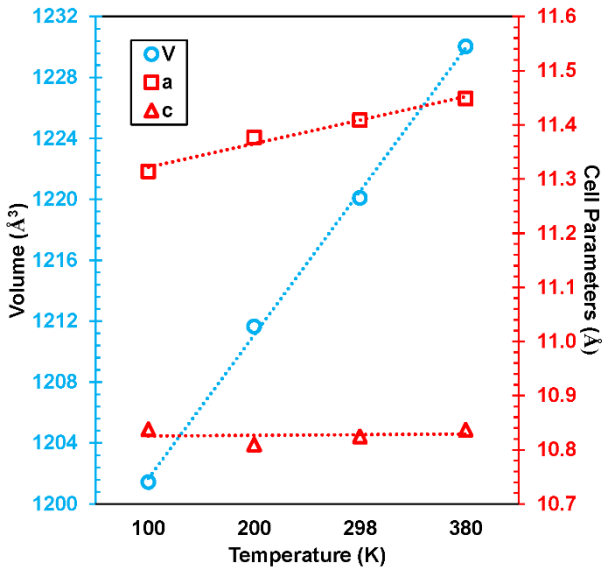

Figure 4-2. Thermal expansion of thaumasite between 100 and 380 K.

It can be observed that the thermal expansion of the *a*- and *b*-axis directions are very different from that of the *c*-axis direction. While the volume and *a*- and *b*-axis parameters expand by 2.38 and 1.19%, respectively, as the temperature increases from 100 to 380 K, the *c*-axis parameters remain relatively unchanged. This is primarily due to the fact that thaumasite has strong ionic-covalent $[Ca_3Si(OH)_6.12H_2O]^{4+}$ columns along the *c*-axis direction. The main intercolumn supports in the *a*- and *b*-axis directions are the hydrogen bonds to the sulfate and carbonate groups,

which expand with increasing temperature. However, the strong nature of Ca-O and Si-O bonds resist the temperature-induced expansion in the *c*-axis direction. Table 4-2 summarizes the mean thermal expansion coefficients of thaumasite within the temperature range considered in this study. The thermal expansion coefficient of thaumasite parallel to the columnar structures is relatively constant and, in some cases negative when compared to that of the transverse direction. This can be attributed to the negative thermal expansion of the silicate octahedra, observed in the past experimental tests (Jacobsen et al., 2003). The thermal expansion coefficients of thaumasite change linearly over the temperature range of 100-380 K, which is consistent with the findings of Martucci and Cruciani (2006).

Table 4-2. Mean thermal expansion coefficients of thaumasite in various temperature ranges.

	100-200 K	**200-298 K**	**298-380 K**	**100-380 K**
α_V **(×10^{-5} K^{-1})**	8.50	7.10	9.94	8.50
α_a **(×10^{-5} K^{-1})**	5.53	2.85	4.26	4.24
α_c **(×10^{-5} K^{-1})**	-2.57	1.39	1.39	-2.54

4.3.2 Mechanical Properties of Thaumasite

Mechanical properties of thaumasite, including those associated with the elastic and plastic ranges, are presented and discussed in this section. Table 4-3 lists the elastic constants as well as the VRH elastic properties of thaumasite computed from the RMD simulations along with those obtained using Brillouin spectroscopy (Scholtzová et al., 2015). It can be seen that the results from the *NVT*-RMD simulations are consistent with those reported in the literature. As expected, it is noted that C_{33} is slightly smaller than C_{11}. This is because the strong covalent bonds that exist in the $[Ca_3Si(OH)_6.12H_2O]^{4+}$ columns result in a higher stiffness in the *a*-*b* plane. This is similar to the behavior observed for the thermal expansion of thaumasite.

Table 4-3. Elastic properties of thaumasite calculated using ReaxFF and obtained from Scholtzová et al.'s (2015) experimental tests.

Elastic Properties	ReaxFF *NVT*-RMD	Experiment
C_{11} (GPa)	41.26	59.9
C_{12} (GPa)	32.88	34.3
C_{13} (GPa)	25.98	24.1
C_{33} (GPa)	65.84	61.4
C_{44} (GPa)	8.77	13.9
C_{66} (GPa)	5.44	12.8
K (GPa)	35.33	38.4
G (GPa)	8.31	14.5
E (GPa)	23.12	38.6
v	0.39	0.33

The direction sensitivity of the mechanical properties of thaumasite is further investigated by analyzing the full stress-strain curves in different directions. The simulated stress-strain curves of thaumasite under uniaxial tensile strains in the *x*/*y* and *z* directions at ambient temperature and pressure conditions are shown in Figure 4-3.

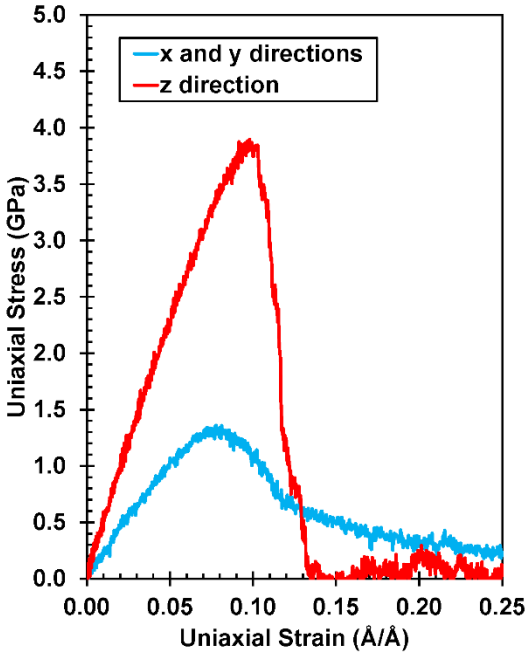

Figure 4-3. Stress-strain curves of thaumasite under tensile strains in the *x*/*y* and *z* directions.

Although thaumasite in the *x*/*y* directions is slightly more ductile than that in the *z* direction, the stress-strain curves indicate that no noticeable plastic deformation takes place before the stress abruptly drops once the ultimate strength is reached. This confirms the brittle nature of structural response of thaumasite under tensile strain. While the stress-strain curves of thaumasite in the *x*/*y* and *z* directions have similar trends, there is a significant difference in the magnitude of the peak stress, often called ultimate strength, as well as the fracture strain. In the *x*/*y* directions, an ultimate strength of 1.36 GPa is reached at a strain of 7.8%, while in the *z* direction, an ultimate strength of 3.89 GPa is obtained at a strain of 9.8%. This highlights that thaumasite is almost three times stronger in the z direction than that in the *x*/*y* directions.

The stress-strain behavior observed in different directions can be further justified using chemical bond analysis. Figure 4-4 shows the changes in the normalized number of Ca-O, Si-O, S-O, C-O, and H-O bonds as a function of applied tensile strain in the *x*/*y* and *z* directions. In the *x*/*y* directions, the number of covalent Ca-O bonds decreases by increasing the applied tensile strain and increases when the minimum value is reached. This behavior is very consistent with the stress-strain curve obtained for thaumasite in the *x*/*y* directions. Contrary to Ca-O, the number of S-O, Si-O, and C-O bonds remains unchanged over the course of tensile straining until the structure collapses at a strain of 19%. This indicates that the Si-O, S-O, and C-O bonds do not have a significant contribution to the tensile strength of thaumasite in the *x*/*y* directions. On the other hand, in the *z* direction, the number of Ca-O, Si-O, S-O, and C-O bonds varies significantly. The *z* axis is parallel to the direction of the strong $[Ca_3Si(OH)_6.12H_2O]^{4+}$ columns, which are connected to the sulfate and carbonate groups with an extensive network of hydrogen bonding. This leads to the higher strength of thaumasite in the *z* direction.

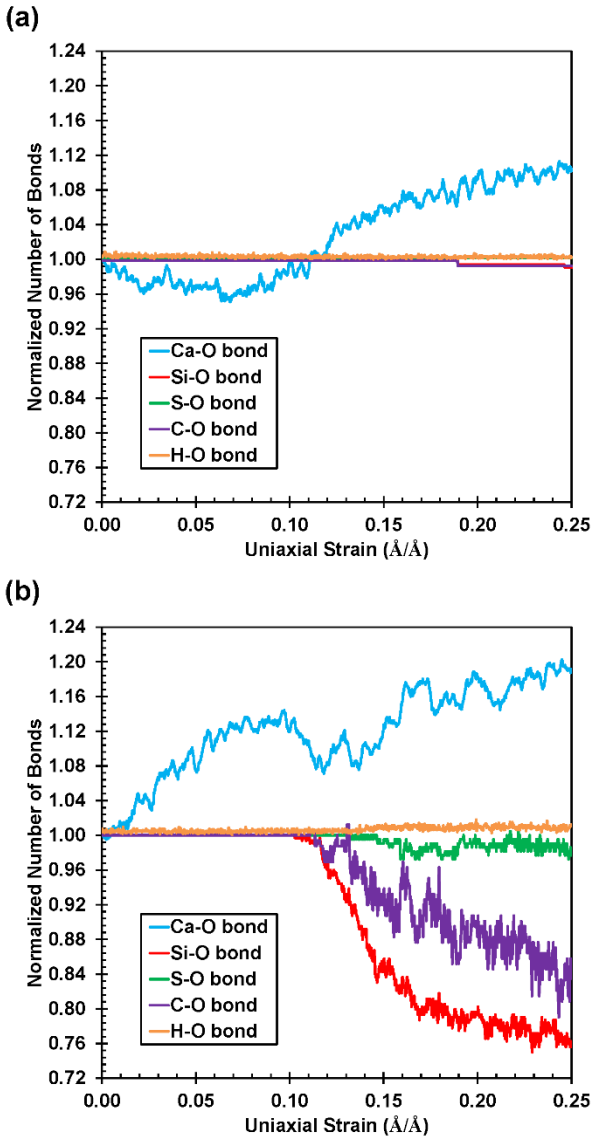

Figure 4-4. Changes in the number of bonds during the straining of thaumasite in the (a) *x*/*y* directions, and (b) *z* direction.

4.3.3 Effect of Temperature Change on Mechanical Properties of Thaumasite

At any nonzero temperature and under no external forces, atoms in a solid still move due to thermal oscillations around equilibrium positions. Therefore, temperature is an important factor in evaluating the mechanical properties of materials given that vibrations lead to variations in bond strength. Here, separate sets of RMD simulations are performed to capture the sensitivity of the mechanical properties of thaumasite to temperature changes. The stress-strain curves of thaumasite

under uniaxial tensile strains at different temperatures ranging from 100 to 380 K are shown in Figure 4-5.

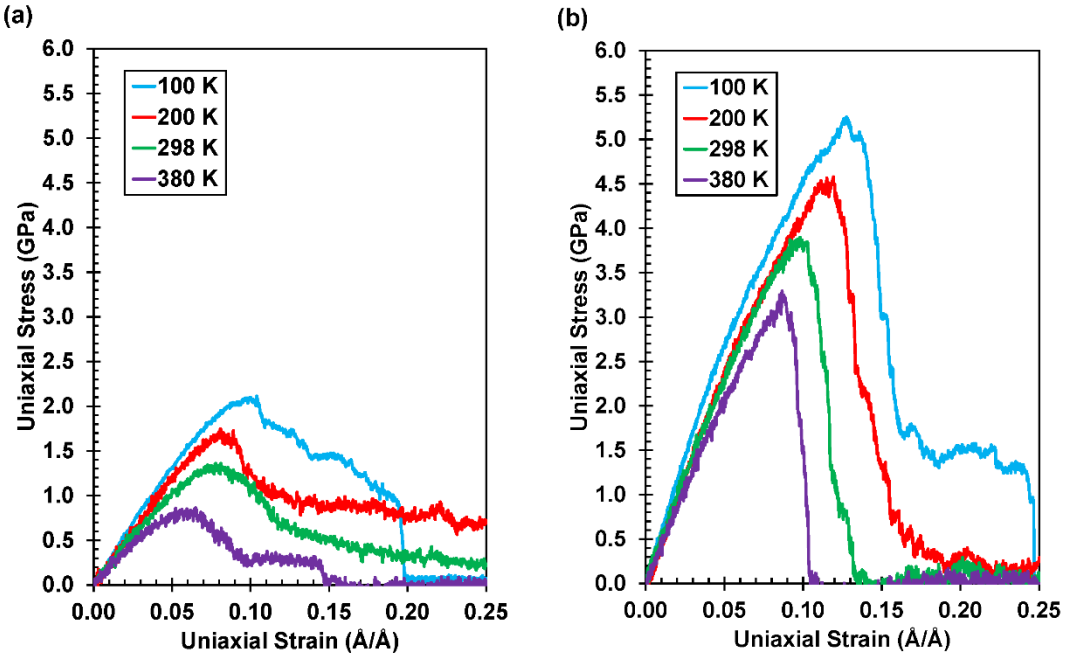

Figure 4-5. Stress-strain curves of thaumasite at different temperatures under uniaxial tensile strains in the (a) *x*/*y* directions, and (b) *z* direction.

It can be seen that temperature exerts a substantial effect on the mechanical properties of thaumasite. With an increase in temperature, the tensile strength, Young's modulus, and fracture strain of thaumasite decrease significantly (Figure 4-6). This behavior, which is referred to as the thermal-softening effect, has been captured for a variety of materials, such as platinum nanowire (Koh et al., 2005), silica glass (Pedone et al., 2008), polymer (Li and Strachan, 2011), silicene (Pei et al., 2014), and calcium hydroxide (Hajilar and Shafei, 2016b) to name a few. By increasing the temperature from 100 to 380 K, the tensile strength, Young's modulus, and tensile strain of thaumasite drop by approximately 59.2, 37.5, and 37.5% in the *x*/*y* directions, respectively, and by 37.4, 22.0, and 32.1% in the *z* direction, respectively.

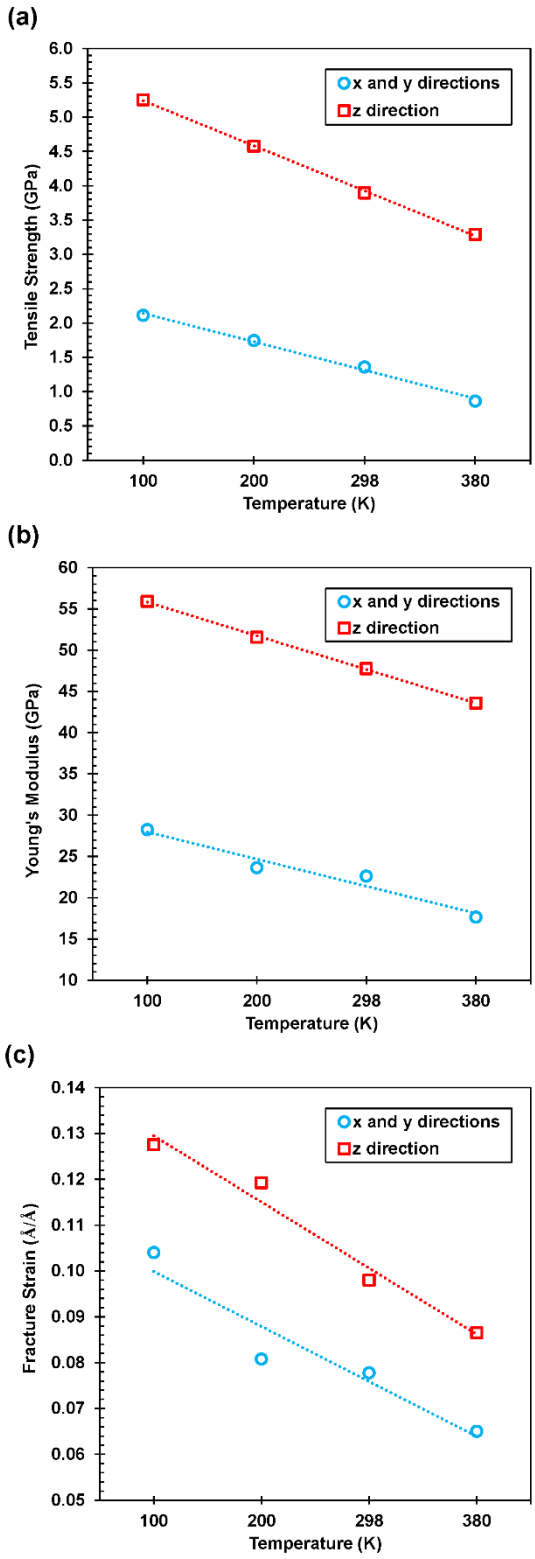

Figure 4-6. Mechanical Properties of thaumasite at different temperatures under uniaxial tensile strains in the *x*/*y* and *z* directions: (a) Tensile strength, (b) Young's modulus, and (c) Fracture strain.

Higher temperatures lead to an increase in the internal energy and entropy of bonds, both of which contribute to the bond structures with lower than equilibrium bond orders. Moreover, because the equilibrium length of bonds is larger at higher temperatures, the bonds can faster reach their breaking length during the tensile straining process (Figure 4-7). As a result, the mechanical properties of thaumasite decrease drastically with increasing temperature.

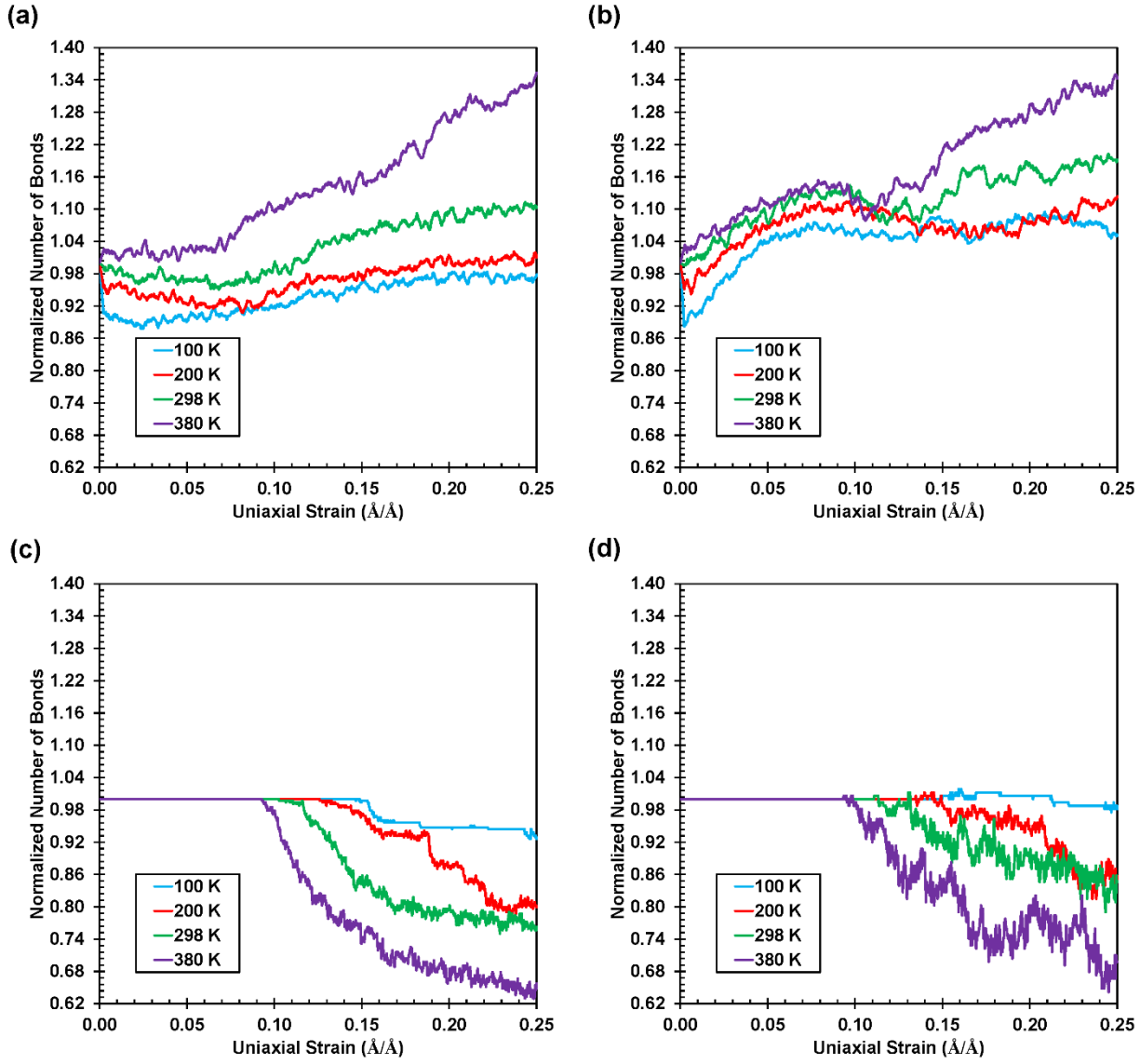

Figure 4-7. Changes in the number of bonds during the straining of thaumasite in different directions with various temperatures: (a) Ca-O bonds in the *x*/*y* directions, (b) Ca-O bonds in the *z* direction, (c) Si-O bonds in the *z* direction, and (d) C-O bonds in the *z* direction.

4.3.4 Effect of Strain Rate on Mechanical Properties of Thaumasite

According to the kinetic theory of solid fracture, the strain rate may significantly affect the mechanical properties of solids (Xiao et al., 2004). To capture the effect of strain rate on the mechanical properties of thaumasite, a number of strain rates ranging from 0.0005 to 0.01 ps^{-1} are chosen. This range is within those reported in previous atomistic simulations associated with the mechanical characterization of materials (Koh et al., 2005; Pedone et al., 2008; Pei et al., 2014; Wu et al., 2014). It must be noted that the selected strain rates are approximately 3 orders of magnitude faster than the dynamic or shock loads accessible through conventional experiments (Zhuang et al., 2002). The short integration time steps in molecular dynamics simulations (0.25 fs in this study) as well as the computational cost of calculating the interatomic forces enforce such limits on the strain rate. Figure 4-8 shows the stress-strain curves of thaumasite at different strain rates under uniaxial tensile strains at ambient temperature (298 K).

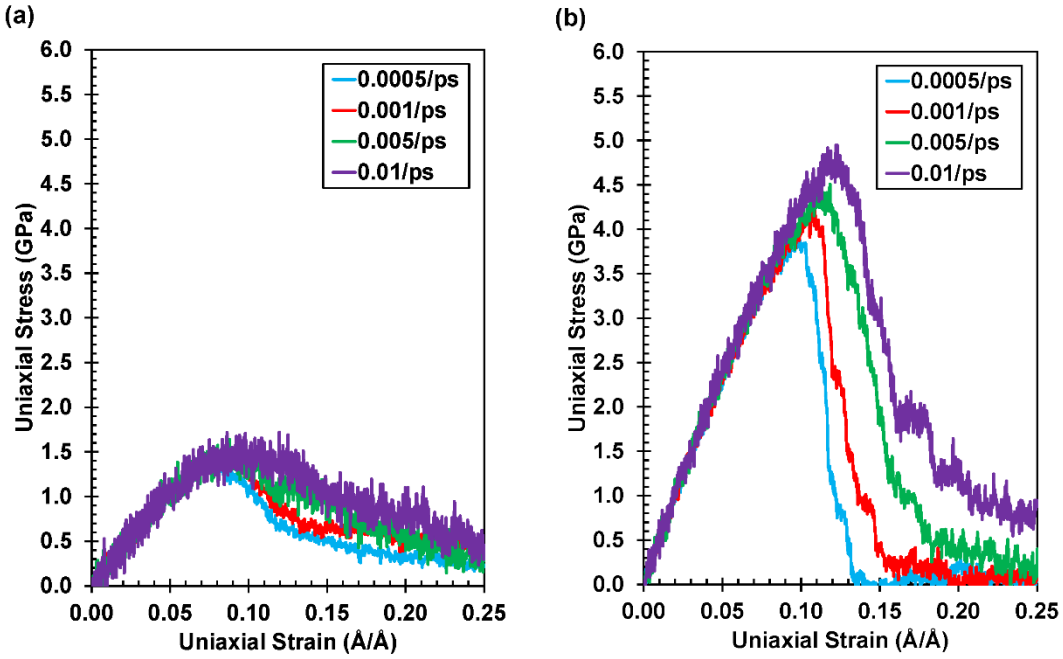

Figure 4-8. Stress-strain curves of thaumasite at different strain rates under uniaxial tensile strains in the (a) *x*/*y* directions, and (b) *z* direction.

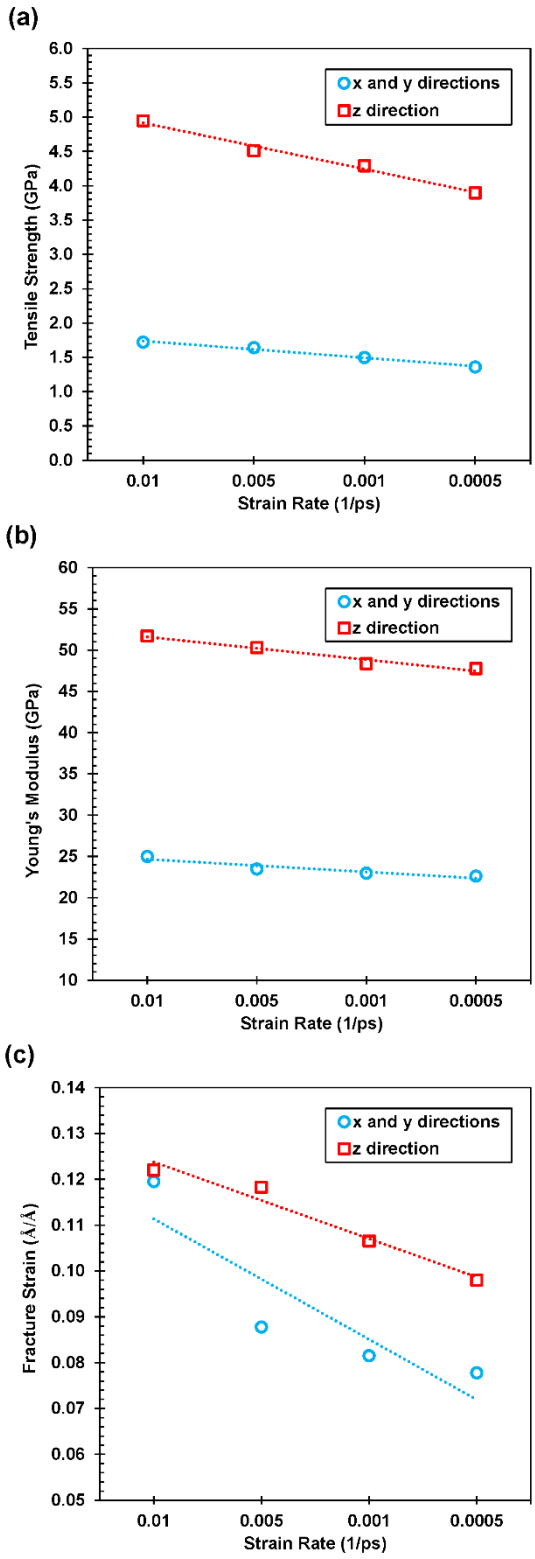

Figure 4-9. Mechanical Properties of thaumasite under uniaxial tensile strains with various strain rates in the *x*/*y* and *z* directions: (a) Tensile strength, (b) Young's modulus, and (c) Fracture strain.

The ultimate strength of thaumasite (and the proportionality limit) slightly increases with increasing the strain rate, while the modulus of elasticity seems to be independent of the strain rate. By decreasing the strain rate from 0.01 to 0.0005 ps^{-1}, the ultimate strength of thaumasite drops from 4.94 to 3.89 GPa in the *z* direction and from 1.72 to 1.36 GPa in the *x*/*y* directions. A similar trend is captured for the fracture strain of thaumasite (Figure 4-9).

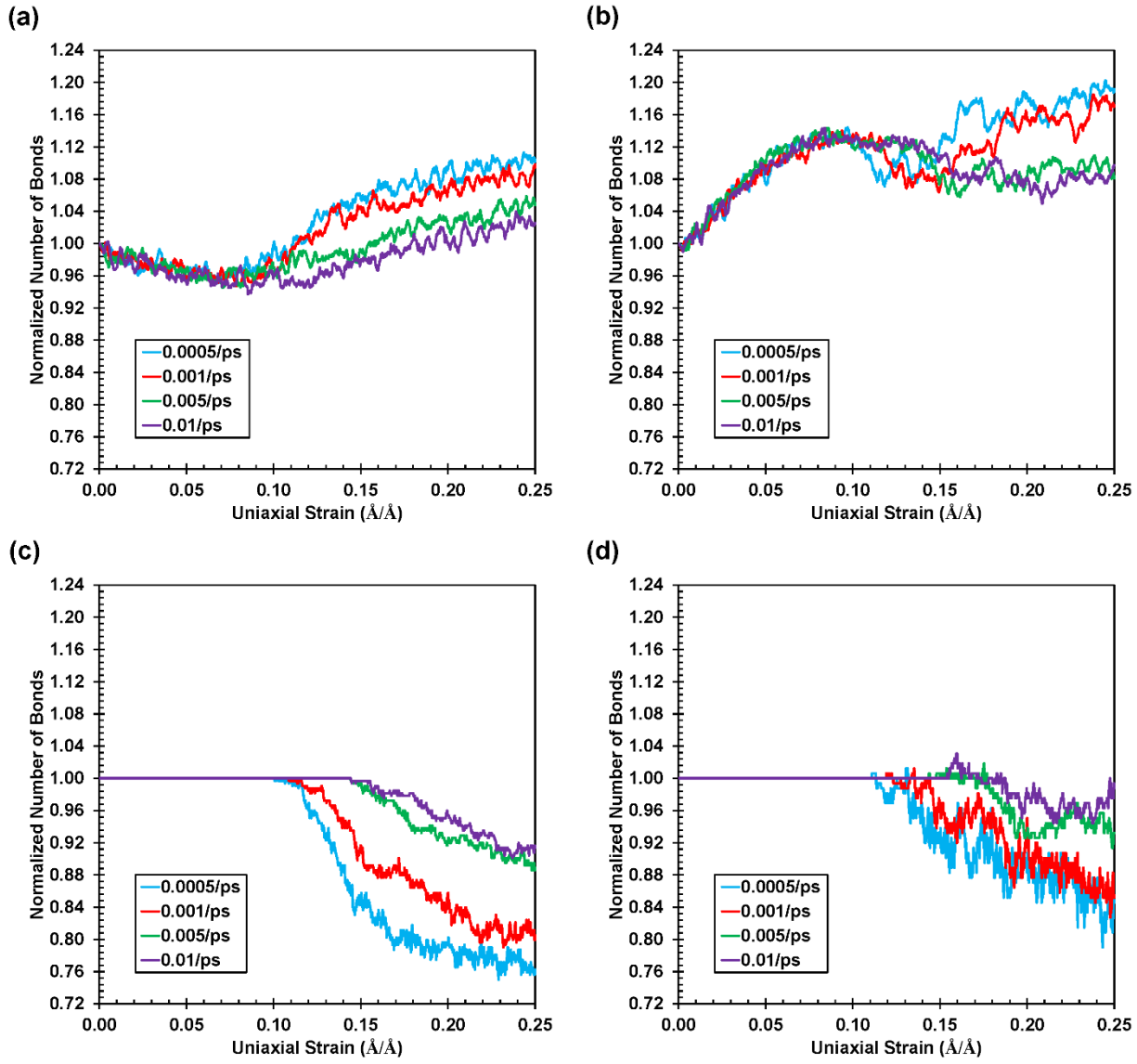

Figure 4-10. Changes in the number of bonds during the straining of thaumasite in different directions with various strain rates: (a) Ca-O bonds in the *x*/*y* directions, (b) Ca-O bonds in the *z* direction, (c) Si-O bonds in the *z* direction, and (d) C-O bonds in the *z* direction.

The fact that a lower strain rate results in reduced mechanical strength has been demonstrated via macroscopic experiments for cementitious materials (Rossi, 1997). Lower strain rates tend to increase the effect of thermal fluctuations that promote bond dissociation. Figure 4-10 confirms this postulate by showing the change in the number of chemical bonds in thaumasite strained with different rates. As the strain rate decreases, the dissociation rate of bonds increases. Moreover, Figure 4-8 shows that at higher strain rates a complete fracture requires a larger strain. This can also be inferred from the chemical bond analysis shown in Figure 4-10, which highlights that as the strain rate increases, a larger strain is needed for bonds to break. In other words, fast mechanical loading may reduce the probability of fracture.

4.4 Conclusions

The mechanical properties of thaumasite were fully characterized in this study for the first time using RMD simulations. The simulation results showed that the stress-strain relationships of thaumasite are substantially dependent on the direction of the applied strain. Thaumasite was found to be three times stronger in the *z* direction than that in the *x*/*y* directions. This was because of the contribution of strong $[Ca_3Si(OH)_6.12H_2O]^{4+}$ columns that exist in the *z* direction. Bond analysis revealed that in the *x*/*y* directions Ca-O bonds are the only bonds that resist tensile deformations. In the *z* direction, however, the contribution of Si-O, S-O, and C-O bonds must be recognized as well. This properly explains the significant difference observed in the mechanical strength of thaumasite in the three orthogonal directions. The effects of temperature change and strain rate on the mechanical properties of thaumasite were also investigated in detail. As the temperature increases, the rate of chemical bond dissociation increases, which in turn results in a substantial reduction in the mechanical strength of thaumasite. On the other hand, a decrease in the strain rate

favors larger atomic fluctuations accompanied by temperature-induced rearrangements, which caused a noticeable reduction in the mechanical strength of thaumasite.

4.5 Acknowledgments

The feedback and support from Dr. Tao Cheng and Dr. Andres Jaramillo-Botero are gratefully acknowledged. The Extreme Science and Engineering Discovery Environment (XSEDE), which is supported by National Science Foundation Grant Number ACI-1548562, was used for part of the atomistic simulations conducted in this study.

4.6 References

1- Bensted J., 1999. "*Thaumasite-background and nature in deterioration of cements, mortars and concretes*", Cement and Concrete Composites 21: 117-121.

2- Bickley J.A., 1999. "*The repair of Arctic structures damaged by Thaumasite*", Cement and Concrete Composites 21: 155-158.

3- Brough A.R., and Atkinson A., 2001. "*Micro-Raman spectroscopy of thaumasite*", Cement and Concrete Research 31: 421-424.

4- Crammond N.J., 1985. "*Thaumasite in failed cement mortars and renders from exposed brickwork*", Cement and Concrete Research 15: 1039-1050.

5- Crammond N.J., 2002. "*The occurrence of thaumasite in modern construction- a review*", Cement and Concrete Research 24: 393-402.

6- Edge R.A., and Taylor H.F.W., 1971. "*Crystal structure of thaumasite, $[Ca_3Si(OH)_6.12H_2O](SO_4)(CO_3)$*", Acta Crystallographica (B) 27: 594-601.

7- Effenberger H., Kirfel A., Will G., and Zobetz E., 1983. "*A further refinement of the crystal structure of thaumasite, $Ca_3Si(OH)_6CO_3SO_412H_2O$*", Neus Jahrbuch fur Mineralogie Monatshefte 2: 60–68.

8- Frost D.J., and Fei Y., 1998. "*Stability of phase D at high pressure and high temperature*", Journal of Geophysical Research 103 (B4): 7463-7474.

9- Gatta G.D., McIntyre G.J., Swanson J.G., and Jacobson S.D., 2012. "*Minerals in cement chemistry: A single-crystal neutron diffraction and Raman spectroscopic study of thaumasite, Ca3Si(OH)6(CO3)(SO4)·12H2O*", American Mineralogist 97: 1060-1069.

10- Glasser F.P., Marchand J., and Samson E., 2008. "*Durability of concrete-degradation phenomena involving detrimental chemical reactions*", Cement and Concrete Research 38: 226-246.

11- Grimmer A.R., Wieker W., Lampe F., Fechner E., Peter R., and Molgedey G., 1980. "*Hochauflosende 29Si-NMR an festen silicaten: Anisotropie der chemischen Verschiebung im thaumasite*", Z Chem 20: 453.

12- Hajilar S., and Shafei B., 2014. "*Nano-scale characterization of elastic properties of AFt and AFm phases of Hydrated Cement Paste*", Proceedings of the European Conference on Computational Modeling of Concrete Structures (EURO-C), Vol. 1, p.p. 299-306.

13- Hajilar S., and Shafei B., 2015. "*Nano-scale investigation of elastic properties of hydrated cement paste constituents using molecular dynamics simulations*", Computational Materials Science 101: 216-226.

14- Hajilar S., and Shafei B., 2016a. "*Mechanical failure mechanisms of hydrated products of tricalcium aluminate: A reactive molecular dynamics study*", Materials and Design 90: 165-176.

15- Hajilar S., and Shafei B., 2016b. "Assessment of structural, thermal, and mechanical properties of portlandite through molecular dynamics simulations". Journal of Solid State Chemistry 24: 164-174.

16- Jacobsen S.D., Smyth J.R., and Swope R.J., 2002. "*Thermal expansion of hydrated six-coordinate silicon in thaumasite, $Ca_3Si(OH)_6(CO_3)(SO_4).12H_2O$*", Physics and Chemistry of Minerals 30: 321-329.

17- Koh S.J.A., Lee H.P., and Cheng Q.H., 2005. "*Molecular dynamics simulation of a solid platinum nanowire under uniaxial tensile strain: Temperature and strain-rate effects*". Physical Review B 72: 085414.

18- Li C., and Strachan A., 2011. "*Molecular dynamics predictions of thermal and mechanical properties of thermoset polymer EPON862/DETDA*". Polymer 52: 2920-2928.

19- Liu L., Jaramillo-Botero A., Goddard III W.A., and Sun H., 2012. "*Development of a ReaxFF reactive force field for ettringite and study of its mechanical failure modes from reactive molecular dynamics*", Journal of Physical Chemistry A 116(5): 3918-3925.

20- Martucci A., and Cruciani G., 2006. "In situ time resolved synchrotron power diffraction study of thaumasite", Physics and Chemistry of Minerals 33: 723-731.

21- Moenke H., 1964. "*Ein weiteres Mineral mit Silizium in 6er-Koordination: Thaumasit*", Naturwissenschaften 51: 239.

22- Neville A., 2004. "*The confused world of sulfate attack on concrete*". Cement and Concrete Research 34: 1275-1296.

23- Rappe T., and Goddard III, W.A, 1991. "*Charge equilibration for molecular dynamics simulations*", The Journal of Physical Chemistry 95 (8): 3358–3363.

24- Jaramillo-Botero A., Naserifar S., Goddard III W.A, 2014. "*A general multi-objective force field optimization framework, with application to reactive force fields for silicon carbide*", Journal of Chemical Theory and Computation 10(4): 1426-1439.

25- Jaramillo-Botero A., Cheng, T., Liu, L., Goddard III W.A. "First-principles based modeling of cement hydration kinetics and dynamics", Nanomechanics for Structural Materials Meeting (DOT award No. DTFH61-10-C-00019), DOT Turner-Fairbank Highway Research Center, Virginia, March 6, 2014.

26- Pedone A., Malavasi G., Menziani M.C., Segre U., and Cormack A.N., 2008. "*Molecular dynamics studies of stress-strain behavior of silica glass under a tensile load*". Chemistry of Materials 20: 4356-4366.

27- Pei Q.X., Sha Z.D., Zhang Y.Y., and Zhang Y.W., 2014. "*Effects of temperature and strain rate on the mechanical properties of silicene*". Journal of Applied Physics 115: 023519.

28- Plimpton S., 1995. "*Fast Parallel Algorithms for Short-Range Molecular Dynamics*". Journal of Computational Physics 117: 1-19.

29- Rossi P., 1997. "*Strain rate effects in concrete structures: the LCPC experience*". Materials and Structures 30(1): 54-62.

30- Santhanam M., Cohen M.D., and Olek J., 2002. "*Mechanism of sulfate attack: A fresh look Part 1: Summary of experimental results*". Cement and Concrete Research 32: 915-921.

31- Santhanam M., Cohen M.D., and Olek J., 2003. "*Mechanism of sulfate attack: a fresh look Part 2. Proposed mechanisms*". Cement and Concrete Research 33: 341-346.

32- Scholtzová E., Tunega D., and Speziale S., 2015. "*Mechanical properties of ettringite and thaumasite-DFT and experimental study*", Cement and Concrete Research 77: 9-15.

33- Stebbins J.F., and Kanzaki M., 1991. "*Local structure and chemical shifts for six-coordinated silicon in high-pressure mantle phases*", Science 251(4991): 294–298.

34- van Duin A.C.T., Dasgupta S., Lorant F., and Goddard III W.A., 2001. "*ReaxFF: A Reactive Force Field for Hydrocarbons*", The Journal of Physical Chemistry A 105(41): 9396-9409.

35- Wu X., Moon R.J., and Martini A., 2014. "*Tensile strength of Iβ crystalline cellulose predicted by molecular dynamics simulation*". Cellulose 21(4): 2233-2245.

36- Wunder B., Jahn S., Koch-Muller M., and Speziale S., (2012), "*The 3.65 Å phase, $MgSi(OH)_6$: Structural insights from DFT-calculations and T-dependent IR spectroscopy*", American Mineralogist 97: 1043-1048.

37- Xiao T., Ren Y., and Liao K., 2004. "*A kinetic model for time-dependent fracture of carbon nanotubes*". Nano Letters 4(6): 1139-1142.

38- Yang H., Prewitt C.T., and Frost D.J., 1997. "*Crystal structure of dense hydrous magnesium silicate, Phase D*", American Mineralogist 82: 651-654.

39- Zhuang S., Lu J., and Ravichandran G., 2002. "*Shock wave response of a zirconium-based bulk metallic glass and its composite*". Journal of Applied Physics Letters 80: 4522.

CHAPTER 5: STRENGTH ANISOTROPY AND TENSION-COMPRESSION ASYMMETRY IN COMPLEX SULFATE-BEARING CRYSTALS

Ettringite and thaumasite are the main byproducts of complex chemical reactions that take place in cementitious materials during sulfate attack. These two sulfate-bearing crystals are known to experience excessive strains and stresses in various crystallographic directions during precipitation. Considering that this process can cause extensive structural damage to the hardened cement paste, the current study investigates, for the first time, the effects of strain intensity and direction by simulating the atomic structures of both ettringite and thaumasite under a range of uniaxial and biaxial strains. For this purpose, the reactive molecular dynamics method is employed to capture the breakage and formation of chemical bonds during the course of straining. A comprehensive bond analysis is performed to unravel the atomistic processes underlying the plastic behavior of ettringite and thaumasite under different straining conditions. From biaxial simulations, the flow stresses are determined, particularly to characterize the plane stress flow surfaces of ettringite and thaumasite. A set of yield criteria are examined to identify the most suitable criterion that captures the intrinsic features observed from the constitutive response of ettringite and thaumasite under various straining states. The outcome of this study is an important step forward to developing representative constitutive models that can be used to evaluate and optimize the mechanical properties of cementitious materials exposed to harsh environmental conditions.

5.1 Introduction

Sulfate attack has been identified as one of the main deterioration mechanisms, which adversely affect the long-term durability and performance of civil infrastructures made of cementitious materials. For this group of materials, sulfate attack refers to a chain of chemical reactions between a sulfate-rich source and the hydrated products of cement. Depending on the source of sulfate, both

external and internal sulfate attack are possible. The former occurs when the sulfates that are present in the water or soil penetrate into the hardened cement paste, while the latter takes place when sulfate-contaminated aggregates or cements with a high sulfate content are used. The chemical reactions associated with sulfate attack are known to result in the formation of a number of sulfate-bearing crystals, including ettringite, $[Ca_6[Al(OH)_6]_2(SO_4)_3.26H_2O]$ and thaumasite $[Ca_3Si(OH)_6(CO_3)(SO_4).12H_2O]$ (Santhanam et al., 2002 and 2003; Neville, 2004). Depending on the hydrated products involved in sulfate attack reactions and the products formed as a result of sulfate attack, deterioration in cementitious materials can be caused by two distinct mechanisms in the hardened cement paste: (1) expansion and spalling, and (2) loss of strength and adhesion.

To address the expansion and spalling of the hardened cement paste, which is mainly due to the formation of ettringite, and the loss of strength and adhesion of the hardened cement paste, which is primarily caused by the precipitation of thaumasite, it is critical to investigate the constitutive response of both ettringite and thaumasite crystals under various strains and stresses. The experimental studies available in the literature are limited to the prediction of the elastic properties of these two crystals using the Brillouin spectroscopy technique (Speziale et al., 2008; Scholtzová et al., 2015). This is because of the challenges involved in the preparation of ideal single crystalline samples for evaluating their plastic response under mechanical loads. Continuum theories of plasticity have been developed to provide a phenomenological description of failure in cementitious materials (Ortiz, 1985; Chen, 2007). Despite the frequent use of such top-down theories, they fail to provide an in-depth understanding of the role of atomic structures in the mechanical properties of cementitious materials. With recent advances in computational tools, this gap can now be addressed through the investigation of the physicochemical properties of

cementitious materials using representative models that complement the classical theories of continuum mechanics and laboratory experimental tests.

Atomistic computational methods, such as classical energy minimization (Manzano, 2009), molecular dynamics (Hajilar and Shafei, 2014 and 2015), and density functional theory (DFT) (Scholtzová et al., 2015) have been employed to characterize the elastic properties of ettringite and thaumasite. It was observed that the elasticity tensor of both ettringite and thaumasite are highly anisotropic along different crystallographic directions. Manzano et al. (2012) studied the effect of hydrostatic pressure on the elastic properties of ettringite using the DFT method. It was revealed that at high pressures (above 2.5 GPa), there is a drastic increase in the bulk modulus of ettringite. This was attributed to the densification of the hydrogen bond network. Liu et al. (2012) investigated the failure modes of ettringite under uniaxial tensile and compressive strains. It was observed that the breakage of Ca-O bonds is the main contributor to the failure of ettringite under uniaxial strains. Hajilar and Shafei (2016a) performed reactive molecular dynamics (RMD) simulations to evaluate the mechanical failure mechanisms of ettringite under uniaxial tensile strains. It was found that the segregation and breakage of the tricalcium aluminate columns lead to the mechanical failure in each crystallographic direction. More recently, the effect of temperature and strain rate on the mechanical response of thaumasite under uniaxial tensile strains were studied using a set of RMD simulations (Hajilar et al., 2017).

Despite the contribution of the previous efforts to characterize the mechanical response of ettringite and thaumasite under uniaxial loads, the constitutive behavior of them under multiaxial loading configurations had remained largely unknown. This was the main motivation of the current study to address this research gap, for the first time, by developing an atomistic computational framework to predict the plastic response of ettringite and thaumasite under various multiaxial

strains. Such a framework replicates the real-world exposure scenarios, in which multiaxial strain states are commonly formed within the cement matrix, due to the precipitation of ettringite and thaumasite during the sulfate attack reactions (Glasser et al., 2008). For simulation purposes, the RMD method is employed to equilibrate the atomic structures of ettringite and thaumasite to the ambient temperature and pressure conditions. The equilibrated structures are then subjected to uniaxial and biaxial states of tensile and compressive strain to obtain full plane stress flow surfaces. A separate bond analysis is performed to unravel the atomistic processes underlying the plastic response of ettringite and thaumasite under various states of straining. Furthermore, various yield criteria, such as von Mises, Drucker-Prager, Hill, and Liu-Huang-Stout, are examined to identify the criterion that can successfully capture the plastic response of ettringite and thaumasite under multiaxial strains. This is expected to transform the understanding of the constitutive response of complex sulfate-bearing phases of cementitious materials, especially under harsh environmental conditions.

5.2 Computational Simulations

5.2.1 Atomic Structures of Sulfate-Bearing Crystals

Ettringite is formed as a result of chemical reactions on monosulfoaluminate [$Ca_4Al_2.4(OH)_{12}.8(SO_4).6(H_2O)$] during sulfate attack. This process is commonly referred to as delayed ettringite formation (DEF), which creates a significant expansion and possibility of damage to the hardened cement paste (Taylor, 1997). Ettringite has a needle-shaped morphology with the chemical composition of $Ca_6[Al(OH)_6]_2(SO_4)_3.26H_2O$ and a density of 1.8 g/cm^3. Ettringite crystallizes in a trigonal system with 256 atoms in its unit cell with the space group of P31c (Figure 5-1).

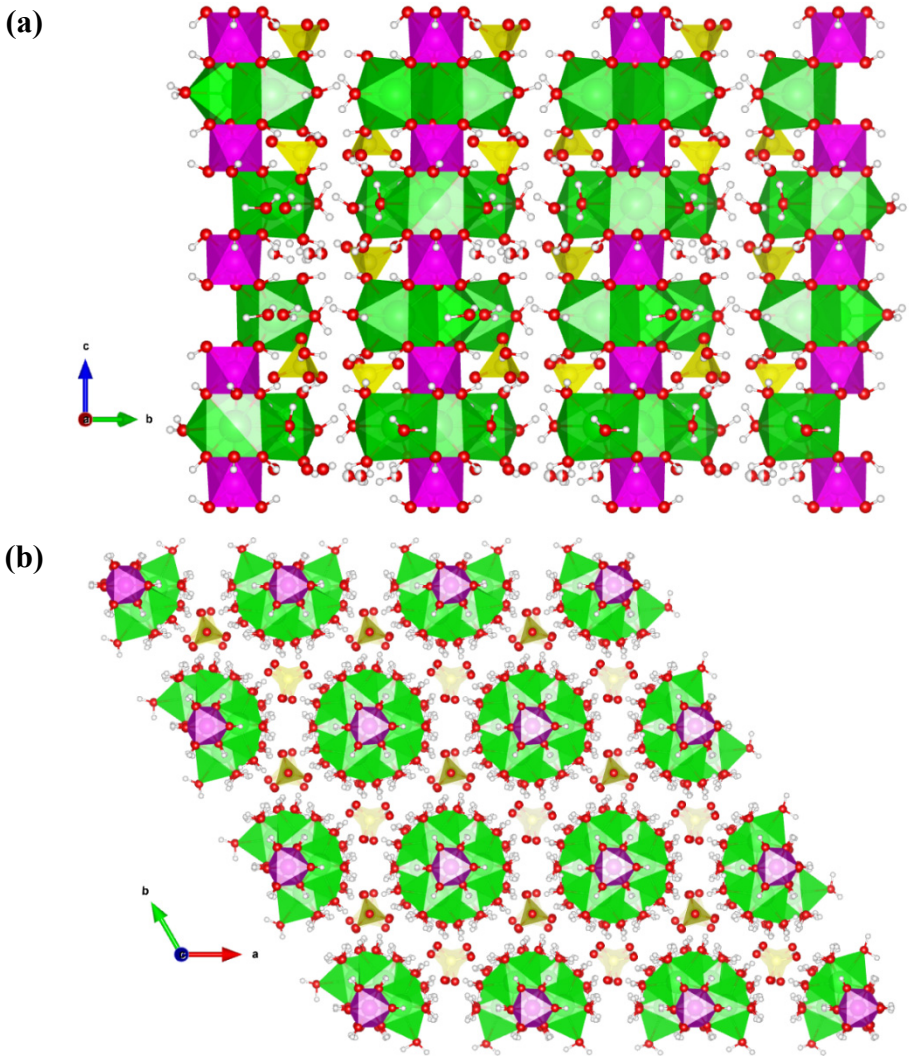

Figure 5-1. A 3 × 3 × 1 crystalline structure of ettringite (a) projected along the *c*-axis, showing the arrangement of tricalcium aluminate columns, and (b) in the *a*-*b* plane, illustrating the sulfate groups and water molecules between the cylindrical tricalcium aluminate columns. The color scheme is as follows: Green: Calcium; Pink: Aluminum; Yellow: Sulfur, Red: Oxygen; and White: Hydrogen.

The crystalline structure of ettringite, which has been fully characterized in the literature (Moore and Taylor, 1968; Hartman and Berliner, 2006), consists of columns and channels running parallel to the *c*-axis of hexagonal prisms (Hajilar and Shafei, 2018). The composition of the columns and the channels are $[Ca_6[Al(OH)_6]_2.24H_2O]^{6+}$ and $[(SO_4)^3.2H_2O]^{6-}$, respectively. Each column is formed from a chain of polyhedra made of one aluminum and three calcium atoms. The aluminum atoms are each six-fold, octahedrally coordinated with six hydroxyl groups. The

calcium atoms, on the other hand, are each eight-fold, coordinated with four hydroxyl groups and four water molecules. A distinct aspect of this crystal is the presence of an extensive network of hydrogen bonds along a central column of aluminum and calcium polyhedra. In ettringite, hydrogen bonds are formed when a hydrogen site is present between two oxygen atoms separated by a distance of 3.3 Å. The hydrogen bond network provides additional structural support to the tricalcium aluminate columns.

In the other category of chemical reactions during sulfate attack, the sulfate groups react with calcium hydroxide ($Ca(OH)_2$ or CH in cement notation) and calcium-silicate-hydrates (C-S-H in cement notation, with unfixed stoichiometry). This results in the formation of gypsum, and subsequently, loss of strength and adhesion, mainly due to the decalcification of C-S-H (Mehta, 1994). If a carbonate-rich source is present in addition to the CH and C-S-H, the sulfate attack reactions lead to the formation of thaumasite. The carbonate ions needed for the formation of thaumasite can be provided either by carbon dioxide dissolved in the penetrating water or the limestone ($CaCO_3$) that exists in the aggregates and fillers. The formation of thaumasite transforms the hardened cement paste into a mushy, incohesive mass with a significantly reduced strength and adhesion (Glasser et al., 2008). This chemical process is often favored by a humid environment and a temperature lower than 15 °C (Crammond, 2002).

Thaumasite [$Ca_3[Si(OH)_6.12H_2O)].CO_3.SO_4$] is a mineral that has a hexagonal structure with 122 atoms in its unit cell and the space group of $P6_3$ (Figure 5-2). With a density of 1.88 g/cm^3, more than half of the weight of this crystal is from water and hydroxyl groups. The crystalline structure of thaumasite was first determined by Edge and Tylor (1971) and later refined by other studies, such as Effenberger et al. (1983) and Gatta et al. (2012).

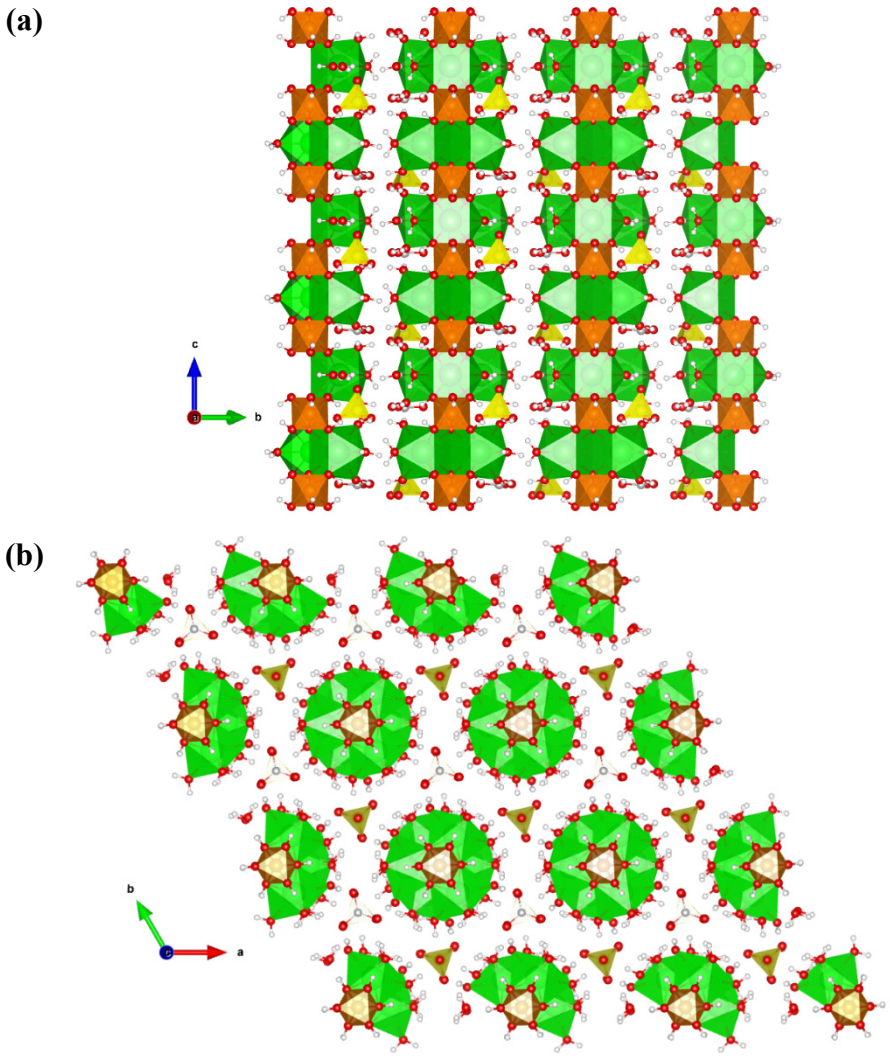

Figure 5-2. A 3 × 3 × 3 crystalline structure of thaumasite (a) projected along the *c*-axis, showing the arrangement of tricalcium silicate columns, and (b) in the *a*-*b* plane, illustrating the sulfate and carbonate groups, as well as the water molecules between the cylindrical tricalcium silicate columns. The color scheme is as follows: Green: Calcium; Orange: Silicon; Yellow: Sulfur, Gray: Carbon; Red: Oxygen; White: Hydrogen.

Thaumasite is the only known mineral that possesses silicon atoms coordinated by six hydroxyl groups stable in the ambient temperature and pressure (Moenke, 1964; Grimmer et al., 1980; Stebbins and Kankazi, 1991). This is a unique feature, as the other silicate minerals that form most of the earth's crust contain silicon atoms coordinated to four oxygen atoms. In thaumasite, six hydroxyl groups are coordinated to Si^{4+}, resulting in $Si(OH)_6^{2-}$, which are balanced by Ca^{2+}. These anions and cations are surrounded by twelve water molecules, which form the cylindrical columns

of $[Ca_3Si(OH)_6.12H_2O]^{4+}$ along the *c*-axis of the unit cell. These columns are interconnected only through hydrogen bonding with the SO_4^{2-} and CO_3^{2-} groups located in the channels between the columns. The sulfate and carbonate groups that neutralize the excess charge of the system are fully ordered and alternate along the *c*-axis of the unit cell.

5.2.2 Model Details

The LAMMPS (Large-scale Atomic/Molecular Massively Parallel Simulator) program (Plimpton, 1995) installed on a parallel Linux cluster is used to perform the RMD simulations. The unit cells of ettringite and thaumasite crystals are constructed in LAMMPS using the latest crystallographic data available in the literature (Hartman and Berliner, 2006; Gatta et al., 2012). Each unit cell is then transformed into an orthorhombic cell (*x*, *y*, and *z* axes) with the *z* axis parallel to the original *c* axis. To maintain the periodicity of the new orthorhombic lattice, it is necessary to double the size in the *a* axis direction, resulting in a pseudo-orthorhombic simulation cell twice the size of the initial unit cell. Therefore, the simulation cell, which hereafter is referred to as orthorhombic supercell, contains 512 and 244 atoms for ettringite and thaumasite, respectively. The orthorhombic supercells are then periodically extended in the *x*, *y*, and *z* directions. The extended ettringite and thaumasite supercells are $2x \times 2y \times 2z$ and $2x \times 3y \times 3z$, which contain a total of 4,096 and 4,392 atoms, respectively. The RMD simulations are performed on three-dimensional computational cells with periodic boundary conditions applied to the *x*, *y*, and *z* directions (Allen and Tildesley, 1987).

To evaluate the atomic interactions, the potential energy of the system must be determined at each step of a simulation. This cannot be achieved without introducing a forcefield (potential energy) that accurately estimates the forces among different atoms. From the variety of available forcefields, the ReaxFF forcefield developed by van Duin et al. (2001) is used in this study.

ReaxFF has been successfully used to investigate the mechanical properties of various cementitious materials (e.g., Liu et al., 2012; Bauchy et al., 2015; Hou et al., 2015; Palkovic et al., 2015 and 2016; Hajilar and Shafei, 2016(a); Hajilar et al., 2017). In ReaxFF, the short-range interactions are determined by length-bond orders. This approach can effectively capture the bond breakage and formation, as the bonded interactions are allowed to decay smoothly to zero. The non-bonded Columbic and van der Waals interactions are calculated for all the atoms in the system using a 7^{th} order taper function with an outer cutoff of 10 Å. The atomic charges are determined by the charge equilibrium (QEq) method (Rappe and Goddard, 1991) and are updated at each time step. Using the ReaxFF/C implementation of ReaxFF in LAMMPS (Aktulga et al., 2012), the supercells of ettringite and thaumasite are equilibrated in the isobaric-isothermal ensemble (*NPT*) for 100 ps (picosecond, 10^{-12} s) at 298 K and 0 atm with a time step of 0.25 fs (femtosecond, 10^{-15} s). To ensure the thermodynamic equilibrium during the RMD simulations, the convergence of a variety of parameters (e.g., total energy and its components, temperature, and pressure) is closely monitored. The equilibrated structures are used as initial configurations for the straining process.

5.2.3 Straining Procedure

Two sets of RMD simulations are performed to explore the plastic deformations of the equilibrated atomic structures of ettringite and thaumasite. While the first set is designed to find the deformations under uniaxial tensile and compressive strains, the second set is intended to develop the biaxial yield surfaces. A total of 80 independent simulations are performed to capture the mechanical response of the two sulfate-bearing crystals under various multiaxial straining conditions applied to different crystallographic directions. Consistent with the previous studies (Hajilar and Shafei 2016(a) and 2016(b); Hajilar et al., 2017), various strain rates ranging from 0.0001 to 0.001/ps are used. During the straining process, the positions of atoms in the straining

direction(s) are remapped to fit within the new dimensions of the supercells. To ensure capturing the Poisson's effect, the direction(s) perpendicular to the one under external strains are allowed to relax anisotropically. This can be achieved by using the *NPT* equations of motion at zero pressure in the unloaded direction(s). The virial stress evolution in the atomic structures is recorded while the supercells are strained. The straining process continues until the target strain of 0.20 Å/Å is reached for each simulation case.

To examine the stress-strain behavior, 1,000 strained structural configurations are employed for further chemical bond analyses. RMD simulations provide valuable information about the dynamic of trajectories, which can be used to explain the mechanical behavior of ettringite and thaumasite crystals, especially under large strains. To this end, the average number of bonds is computed for all the bonds that exist in each supercell. The bonds that can potentially contribute to resisting the applied tensile/compressive strains are then identified through a constant monitoring of changes in the number of bonds present in the system. The outcome of such a holistic bond analysis is used to characterize, for the first time, the atomistic origin of the mechanical response of ettringite and thaumasite under various states of straining.

5.3 Results and Discussions

5.3.1 Uniaxial Straining

The stress-strain curves of ettringite and thaumasite subjected to uniaxial tensile and compressive strains in the *y* and *z* directions are presented in Figure 5-3. It can be seen in this figure that the initial portion of all the stress-strain curves is linear, confirming the elastic behavior expected under small strains. Beyond the elastic range, there is an onset of nonlinearity corresponding to the plastic range, in which stress either suddenly drops after the maximum stress

is reached (e.g., in the *z* direction) or decreases gradually with increasing the strain, representing a strain softening behavior (e.g., in the *y* direction).

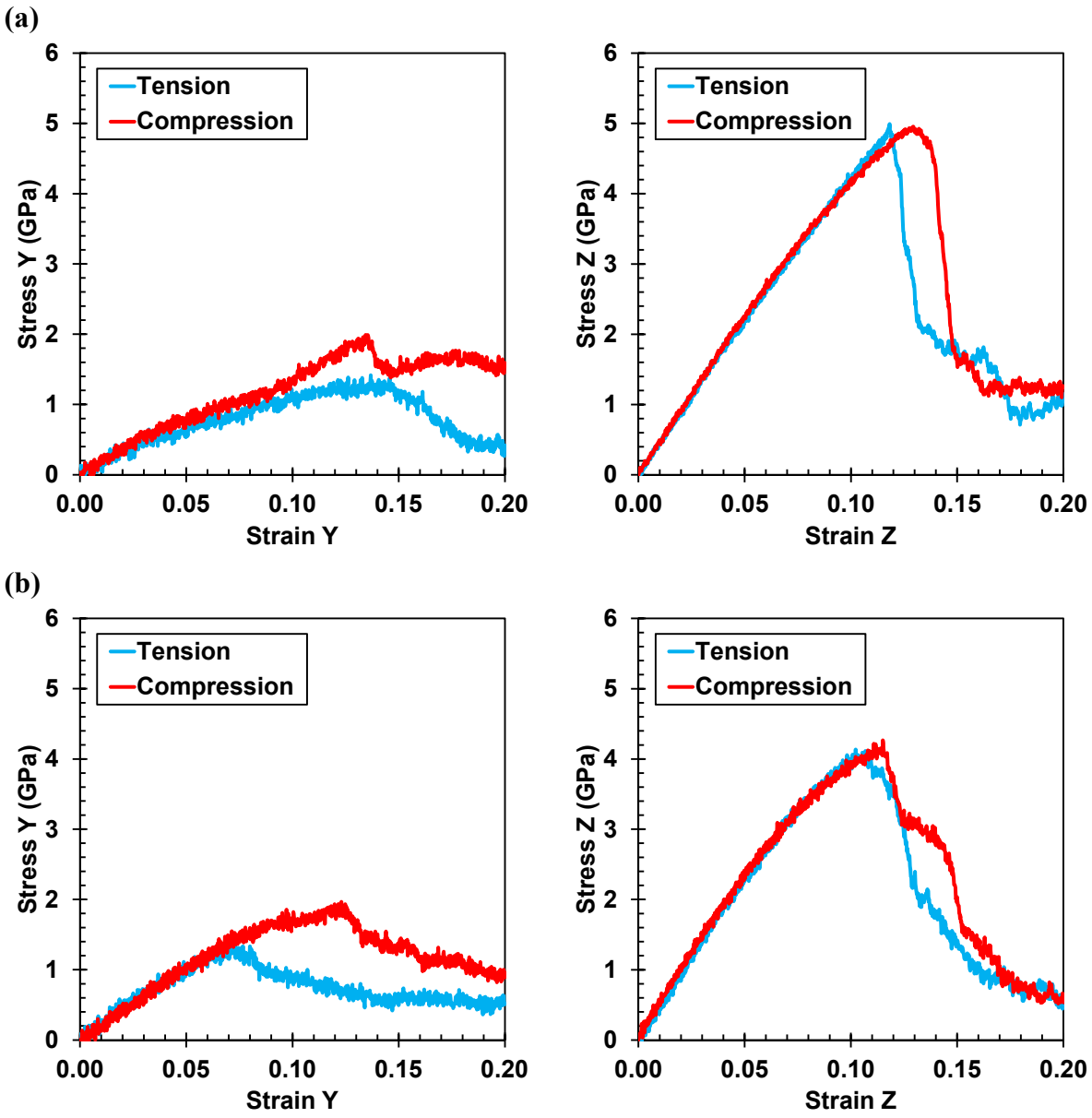

Figure 5-3. Stress-strain relationship of (a) ettringite and (b) thaumasite under uniaxial tensile and compressive strains in the individual *y* and *z* directions.

The maximum tensile stress in the *y* and *z* directions are 1.42 and 4.99 GPa for ettringite and 1.36 and 4.13 GPa for thaumasite, respectively. A similar trend is observed for compressive strains in the *y* and *z* directions. This strength anisotropy highlights that both crystalline structures are

mechanically stronger in the *z* direction than in the *y* direction. While the maximum tensile and compressive stresses are very close to each other in the *z* direction, the maximum compressive stress is 40% larger than the maximum tensile stress for both ettringite and thaumasite in the *y* direction. The evident asymmetry in the plastic response is a characteristic of cementitious materials, frequently observed in the macroscopic laboratory tests (e.g., Sfer et al., 2002; Hampel et al., 2009; Ritter and Curbach, 2016; Wang et al., 2016). The chemical bond analysis conducted on RMD simulation results sheds light on the atomistic origins of the strength anisotropy and tension-compression asymmetry observed for ettringite and thaumasite.

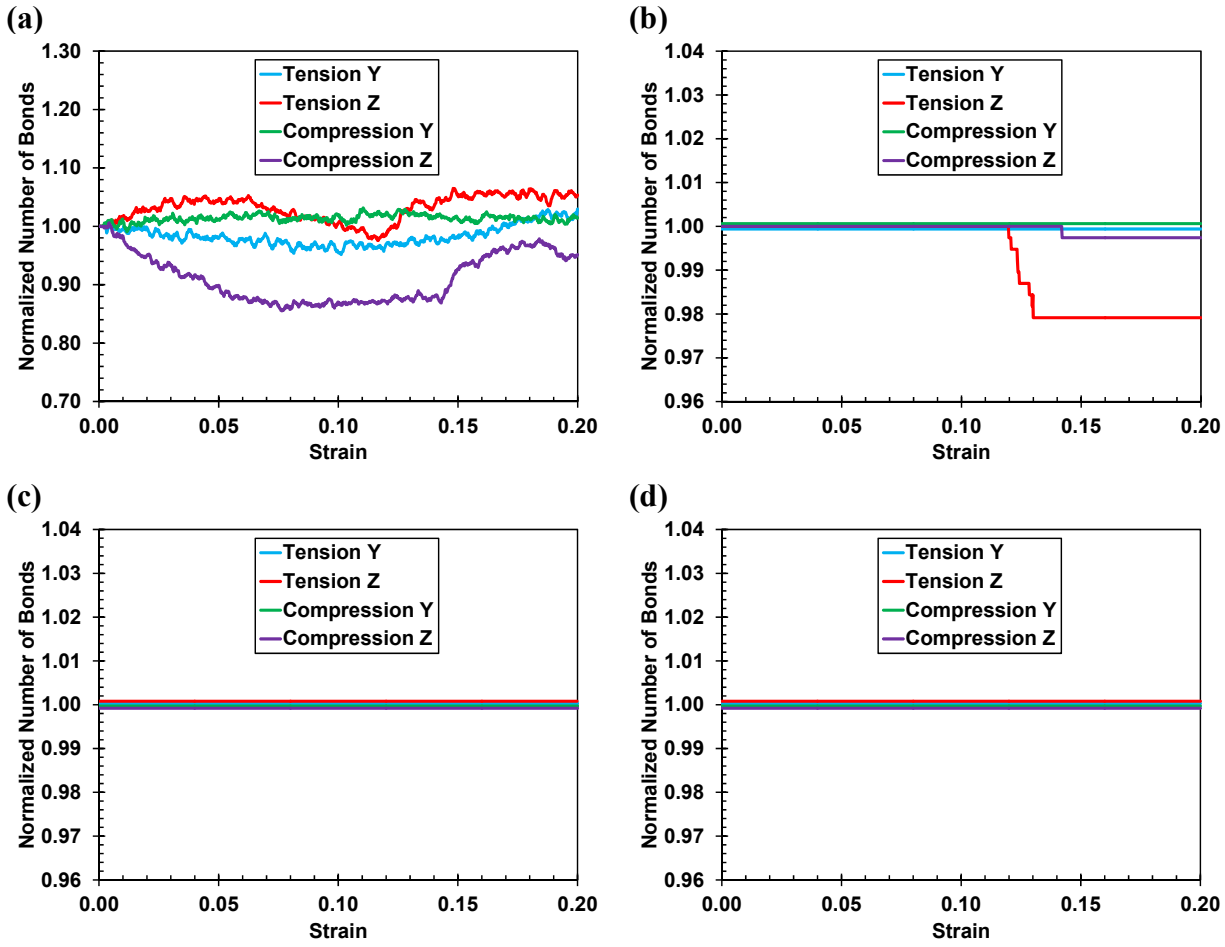

Figure 5-4. Changes in the number of (a) Ca-O, (b) Al-O, (c) S-O, and (d) H-O bonds during the uniaxial straining of ettringite in the individual *y* and *z* directions.

Figure 5-4 shows the normalized number of Ca-O, Al-O, S-O, and H-O bonds as the tensile and compressive strains increase in the *y* and *z* directions. It can be seen that the number of Ca-O bonds changes significantly during the tensile and compressive straining in the *y* and *z* directions. While the number of Al-O bonds in the *y* direction remains unchanged, this number experiences a sudden drop in the *z* direction when a tensile and compressive strain of 0.12 and 0.14 is reached, respectively. This is completely consistent with the observations made on the stress-strain curves (see Figure 5-3) and highlights the fact that the covalent Ca-O and high-energy Al-O bonds in the tricalcium aluminate columns placed along the *c*-axis directly contribute to providing the additional mechanical strength in the *z* direction (compared to the *y* direction). Unlike Ca-O and Al-O bonds, the number of S-O and H-O bonds do not undergo any observable changes in any of the strain configurations, indicating their negligible contribution to resisting external mechanical strains.

Changes in the number of Ca-O, Si-O, S-O, and C-O bonds during the uniaxial straining of thaumasite in the *y* and *z* directions are presented in Figure 5-5. In the *y* direction, only the number of covalent Ca-O bonds changes with the applied tensile and compressive strains. Unlike Ca-O, the number of S-O, Si-O and C-O bonds remains unchanged over the course of straining until the target strain is reached. This indicates that the bonds other than Ca-O have a minimal effect on the mechanical strength of thaumasite in the *y* direction. On the other hand, in the *z* direction, the number of Ca-O, Si-O, S-O, and C-O bonds vary significantly. The *z*-axis is parallel to the direction of strong tricalcium silicate columns, which are connected to the sulfate and carbonate groups with an extensive network of hydrogen bonds. This leads to the contribution of a diverse set of bonds in the *z* direction.

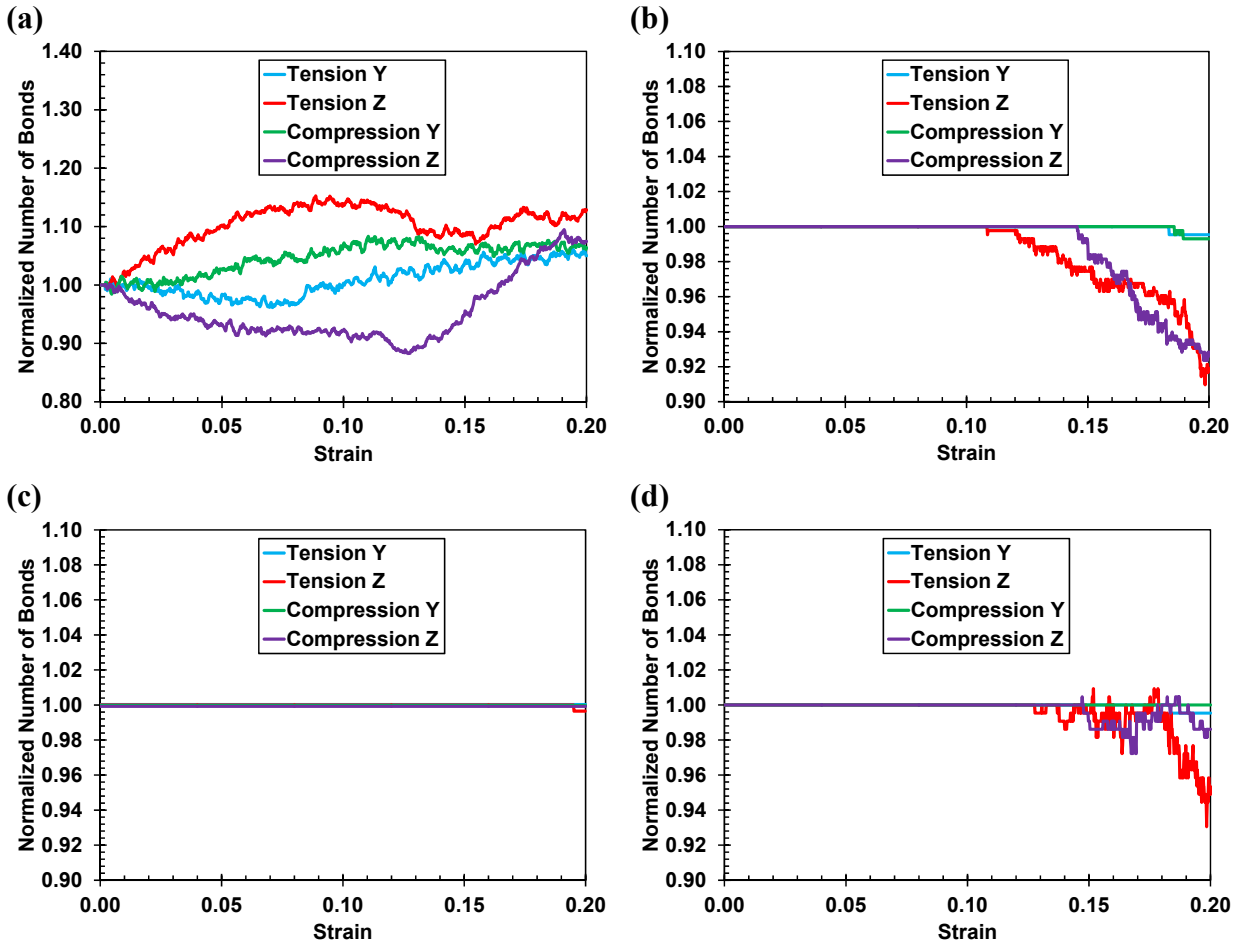

Figure 5-5. Changes in the number of (a) Ca-O, (b) Si-O, (c) S-O, and (d) C-O bonds during the uniaxial straining of thaumasite in the individual *y* and *z* directions.

The bond analysis of ettringite and thaumasite in the *z* direction shows that damage to their atomic structures is primarily due to the breakage and formation of Ca-water bonds under tensile and compressive strains. Since the *z* direction is parallel to the strong tricalcium aluminate and tricalcium silicate columns of ettringite and thaumasite, respectively, the mechanical strength in this direction is higher than that in the *y* direction. This properly explains the strength anisotropy observed in the stress-strain curves. Under the tensile strains in the *y* direction, the hydrogen bond network between the columns is rapidly lost, decreasing the tensile strength of ettringite and thaumasite in the *y* direction. However, under compressive strains in the same direction, the columns are integrated to each other, and as a result of densification of hydrogen bonds, the

mechanical strength of ettringite and thaumasite increases. Thus, it can be concluded that the breakage and densification of the hydrogen bond network are mainly responsible for the stress asymmetry that has been captured in the stress-strain relationships under tensile and compressive strains, respectively.

5.3.2 Biaxial Straining

To obtain an in-depth understanding of how the strain intensity and direction affect the mechanical response of ettringite and thaumasite, the investigations are extended to biaxial straining states. This is achieved by deforming the ettringite and thaumasite crystals in the *y* and *z* directions, while the stress in the *x* axis is maintained at or very close to zero. Figures 5-6 and 5-7 illustrate the mechanical response of ettringite and thaumasite under a balanced biaxial tensile and compressive straining condition, in which the target strain in both *y* and *z* directions are set to 0.2 Å/Å. Similar to uniaxial straining, the maximum stresses in the *z* direction are always larger than those in the *y* direction. It must be noted that the maximum stresses obtained from the biaxial simulations are consistently smaller than the ones extracted from the uniaxial simulations. This is due to the fact that a biaxial strain induces damage to more than one crystallographic direction. A tension-compression strength asymmetry similar to the uniaxial straining states is evident in the biaxial straining states of opposite sign. As can be inferred from Figures 5-6 and 5-7, the compressive flow stresses are always greater than the tensile ones, particularly in the *y* direction.

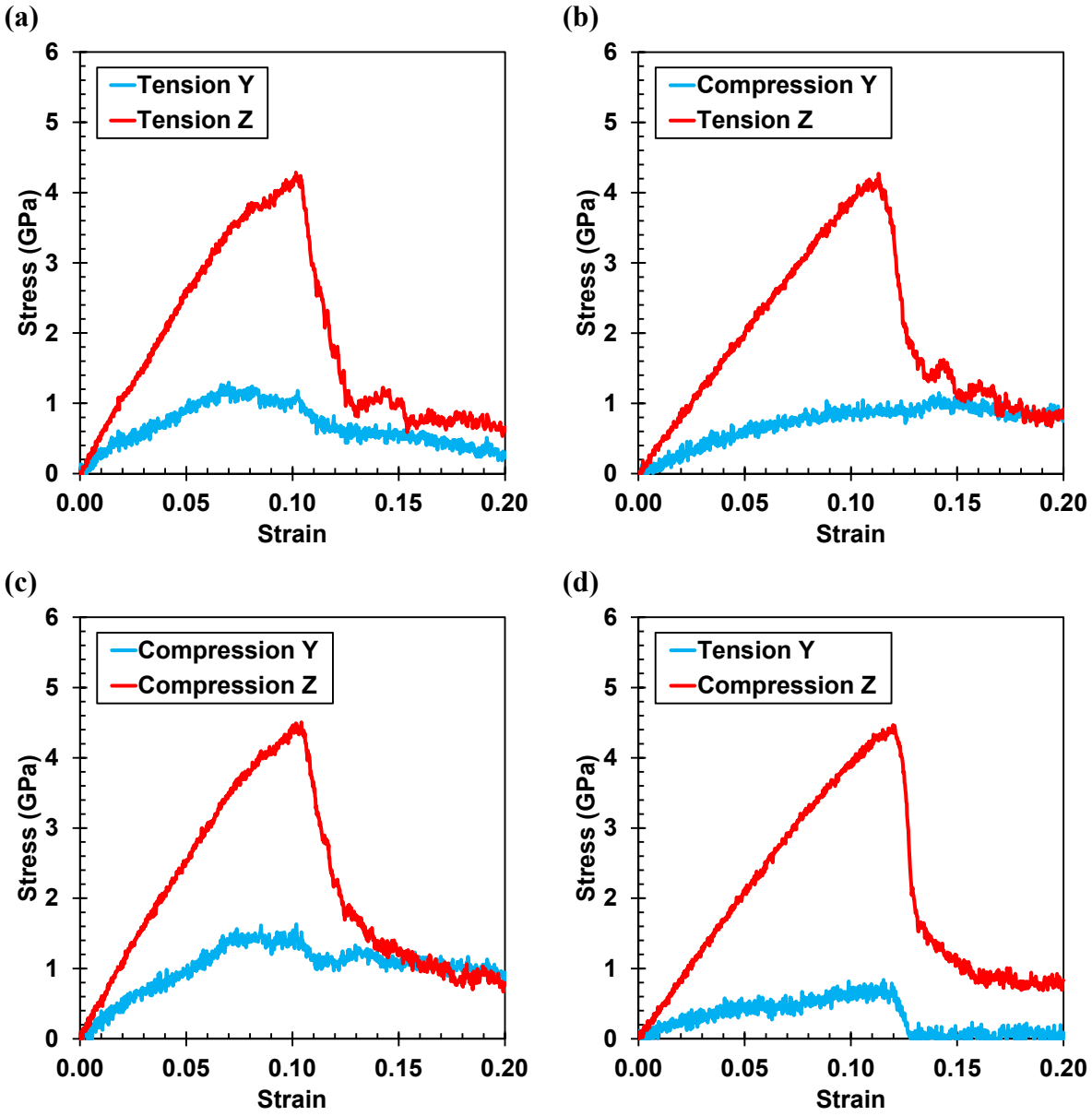

Figure 5-6. Stress-strain relationship of ettringite under biaxial strains in both *y* and *z* directions.

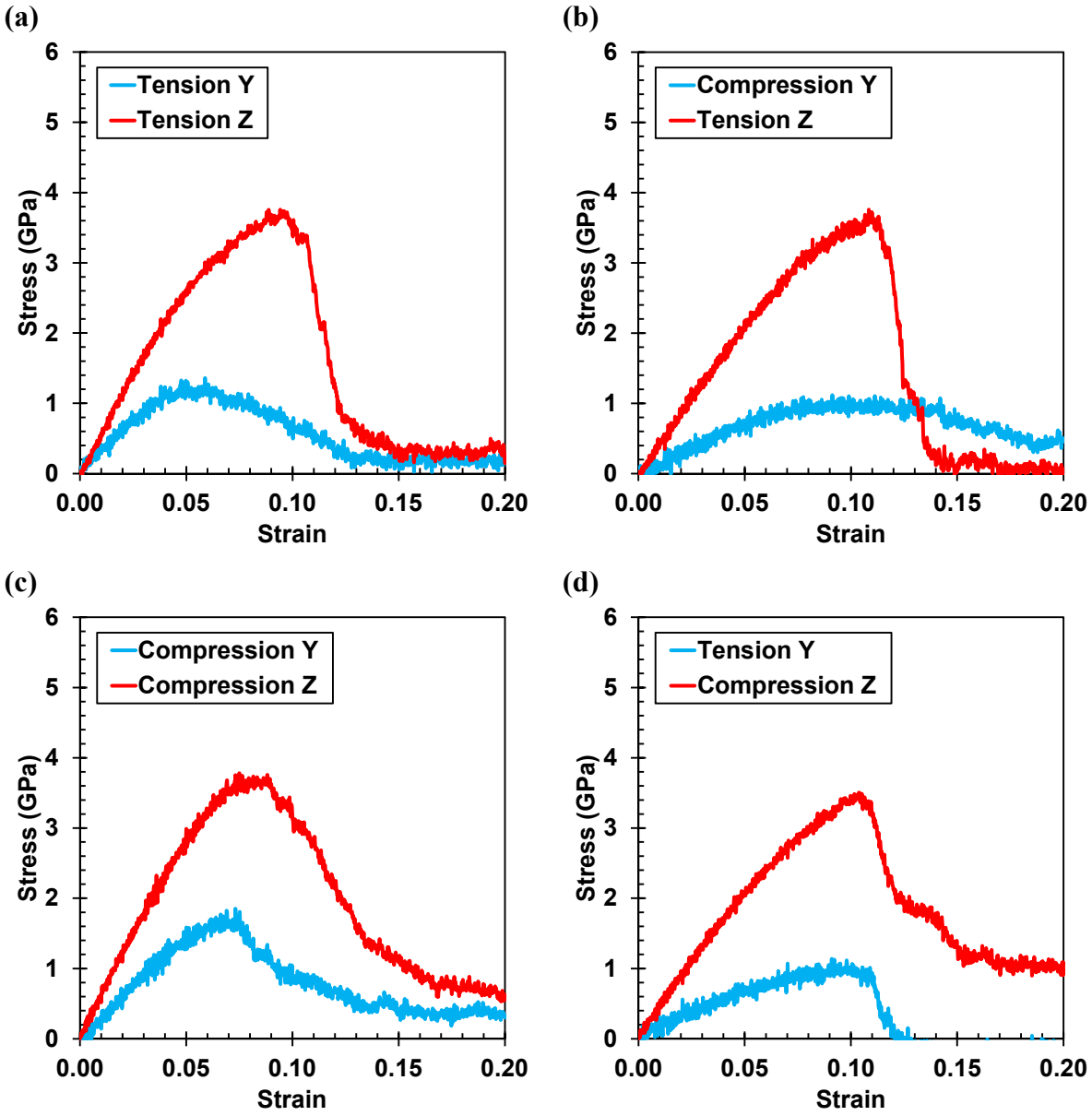

Figure 5-7. Stress-strain relationship of thaumasite under biaxial strains in both *y* and *z* directions.

Figures 5-8 and 5-9 demonstrate the change in the number of chemical bonds over the course of biaxial straining of ettringite and thaumasite, respectively. As for ettringite, it can be seen that the number of Ca-O bonds decreases substantially when the supercell is compressed in the *z* direction for both compression and tension in the *y* direction. Under tensile strains in the *z* direction, however, the number of Ca-O bonds can increase, due to the densification of tricalcium

aluminate groups and formation of Ca-water bonds (as a result of the Poisson's effect in the *x* direction). As expected, the strong Al-O bonds are stretched only under tensile strains in the *z* direction. The number of S-O and H-O bonds, however, do not undergo any changes during the biaxial straining conditions. This was observed under the uniaxial straining conditions as well. As for thaumasite, changes in the number of Ca-O bonds is similar to what captured for ettringite under the biaxial straining simulations. In addition, the Si-O bonds are found to effectively resist the deformations in the *y* and *z* directions, regardless of the sign of strain. While the C-O bonds also contribute to resisting the biaxial strains (similar to the uniaxial ones), less than 3% of the S-O bonds are affected, only after the peak stresses are reached.

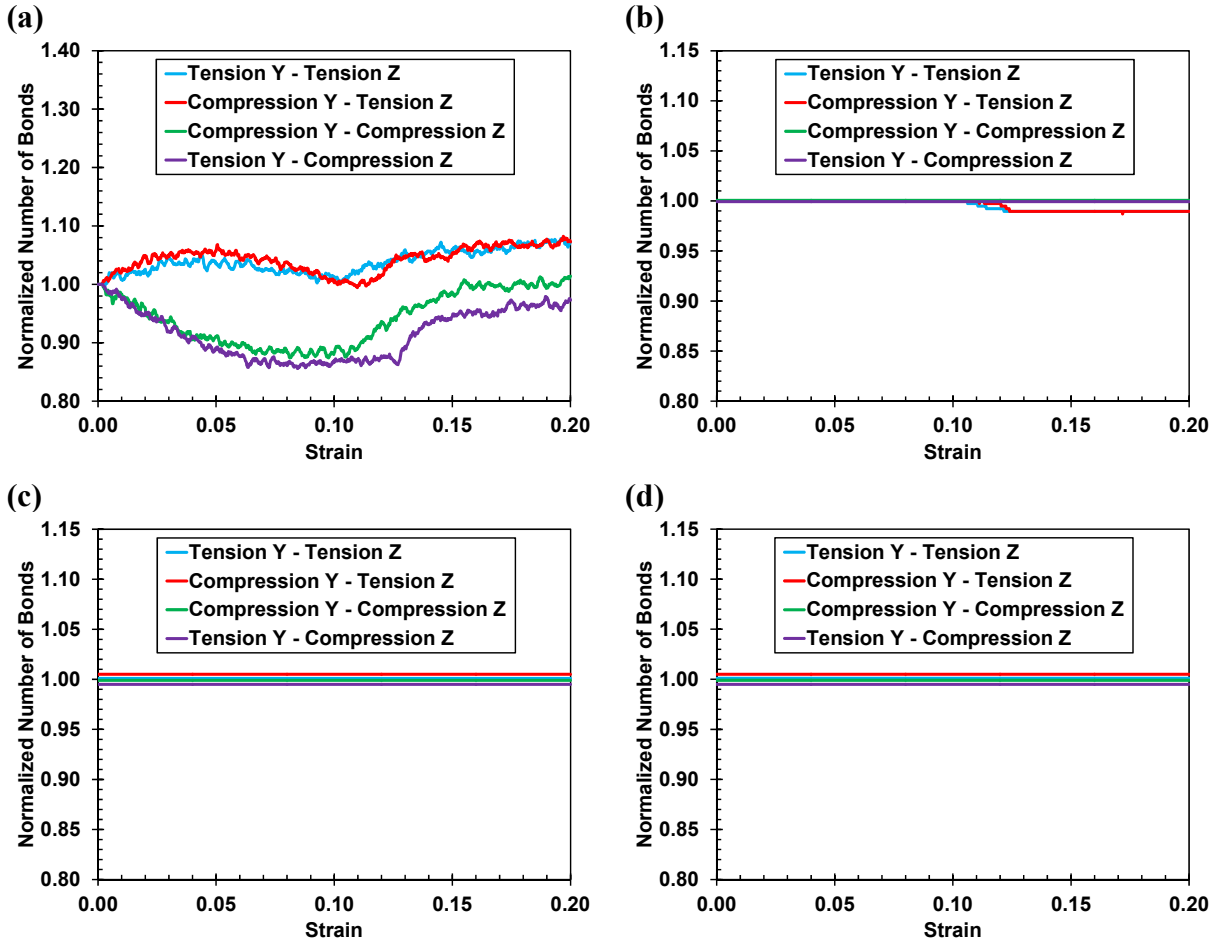

Figure 5-8. Changes in the number of (a) Ca-O, (b) Al-O, (c) S-O, and (d) H-O bonds during the biaxial straining of ettringite in both *y* and *z* directions.

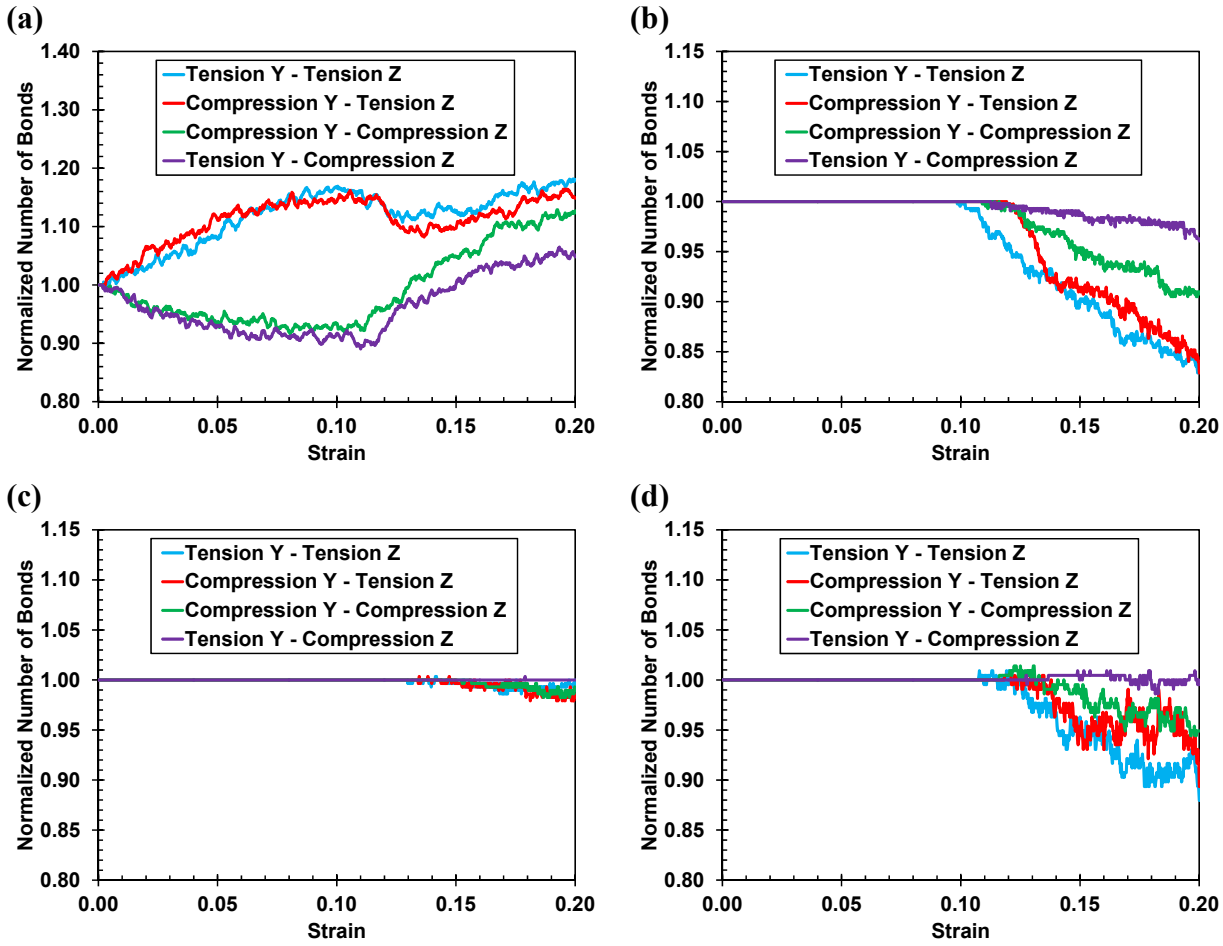

Figure 5-9. Changes in the number of (a) Ca-O, (b) Si-O, (c) S-O, and (d) C-O bonds during the biaxial straining of thaumasite in both *y* and *z* directions.

To evaluate the yield surface for ettringite and thaumasite, the RMD simulations are extended to various states of unbalanced biaxial straining, in which while the target strain in one direction is set to 0.20 Å/Å, the other direction is strained only until a fraction of 0.20 Å/Å (i.e., 0.04, 0.08, 0.12, and 0.16 Å/Å). The sign of the applied strain (i.e., tension and compression) is also changed in the *y* and *z* directions to produce various dual tension, dual compression, and mixed tension-compression biaxial straining conditions. Because of natural oscillations in the regions of nonlinear elastic-plastic behavior, the yield stress cannot be consistently extracted from the stress-strain curves. Thus, with no significant approximation, the flow stress is employed in the current study for further investigations. As the flow stress can be directly converted to the yield stress using

empirical equations, the flow surface is believed to be very similar to the yield surface (Lund and Schuh, 2005). Figure 5-10 presents the flow surface of ettringite and thaumasite under various biaxial straining states. The dual tension and compression states appear in quadrant I and III, respectively. The mixed tension and compression biaxial states are captured in quadrants II and IV. The uniaxial straining states fall on the axes separating the quadrants. For both ettringite and thaumasite, the ellipsoidal surfaces are stretched along the *z* direction, reflecting the strength anisotropy discussed in the previous section. The semi-major axis of the ettringite's ellipse is found to be longer than that of the thaumasite's ellipse. This indicates that the tricalcium aluminate columns of ettringite are stronger than the tricalcium silicate columns of thaumasite.

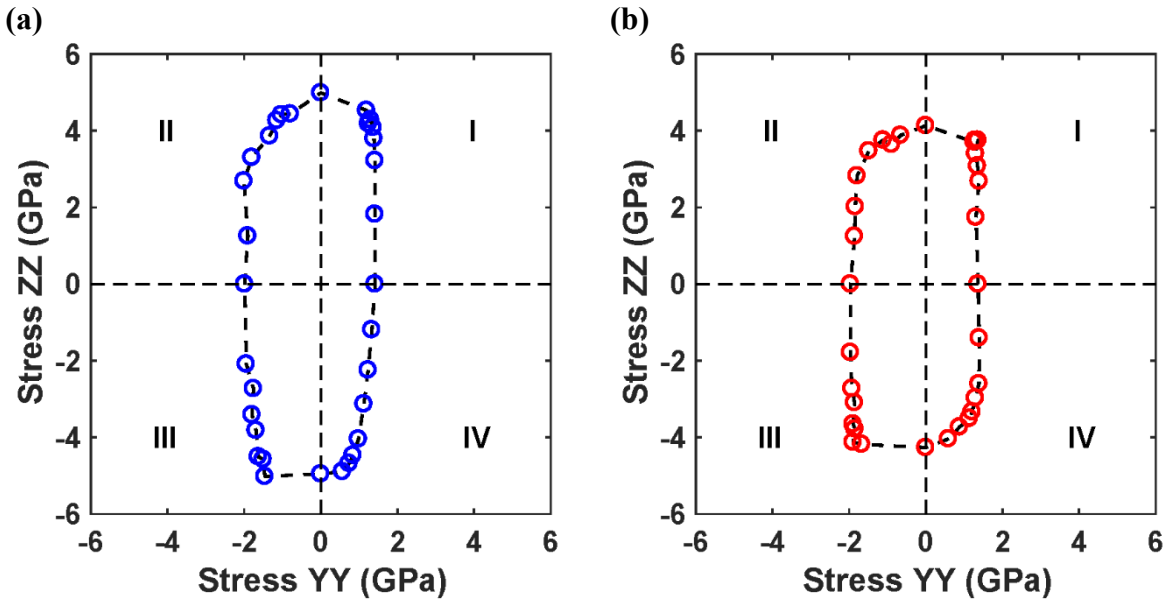

Figure 5-10. Biaxial flow surface of (a) ettringite and (b) thaumasite obtained from RMD simulations.

5.3.3 Yield Criteria

Yield criteria are investigated to predict the onset of plastic deformation (or flow stress) in the crystalline structures under consideration. Due to the fact that ettringite and thaumasite can experience strains and stresses in various directions during sulfate attack, identification of a

representative constitutive model for them is an important step forward to evaluate and optimize the mechanical properties of the sulfate-bearing crystals exposed to harsh environmental conditions. The most conventional yield criteria for ductile materials, such as metals and alloys, are Tresca and von Mises, in which the yield stress is determined by the deviatoric stress experienced by the material under a given state of external loads. In the Tresca criterion, the intermediate principal stresses are excluded and a piecewise linear model is used. On the other hand, the von Mises criterion, which applies an equal weight to the three orthogonal principal stresses, is believed to provide a better fit due to its curvature. Assuming σ_{ij} as a stress component in a Cartesian coordinate system, the deviatoric part of the stress (S_{ij}) is determined as:

$$S_{ij} = \sigma_{ij} - \frac{1}{3}\sigma_{kk}\delta_{ij} \qquad (5-1)$$

where δ_{ij} is the Kronecker delta. The von Mises criterion (von Mises, 1913) is defined as:

$${J_2}^{1/2} - k = 0 \qquad (5-2)$$

where J_2 is the second invariant of the deviatoric stress tensor, and k is the yield stress in the state of pure shear. Figures 5-11(a) and 5-12(a) show the von Mises yield criterion fitted to the flow surfaces of ettringite and thaumasite, respectively. The solid and dashed lines indicate the upper and lower bounds of the fit, respectively. It can be observed that the von Mises criterion represents an ellipsoidal surface, which is symmetric with respect to its origin. Therefore, it is unable to capture the tension-compression asymmetry effect evident in the biaxial flow data obtained from the RMD simulations. In addition, the major axis of the yield locus is inclined with a 45° angle with respect to the horizontal coordinate axis, preventing its appropriate fit to the strength anisotropy between the *y* and *z* directions. This highlights that the maximum shear criterion is not sufficient to explain the plastic behavior of the ettringite and thaumasite crystals. The von Mises yield criterion fits materials that deform by a reversible shear mechanism. This requires a yielding

criterion that only depends on the magnitude of the resolved shear stress. An efficient way of extending the von Mises criterion to include the stress asymmetry effect is to add a factor to the first invariant of the stress tensor (I_1). This has been proposed by Drucker and Prager (1952):

$$J_2^{1/2} + \alpha I_1 - k = 0 \qquad (5-3)$$

where α is the material parameter, which accounts for the effect of normal stress (or hydrostatic pressure) on the yield condition. While the Drucker-Prager criterion can be reduced to the von Mises criterion if α is assumed equal to zero, the yield locus of the Drucker-Prager criterion, in the general form, is not required to be centered on the origin, as can be seen in Figures 5-11(b) and 5-12(b). As a result, the Drucker-Prager criterion can effectively capture tension-compression stress asymmetry in the plastic behavior of ettringite and thaumasite. Nonetheless, this criterion is not capable of describing the biaxial flow data with unequal stresses in the *y* and *z* directions. As an alternative, Hill (1948) proposed an anisotropic yield function by extending the theoretical framework of the von Mises criterion to include the states of anisotropy, which possess three mutually orthogonal planes of symmetry. The Hill criterion, which is a quadratic function of the components of stress tensor, can be expressed as:

$$F(\sigma_{22} - \sigma_{33})^2 + G(\sigma_{33} - \sigma_{11})^2 + H(\sigma_{11} - \sigma_{22})^2 + 2L\sigma_{23}^2$$
$$+2M\sigma_{31}^2 + 2N\sigma_{12}^2 - 1 = 0 \qquad (5-4)$$

where *F*, *G*, *H*, *L*, *M*, and *N* are the material parameters that describe the current state of anisotropy. This function is reduced to the von Mises criterion if the anisotropy is neglected. The upper and lower bounds of the Hill criterion exhibit a good fit to the simulation results, which capture the directionality effect of stresses under tensile and compressive strains, respectively (see Figures 5-11(c) and 5-12(c)). Furthermore, the yield locus of the Hill criterion represents an ellipsoidal surface, which is still symmetric about the origin. It can be observed that this criterion consistently

underestimates the flow surfaces in compression, while it overestimates the ones in tension. Hence, it is found not capable of capturing the hydrostatic pressure effects due to the tension-compression asymmetry. Liu et al. (1997) addressed this shortcoming by extending the Hill criterion with the addition of the diagonal components of the stress tensor:

$$\{F(\sigma_{22}-\sigma_{33})^2+G(\sigma_{33}-\sigma_{11})^2+H(\sigma_{11}-\sigma_{22})^2+2L\sigma_{23}^2+2M\sigma_{31}^2+2N\sigma_{12}^2\}^{\frac{1}{2}}$$
$$+I\sigma_{11}+J\sigma_{22}+K\sigma_{33}-1=0 \qquad (5-5)$$

where *I*, *J*, and, *K* are the material parameters that describe the stress differential effect due to the dependency of the yield surface to the normal stress (or hydrostatic pressure). The Liu-Huang-Stout criterion provides a great fit to the biaxial flow data of ettringite and thaumasite obtained from the RMD simulations (see Figures 5-11(d) and 5-12(d)). The eccentricity of the yield surfaces with respect to the origin successfully accounts for the tension-compression asymmetry and strength anisotropy effects. It can be observed that a quadratic yield function with nine anisotropy coefficients can adequately capture all the major features of the biaxial flow surface, such as ellipsoidal characteristic, anisotropy in the plastic behavior, and asymmetry in the flow stress. The fitness of the yield criterion can be further refined with increasing either the order of the polynomial yield function or the number of anisotropy coefficients included in Equation 5. Such refinements are, however, not necessarily favorable for engineering applications, as they not only sophisticate the calculations, but also require additional experimental tests to determine all the necessary material coefficients.

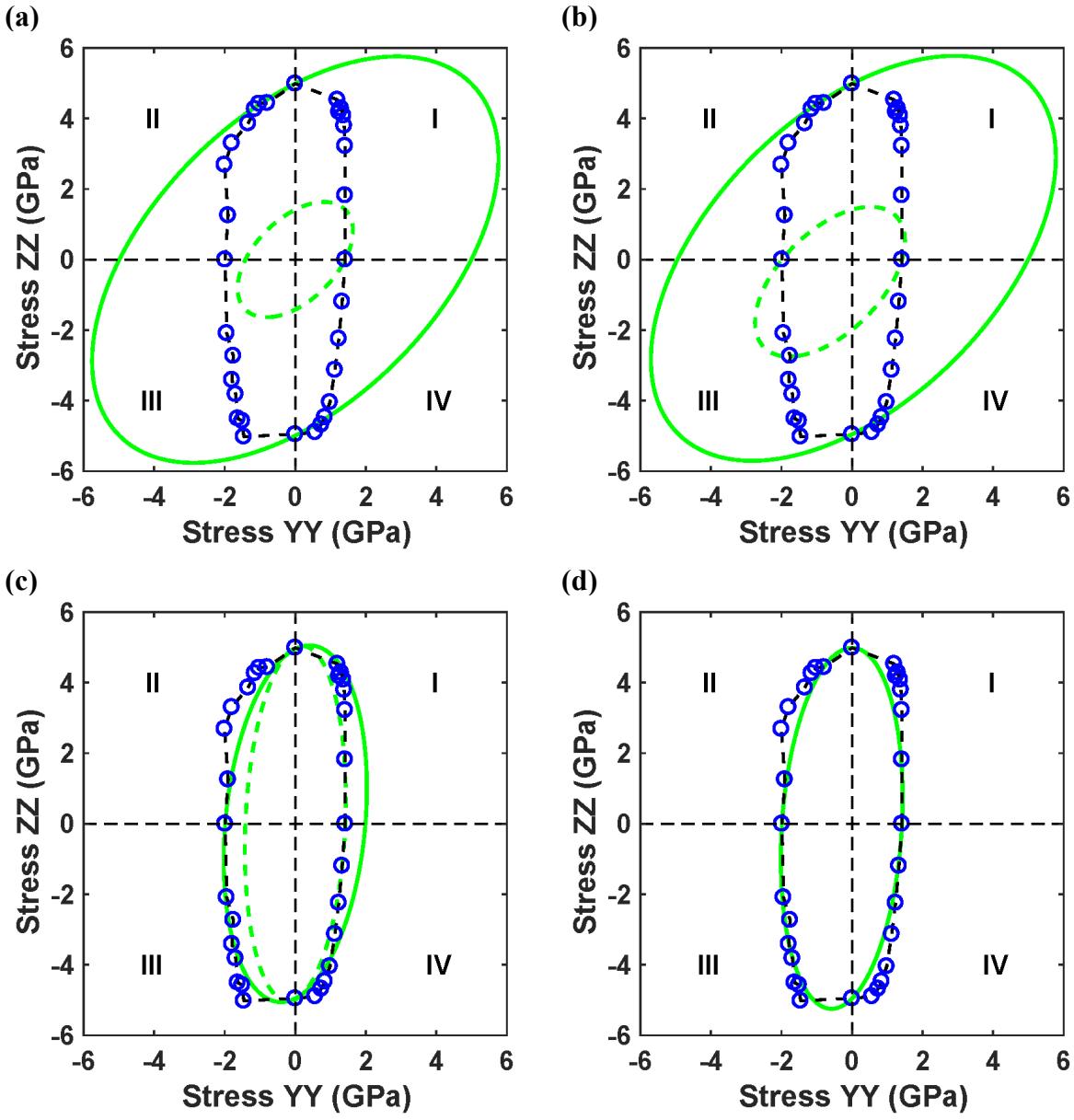

Figure 5-11. Predicted flow surface for ettringite using (a) von Mises, (b) Drucker-Prager, (c) Hill, and (d) Liu-Huang-Stout yield criteria.

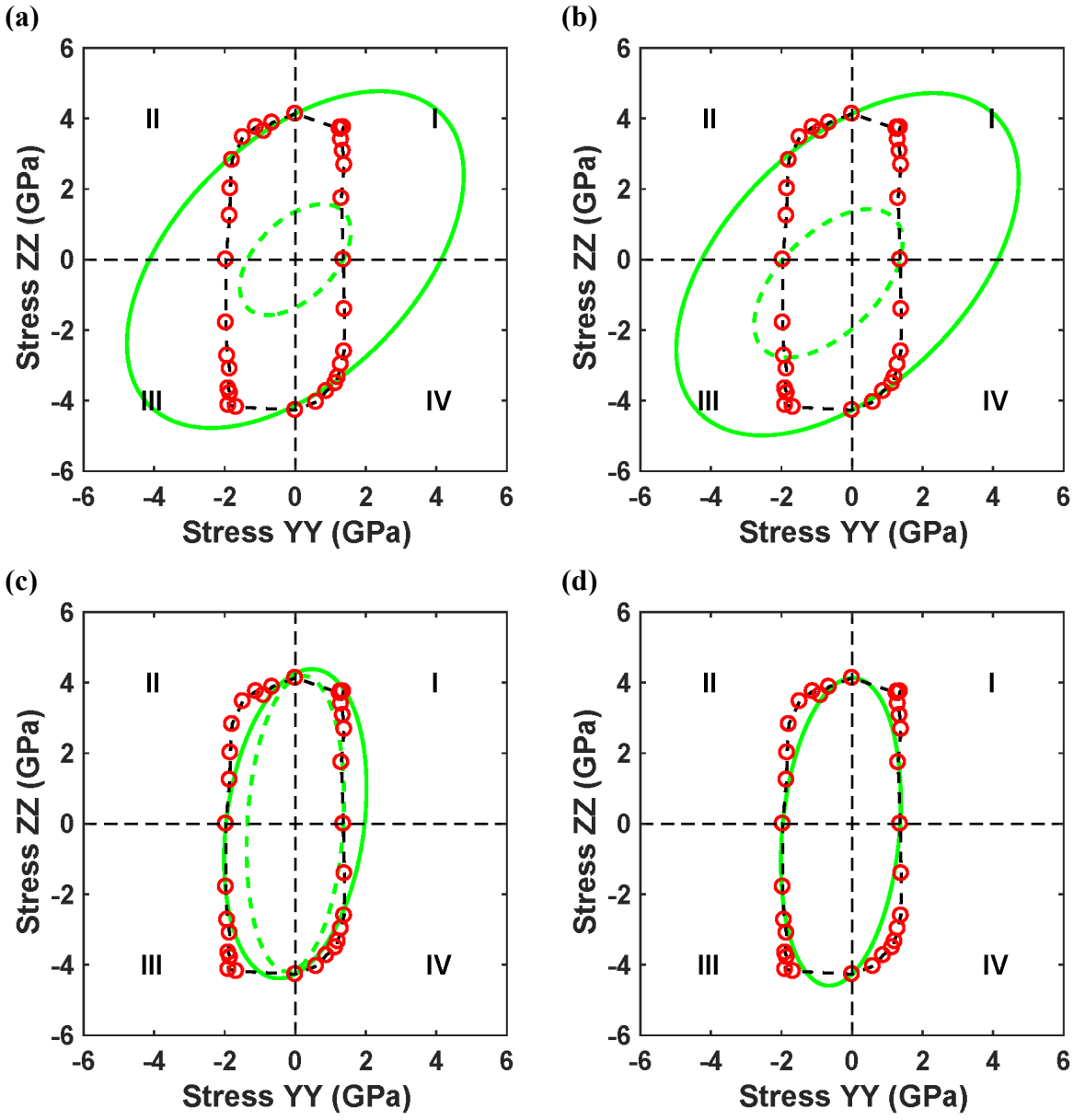

Figure 5-12. Predicted flow surface for thaumasite using (a) von Mises, (b) Drucker-Prager, (c) Hill, and (d) Liu-Huang-Stout yield criteria.

5.4 Conclusions

The RMD method was employed to investigate the elastic-to-plastic transition in the atomic structure of two of the most important sulfate-bearing crystals, i.e., ettringite and thaumasite, under multiaxial straining conditions. The stress-strain relationships obtained from uniaxial straining showed an initial linear elastic response, followed by a gradual transition to a fully plastic behavior.

It was observed that ettringite and thaumasite are about three times stronger in the *z* direction compared to the *y* direction, reflecting a strength anisotropy. While the tensile and compressive strengths were very close to each other in the *z* direction, both ettringite and thaumasite were found to be stronger under compression than tension in the *y* direction. This tensile-compressive stress asymmetry, which was evident at the atomic scale, resembles the similar feature of cementitious materials observed at large length scales. To understand the atomistic origins of the constitutive response of ettringite and thaumasite under various tensile and compressive straining conditions, a holistic chemical bond analysis was performed. It was revealed that the contribution of dissimilar chemical bonds to resisting the applied strains is the main reason for the strength anisotropy observed in the stress-strain relationships of ettringite and thaumasite. Furthermore, the stress asymmetry in the tension and compression was attributed to the breakage and densification of the hydrogen bond network between the tricalcium aluminate and tricalcium silicate columns of ettringite and thaumasite, respectively.

In addition to the uniaxial straining conditions, the atomic structures of ettringite and thaumasite were subjected to various states of biaxial straining. For all the biaxial straining simulations, the strength in the *z* direction was consistently larger than that in the *y* direction. The stress asymmetry was also evident for the states of biaxial straining in the *y* direction under both tension and compression. Based on the flow surfaces developed for ettringite and thaumasite, various yield criteria were examined to identify a criterion that can mathematically represent the main features captured in the biaxial flow data extracted from the RMD simulations. It was found that the Liu-Huang-Stout criterion provides the best fit to the flow surfaces of ettringite and thaumasite. The identified yield criterion included a quadratic function that was calibrated to effectively capture the ellipsoidal characteristic, strength anisotropy, and stress asymmetry in the flow surfaces of

both crystalline structures under consideration. This led to the first-known constitutive model for the complex sulfate-bearing crystals that are formed in cementitious materials.

5.5 Acknowledgments

The feedback and support from Dr. Andres Jaramillo-Botero are gratefully acknowledged. The Extreme Science and Engineering Discovery Environment (XSEDE), which is supported by National Science Foundation grant number ACI-1548562, was used for part of the atomistic simulations conducted in this study.

5.6 References

1- Aktulga H.M., Fogarty J.C., Pandit S.A., and Grama A.Y., 2012. "*Parallel reactive molecular dynamics: Numerical methods and algorithmic techniques*", Parallel Computing 38(4-5): 245-259.

2- Allen M., and Tildesley D., 1987. "*Computer simulation of liquids*", New York: Oxford University Press.

3- Bauchy M., Laubie H., Qomi M.J.A., Hoover C.G., Ulm F.-J., and Pellenq R.J.-M., 2015. "*Fracture toughness of calcium–silicate–hydrate from molecular dynamics simulations*", Journal of Non-Crystalline Solids 419: 58-64.

4- Chen W.-F., 2007. "*Plasticity in Reinforced Concrete*", Lauderdale, Florida: J. Ross Publishing Inc.

5- Dracker D.C., and Prager W., 1952. "*Soil mechanics and plastic analysis for limit design*", Quarterly of Applied Mathematics 10(2): 157-165.

6- Edge R.A., and Taylor H.F.W., 1971. "*Crystal structure of thaumasite, [Ca3Si(OH)6.12H2O](SO4)(CO3)*", Acta Crystallographica (B) 27: 594-601.

7- Effenberger H., Kirfel A., Will G., and Zobetz E., 1983. "*A further refinement of the crystal structure of thaumasite, $Ca_3Si(OH)_6CO_3SO_412H_2O$*", Neus Jahrbuch fur Mineralogie Monatshefte 2: 60–68.

8- Gatta G.D., McIntyre G.J., Swanson J.G., and Jacobson S.D., 2012. "*Minerals in cement chemistry: A single-crystal neutron diffraction and Raman spectroscopic study of thaumasite, Ca3Si(OH)6(CO3)(SO4)·12H2O*", American Mineralogist 97: 1060-1069.

9- Glasser F., Marchand J., and Samson E., 2008. "*Durability of concrete--Degradation phenomena involving detrimental chemical reactions*", Cement and Concrete Research 38: 226-246.

10- Grimmer A.R., Wieker W., Lampe F., Fechner E., Peter R., and Molgedey G., 1980. "*Hochauflosende 29Si-NMR an festen silicaten: Anisotropie der chemischen Verschiebung im thaumasite*", Z Chem 20: 453.

11- Hajilar S., and Shafei B., 2014. "*Nano-scale characterization of elastic properties of AFt and AFm phases of hydrated cement paste*", Proceedings of the European Conference on Computational Modeling of Concrete Structures (EURO-C) 1: 299-306, St. Anton Am Arlberg, Austria.

12- Hajilar S., and Shafei B., 2015. "*Nano-scale investigation of elastic properties of hydrated cement paste*

constituents using molecular dynamics simulations", Computational Materials Science 101: 216-226.

13- Hajilar S., and Shafei B., 2016(a). "*Mechanical failure mechanisms of hydrated products of tricalcium aluminate: A reactive molecular dynamics study*". Materials and Design 90: 165-176.

14- Hajilar S., and Shafei B., 2016(b). "*Assessment of structural, thermal, and mechanical properties of portlandite through molecular dynamics simulations*", Solid State Chemistry 244: 164-174.

15- Hajilar S., Shafei B., Cheng T., and Jaramillo-Botero A., 2017. "*Reactive molecular dynamics simulations to understand mechanical response of thaumasite under temperature and strain rate effects*". Journal of Physical Chemistry A 121(24): 4688-4697.

16- Hajilar S., and Shafei B., 2018. "*Atomic-scale investigation of physical adsorption of water molecules and aggressive ions to ettringite's surfaces*". Journal of Colloid and Interface Science 513: 104-116.

17- Hampel T., Speck K., Scheerer, and Ritter R., 2009. "*High-performance concrete under biaxial and triaxial loads*", ASCE Journal of Engineering Mechanics 135(11): 1274-1280.

18- Hartman M., and Berliner R., 2006. "*Investigation of the structure of ettringite by time-of-flight neutron powder diffraction techniques*", Cement and Concrete Research 36(2): 364-370.

19- Hill R., 1948. "*A theory of the yielding and plastic flow of anisotropic metals*", Proceedings of the Royal Society A: Mathematical, Physical, and Engineering Sciences, London, 193(1033): 207-215.

20- Hou D., Zhao T., and Li Z., 2015. "*Structure, reactivity and mechanical properties of water ultra-confined in the ordered crystal: A case study of jennite*", Microporous and Mesoporous Materials 204: 106-114.

21- Jaramillo-Botero A., Naserifar S., Goddard III W.A., 2014. "*A General Multi-Objective Force Field Optimization Framework, with Application to Reactive Force Fields for Silicon Carbide*", Journal of Chemical Theory and Computation 10: 1426-1439.

22- Liu C., Huang Y., and Stout M.G., 1997. "*On the asymmetric yield surface of plastically orthotropic materials: A phenomenological study*", Acta Materialia 45(6): 2397-2406.

23- Liu L., Jaramillo-Botero A., Goddard III W.A., and Sun H., 2012. "*Development of a ReaxFF reactive force field for ettringite and study of its mechanical failure modes from reactive molecular dynamics simulations*". The Journal of Physical Chemistry A 116(15): 3918-3925.

24- Lund A.C., and Schuh C.A., 2005. "*Strength asymmetry in nanocrystalline metals under multiaxial loadings*". Acta Materialia 53: 3193-3205.

25- Manzano H., 2009. "*Atomistic simulation studies of the cement paste components*", Ph.D. Thesis, Universidad del Pais Vasco, Guipúzcoa, Spain.

26- Manzano H., Ayuela A., Telesca A., Monteiro P.J.M., and Dolado J.S., 2012. "*Ettringite strengthening at high pressure induced by the densification of the hydrogen bond network*", Journal of Physical Chemistry C 116: 16138-16143.

27- Mehta P.K., 1994. "*Concrete technology at the crossroads--Problems and opportunities*", in *Concrete Technology: Past, Present and Future*, Farmington Hills, MI.

28- Moore A., and Taylor H., 1968. "*Crystal structure of ettringite*", Nature 218(5146): 1048-1049.

29- Neville A., 2004. "*The confused world of sulfate attack on concrete*", Cement and Concrete Research 34: 1275-1296.

30- Ortiz M., 1985. "*A constitutive theory for the inelastic behavior of concrete*", Mechanics of Materials 4(1): 67-93.

31- Palkovic S.D., Moeini S., Yip S., and Buyukozturk O., 2015. "*Mechanical behavior of a composite interface: Calcium-silicate-hydrates*", Journal of Applied Physics 118: 034305.

32- Palkovic S.D., Yip S., and Buyukozturk O., 2016. "*Constitutive response of calcium-silicate-hydrate layers under combined loading*", Journal of American ceramic Society 100(2): 713-723.

33- Plimpton S., 1995. "*Fast Parallel Algorithms for Short-Range Molecular Dynamics***"**, Journal of Computational Physics 117 (1): 1-19.

34- Rappe A.K., and Goddard III W.A., 1991. "*Charge Equilibration for Molecular Dynamics Simulations*", Journal of Physical Chemistry 95: 3358-3363.

35- Ritter R., and Curbach M., 2016. "*Shape of hypersurface of concrete under multiaxial loading*", ACI Materials Journal 113(1): 55-65.

36- Santhanam M., Cohen M., and Olek J., 2002. "*Mechanism of sulfate attack: A fresh look, Part 1: Summary of experimental results*", Cement and Concrete Research 32: 915-921.

37- Santhanam M., Cohen M., and Olek J., 2003. "*Mechanism of sulfate attack: a fresh look, Part 2. Proposed mechanisms*", Cement and Concrete Research 33: 341-346.

38- Scholtzová E., Tunega D., and Speziale S., 2015. "*Mechanical properties of ettringite and thaumasite-DFT and experimental study*", Cement and Concrete Research 77: 9-15.

39- Sfer D., Carol I., Gettu R., and Etse G., 2002. "*Study of the bheavior of concrete under triaxial compression*", ASCE Journal of Engineering Mechanics 128(2): 156-163.

40- Speziale S., Jiang F., Mao Z., Monteiro P.J.M., Wenk H.-R., Duffy T.S., and Schilling F.R., 2008. "*Single-crystal elastic constants of natural ettringite*", Cement and Concrete Research 38: 885-889.

41- Stebbins J.F., and Kanzaki M., 1991. "*Local structure and chemical shifts for six-coordinated silicon in high-pressure mantle phases*", Science 251(4991): 294-298.

42- Taylor H., 1997. "*Cement Chemistry*", 2 ed., London: Thomas Telford Publishing.

43- Von Mises R., 1913. "*Mechanik der festen Körper im plastisch deformablen Zustand*", Göttingen, Mathematisch-Physikalische 1: 582-592.

44- Wang Y.-B., Liew J.Y.R., Lee S.C., and Xiong D.X., 2016. "*Experimental study of ultra-high-strength concrete under triaxial compression*", ACI Materials Journal 113(1): 105-112.

CHAPTER 6: ATOMIC-SCALE INVESTIGATION OF PHYSICAL ADSORPTION OF WATER MOLECULES AND AGGRESSIVE IONS TO ETTRINGITE'S SURFACES

The strength and durability of cementitious composite materials are adversely affected by the ingress of water and aggressive ions into their intrinsic meso- and nano-pore spaces. Among various phases of hydrated cement paste (HCP), the aluminum-rich phases play a critical role in controlling the diffusivity of aqueous solutions containing aggressive ions. To this date, however, there has been no systematic study to understand the adsorption mechanisms and chloride binding capacity of aluminum-rich phases of HCP. This research gap has been the motivation of the current study to investigate the physical adsorption characteristics of ettringite as the main aluminum-rich phase of HCP and the primary hydrated product of calcium sulfoaluminate cement. Through a set of Molecular Dynamics simulations supported by macro-scale experimental tests, a fundamental insight into the molecular origins of the diffusion of water molecules, as well as sodium and chloride ions, in contact with ettringite is provided. As the primary objective of this study is to evaluate the transport properties at and near the solution/solid interfaces, the molecular mechanisms of adsorption are characterized for inner- and outer-sphere distances from the solid substrate. With an in-depth understanding of the structure and dynamics of water molecules and aggressive ions in contact with ettringite's surfaces, the outcome of this study provides reliable measures of physical adsorption, binding capacity, and self-diffusion coefficient, which can be further employed to introduce strategies to avoid the degradation of a wide variety of cementitious materials exposed to harsh environmental conditions.

6.1 Introduction

The adsorption of water and diffusive ions to a solid's surface has a critical importance in a variety of chemical and physical processes, involving pollutant diffusion, waste disposal, mineral weathering, and structural degradation. This has dramatically increased the interest in the

investigation of the solution-solid interface in several disciplines, ranging from environmental engineering and materials science to geology and cement chemistry. In microporous materials, such as hydrated cement paste (HCP), physical, chemical, and mechanical properties are greatly influenced by the ingress of water molecules and aggressive ions into intrinsic pore spaces (Anderson et al., 1989; Tritthart, 1989; Beaudoin et al., 1990). For the concrete structures exposed to harsh environmental conditions, chloride ions are known as one of the main aggressive ions, which can be originated from exposure to seawater, deicing salts used during the winter, or soils with a saline environment. Chloride ions can also come from internal sources, which can be contaminated aggregates or the admixtures that contain chlorides (e.g., calcium chloride added to the concrete mix to improve cold weather pouring). In the chloride-contaminated concrete structures, chloride ions that exist in the pore solution tend to diffuse towards reinforcing steel bars embedded in the concrete matrix. As a result, the pH near the embedded bars decreases; the protective film surrounding the reinforcement is damaged; and the degradation of the concrete structure is initiated, leading to the long-term strength and durability issues in this important category of cementitious composite materials (Alipour et al., 2011 and 2013; Shafei et al., 2012 and 2013; Shafei and Alipour, 2015a,b). Despite the growing concerns about such degradations, there is a major gap in the literature to understand the origin of chloride diffusion mechanisms at the molecular level and characterize how water molecules, as well as sodium and chloride ions, interact at the surfaces of HCP.

Water molecules in contact with HCP are often classified into three main types of chemically-bounded, physically-bounded, and unbounded (or free) water molecules. The chemically-bounded water molecules refer to the ones that are connected to the HCP by forming chemical bonds. The physically-bounded water molecules, on the other hand, are the ones that interact with the surface

of the HCP with no chemical bonds. Finally, the unbounded water molecules are the ones that are confined within capillary pores with no interactions with the surface of the HCP. The three types of water molecules in the HCP were investigated using ^{1}H Fourier transform nuclear magnetic resonance (NMR) at 400 MHz (Wang et al., 1998). It was found that the physically-bounded water molecules diffuse out of the sample when heated to 105 °C. In contrast, the chemically-bounded water molecules remain in a stable form as calcium hydroxide complexes. Bordallo et al. (2006) employed the quasi-elastic neutron scattering (QENS) technique to study water mobility in the HCP. Since no QE signal was observed when the samples were heated to 105 °C, it was concluded that both physically-bounded and unbounded water molecules evaporate, while the chemically-bounded water molecules remain in place. The study revealed two distinct diffusion processes: one due to unbounded water molecules with a diffusion coefficient in the range of 10^{-9} m^2/s, and the other attributed to water molecules in the gel pore with a diffusion coefficient one order of magnitude smaller than that of the unbounded one's.

Similar to water molecules, chloride ions interact with the HCP as either "bound" or "free" ions. The former refers to the ions chemically bounded to the surrounding surfaces, whereas the latter denotes the ones encapsulated in the gel's pore spaces. It must be noted that free chloride ions are the aggressive ions that can freely diffuse into the HCP. In the existing literature, Yu and Kirkpatrick (2001) studied the mechanisms of chloride sorption to the HCP, including calcium hydroxide, carboaluminate, and calcium silicate hydrates, using NMR experiments. Among the phases considered, it was found that chloride ions have the highest and lowest affinity to calcium hydroxide and calcium silicate hydrates, respectively. Jones et al. (2003) employed magnetic angle spinning (MAS) NMR spectroscopy to study the chemical environment of the ^{27}Al-bearing phases of HCP. It was revealed that the calcium aluminate trisulfate hydrates (AFt) have virtually no

capacity to chemically react with chlorides. In contrast, through the exchange of chloride ions with hydroxide ones, calcium aluminate monosulfate hydrates (AFm) are transformed to a new phase called Friedel's salt. Barberon et al. (2005) studied the effect of sodium and chloride ions on the structural chemistry of HCP. It was observed that sodium ions were not affected by the hydration process, while the ^{27}Al and ^{29}Si spectroscopy confirmed that only the aluminum-rich hydrated phases of cement interact with chlorides.

Despite the wealth of information provided by experimental studies, many of atomic-level interactions between water molecules, aggressive ions, and HCP phases have remained poorly understood. This is primarily due to the challenges associated with experimental tests, from sample preparation to accurate measurement at relevant length and time scales. Atomistic simulations, however, can offer a promising solution, which not only plays a critical role to further interpret the experimental test results, but also advances the fundamental knowledge of the structure and dynamics of solid-aqueous interfaces (Liu et al., 2012; Manzano et al., 2012; Hajilar and Shafei 2014, 2015, and 2016a,b; Hajilar et al., 2017; Manzano et al., 2015; Krishnan et al., 2016). A limited number of molecular dynamics (MD) studies are available in the literature to characterize the diffusion of water molecules and chloride ions within the nano-pores of HCP. Kalinichev and Kirkpatrick (2002) investigated chloride binding to the surfaces of calcium hydroxide, hydrated calcium aluminate, and calcium silicate phases. Among the phases studied, it was found that Friedel's salt and calcium silicate hydrates have the highest and lowest chloride binding capacity, respectively. The structure, dynamics, and energetics of water at the surfaces of calcium silicate hydrates were explored by Kalinichev et al. (2007). A strong structuring of water molecules was observed in the channels between the driekette silicate chains and above the (001) surface of calcium silicate hydrates. This was attributed to the integrated H-bond network between the water

and surface sites. In a separate effort, the transport of water and ions in the nano-pores of calcium hydroxide and calcium silicate hydrates was studied by Hou and Li (2014a,b) and Hou et al. (2016). The water molecules in the channels were categorized into two types with structural and dynamic similarity to the interlayer water molecules that exist in the calcium silicate hydrate gel. It was reported that the chloride ions are mostly repulsed by the negatively-charged surfaces of calcium silicate hydrates, resulting in a low binding capacity. On the other hand, the ion adsorption capacity of calcium hydroxide was found to be relatively high due to the stable Na-Cl connections in the electrolyte solution.

The MD simulations conducted to this date for understanding the diffusion of aggressive ions in the HCP have been primarily focused on calcium hydroxide and calcium silicate hydrates, without taking into account the contribution of the other important hydrated cement phases, particularly calcium aluminate hydrates. As suggested by the previous experimental tests (Yu and Kirkpatrick, 2001; Jones et al., 2003; Barberon et al., 2005), the chloride binding capacity of cementitious materials is dominated by the content of calcium aluminate hydrates (i.e., AFm and AFt). This is completely in line with the fact that under chloride attack, AFm compounds are the ones that bind chloride ions through chemical substitutions, resulting in the formation of a secondary phase called Friedel's salt (Arya et al., 1990; Suryavanshi et al., 1996; Glasser et al., 1999). At certain chloride concentrations, however, AFm compounds are completely dissociated, while AFt compounds remain stable and can physically adsorb the diffusing chloride ions (Ekolu et al., 2006). This was the main motivation for the current study to characterize the physical adsorption of water molecules and aggressive ions to the surfaces of ettringite, which is known as the main AFt compound (Taylor, 1997). Ettringite is not only the most abundant aluminum-rich phase of HCP, but also is the most important binding phase in the calcium sulfoaluminate cement,

which has been recognized as an environment-friendly alternative to Portland cement. In this study, an extensive set of MD simulations are performed to investigate the structure and dynamics of water, as well as sodium and chloride ions, in contact with ettringite's surfaces. The aqueous layer is comprised of NaCl solutions with concentrations ranging from 0.1 to 1.5 M. In each simulation, the aqueous layer is placed in contact with two ettringite's surfaces; the entire system is fully equilibrated; and then the trajectories are recorded for further analysis. The analyses performed on the recorded trajectories determine atomic density profiles, adsorption statistics, binding isotherms, planar atomic density distributions, dipolar and HH orientation profiles, radial distribution functions, and self-diffusion coefficients. The outcome of this study, which is supported by a range of experimental tests, is an important step forward to unravel the molecular origins of degradation of aluminum-rich hydrated phases of cement paste at their interfaces with water molecules and aggressive ions.

6.2 Computational Methodology

6.2.1 Structural Models

Ettringite has a needle-shape morphology with the chemical composition of $Ca_6[Al(OH)_6]_2(SO_4)_3 \cdot 26H_2O$. A distinct aspect of this crystal is the existence of a network of hydrogen bonds along a central column of aluminum and calcium polyhedra. The aluminum atoms are each six-fold, octahedrally coordinated with six hydroxyl groups. The calcium atoms, on the other hand, are each eight-fold, coordinated with four hydroxyl groups and four water molecules. The excess charge of the tricalcium aluminate columns is neutralized with the sulfate ions that exist in the channels between them. Ettringite has a trigonal unit cell with a space group of P31c and a density of 1.8 g/cm^3. In this study, the crystallographic data needed to model the atomic structure of ettringite is obtained from Moore and Taylor (1970). The unit cell of ettringite is

converted into an orthogonal cell following the procedure described by Hajilar and Shafei (2016a). The orthogonal unit cell of ettringite is then repeated in the *x*, *y*, and *z* directions to form a 2×2×2 super cell. The super cell of ettringite is cleaved parallel to the (100) plane to create the contact surfaces that expose the hydroxyl groups and oxygen atoms located on the surface of ettringite to aqueous solutions, as also suggested by Brown (2001).

The simulation cell is generated by adding a vacuum slab of 60 Å thick between the ettringite's surfaces. This slab is later filled with water molecules and NaCl to form the aqueous layer. Since a three-dimensional periodic boundary condition is applied to the simulation cell (Allen and Tildesley, 1987), the thickness of the solution layer is chosen large enough to eliminate any direct interactions between the two solution-ettringite interfaces. To obtain the expected density of bulk aqueous solution under ambient conditions (i.e., 1.0 g/cm^3), close to 4,000 water molecules are packed in the vacuum slab. A total of 7, 14, 35, 71, and 106 sodium and chloride ions are then added to the aqueous layer to produce 0.1, 0.2, 0.5, 1.0, and 1.5 M NaCl solutions, respectively. To avoid biased adsorptions, the added ions are placed (at least) 15 Å away from solid substrates. The final simulation cells, which contain approximately 16,000 atoms, are large enough to deliver stable statistical results. The dimension of the simulation cell, which is 80.00, 45.04, and 42.96 Å, in the *x*, *y*, and *z* directions, respectively, is fixed during the entire MD simulations (Towns et al., 2014). Figure 6-1 illustrates the initial configuration of the 0.5 M NaCl solution in contact with the ettringite's surfaces. All the MD simulations start with a configuration similar to the one shown in this figure.

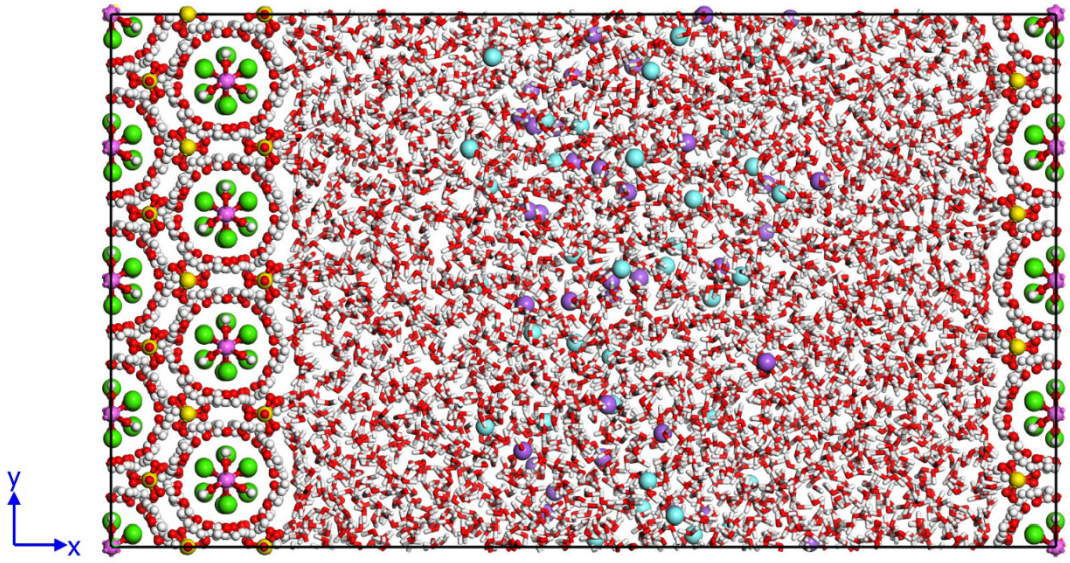

Figure 6-1. Initial configuration of the 0.5 M NaCl concentration solution in contact with the ettringite's surfaces. Color code: green (Ca), yellow (S), pink (Al), red (O), white (H), cyan (Cl^-), and purple (Na^+).

6.2.2 MD Simulations

The CLAYFF forcefield (Cygan et al., 2004) is used in the current study to model ettringite and its interactions with the aqueous solutions of NaCl. The CLAYFF forcefield has been specifically developed to simulate the ion-ion and ion-water interactions of oxide and hydroxide phases that exist in cementitious materials. Furthermore, a comprehensive review of the literature indicates that CLAYFF has been successfully employed to model the interactions between the other cementitious phases and aqueous solutions (Kalinichev and Kirkpatrick, 2002; Kalinichev et al., 2007; Korb et al., 2007; Yoon and Monteiro, 2013; Hou and Li, 2014a,b; Hou et al., 2016). The energy term in CLAYFF is formulated with the superposition of two-body and three-body interactions expressed by a summation of bonded (valance) and nonbonded interactions. The harmonic bond stretching and angle bending terms are used to describe the bonded interactions. The nonbonded interactions, i.e., electrostatic and van der Waals energies, are defined using the

Coulomb and Lennard-Jones 12-6 functionals, respectively. In Equation 1, the first two terms designate the bonded energy terms, while the last two represent the nonbonded interactions:

$$E_{total} = \sum_{ij\ bonded} k_{r,ij}\left(r_{ij} - r_{0,ij}\right)^2 + \sum_{ijk\ bonded} k_{\theta,ijk}\left(\theta_{ijk} - \theta_{0,ijk}\right)^2$$

$$+\frac{e^2}{4\pi\varepsilon_0}\sum_{ij\ nonbonded}\frac{q_i q_j}{r_{ij}} + \sum_{ij\ nonbonded} D_{ij}\left[\left(\frac{R_{ij}}{r_{ij}}\right)^{12} - 2\left(\frac{R_{ij}}{r_{ij}}\right)^{6}\right] \qquad (6-1)$$

where i, j, and k are atom numbers and $k_{r,ij}$ and $k_{\theta,ijk}$ are the force constants; $r_{0,ij}$ and $\theta_{0,ijk}$ represent the equilibrium bond length and bond angle, respectively; e is the electron's charge (1.602×10^{-19} c); ε_0 is the dielectric permittivity of vacuum (8.85×10^{-12} F/m); q_i and q_j are the partial charges of the i-th and j-th atoms derived by the quantum chemistry methods; and D_{ij} and R_{ij} are the energy and distance parameters of Lennard-Jones 12-6, respectively. All long-range electrostatic interactions are treated using the Ewald summation method (Ewald, 1921; Allen and Tildesley, 1987). The flexible single point charge (SPC) (Berendsen et al., 1981) water model is employed to describe the water molecules and hydroxyl groups. The SPC model, which has been widely used to study the structure and properties of water molecules and aqueous systems (Berendsen et al., 1987; Teleman et al., 1987; Wallqvist and Teleman, 1991; Smith and Haymet, 1993; Smith and Dang, 1994; van der Spoel et al., 1998; Kalinichev et al., 2000; Vasconcelo et al., 2007), is based on partial charges centered directly on the oxygen and hydrogen atoms. Further to water molecules and hydroxyl groups, the sulfate groups are described using the bonded interactions (Cannon et al., 1994). The van der Waals interaction parameters between unlike atoms are calculated according to the arithmetic and geometric mean rule for the distance (D) and energy (R) parameters, respectively.

The LAMMPS (Large-scale Atomic/Molecular Massively Parallel Simulator) program (Plimpton, 1995) installed on a parallel Linux cluster is used to perform the MD simulations. The

canonical ensemble, which represents the constant number of atoms (N), volume (V), and temperature (T) at 300 K, is used. The Nosé-Hoover thermostat (Nosé, 1984; Hoover, 1985) is employed to control the temperature in the MD simulations with a relaxation time of 100 fs (femtosecond, 10^{-15} s). The equations of motion are integrated using the Verlet's algorithm (Verlet, 1967 and 1968) with a time step of 1.0 fs. The MD simulations contain two stages of equilibration and production. The simulation cell is first equilibrated for 500 ps (picosecond, 10^{-12} s) and the convergence of a variety of thermodynamic parameters (e.g., total energy and its components, temperature, and pressure) is closely monitored and ensured. This is followed by the production stage, in which the simulation cell is equilibrated for 5.0 ns (nanosecond, 10^{-9} s). The dynamic trajectories are recorded every 500 fs to produce 10,000 atomic configurations, which are large enough to guarantee the statistical stability of data analysis.

6.3 Results and Discussions

6.3.1 Atomic Density Profiles

Atomic density profile, $\rho_\alpha(x)$, is defined as the average number of atoms of type α in a slab of thickness Δx located at a distance of x from the ettringite's surface, normalized by the volume of the system, V:

$$\rho_\alpha(x) = \frac{\langle N_\alpha(\Delta x)\rangle}{V} \qquad (6-2)$$

where the angle bracket, < >, denotes the average operator, and N_α is the number of atoms of type α. The density profiles are calculated by averaging the trajectories of each atomic species during the 5000 ps production dynamic equilibrium.

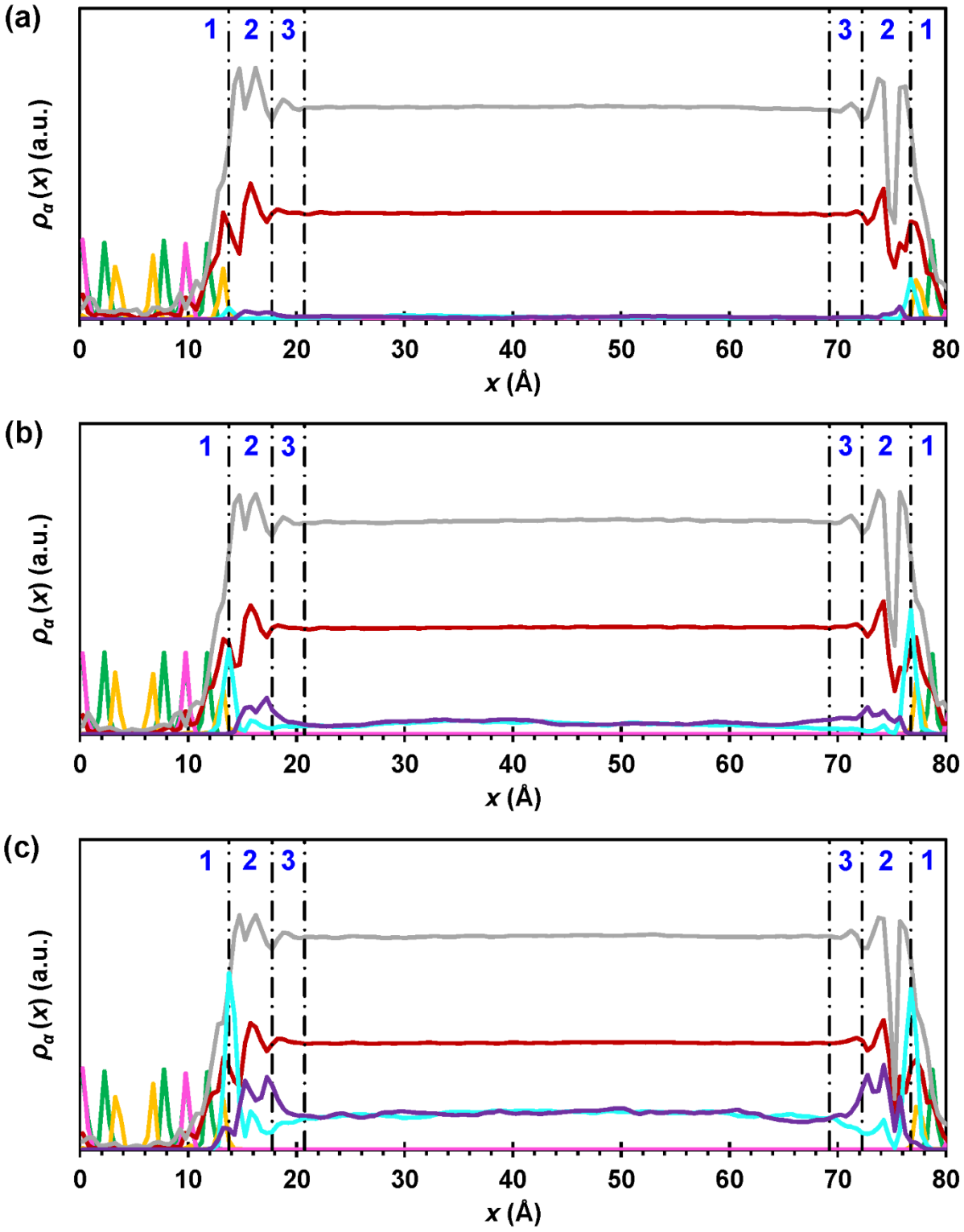

Figure 6-2. Atomic density profiles of the equilibrated (a) 0.1, (b) 0.5, and (c) 1.5 M NaCl solutions in contact with the surfaces of ettringite. Region 1, 2, and 3 designate the solid substrate, inner-sphere, and outer-sphere range, respectively. Color code: green (Ca), yellow (S), pink (Al), red (Wat-O), gray (Wat-H), cyan (Cl^-), and purple (Na^+).

Figure 6-2 shows the atomic density profiles of various species for the NaCl solutions of 0.1, 0.5, and 1.5 M in equilibrium with the ettringite's surfaces. The arithmetic average of the *x*-coordinates of the utmost oxygen atoms of the surface sulfate groups is considered as the surface level. Region 1, 2, and 3 correspond to the solid substrate, inner-sphere, and outer-sphere range, respectively. In this study, the inner-sphere range refers to an adsorbed ion located at a maximum distance of 2.5-3.0 Å away from the solid substrate with no water molecules present between the ion and the surface. The outer-sphere range, however, defines the region 2.5-3.0 Å beyond the inner-sphere range, where the intermediate water molecules separate the ion from the surface. The ions that are located further away from the outer-sphere range are considered as free ions. The introduced ranges (as also shown in Figure 6-3) will remain unchanged in all the results and discussions provided within this work.

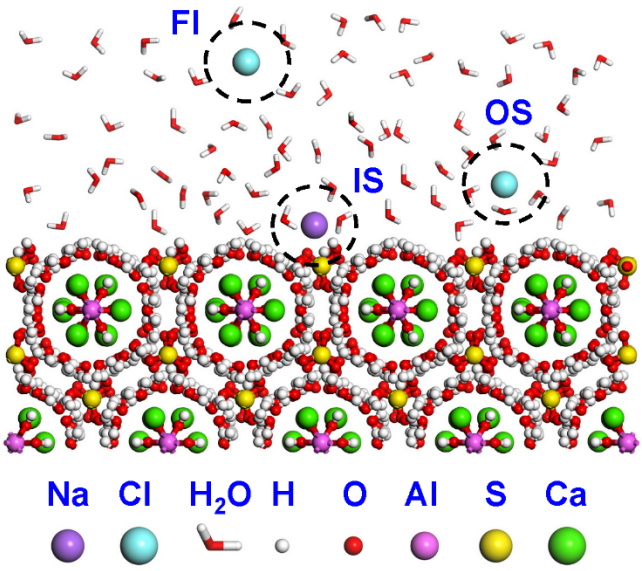

Figure 6-3. The (100) surface of ettringite in contact with a sodium chloride aqueous solution. The IS, OS, and FI denote the inner-sphere adsorption, outer-sphere adsorption, and free ions in the solution, respectively.

Figure 6-2 shows that the first peak of the water oxygen atoms is centered at the surface level, while the first peak of the water hydrogen atoms is almost 1.0 Å away from the surface. This

indicates that the water oxygen atoms are energetically more favorable for the ettringite's surfaces. It can be observed that there are three distinct peaks for the atomic density profiles of water oxygen atoms on both surfaces. Moreover, the peaks have occurred at the exact similar distances from each surface, i.e. 0.0, 2.0 and 5.0 Å for the first, second, and third peak, respectively. A Similar trend is observed for the atomic density profiles of water hydrogen atoms with three distinct peaks, which are located at a distance of 1.0, 2.5, and 5.5 Å away from each surface. For all the solution concentrations, there are one and two distinct peaks of oxygen and hydrogen atoms, respectively, which correspond to the water molecules present in the inner-sphere region. The strong orientation of water molecules is due to the formation of hydrogen bonds between the hydrogen and oxygen of water molecules with those of the ettringite's surfaces. As the tails of the atomic density profile of the oxygen and hydrogen atoms extend to the solid substrate, it can be noted that strong chemical interactions exist between the ettringite's surfaces and the water molecules. There is also one distinct peak for the water oxygen and hydrogen atoms in the outer-sphere region, which highlights that the presence of ettringite can affect the orientation of water molecules up to about 7.0 Å from each solid substrate. In the bulk solution, the atomic density profiles are relatively flat, as expected, suggesting that the water molecules are randomly oriented. Since the density profiles of the water oxygen and hydrogen atoms remain similar for solutions with different NaCl concentrations, it is inferred that the orientation of water molecules in contact with the ettringite's surfaces is independent of the number of ions in the solution.

The two ettringite's surfaces that are in contact with the aqueous solution contain positively-charged calcium and aluminum bonded hydroxyl groups ready to attract the chloride ions present in the solution. For 0.1 M NaCl solution, however, most of the chloride ions are found to be attracted to only one surface. Since the chemistry of both surfaces is identical, this behavior is due

to the small number of ions in that solution, which may lead to poor statistical results. This issue has been addressed in the current study, in which various NaCl solution concentrations are investigated. With this extension, the peaks in the inner-sphere regions of both surfaces are clearly observed, particularly for simulation cells with a high ionic concentration. The narrow peaks captured in the inner-sphere regions suggest a substantial interaction between the chloride ions and the ettringite's surfaces. On the other hand, because of the presence of the negatively-charged sulfate groups in the ettringite's surfaces, the sodium ions are also drawn to the solid substrate. The inner-sphere Na^+ peak, however, is relatively wide due to the superposition of two/three closely spaced peaks, indicating that the sodium ions do not bind to the surface as strong as chloride ions. This can be attributed to the smaller size of the sodium ion, which makes it more diffusive at the ettringite's surfaces. For both Cl^- and Na^+ density profiles, the intensity of the peaks increases with increasing the concentration. This is mainly due to the correlation between the ions adsorbed to the surfaces and the ones still present in the solution.

6.3.2 Adsorption Statistics

The information provided by the atomic density profiles can be further used to obtain adsorption statistics. To this end, the integral of $\rho_\alpha(x)$ is taken over Δx to determine the number of atoms of type α present in the slab of volume $\Delta x \times b \times c$, where b and c are the dimensions of the simulation cell in the y and z directions, respectively. For the NaCl solution concentrations considered in this study, the density profiles of water, as well as chloride and sodium ions, are integrated to obtain the adsorption statistics in the inner- and outer-sphere regions (Tables 6-1 to 6-3). In these tables, N_t is the total number of water/ion species in the simulation cell; N_{ad} is the number of species within the region of interest; X_{ad} is the fraction of surface-bound species; and ρ is the surface site density ($1/nm^2$). As can be found in Table 6-1, the inner-sphere and total (summation of inner- and

outer-sphere) surface-bound fractions of water molecules experience only a small reduction if the ionic strength increases from 0.1 M to 1.5 M NaCl. This observation was expected as the atomic density profiles of water molecules (discussed in the previous section) are reasonably consistent for the range of NaCl concentrations considered in this study. The obtained results indicate the strong water binding capacity of the ettringite's surfaces, which is originated mainly from the integrated H-bond network between the water molecules and surface sites.

Table 6-1. Adsorption statistics calculated from atomic density profiles of the water molecules.

		Inner-Sphere			Total Surface-Bound		
	N_t	N_{ad}	X_{ad} (%)	ρ (nm^{-2})	N_{ad}	X_{ad} (%)	ρ (nm^{-2})
0.1 M	3933	362.18	9.21	18.72	540.69	13.75	27.94
0.2 M	3933	364.05	9.26	18.81	542.29	13.79	28.03
0.5 M	3933	350.48	8.91	18.11	530.93	13.50	27.44
1.0 M	3933	343.14	8.72	17.73	524.74	13.34	27.12
1.5 M	3933	347.05	8.82	17.94	529.35	13.46	27.36

For 0.1 M NaCl, a mean of 1.24 and 1.38 chloride ions are found in the inner- and inner- plus outer-sphere regions, respectively, while a mean of 0.95 and 1.25 sodium ions is located in the same regions (Tables 6-2 and 6-3). The fact that the fraction of surface-bound Cl^- is higher than that of Na^+ for all the NaCl concentrations indicates that the chloride ions have a higher affinity to the ettringite's surfaces compared to the sodium ions. In a previous study conducted by Kalinichev and Kirkpatrick (2002), there was no chloride ion detected at the surfaces of ettringite, which could be due to the small number of ions (only four) or short duration of simulation (only 100 ps). Nonetheless, the fraction of the surface-bound Na^+ recorded for the 0.1 M NaCl concentration in the current study (i.e., 17.92 %) is close to the one reported by Kalinichev and Kirkpatrick (2002), i.e., 25%.

Table 6-2. Adsorption statistics calculated from atomic density profiles of the chloride ions.

		Inner-Sphere			Total Surface-Bound		
	N_t	N_{ad}	X_{ad} (%)	ρ (nm^{-2})	N_{ad}	X_{ad} (%)	ρ (nm^{-2})
0.1 M	7	1.24	17.68	0.06	1.38	19.69	0.07
0.2 M	14	2.21	15.81	0.11	2.58	18.46	0.13
0.5 M	35	6.08	17.37	0.31	6.93	19.81	0.36
1.0 M	71	7.56	10.65	0.39	9.21	12.97	0.48
1.5 M	106	11.91	11.23	0.62	15.43	14.56	0.80

Table 6-3. Adsorption statistics calculated from atomic density profiles of the sodium ions.

		Inner-Sphere			Total Surface-Bound		
	N_t	N_{ad}	X_{ad} (%)	ρ (nm^{-2})	N_{ad}	X_{ad} (%)	ρ (nm^{-2})
0.1 M	7	0.95	13.63	0.05	1.25	17.92	0.06
0.2 M	14	1.38	9.83	0.07	2.08	14.87	0.11
0.5 M	35	3.73	10.67	0.19	5.61	16.02	0.29
1.0 M	71	5.46	7.68	0.28	8.58	12.08	0.44
1.5 M	106	10.66	10.06	0.55	15.56	14.68	0.80

While the fraction of surface-bound ions decreases with increasing the solution concentration, the surface site density of the chloride and sodium ions have an increasing trend. This is in complete agreement with the binding isotherm and ^{35}Cl NMR relaxation studies performed by Yu and Kirkpatrick (2001) on cement hydrate suspensions. It is worth noting that the surface site density increases significantly as the concentration increases from 1.0 to 1.5 M. This reflects that even the 1.0 M NaCl solution is still far from the saturation of ion adsorption sites located on the ettringite's surfaces. For the highest ionic strength, approximately 85% of the ions remain within the bulk solution for a long period of time (i.e., 5000 ps). This suggests that the ettringite's surfaces do not have a significant ion adsorption capacity, which is consistent with the findings of the MAS NMR spectroscopy performed by Jones et al. (2003).

6.3.3 Binding Isotherms

The relationship between the concentration of free and bound ions at a given temperature is commonly referred to as binding isotherm. Based on experimental test results, a number of binding isotherms have been introduced to describe the chloride binding capacity of cementitious materials. Tuutti (1982) proposed a linear relationship between the free and bound chlorides. This relationship, however, was found to be accurate only in the medium chloride concentration range, while it overestimates and underestimates the chloride binding capacity at high and low chloride concentrations, respectively (Ramachandran et al., 1984; Arya et al., 1990; Sandberg, 1999; Mohammed and Hamada, 2003). Nonlinear relationships between the bound and free chlorides are often used based on the Langmuir and Freundlich isotherms. The Langmuir isotherm assumes that all the adsorption sites are occupied at high concentrations (Sergi et al., 1992), while the Freundlich isotherm suggests that monolayer adsorption occurs at low concentrations (Luping and Nilsson, 1993).

Despite the wealth of information obtained from experimental tests, there is a major gap in the literature to characterize the molecular origins of the chloride binding mechanism. The current study provides the first holistic effort to investigate this critical aspect using the MD simulations performed on a wide range of solution concentrations over a period of simulation time, which is long enough to properly capture the transport of diffusing species. Since there is no universal definition for the ions that are considered bounded to a surface, the plots for both inner-sphere and total surface-bound ions are shown in Figure 6-4. For both cases, it can be seen that there is a linear relationship between the bound and free ions at concentrations below 0.5 M (23.9 g/L) NaCl. This is in a complete agreement with the observations from the experimental tests, in which a linear relationship was reported for the concentrations lower than 20 g/L (Arya et al., 1990).

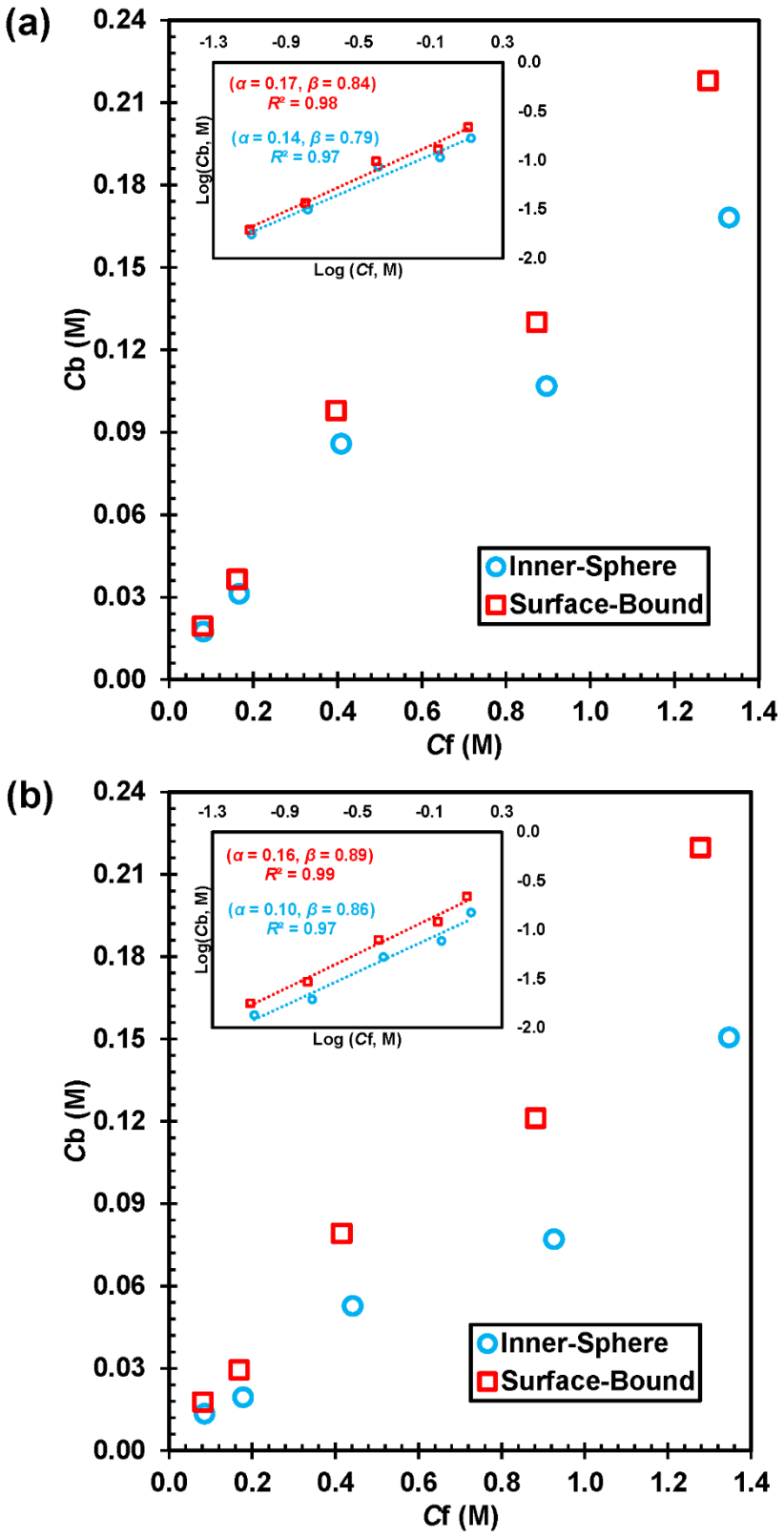

Figure 6-4. The inner-sphere and total surface-bound binding isotherms of (a) chloride ions and (b) sodium ions.

Figure 6-4 also shows that, as the chloride concentration increases, the relationship between the bound and free chloride ions deviates from the linear isotherm. In the logarithmic scale, however, a perfect linear relationship is captured between the bound and free ions with an R-squared value exceeding 0.97. Such a logarithmic relationship is very much similar to the relationship provided by the Freundlich binding isotherm, which has been obtained from macro-scale experimental tests. The Freundlich isotherm can be expressed as:

$$C_b = \alpha {C_f}^{\beta} \qquad (6-3)$$

where C_b and C_f are the concentration of bound and free chloride ions, respectively, and α and β are the binding constants. The Freundlich binding isotherm is found to fit the binding data for the range of NaCl solution concentrations considered in this study very well. This supports the outcome of Luping and Nilsson (1993), which particularly reported the Freundlich binding isotherm as the best fit for the chloride concentrations up to 1.0 M.

6.3.4 Dipolar and HH Orientation Profiles

Based on a comprehensive water orientation profile analysis, detailed information is obtained for the types of water molecules that reside at the ettringite's interfaces. In this analysis, the probability distributions of dipole moments and hydrogen positions are determined for water molecules in different orientations relative to the normal surface using dipolar (θ_d) and HH (θ_{hh}) angles (Jin et al., 2014). As illustrated in Figure 6-5, θ_d refers to the angle between the dipolar vector (v_d) of a water molecule and the surface's normal vector [100]. On the other hand, θ_{hh} represents the angle between the vector passing the two hydrogen atoms of a water molecule (v_{hh}) and the surface's normal vector.

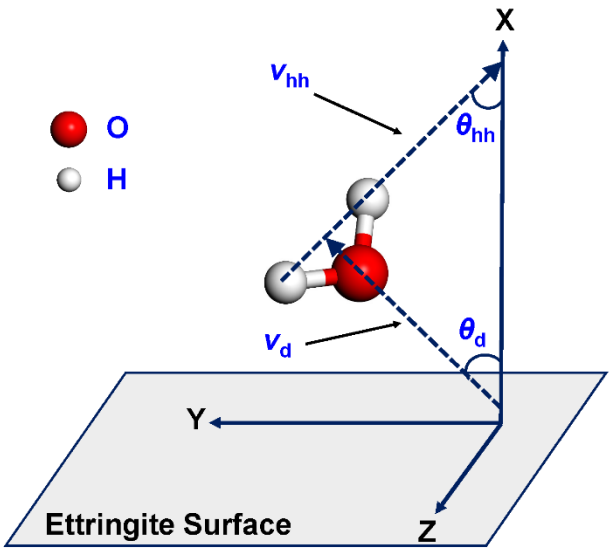

Figure 6-5. Schematic illustration describing dipolar (v_d) and HH (v_{hh}) vectors.

The orientation profiles that describe the distribution of θ_d and θ_{hh} angles are calculated for four water layers, each with a thickness of 1 Å (Figure 6-6). The first three orientation profiles are obtained for the layers that describe the first three peaks of the water oxygen atoms captured in the atomic density profiles of the 1.5 M NaCl solution. The last orientation profile is included as a benchmark for a water layer in the middle of the aqueous solution. It can be observed in Figure 6-6(a) that water molecules at the first layer are predominantly oriented with θ_d at 37.5°, indicating that the dipole axis is tilted away from the surface. This implies that the water oxygen atoms are strongly adsorbed by the positively-charged tricalcium aluminate columns at the surface of ettringite. It is interesting to note that this orientation preference is consistent with the finding from the atomic density profiles (as described in Section 6.3.1), in which the water oxygen atoms are energetically more favorable for the ettringite's surfaces compared to the water hydrogen atoms. In the second layer, there is an intensity peak at 122.5°, reflecting that the dipolar vector points downward to the surface. In the layers farther from the surface, the peak shifts to the center (i.e., 90°), highlighting that the H-O bonds are parallel to the surface. The lack of orientation preference

is attributed to the fact that the interactions between the water molecules and the surface have significantly been weakened.

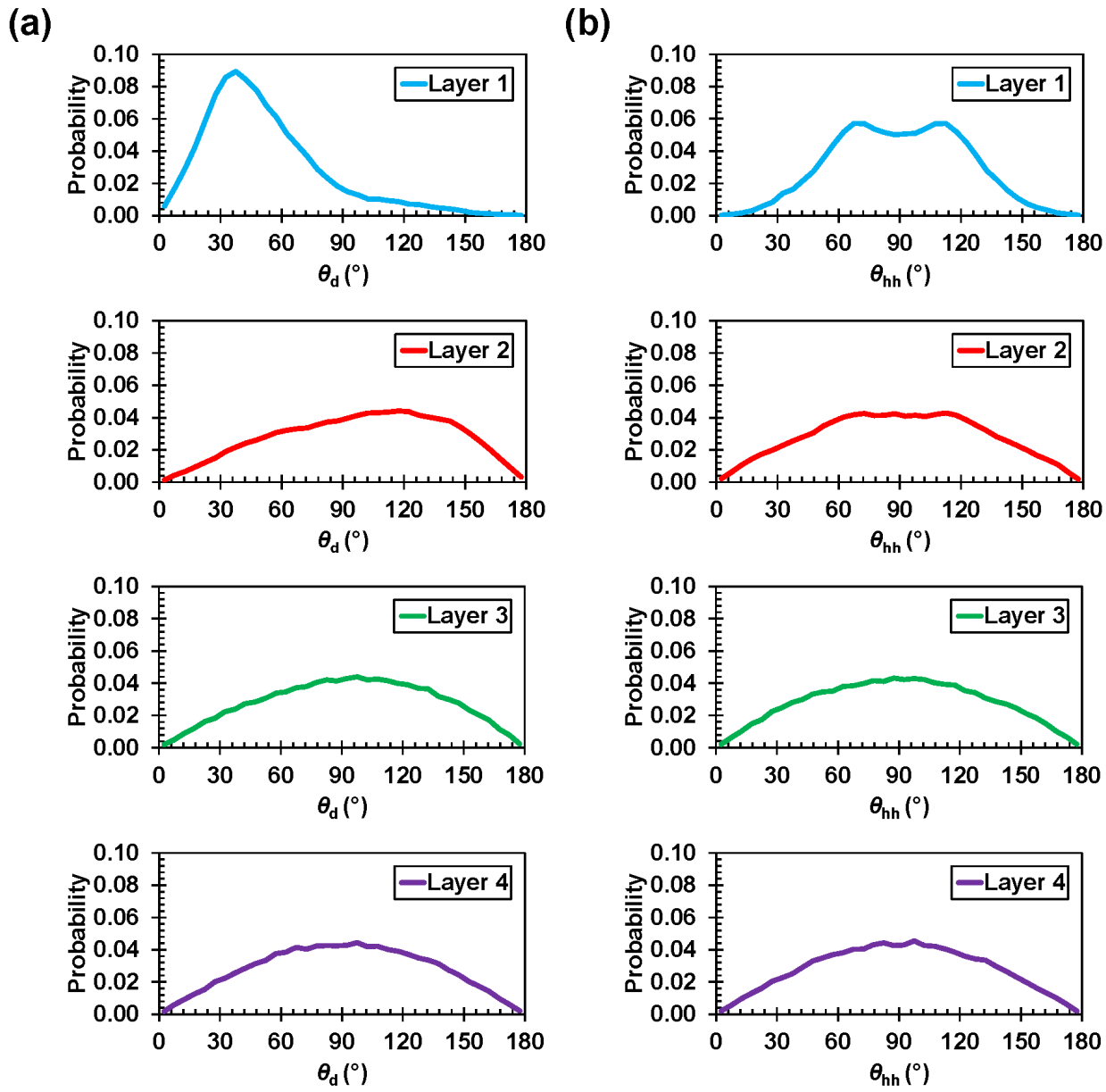

Figure 6-6. Orientation profiles: (a) dipolar and (b) HH angle distribution.

As for the distribution of HH angles shown in Figure 6-6(b), there are two peaks in the first layer at 72.5° and 112.5°, showing that the water hydrogen atoms are elevated slightly different with respect to the *x* direction. For the second layer, the two peaks are merged together, resulting

in a wide peak from 82.5° to 97.5°. With moving away from the ettringite's surface (i.e., third and fourth layer), there is a dominant orientation at 90°, implying that the two hydrogen atoms in a water molecule tend to elevate at the same distance in the *x* direction.

6.3.5 Planar Atomic Density Distributions

To further understand the adsorption mechanisms of sodium and chloride ions to the ettringite's surfaces, the planar atomic density distributions (PADDs) of the Cl^- and Na^+ are extracted from the MD simulations. PADD is a map of the atomic density of the atom types of interest calculated over the production time. For various sections selected along the *x* axis of the simulation cell, the atomic trajectories are recorded and then mapped to a grid in the *y*-*z* plane. Figure 6-7 shows the PADDs of the Cl^- and Na^+ ions present within the inner-sphere range superimposed on the equilibrium locations of calcium, aluminum, and sulfur atoms of ettringite. The PADDs for the 0.1 M NaCl solution indicates that the inner-sphere chloride ions are preferentially found over the positively-charged tricalcium aluminate columns, while the inner-sphere sodium ions locate themselves over the sulfate groups that have negative charges. Some of the sodium ions, however, are not located within the channels between the tricalcium aluminate columns. This can be attributed to the smaller ionic radius of the sodium ions, which makes them more mobile compared to the chloride ions. It is worth noting that Na^+-Cl^- pair formation is also observed, mainly due to the coadsorption of the ions to the ettringite's surfaces. This behavior is more pronounced when the ionic strength increases (as can be clearly seen in the PADDs of the 1.5 M NaCl solution). This indicates that a considerable number of Na^+ locate themselves over the columns, where the chloride ions are also present and form stable NaCl compounds.

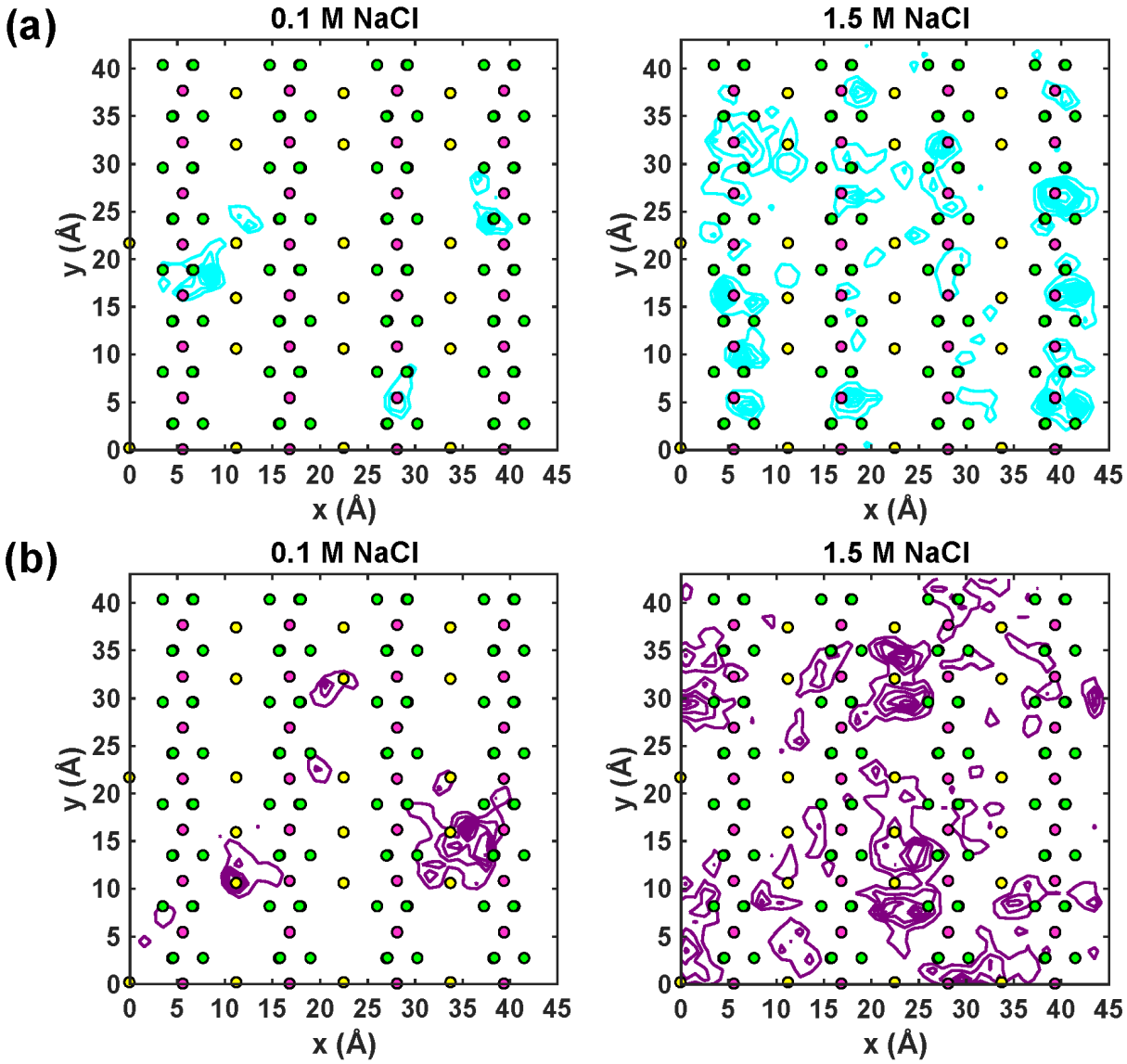

Figure 6-7. Planar atomic density distributions of (a) Cl^- and (b) Na^+ within the inner-sphere distance from the ettringite's surfaces superimposed on the equilibrium locations of Ca (green), Al (pink), and S (yellow).

In order to identify the Na^+-Cl^- ion pairing, the coordinates of all sodium and chloride ions that reside within the inner-sphere distance from the ettringite's surfaces are recorded. A comprehensive cluster analysis is performed to enumerate the ion pair formation. It is assumed that ions within a given distance ρ are associated with each other. The distance ρ is determined from the first minimum in the Na^+-Cl^- pair distribution function (i.e., ~ 2.9 Å). For the 1.5 M NaCl solution, it is found that the probability of ion pairing is almost 9.6%. Since there are more than

22 Na^+ and Cl^- within the inner-sphere range (as reported in Tables 6-2 and 6-3), it can be inferred that there is (at least) one long-lived Na^+-Cl^- ion pairing in the inner-sphere range. It is important to note that a number of large $(Na_mCl_n)^{n-m}$ ($2 < n+m < 5$) clusters with a short lifetime are also identified from the cluster analysis. However, the stability of such large clusters is statistically unlikely as their formation probability is less than 1%.

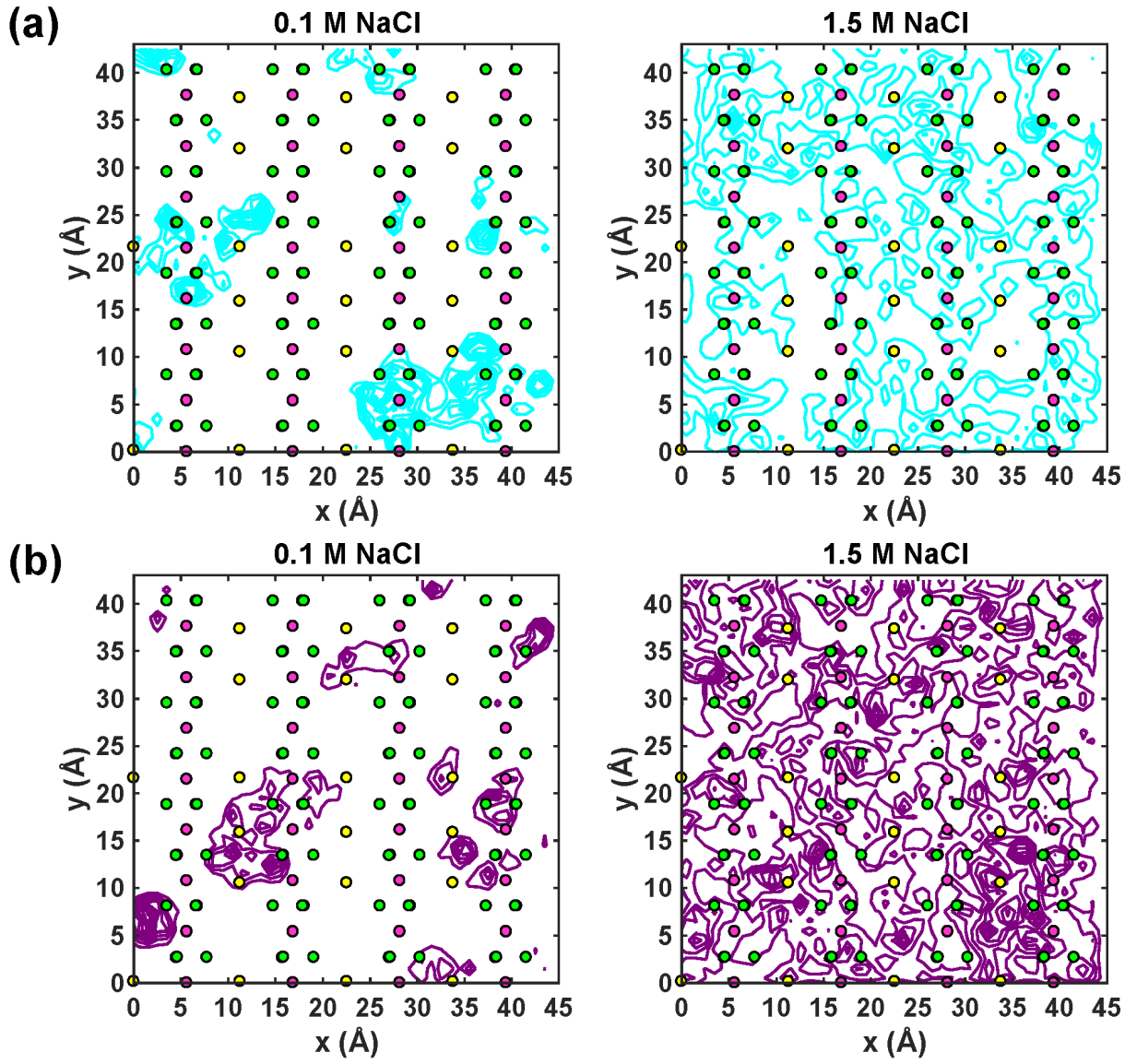

Figure 6-8. Planar atomic density distributions of (a) Cl^- and (b) Na+ within the outer-sphere distance from the ettringite's surfaces superimposed on the equilibrium locations of Ca (green), Al (pink), and S (yellow).

The outer-sphere PADDs of the Cl^- and Na^+ in the *y-z* plane are shown in Figure 6-8. For the 0.1 M NaCl solution, the outer-sphere PADDs are more mobile than the inner-sphere ones. This higher mobility is expected as the outer-sphere ions are in a longer distance from the ettringite's surfaces, and thus, are less affected by the electrostatic attractions from the ettringite's surfaces. The presence of water molecules between the ions and the solid substrate makes the outer-sphere adsorption complexes less stable compared to the ones formed in the inner-sphere range. Nonetheless, it must be noted that stable, long-lived adsorption complexes are still observed in the outer-sphere range. For the 1.5 M NaCl solution, however, the PADDs are found to diffuse over the entire ettringite's surface with a minimum indication of a long-lived complex formation. This can be an indication of the fact that adsorption sites on the ettringite's surfaces are close to becoming fully saturated.

6.3.6 Radial Distribution Functions

Atom-atom radial distribution function (RDF) is a robust tool to characterize the structure of adsorption sites on the ettringite's surfaces. An RDF, $g_{ij}(r_{ij})$, specifies the probability density function of finding the atoms of type *j* at a distance r_{ij} from the reference atoms of type *i* averaged over time:

$$g_{ij}(r_{ij}) = \frac{\langle N_{ij} \rangle}{4\pi\rho_j r_{ij}} \qquad (6-4)$$

where ρ_j is the density of atoms of type *j*, and $<N_{ij}>$ is the average number of atoms with type *j* found at the distance r_{ij} from the atoms of type *i*. The presence of a peak in the RDF indicates the existence of a coordinated shell of atoms of type *j* with the distance of r_{ij} from atoms of type *i*. The number of atoms in this shell, which is often called coordination number, $n_{ij}(r_{ij})$, is calculated by integrating the RDF function from zero to immediately after the first peak:

$$n_{ij}(r_{ij}) = 4\pi\rho_j \int_0^{r_{ij}} g(r) r^2 \, dr \qquad (6-5)$$

The curve that presents the coordination numbers with respect to distance from the central atom of interest is referred to as running coordination number (RCN) curve. Figure 6-9 shows the RDFs (solid lines) and RCNs (dashed lines) of Cl^- and Na^+ in the central position averaged over 5000 ps for the 1.5 M NaCl solution in contact with the ettringite's surfaces. The inner-sphere and bulk ions are included in the calculation of the adsorbed and aqueous RDFs, respectively. In the Cl^--WatO RDFs, the first peak is located at 3.25 Å, consistent for both adsorbed and aqueous ions. The coordination number associated with the first hydration shell for the adsorbed and aqueous ions is 7.01 and 7.46, respectively. Although this is comparable with the value of 6.0 obtained from the Infrared spectroscopic study (Bergstrom et al., 1991) and 5.6 from the Car-Parrinello MD simulation (Bakker, 2008), the difference can be attributed to the fact that the referenced values were obtained for the sodium chloride salt solutions without the presence of ettringite, the dense hydrogen networks of which can increase the corresponding coordination numbers. While a clear peak pertained to the second hydration shell is evident at 4.95 Å for the aqueous Cl^-, a broad peak is observed for the adsorbed chloride ions. The lower coordination number for the first hydration shell and the absence of a clear separation between the first and second hydration shell indicate a weak interaction between the chloride ions and water molecules in contact with the ettringite's surfaces. The Na^+-WatO RDFs present two pronounced peaks centered at 2.35 and 4.55 Å from the Na^+, which correspond to the first and second hydration shells, respectively. The coordination numbers of the first and second oxygen shells are 5.65, and 22.55, respectively. The presence of the two distinct hydration shells indicates a strong interaction between the Na^+ and water molecules. As the distances, intensities, and coordination numbers extracted from the MD simulations are almost identical for adsorbed and aqueous interactions, it is inferred that the

ettringite's surfaces have a minimal effect on the orientation of the sodium ions with respect to the water molecules.

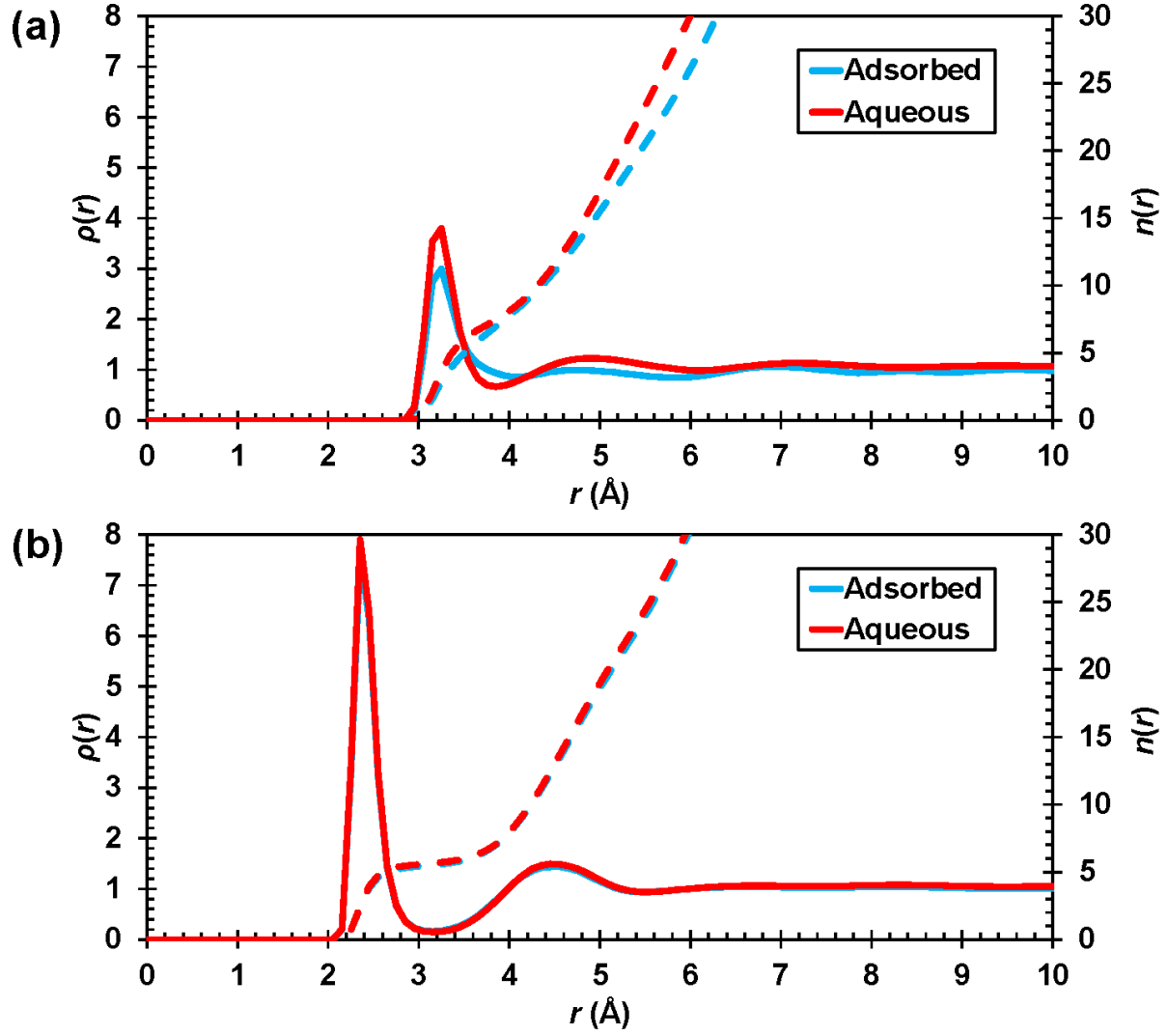

Figure 6-9. Radial distribution functions (solid lines) and running coordination numbers (dash lines) of (a) Cl^--WatO and (b) Na^+-WatO calculated for 1.5 M NaCl solution in equilibrium with the ettringite's surfaces.

Figure 6-10 shows the RDFs of the sodium and chloride ions and the main structural elements of the ettringite's surfaces at the inner-sphere range. To generate this set of RDFs, the ions present in the outer-sphere and aqueous regions are excluded from the calculations. For the Cl^--Al, Cl^--Ca, and Cl^--Ho RDFs, several peaks are observed up to a long distance from the chloride ions, which can be attributed to the crystalline structure of ettringite. The first peak in the Cl^--Al, Cl^--Ca, and

Cl^--Ho RDFs corresponds to 2.65, 4.35, and 2.45 Å from the chloride ions, respectively. This is consistent with the inner-sphere adsorption of chloride ions to the tricalcium aluminate columns as discussed in the previous section.

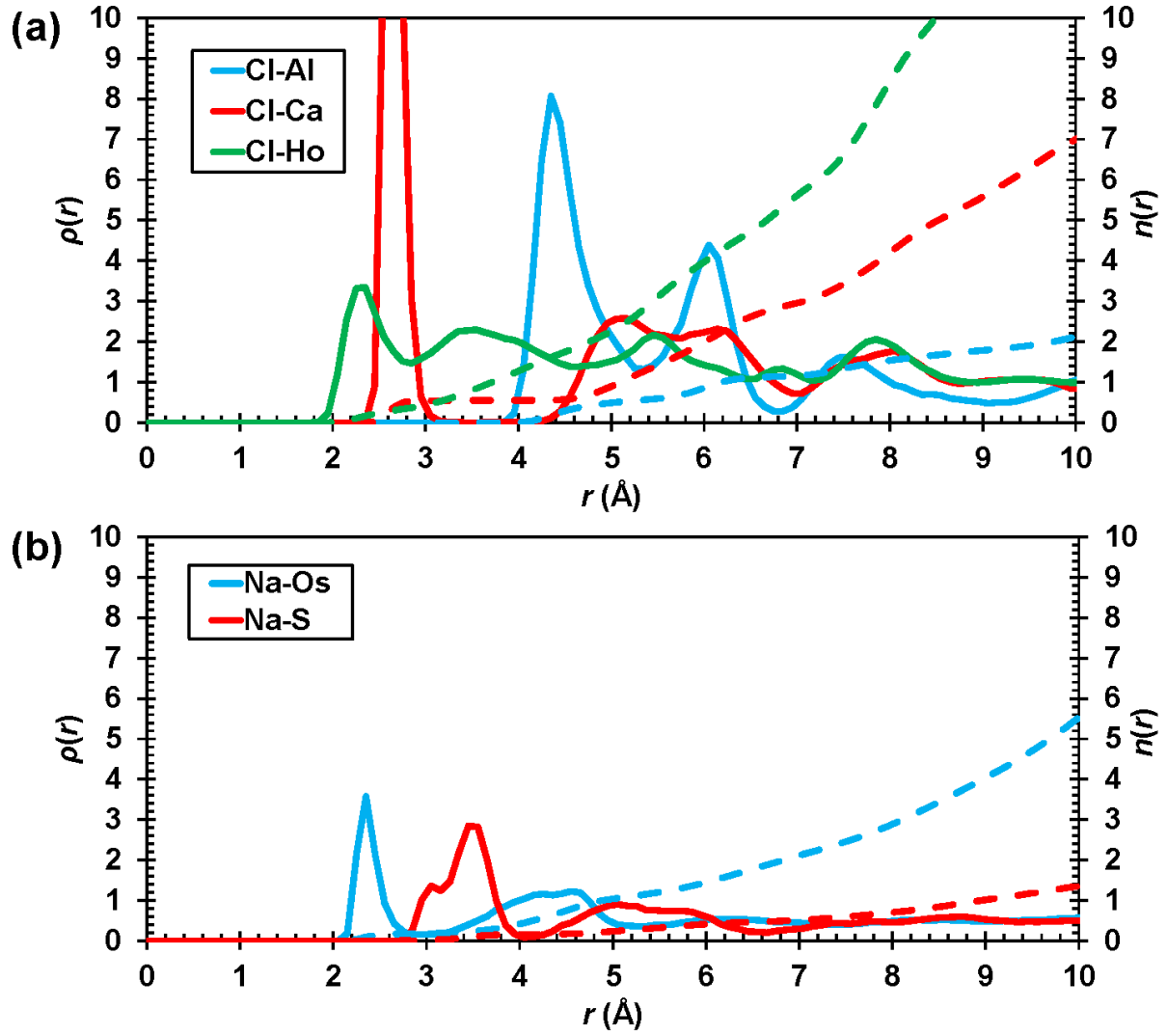

Figure 6-10. Radial distribution functions (solid lines) and running coordination numbers (dash lines) of (a) chloride ions and the elements of the tricalcium aluminate columns (Al, Ca, and Ho), and (b) sodium ions and the elements of the sulfate groups (S and Os) calculated for 1.5 M NaCl solution in equilibrium with the ettringite's surfaces.

It can be observed that the first peak in the Na^+-Os and Na^+-S RDFs is centered at 2.35 and 3.45 Å, respectively. As expected, the oxygen atoms of the sulfate groups locate themselves closer to the adsorbed sodium ions compared to the sulfur atoms. The coordination number corresponding

to the first peak in the Na^+-Os RDF is less than one, which suggests that the sodium ions energetically prefer to reside directly above one of the oxygens of each sulfate group. This description confirms that the inner-sphere sodium ions are adsorbed on the negatively-charged sulfate groups of the ettringite's surface.

6.3.7 Self-Diffusion Coefficients

To characterize the dynamic properties of the water molecules, as well as sodium and chloride ions, in contact with the ettringite's surfaces, the self-diffusion coefficient of them are calculated. The self-diffusion coefficient of the solution species can be determined from the mean square displacement (MSD) as below:

$$D = \frac{1}{2\xi N} \lim_{t\to\infty} \left(\frac{d}{dt} \sum_{i=1}^{N} \langle |r_i(t) - r_i(t_0)|^2 \rangle \right) \qquad (6-6)$$

where N is the total number of atoms; t and t_0 are the current time and time at origin, respectively; and ξ is the dimension of the system, e.g., 3 for three-dimensional diffusion coefficients. The MSD of water molecules for various NaCl concentrations at the inner- and outer-sphere regions is obtained from the MD simulations (Figure 6-11). It can be observed that the MSDs for the outer-sphere region are higher than the ones for the inner-sphere region. This outcome was anticipated as the chemical interactions from the ettringite's surfaces lower the rate of diffusion when the ions approach the surface. The self-diffusion coefficients of various species are calculated following the procedure described in Ngouana and Kalinichev (2014), in which the quasi-linear part of the MSD curve over time is divided into four blocks and the arithmetic average of the slopes of the four independent blocks is calculated to determine the self-diffusion coefficient.

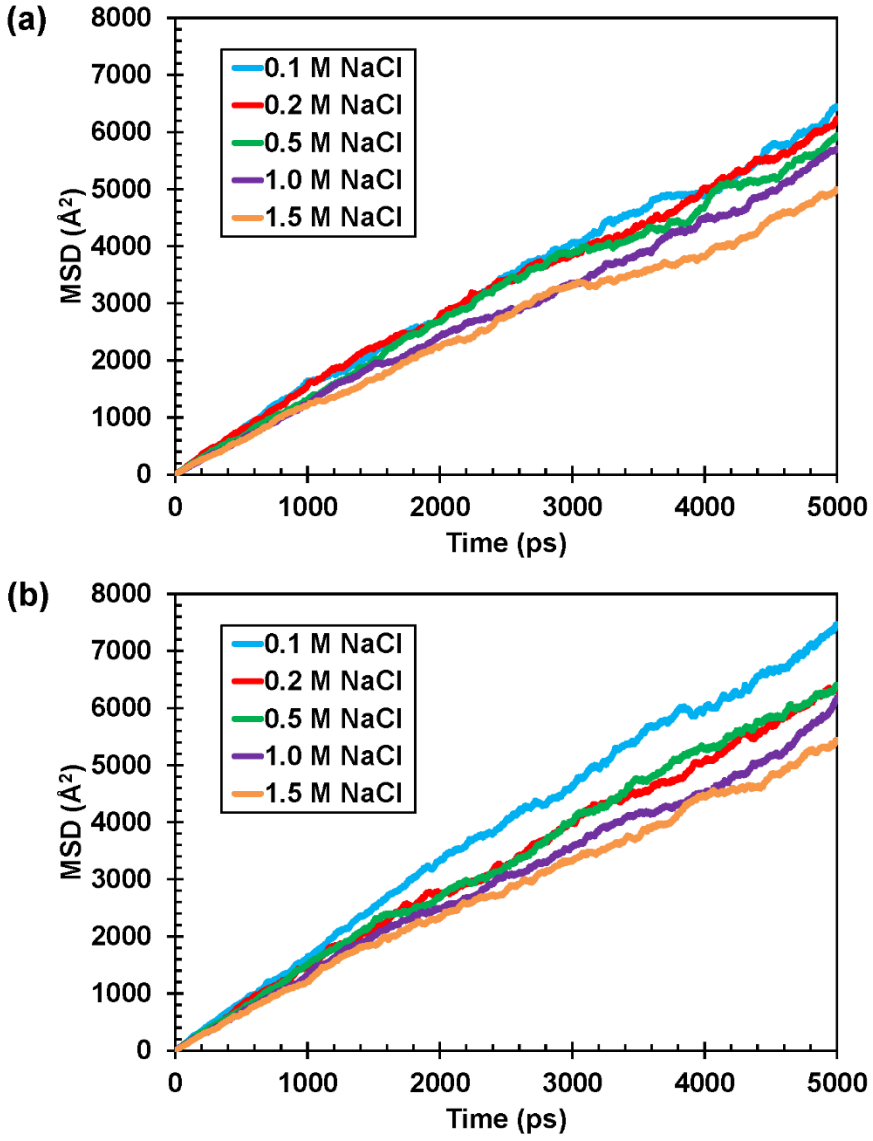

Figure 6-11. The MSD of water molecules for various NaCl concentrations for (a) inner-sphere, and (b) outer-sphere regions.

As shown in Figure 6-12, the self-diffusion coefficient for the inner-sphere, outer-sphere, and total surface-bound water molecules fall in the range of 1.65-2.22 $\times 10^{-9}$, 1.71-2.48 $\times 10^{-9}$, and 1.68-2.33 $\times 10^{-9}$ m^2/s, respectively. This is consistent with the range of 0.6-2.0 $\times 10^{-9}$ m^2/s obtained by the QENS experiments on the samples of hardened cement paste (Bordallo et al., 2006). It is observed that as the NaCl concentration increases from 0.1 to 1.5 M, the self-diffusion coefficients of the inner- and outer-sphere water molecules decrease by 25% and 31%, respectively. This can

be attributed to the low diffusivity of the ions in the system, which decelerates the mobility of neighboring water molecules.

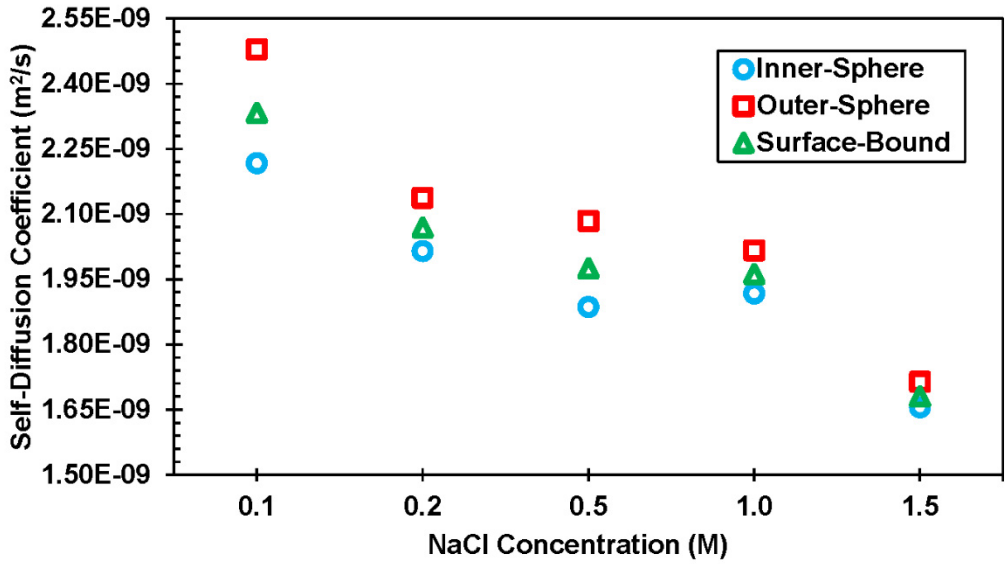

Figure 6-12. Self-diffusion coefficients as a function of NaCl concentration for the inner-sphere, outer-sphere, and total surface-bound water molecules.

The self-diffusion coefficients calculated for the 1.5 M NaCl solution species are listed in Table 6-4. The diffusion coefficients are reported for the inner- and outer-sphere, as well as the total surface-bound species. It is noted that the diffusion coefficients of the species reside in the inner-sphere range are smaller than those of present in the outer-sphere range. The diffusion coefficient of the adsorbed chloride ions at the inner-sphere region is almost half of that of the sodium ions. This is because of the small size of sodium ions, which makes them more diffusive on the ettringite's surfaces. This is verified with a very similar behavior observed in the PADDs shown in Figure 6-7.

Table 6-4. Self-diffusion coefficients of 1.5 M NaCl solution species in contact with the ettringite's surfaces.

Self-diffusion coefficient	H_2O	Cl^-	Na^+
Inner-Sphere (× 10^{-9} m^2/s)	1.65	0.43	0.83
Outer-Sphere (× 10^{-9} m^2/s)	1.71	1.48	1.01
Total Surface-Bound (× 10^{-9} m^2/s)	1.68	0.74	0.94

6.4 Conclusions

In this study, the physical adsorption mechanisms of water molecules, as well as sodium and chloride ions, were investigated at the inner- and outer-sphere distance ranges from the ettringite's surfaces through MD simulations. For this purpose, various NaCl solution concentrations, ranging from 0.1 to 1.5 M, were placed in contact with the (100) surfaces of ettringite. With a total simulation time of 5500 ps, the equilibrated trajectories were recorded for further analysis to determine the transport and structural properties of the species of interest. The atomic density profiles of the water molecules indicated that the oxygen atoms are energetically more favorable for the ettringite's surfaces compared to the hydrogen atoms. Furthermore, it was revealed that the atomic density profiles of the ions under consideration directly depend on the solution concentration. The statistical analysis showed that the fraction of the total chloride ions bounded to the surfaces of ettringite is more than 10% for the NaCl concentrations considered in this study. The Cl^- and Na^+ binding isotherms showed that the relation between the free and bound ions is not always linear. This is an important finding, which supports the data obtained from experimental tests on real-size cementitious materials. A complementary investigation suggested that a logarithmic relation, similar to the Freundlich isotherm, can properly capture the binding capacity in the concentrations up to 1.0 M. Moreover, the orientation of water molecules at the ettringite's interfaces was investigated using water orientation profile analysis. It was determined that the water molecules are highly oriented close to the surface of ettringite. However, with moving away from the surface, no preferred orientation was observed for them. This was attributed to the weakened interactions between water molecules and ettringite's surfaces.

In the inner-sphere distances from the ettringite's surfaces, the chloride ions were mostly found on the tricalcium aluminate columns, while the sodium ions were located on the top of the oxygen

atoms of sulfate groups. Moreover, the Na^+-Cl^- pair formation was observed due to the coadsorption of the ions to the ettringite's surfaces. In the outer-sphere range, however, the Na^+ and Cl^- were found to be diffusive with almost no indication of long-lived complex formations. The calculated RDFs indicated that unlike chloride ions, there is a weak interaction between the sodium ions and water molecules near the ettringite's surfaces. It was observed that the water and ions present in the inner-sphere range are less mobile than those in the outer-sphere range. This was related to the strong electrostatic interactions between various species as they approach the ettringite's surfaces. The diffusion rate of the Na^+ and Cl^- ions were approximately two and three times smaller than the water molecules, respectively. This reduced the mobility of water molecules as the number of ions present in the solution increased.

6.5 Acknowledgments

The feedback and support from Dr. Andrey Kalinichev are gratefully acknowledged. The Extreme Science and Engineering Discovery Environment (XSEDE), which is supported by National Science Foundation grant number ACI-1548562, was used for part of the atomistic simulations conducted in this study.

6.6 References

1- Alipour A., Shafei B., and Shinozuka M., 2011. "*Performance evaluation of deteriorating highway bridges located in high seismic areas*". Journal of Bridge Engineering 16(5): 597-611.

2- Alipour A., Shafei B., and Shinozuka M., 2013. "*Capacity loss evaluation of reinforced concrete bridges located in extreme chloride-laden environments*". Structure and Infrastructure Engineering 9(1): 8-27.

3- Allen M., and Tildesley D., 1987. "*Computer simulation of liquids*". Oxford University Press, New York.

4- Anderson K., Allard B., Bengtsson M., and Magnusson B., 1989. "*Chemical composition of cement pore solutions*". Cement and Concrete Research 19: 327-332.

5- Arya C., Buenfeld N.R., and Newman J.B., 1990. "*Factors influencing chloride binding in concrete".* Cement and Concrete Research 20(2): 291-300.

6- Bakker H.J., 2008. "Structural dynamics of aqueous salt solutions". Chemistry Reviews 108: 1456-1473.

7- Barberon F., Barpghel-Bouny V., Zanni H., and Bresson B., 2005. "*Interactions between chloride and cement-paste materials".* Magnetic Resonance Imaging 23: 267-272.

8- Beaudoin J.J., Ramachandran V.S., and Feldman R.F., 1990. "*Interaction of chloride and C-S-H*". Cement and Concrete Research 20(6): 875-883.

9- Berendsen H.J.C., Postma J.P.M., van Gunsteren W.F. and Hermans J., 1981. "*Interaction models for water in relation to protein hydration*". The Jerusalem Symposia on Quantum Chemistry and Biochemistry 14: 331-342.

10- Berendsen H.J.C., Grigera J.R., and Straatsma T.P., 1987. "The missing term in effective pair potentials". The Journal of Physical Chemistry 91(24): 6269-6271.

11- Bergstrom P.A., Lindgren J., and Kristiansson O., 1991. "*An IR study of the hydration of ClO_4^-, NO_3^-, I^-, Br^-, Cl^-, and SO_4^{2-} anions in aqueous solution*". Journal of Physical Chemistry 95: 8575-8580.

12- Bordallo H.N., Aldridge L.P., and Desmedt A., 2006. "*Water dynamics in hardened ordinary Portland cement paste or concrete: From quasielastic neutron scattering*". Journal of Physical Chemistry B 110: 17966-17976.

13- Brown G.E., 2001. "*How minerals react with water*". Science 294(5540): 67-69.

14- Cannon W.R., Pettitt B.M., and McCammon J.A., 1994. "*Sulfate anion in water: Model structural, thermodynamic, and dynamic properties*". The Journal of Physical Chemistry 98: 6225-6230.

15- Cygan R.T., Liang J.J., and Kalinichev A.G., 2004. "*Molecular models of hydroxide, oxyhydroxide, and clay phases and the development of a general force field*". The Journal of Physical Chemistry B 108(4): 1255-1266.

16- Ekolu S.O., Thomas M.D.A., and Hootan R.D., 2006. "*Pessimum effect of externally applied chlorides on expansion due to delayed ettringite formation: Proposed mechanism*". Cement and Concrete Research 36: 688-696.

17- Ewald P.P., 1921. "*Die Berechnung optischer und elektrostatischer Gitterpotentiale"*. Annalen der Physik 64: 253.

18- Glasser F.P., Kindness A., and Stronach S.A., 1999. "*Stability and solubility relationships in AFm phases Part I. Chloride, sulfate and hydroxide*". Cement and Concrete Research 29: 861-866.

19- Hajilar S., and Shafei B., 2014. "*Nano-scale characterization of elastic properties of AFt and AFm phases of hydrated cement paste*". Proceedings of the European Conference on Computational Modeling of Concrete Structures (EURO-C) 1: 299-306.

20- Hajilar S., and Shafei B., 2015. "*Nano-scale investigation of elastic properties of hydrated cement paste constituents using molecular dynamics simulations*". Computational Materials Science 101: 216-226.

21- Hajilar S., and Shafei B., 2016 (a). "*Mechanical failure mechanisms of hydrated products of tricalcium aluminate: A reactive molecular dynamics study*". Materials and Design 90: 165-176.

22- Hajilar S., and Shafei B., 2016 (b). "*Assessment of structural, thermal, and mechanical properties of portlandite through molecular dynamics simulations*". Journal of Solid State Chemistry 244: 164-174.

23- Hajilar S., Shafei B., Cheng T., and Jaramillo-Botero A., 2017. "*Reactive molecular dynamics simulations to understand mechanical response of thaumasite under temperature and strain rate effects*". Journal of Physical Chemistry A. 121(24): 4688-4697.

24- Hoover W.G., 1985. "*Canonical dynamics: Equilibrium phase-space distributions*". Physical Review A 31(3): 1695-1697.

25- Hou D., and Li Z., 2014 (a). "*Molecular dynamics study of water and ions transported during the nanopore calcium silicate phase: Case study of jennite*". Journal of Materials in Civil Engineering 26(5): 930-940.

26- Hou D., and Li Z., 2014 (b). "*Molecular dynamics study of water and ions transport in nano-pore of layered structure: A case study of tobermorite*". Microporous and Mesoporous Materials 195: 9-20.

27- Hou D., Zeyu L., Peng Z., and Qingjun D., 2016. "*Molecular structure and dynamics of an aqueous sodium chloride solution in nano-pores between portlandite surfaces: A molecular dynamics study*". Physical Chemistry Chemical Physics 18: 2059-2069.

28- Jin J., Miller J.D., and Dang L.X., 2014. "*Molecular dynamics simulation and analysis of interfacial water at selected sulfide mineral surfaces under anaerobic conditions*". International Journal of Mineral Processing 128: 55-67.

29- Jones M.R., Macphee D.E., Chudek J.A., Hunter G., Lannegrand R., Talero R., and Scrimgeour S.N., 2003. "*Studies using ^{27}Al MAS NMR of AF_m and AF_t phases and the formation of Friedel's salt*". Cement and Concrete Research 33: 177-182.

30- Kalinichev A.G., Kirkpatrick R.J., and Cygan R.T., 2000. "*Molecular modeling of the structure and dynamics of the interlayer and surface species of mixed-metal layered hydroxides: Chloride and water in hydrocalumite (Friedel's salt)*". American Mineralogist 85: 1046-1052.

31- Kalinichev A.G., and Kirkpatrick R.J., 2002. "*Molecular dynamics modeling of chloride binding to the surfaces of calcium hydroxide, hydrated calcium aluminate, and calcium silicate phases*". Chemistry of Materials 14: 3539-3549.

32- Kalinichev A.G., Wang J., and Kirkpatrick R.J., 2007. "*Molecular dynamics modeling of the structure, dynamics and energetics of mineral-water interfaces: Application to cement materials*". Cement and Concrete Research 37: 337-347.

33- Korb J.P., McDonald P.J., Monteilhet L., Kalinichev A.G., and Kirkpatrick R.J., 2007. "*Comparison of proton field-cycling relaxometry and molecular dynamics simulations for proton–water surface dynamics in cement-based materials*". Cement and Concrete Research 37: 348-350.

34- Krishnan N.M.A., Wang B., Falzone, G., Pape Y.L., Neithalath N., Pilon L., Bauchy M., and Sant G., 2016. "*Confined water in layered silicates: The origin of anomalous thermal expansion behavior in calcium-silicate-hydrates*". Applied Materials and Interfaces 8(51): 35621–35627.

35- Liu L., Jaramillo-Botero A., Goddard III W.A., and Sun H., 2012. "*Development of a ReaxFF reactive force field for ettringite and study of its mechanical failure modes from reactive molecular dynamics simulations*". The Journal of Physical Chemistry A 116(15): 3918-3925.

36- Luping T., and Nilsson L.O., 1993. "*Chloride binding capacity and binding isotherms of OPC pastes and mortars*". Cement and Concrete Research 23(2): 247-253.

37- Manzano H., Ayuela A., Telesca A., Monteiro P.J.M., and Dolado J.S., 2012. "*Ettringite strengthening at high pressure induced by the densification of the hydrogen bond network*". The Journal of Physical Chemistry C 116(30): 16138-16143.

38- Manzano H., Durgun E., Lopez-Arbeloa I., and Grossman J.C., 2015. "*Insight on tricalcium silicate hydration and dissolution mechanism from molecular simulations*". Applied Materials and Interfaces 7(27): 14726-14733.

39- Mohammed T.U., and Hamada H., 2003. "*Relationship between free chloride and total chloride contents in concrete*". Cement and Concrete Research 33: 1487-1490.

40- Moore A.E., and Taylor H.F.W., 1970. "*Crystal Structure of Ettringite*". Acta Crystallographica B26: 386-393.

41- Ngouana B.F., and Kalinichev A.G., 2014. "*Structural arrangements of isomorphic substitutions in smectites: Molecular simulation of the swelling properties, interlayer structure, and dynamics of hydrated Cs-Montmorillonite revisited with new clay models*". The Journal of the Physical Chemistry C 118(24): 12758-12773.

42- Nosé S., 1984. "*A unified formulation of the constant temperature molecular dynamics methods*". The Journal of Chemical Physics 81(1): 511-519.

43- Plimpton S., 1995. "*Fast parallel algorithms for short-range molecular dynamics*". Journal of Computational Physics 117(1): 1-19.

44- Ramachandran V.S., Seeley R.C., and Polomark G.M., 1984. "*Free and combined chloride in hydrating cement and cement components*". Matériaux et Construction 17(4): 285-289.

45- Sandberg P., 1999. "*Studies of chloride binding in concrete exposed in a marine environment*". Cement and Concrete Research 29: 473-477.

46- Sergi G., Yu S.W., and Page C.L., 1992. "*Diffusion of chloride and hydroxyl ions in cementitious materials exposed to a saline environment*". Magazine of Concrete Research 44(158): 63-69.

47- Shafei B., Alipour A., and Shinozuka M., 2012. "*Prediction of corrosion initiation in reinforced concrete members subjected to environmental stressors: A finite-element framework*". Cement and Concrete Research 42: 365-376.

48- Shafei B., Alipour A., and Shinozuka M., 2013. "*A stochastic computational framework to investigate the initial stage of corrosion in reinforced concrete superstructures*". Computer-Aided Civil and Infrastructure Engineering 28: 482-494.

49- Shafei B., and Alipour A., 2015 (a). "*Application of large-scale non-Gaussian stochastic fields for the study of corrosion-induced structural deterioration*". Journal of Engineering Structures 88: 262-276.

50- Shafei B., and Alipour A., 2015 (b). "*Estimation of corrosion initiation time in reinforced concrete bridge columns: How to incorporate spatial and temporal uncertainties*". ASCE Journal of Engineering Mechanics 141(10): 04015037.

51- Smith D.E., and Dang L.X., 1994. "*Computer simulations of NaCl association in polarizable water*". The Journal of Chemical Physics 100(5): 3757-3766.

52- Smith D.E., and Haymet A.D.J., 1993. "*Simulations of aqueous solutions: the role of flexibility and the treatment of long-range forces*". Fluid Phase Equilibria 88: 79-87.

53- Suryavanshi A.K., Scantlebury J.D., and Lyon S.B., 1996. "*Mechanism of Friedel's salt formation in cements rich in tricalcium aluminate"*. Cement and Concrete Research 26(5): 717-727.

54- Taylor, H.F.W., 1997. "*Cement Chemistry*". 2nd Edition, Thomas Telford Publishing, London.

55- Teleman O., Jonsson B., and Engstrom S., 1987. "*A molecular dynamics simulation of a water model with intramolecular degrees of freedom*". Journal of Molecular Physics 60(1): 193-203.

56- Towns J., Cockerill T., Dahan M., Foster I., Gaither K., Grimshaw A., Hazelwood V., Lathrop S., Lifka D., Peterson G.D., Roskies R., Scott J.R., and Wilkins-Diehr N., 2014. "*XSEDE: Accelerating Scientific Discovery*". Computing in Science and Engineering 16(5): 62-74.

57- Tritthart J., 1989. "*Chloride binding in cement II. The influence of the hydroxide concentration in the pore solution of hardened cement paste on chloride binding*". Cement and Concrete Research 19(5): 683-691.

58- Tuutti K., 1982. "*Analysis of pore solution squeezed out of cement and mortar*". Nordic Concrete Research 1:25.1-16.

59- Yoon S., and Monteiro P., 2013. "*Molecular dynamics study of water molecules in interlayer of 14 Å tobermorite*". Journal of Advanced Concrete Technology 11: 180-188.

60- Yu P., and Kirkpatrick R.J., 2001. "*^{35}Cl NMR relaxation study of cement hydrate suspensions*". Cement and Concrete Research 31(10): 1479-1485.

61- Van der Spoel D., van Maaren P.J., and Berendsen H.J.C., 1998. "*A systematic study of water models for molecular simulation: Derivation of water models optimized for use with a reaction field*". The Journal of Chemical Physics 108(24): 10220-10230.

62- Vasconcelos I.F., Bunker B.A., and Cygan R.T., 2007. "*Molecular dynamics modeling of ion adsorption to the basal surfaces of kaolinite".* The Journal of the Physical Chemistry C 111: 6753-6762.

63- Verlet L., 1967. "*Computer "Experiments" on classical fluids. I. Thermodynamical properties of Lennard-Jones molecules*". Physical Review 159(1): 98-103.

64- Verlet L., 1698. "*Computer "Experiments" on classical fluids. II. Equilibrium correlation functions*". Physical Review 165(1): 201-214.

65- Wallqvist A., and Teleman O., 1991. "*Properties of flexible water models*". Journal of Molecular Physics 74(3): 515-533.

66- Wang P.S., Ferguson M.M., Eng G., Bentz D.P., Ferraris C.F., and Clifton J.R., 1998. "*^{1}H nuclear magnetic resonance characterizations of Portland cement: molecular diffusion of water studied by spin relaxation and relaxation time-weighted imaging*". Journal of Materials Science 33: 3065-3071.

CHAPTER 7: STRUCTURE, ORIENTATION, AND DYNAMICS OF WATER-SOLUBLE IONS ADSORBED TO BASAL SURFACES OF CALCIUM MONOSULFOALUMINATE HYDRATES

Ingress of water molecules and aggressive ions into nanopores of hydrated cement paste (HCP) is known to adversely affect the long-term durability of reinforced concrete structures exposed to seawater or deicing salts. The ability of reinforced concrete structures to resist chloride attack is primarily associated with the chloride binding capacity of the main constituents of HCP. Experimental tests revealed that the calcium aluminate monosulphate hydrates (AFm) phases of HCP play a central role in binding free chloride ions, and thus, decelerating steel corrosion. Nevertheless, many aspects of AFm-solution interactions remained largely unknown, especially at their interfaces. This was the main motivation of the current study, in which the atomistic processes underlying the diffusion of water molecules and chloride ions are investigated in detail using the classical molecular dynamics (MD) method. To this end, an aqueous layer containing various concentrations of sodium chloride solution is sandwiched between the basal surfaces of calcium monosulfoaluminate hydrate, which is the most abundant phase of AFm. The molecular mechanisms of adsorption of water molecules and diffusing ions are characterized for inner- and outer-sphere distance ranges measured from the basal surfaces. The MD simulation results, which are supported by experimental tests, provide for the first time an in-depth insight into the molecular structures, dynamic motions, and chemical interactions between sodium chloride solutions and AFm solid surfaces. The outcome of this study is expected to be directly employed to introduce strategies to prevent the degradation of a wide variety of cementitious materials exposed to harsh environmental conditions.

7.1 Introduction

Corrosion of steel reinforcement embedded in concrete structures is the most destructive form of deterioration in a variety of structures exposed to seawater or deicing salts. This is triggered by the diffusion of chloride ions carried by water molecules through nanopores of hydrated cement paste (HCP) towards the steel reinforcement covered by concrete. Once the concentration of chloride ions at the surface of steel reinforcement exceeds the maximum threshold, the protective film is disrupted and corrosion is initiated (Shafei et al., 2012; Alipour et al., 2011 and 2013; Shafei et al., 2013; Shafei and Alipour, 2015a,b). Considering the consequences of corrosion, design of concrete materials capable of resisting chloride attack has received a significant attention in various fields of science and engineering. This entails an in-depth understanding of the physicochemistry of the interface of cementitious materials and aqueous solutions. It is known that chloride ions interact with cementitious materials as either “bound” or “free” ions. The former category refers to the ions chemically or physically bound to their surrounding surfaces, whereas the latter category denotes the ones encapsulated in the gel’s pore spaces. It must be noted that free chloride ions are the ions that can freely diffuse into the nanopores of HCP and reach the embedded reinforcement (Anderson et al., 1989; Tritthart, 1989; Beaudoin et al., 1990). In contrast, the bound chloride ions retard the penetration process and contribute to preventing steel corrosion. Nevertheless, the chloride binding capacity is substantially different for various products of HCP, depending on the type of cement, mix proportion, and degree of hydration (Florea and Brouwers, 2012; Ye et al., 2016). The cement hydration products can be divided into four main groups: (i) calcium silicate hydrates (C-S-H), (ii) calcium hydroxide (portlandite), (iii) calcium aluminate monosulphate hydrates (AFm), and (iv) calcium aluminate trisulphate hydrates (AFt). To address the issues regarding the diffusion of chloride ions in reinforced concrete structures, it is critical to

take into account the structure, orientation, and dynamics of water molecules and chloride ions, particularly at the surfaces of HCP products.

The transport of water molecules and chloride ions in HCP products has been investigated using experimental techniques. Yu and Kirkpatrick (2001) studied the mechanisms of chloride sorption to the HCP, including calcium hydroxide, carboaluminate, and calcium silicate hydrate, using NMR experiments. Among the phases considered, it was found that chloride ions have the highest and lowest affinity to calcium hydroxide and calcium silicate hydrate, respectively. Jones et al. (2003) employed magic angle spinning (MAS) NMR spectroscopy to study the chemical environment of the ^{27}Al-bearing phases of HCP. It was revealed that calcium aluminate trisulfate hydrates (AFt) have virtually no capacity to chemically react with chlorides. In contrast, through the exchange of chloride ions with hydroxide ones, calcium aluminate monosulfate hydrates (AFm) are transformed to a new phase called Friedel's salt. Barberon et al. (2005) studied the effect of sodium and chloride ions on the structural chemistry of the HCP. It was observed that sodium ions were not affected by the hydration process, while the ^{27}Al and ^{29}Si spectroscopy confirmed that only the aluminum-rich hydrated phases of cement interact with chlorides. Mesbah et al. (2012) investigated the uptake of chloride ions by the calcium monosulfoaluminate hydrate. The X-ray diffraction patterns revealed that chloride ions have a very slow reaction with calcium monosulfoaluminate hydrate, leading to the formation of various chloride-containing products, such as Kuzel's and Friedel's salt. In separate studies, the structure and dynamics of water molecules in contact with HCP were probed by ^{1}H NMR (Wang et al., 1998; Greener et al., 2000), quasi-elastic neutron scattering (QENS) technique (Bordallo et al., 2006), and proton field cycling relaxometry (PFCR) (Korb et al., 2007). It was found that water molecules in contact with HCP can be classified into three main types of chemically-bound, physically-bound, and unbound (or

free) water molecules. The chemically-bound water molecules refer to the ones that are connected to the HCP by forming chemical bonds. The physically-bound water molecules, on the other hand, are the ones that interact with the surface of the HCP with no chemical bonds. Finally, the unbound water molecules are the ones that are confined within capillary pores with no interactions with the surface of the HCP. Two distinct diffusion processes are detected for water molecules: one due to unbound water molecules with a diffusion coefficient in the range of 10^{-9} m^2/s, and the other attributed to the water molecules confined in the gel's pore spaces with a diffusion coefficient one order of magnitude smaller than the unbound one.

Despite the wealth of information provided by experimental studies, many of the atomic-level interactions between water molecules, aggressive ions, and cement phases have remained poorly understood. This is primarily due to the challenges associated with experimental tests, ranging from preparing pure samples to performing accurate measurements, especially at small length and time scales. Atomistic simulations, however, can offer a promising solution, which not only helps further interpret the experimental test results, but also advances the fundamental knowledge of the structure and dynamics of solid-aqueous interfaces (Vasconcelos et al., 2007; Youssef et al., 2011; Ji et al., 2012; Abdolhosseini Qomi et al., 2014; Hajilar and Shafei 2014, 2015, and 2016a,b; Hajilar et al., 2017; Manzano et al., 2015; Krishnan et al., 2016). A limited number of molecular dynamics (MD) studies are available in the literature to characterize the diffusion of water molecules and chloride ions within the nanopores of HCP. Kalinichev and Kirkpatrick (2002) investigated chloride binding to the surfaces of portlandite, AFt, Friedel's salt, and C-S-H phases. Among the phases studied, it was found that Friedel's salt and C-S-H have the highest and lowest chloride binding capacity, respectively. The structure, dynamics, and energetics of water at the surfaces of C-S-H were explored by Kalinichev et al. (2007). A strong structuring of water

molecules was observed in the channels between the driekette silicate chains and above the (001) surface of C-S-H. This was attributed to the integrated H-bond network between the water and surface sites. In a separate effort, the transport of water and ions in the nanopores of C-S-H and portlandite was studied by Hou and Li (2014a,b) and Hou et al. (2016). The water molecules in the channels were categorized into two types based on the structural and dynamic similarity to the interlayer water molecules that exist in the calcium silicate hydrate gel. It was reported that the chloride ions are mostly repulsed by the negatively-charged surfaces of calcium silicate hydrates, resulting in a low binding capacity. On the other hand, the ion adsorption capacity of calcium hydroxide was found to be relatively high due to the stable Na-Cl connections in the electrolyte solution. More recently, the physical adsorption mechanisms of water molecules, as well as sodium and chloride ions, were investigated at the inner- and outer-sphere distance ranges from the ettringite's surfaces through MD simulations (Hajilar and Shafei, 2018). It was revealed that a logarithmic relation, similar to the Freundlich isotherm, can properly capture the binding capacity in the NaCl concentrations up to 1.5 M.

The atomistic simulations of HCP-liquid interfaces have been limited to C-S-H, AFt, and portlandite to date. However, it is well-known that the AFm phases of HCP are the ones that play the most critical role in binding chloride ions after a chloride attack to reinforced concrete structures (Arya et al., 1990; Suryavanshi et al., 1996; Glasser et al., 1999; Ekolu et al., 2006). The AFm phases have a lamellar double hydroxide (LDH) structure composed of positively charged $[Ca_2Al(OH)_6]^+$ layers and negatively charged $[X.nH_2O]^-$ interlayers, where X is one monovalent anion (e.g., Cl^-, I^-, Br^-, NO_3^-) or half a divalent anion (e.g., SO_4^{2-} and CO_3^{2-}). The most abundant phase of AFm contains divalent sulfate groups in its structure and is called calcium monosulfoaluminate hydrate, which is hereafter referred to as monosulfoaluminate for brevity

(Taylor, 1997; Mesbah et al., 2012). The absence of a holistic atomic-level study on the chloride binding capacity of the AFm phases was the main motivation for the current study to characterize the physical adsorption of water molecules and chloride ions to the basal surfaces of monosulfoaluminate. Furthermore, the LDH structure of monosulfoaluminate provides a unique opportunity to examine the effect of its basal (001) and (00-1) surfaces, which possess opposite charges, on the diffusion of water molecules and chloride ions. In this study, a layer of the aqueous solution with various NaCl concentrations is modeled between the basal surfaces of monosulfoaluminate. Each system is fully equilibrated, and then the trajectories are recorded for further analysis. This is to determine, for the first time, atomic density profiles, adsorption statistics, binding isotherms, planar atomic density distributions, dipolar and HH orientation profiles, radial distributions functions, and self-diffusion coefficients of water molecules and chloride ions adsorbed to the basal surfaces of monosulfoaluminate. The outcome of this study, which is supported by a range of experimental tests, provides an in-depth insight to unravel the molecular origins of water and chloride binding capacity in the AFm phases of HCP.

7.2 Computational Methodology

7.2.1 Structural Models

Monosulfoaluminate has a layered structure derived from calcium hydroxide, with one-third of calcium atoms replaced with aluminum atoms. The water content in monosulfoaluminate ranges from 12 to 18 (Taylor, 1997). The structure of monosulfoaluminate with 18 water molecules in the interlayer space has a natural analogue called kuzelite. The crystalline structure of kuzelite has been fully characterized by Allmann (1977). Kuzelite with the chemical composition of $[Ca_2Al(OH)_6]^+.[0.5SO_4.3H_2O]^-$ has a trigonal unit cell, a space group of $R\bar{3}$, and a density of 2.0 g/cm^3. The main layer of kuzelite consists of the brucite-like $Ca_2Al(OH)_6$ octahedral sheet with a

positive charge, neutralized by the sulfate groups existing in the interlayer. The calcium atoms of the main layer become seven-coordinated after connecting with the two-thirds of the water molecules present in the interlayer. The remaining water molecules together with the sulfate groups make the interlayer disordered. To account for the partial occupancy of sulfate groups in the interlayer, the unit cell is replicated in the *a*-*b* plane and then the sulfate groups at the partial occupancy sites are replaced with water molecules in every other cell. It must be noted that this group of water molecules are not involved in the hydrogen bond network, mainly because the distance between them and their next nearest sulfate oxygen atoms is greater than 4 Å. The extended unit cell of monosulfoaluminate is converted into an orthogonal cell following the procedure described by Hajilar and Shafei (2016a). The orthogonal unit cell of monosulfoaluminate is then repeated in the *x*, *y*, and *z* directions to form a 2×4×1 supercell, which contains 5,088 atoms.

The supercell of monosulfoaluminate is cleaved parallel to the (001) plane at the middle of the interlayer space to create the (001) and (00-1) basal surfaces. The former surface exposes the positively-charged octahedral sheet of $Ca_2Al(OH)_6$, while the latter surface presents the negatively-charged sheet of $0.5SO_4.3H_2O$. To simulate the solid-liquid interface, the basal surfaces of monosulfoaluminate are placed in contact with a vacuum slab of 55 Å thick, which is filled with water molecules and NaCl to form the aqueous layer. The thickness of the aqueous layer is chosen large enough to eliminate the direct influence of one surface on the adsorption of water and ions to the other surface. Moreover, this thickness suitably represents the size of nanopores in cementitious materials (i.e., 50-100 Å) reported in the literature (e.g., Ma and Li, 2013). The dimension of the simulation cell, which is 39.90, 46.07, and 80.59 Å, in the *x*, *y*, and *z* directions, respectively, is fixed during each MD simulation. The vacuum slab is packed with close to 3,400

water molecules, which represent a liquid water density of 1.0 g/cm^3. A total of 6, 12, 30, 61, and 92 sodium and chloride ions are then added to the aqueous layer to produce 0.1, 0.2, 0.5, 1.0, and 1.5 M NaCl solutions, respectively. To avoid biased adsorptions, the added ions are placed randomly at least 15 Å away from the solid substrates. The final simulation cells, which consist of a NaCl aqueous layer sandwiched between the basal surfaces of monosulfoaluminate, contain approximately 15,500 atoms, which are large enough to deliver stable statistical results. Figure 7-1 illustrates the initial configuration of the 0.5 M NaCl solution in contact with the basal surfaces of monosulfoaluminate. All the MD simulations start with a configuration similar to the one shown in this figure.

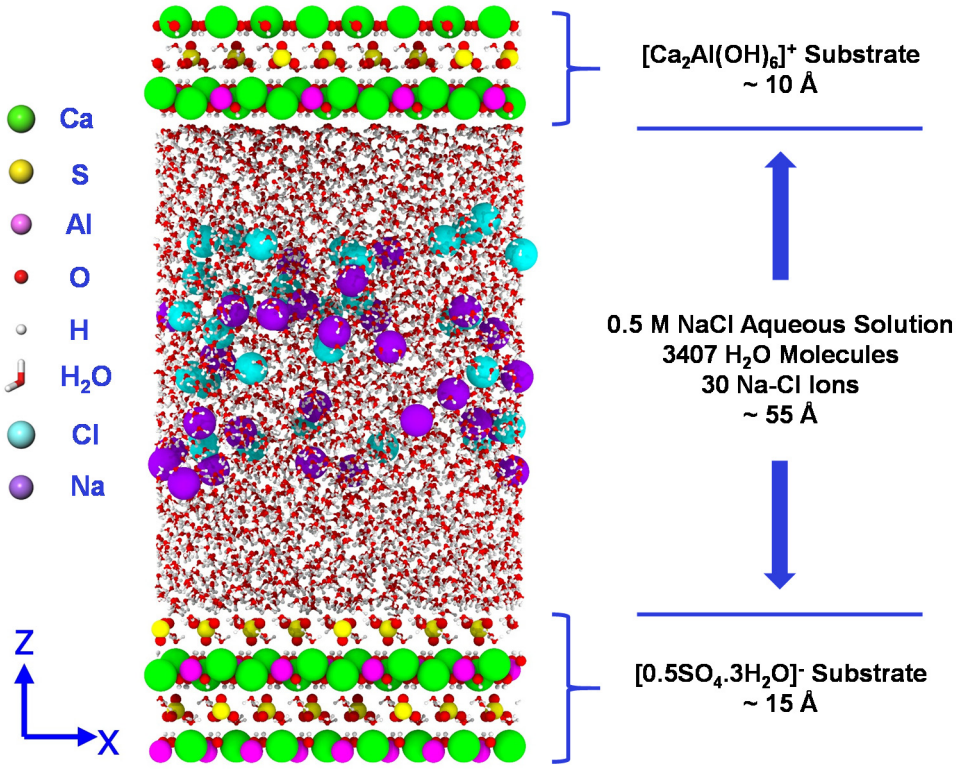

Figure 7-1. Graphical representation of the initial configuration of the 0.5 M NaCl solution in contact with the surfaces of monosulfoaluminate.

7.2.2 MD Simulations

The CLAYFF forcefield developed by Cygan et al. (2004) is employed in this study to model the interactions of the basal surfaces of monosulfoaluminate and the aqueous solutions of NaCl. The CLAYFF forcefield was originally developed to simulate the ion-ion and ion-water interactions of oxide and hydroxide phases. A comprehensive review of the existing literature indicates that CLAYFF has been successfully employed to model the interactions between cementitious phases and aqueous solutions (e.g., Kalinichev and Kirkpatrick, 2002; Kalinichev et al., 2007; Korb et al., 2007; Yoon and Monteiro, 2013; Hou and Li, 2014a,b; Hou et al., 2016; Hajilar and Shafei, 2018). The energy expression in CLAYFF is described with the superposition of two-body and three-body interactions formulated by a summation of bonded (valance) and nonbonded interactions. The nonbonded interactions, i.e., electrostatic and van der Waals energies, are defined using the Coulomb and Lennard-Jones (L-J) 12-6 functionals, respectively. The partial atomic charges in CLAYFF are derived from periodic density functional calculations for the atomic models of various well-characterized minerals. The L-J 12-6 parameters between different atoms are calculated following the arithmetic and geometric mean rule for the distance and energy parameters, respectively. All long-range electrostatic interactions are treated using the Ewald summation method (Ewald, 1921; Allen and Tildesley, 1987) with a precision of 10^{-4} in combination with the direct pairwise interactions calculated within a spherical cutoff of 10 Å. The harmonic bond stretching and angle bending terms are used to describe the bonded interactions. The only bonded interactions are those within water molecules (bond stretch and angle bend), hydroxyls (bond stretch), and sulfate groups (bond stretch and angle bend). The flexible single point charge (SPC) (Berendsen et al., 1981) water model is employed to describe the water molecules and hydroxyl groups. The SPC model, which has been widely used to study the structure

and properties of water molecules and aqueous systems, is based on partial charges centered directly on the oxygen and hydrogen atoms (Berendsen et al., 1987; Teleman et al., 1987; Wallqvist and Teleman, 1991; Smith and Haymet, 1993; Smith and Dang, 1994; van der Spoel et al., 1998; Kalinichev et al., 2000; Vasconcelo et al., 2007).

The LAMMPS (Large-scale Atomic/Molecular Massively Parallel Simulator) program (Plimpton, 1995) installed on a parallel Linux cluster is used to perform the MD simulations. A three-dimensional periodic boundary condition is applied to each of the simulation cells before the MD simulation begins (Allen and Tildesley, 1987). The canonical ensemble (*NVT*), which represents the constant number of atoms (*N*), volume (*V*), and temperature (*T*), is used. The Nosé-Hoover thermostat (Nosé, 1984; Hoover, 1985) is employed to control the temperature at 300 K in the MD simulations with a relaxation time of 100 fs (femtosecond, 10^{-15} s). The equations of motion are integrated using the Verlet's algorithm (Verlet, 1967 and 1968) with a time step of 1.0 fs. The MD simulations contain two stages of equilibration and production. The simulation cell is first equilibrated for 500 ps (picosecond, 10^{-12} s) and the convergence of a variety of thermodynamic parameters (e.g., total energy and its components, temperature, and pressure) is closely monitored and ensured. This is followed by the production stage, in which the simulation cell is equilibrated for 5.0 ns (nanosecond, 10^{-9} s). The production dynamic trajectories are recorded every 500 fs to produce 10,000 atomic configurations, which are large enough to ensure the statistical stability of data analysis. The Open Visualization Tool (OVITO) package is utilized to demonstrate the simulation results (Stukowski, 2010).

7.3 Results and Discussions

7.3.1 Configurational Analysis

Figure 7-2 demonstrates the snapshots of the 0.1, 0.5, and 1.5 M NaCl solutions in contact with the basal surfaces of monosulfoaluminate at different stages of the MD simulations.

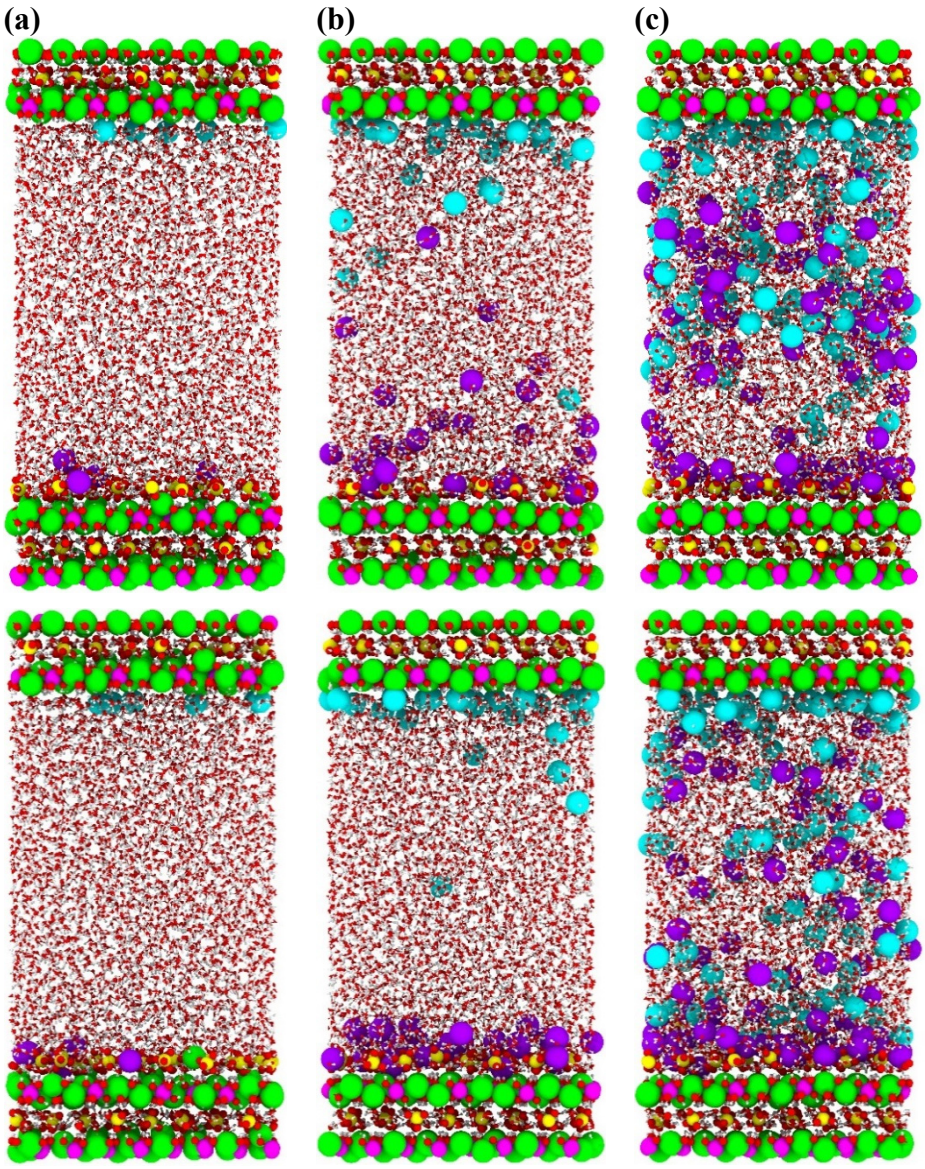

Figure 7-2. Surfaces of monosulfoaluminate equilibrated with (a) 0.1, (b) 0.5, and (c) 1.5 M NaCl solutions for 500 ps (top) and 5.0 ns (bottom). Color code: green (Ca), yellow (S), pink (Al), red (O), white (H), cyan (Cl^-), and purple (Na^+)

After only a few hundreds of picoseconds, the chloride and sodium ions diffuse preferentially towards the $[Ca_2Al(OH)_6]^+$ and $[0.5SO_4.3H_2O]^-$ surfaces, respectively. The distribution pattern of the ions is then found to remain unchanged until the end of the equilibration dynamics. This observation together with a stable potential energy for the system confirms that the state of equilibrium is reached after the initial 500 ps. It is noticed that there is a complete separation between chloride and sodium ions at 0.1 M NaCl, as all the ions migrate to the solid surfaces of opposite charge. This indicates that the 0.1 M NaCl solution is far from the state of saturation. The chloride ions lose part of their hydration shell and reside very close to the $[Ca_2Al(OH)_6]^+$ substrate forming an inner-sphere adsorption. In contrast, there is a layer of water molecules between some of the sodium ions and the $[0.5SO_4.3H_2O]^-$ surface, indicating an outer-sphere adsorption. In this study, the inner-sphere ions are the ones located at a maximum distance of 2.5-3.0 Å from the solid substrate, with no water molecules present in between. On the other hand, the outer-sphere ions are the ones that reside within 3.0 Å beyond the inner-sphere distance range, where the intermediate water molecules separate the ion from the surface.

As the concentration of sodium chloride solution increases, some ions are observed in the aqueous layer, in addition to those adsorbed to the surfaces. The number of such ions is small in 0.5 M NaCl solution. However, with the increase of concentration to 1.5 M NaCl, close to 75% of the ions are found to remain in the bulk solution after 5.0 ns. This underscores that the solution is approaching a saturation state. Furthermore, the presence of ions close to the solid substrates of opposite charge is evident, especially beyond the outer-sphere range. The coadoption of sodium and chloride ions indicates the formation of ion pairing clusters on the basal surfaces of monosulfoaluminate. Nonetheless, consistent with low ionic concentrations, the sodium and chloride ions mainly form outer- and inner-sphere complexes on the $[0.5SO_4.3H_2O]^-$ and

$[Ca_2Al(OH)_6]^+$ substrates, respectively. This highlights the strong and weak affinity of the Cl^- and Na^+ ions to the basal surfaces of monosulfoaluminate, respectively. A detailed investigation of the recorded trajectories, which will be presented in the following sections, further support the observations made during MD simulations.

7.3.2 Atomic Density Profiles

Atomic density profile, $\rho_\alpha(z)$, is defined as the average number of atoms of type α in a slab of thickness Δz located at the distance of z from the solid's surface, normalized by the total volume of the system. The atomic density profiles provide an insight on how the structure of water molecules and aggressive ions is affected by the presence of the solid surfaces. In this study, the density profiles are calculated by averaging the trajectories of each atomic species during the 5.0 ns production stage. Figure 7-3 shows the atomic density profiles for the 0.1, 0.5, and 1.5 M NaCl solutions in equilibrium with the basal surfaces of monosulfoaluminate. The arithmetic average of the z-coordinates of the utmost hydrogen atoms of the surface hydroxyl groups is considered as the surface level. Regions 1, 2, and 3 refer to the solid substrate, inner-sphere, and outer-sphere range, respectively. It is observed that there are distinct peaks in the density profiles of both hydrogen and oxygen atoms of water molecules (hereafter referred to as WatH and WatO, respectively). Such a strongly-ordered structure suggests that the water molecules at the vicinity of both surfaces form hydrogen bonds with the oxygen and hydrogen atoms of each other, in addition with those from solid substrates.

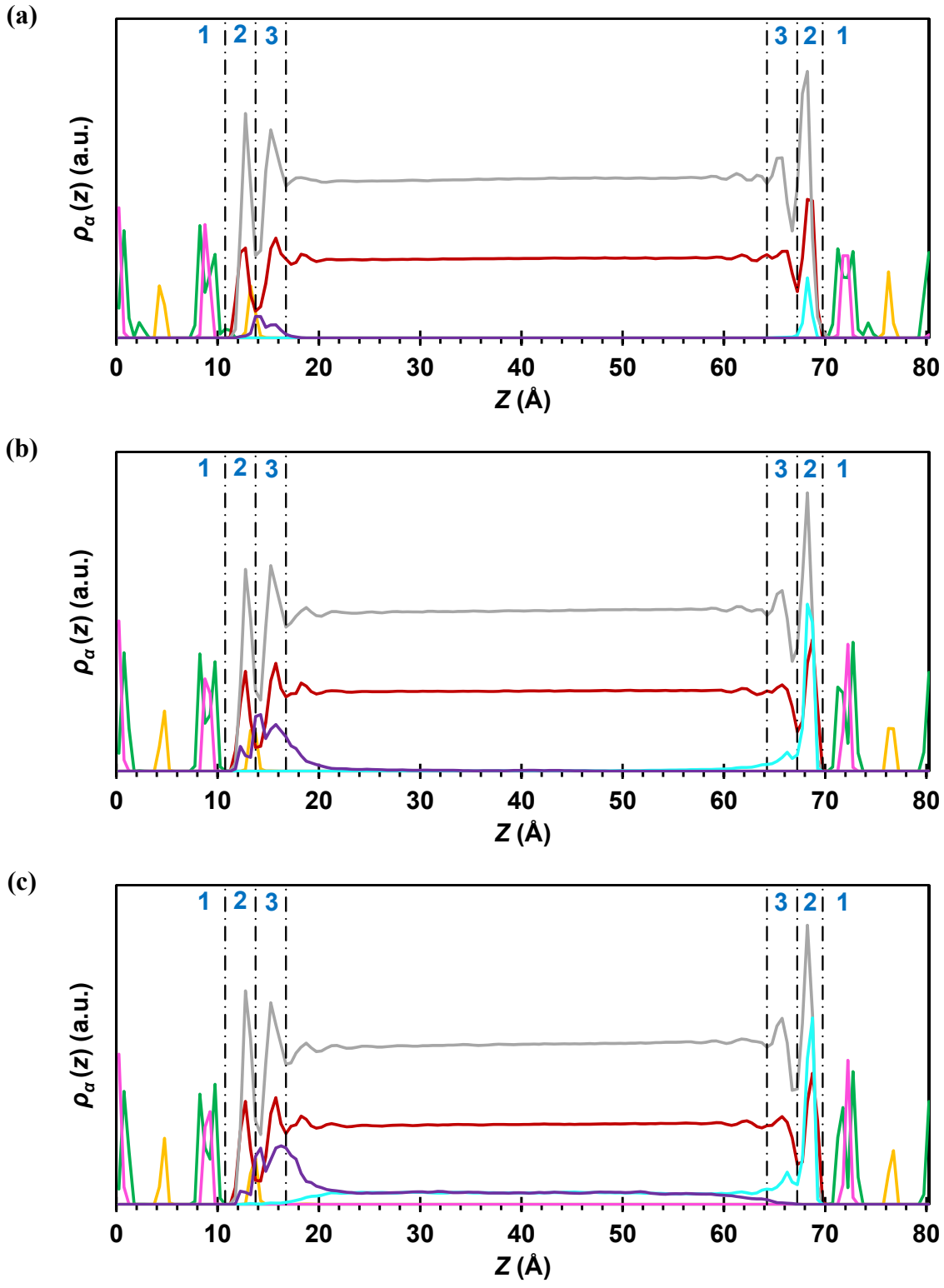

Figure 7-3. Atomic density profiles of the equilibrated (a) 0.1, (b) 0.5, and (c) 1.5 M NaCl solutions in contact with the surfaces of monosulfoaluminate. Regions 1, 2, and 3 designate the solid substrate, inner-sphere, and outer-sphere range, respectively. Color code: green (Ca), yellow (S), pink (Al), red (WatO), gray (WatH), cyan (Cl^-), and purple (Na^+).

There is one distinct peak in each of the inner- and outer-sphere ranges of the density profiles obtained for WatO atoms. The two peaks are, however, separated on the left side of the density profile plots by a pronounced peak for the sulfur atom, reflecting that the water molecules have diffused to the channel spaces between the structural sulfate groups. This also indicates that the structure of water molecules adsorbed to the negatively-charged surface is substantially different than that of the positively-charged surface. It is observed that interactions with the surface can affect the orientation of water molecules up to 10 Å from the surface on each side. The absence of variation in the atomic density profiles of WatO and WatH atoms at the distances beyond 10 Å from each surface reflects the random orientation of water molecules in the bulk water. Since the peaks in the atomic density profiles of WatO and WatH atoms have a similar pattern for different concentrations of NaCl solution, it can be inferred that the overall distribution of water molecules with respect to the basal surfaces of monosulfoaluminate is not greatly influenced by the concentration.

In the positively-charged side (i.e., $[Ca_2Al(OH)_6]^+$ surface), there is a narrow peak in the Cl^- atomic density profiles inside the inner-sphere region. As the concentration increases, a second peak in the Cl^- atomic density profiles emerges in the outer-sphere region. This highlights the fact that there is a relatively strong interaction between the chloride ions and the $[Ca_2Al(OH)_6]^+$ substrate. It must be noted that the long-lived presence of some Na^+ close to the outer-sphere region for the 1.5 M NaCl confirms the ion pairing mechanism. On the other hand, in the negatively-charged side (i.e., $[0.5SO_4.3H_2O]^-$ surface), it is observed that most of the Na^+ ions are at the outer-sphere range. This is supplemented with a small peak in the inner-sphere range, as the ionic strength increases. The density profiles of Na^+ can be understood as a superposition of two very closely spaced peaks in the outer-sphere region. Such a profile underscores the fact that the Na^+

ions have a weak affinity to the basal surfaces of monosulfoaluminate (compared to Cl^- ions). In the atomic density profiles of both Na^+ and Cl^- ions, there is a significant increase in the intensity of the peaks as the NaCl concentration increases from 0.1 to 0.5 M. This is mainly due to the correlation between the ions adsorbed to the surfaces and the ones still present in the solution. The increase, however, is not substantial from 0.5 to 1.5 M, suggesting that even the 0.5 M NaCl solution is not far from the state of saturation.

7.3.3 Adsorption Statistics

To further evaluate the information provided by the atomic density profiles, a statistical analysis of adsorption is performed by integrating the density profiles of water molecules, as well as chloride and sodium ions, in the inner- and outer-sphere regions. The result are summarized in Tables 7-1 to 7-4, where N_t is the total number of water/ion species in the simulation cell; N_{ad} is the number of species within the region of interest; X_{ad} is the fraction of surface-bound species; and ρ is the surface site density ($1/nm^2$). As can be seen in Tables 7-1 and 7-2, the inner-sphere and total (i.e., summation of inner- and outer-sphere) surface-bound fractions of water molecules in the vicinity of the $[Ca_2Al(OH)_6]^+$ surface are (on average) 50% and 25% larger than those in the vicinity of the $[0.5SO_4.3H_2O]^-$ surface, respectively. This highlights that the positively-charged substrate has a higher water binding capacity compared to the negatively-charged substrate. Furthermore, it is observed that as the ionic strength increases from 0.1 M to 1.5 M NaCl, the adsorption site density decreases. This can be attributed to the fact that the Na^+ and Cl^- ions replace some of the water molecules at the basal surfaces of monosulfoaluminate.

Table 7-1. Adsorption statistics calculated from the atomic density profiles of water molecules in contact with $[0.5SO_4.3H_2O]^-$ substrate.

		Inner-Sphere			Total Surface-Bound		
	N_t	N_{ad}	X_{ad} (%)	ρ (nm^{-2})	N_{ad}	X_{ad} (%)	ρ (nm^{-2})
0.1 M	3407	106.33	3.12	5.79	270.56	7.94	14.72
0.2 M	3407	110.27	3.24	6.00	275.39	8.08	14.98
0.5 M	3407	98.44	2.89	5.36	259.15	7.61	14.10
1.0 M	3407	97.53	2.86	5.31	256.29	7.52	13.94
1.5 M	3407	101.94	2.99	5.55	259.29	7.61	14.11

Table 7-2. Adsorption statistics calculated from the atomic density profiles of water molecules in contact with $[Ca_2Al(OH)_6]^+$ substrate.

		Inner-Sphere			Total Surface-Bound		
	N_t	N_{ad}	X_{ad} (%)	ρ (nm^{-2})	N_{ad}	X_{ad} (%)	ρ (nm^{-2})
0.1 M	3407	161.89	4.75	8.81	342.87	10.06	18.65
0.2 M	3407	156.23	4.59	8.50	338.49	9.94	18.42
0.5 M	3407	147.37	4.33	8.02	325.28	9.55	17.70
1.0 M	3407	146.34	4.30	7.96	323.75	9.50	17.61
1.5 M	3407	150.40	4.41	8.18	329.43	9.67	17.92

For 0.1 M NaCl, a mean of 5.80 and 5.99 chloride ions are found in the inner- and inner- plus outer-sphere regions, respectively, while a mean of 1.72 and 5.78 sodium ions are located in the same regions (Tables 7-3 and 7-4). This is in agreement with the density profiles obtained for Cl^- and Na^+ ions in the inner- and outer-sphere regions. The fact that the adsorption site density of Cl^- is higher than that of Na^+ for all the NaCl concentrations indicates that the chloride ions have a higher affinity to the monosulfoaluminate compared to the sodium ions. Moreover, it is observed that as the ionic strength increases from 0.2 to 1.0 M NaCl, the fraction of the total surface-bound Cl^- and Na^+ decreases by 51% and 57%, respectively, indicating that some ions reside in the bulk solution for the entire duration of simulation. While the fraction of the total surface-bound ions decreases with increasing the solution concentration, the surface site density of the chloride and sodium ions show an increasing trend. This is in complete agreement with the binding isotherm and ^{35}Cl NMR relaxation studies performed by Yu and Kirkpatrick (2001) on the other suspensions

of HCP. If the NaCl concentration is further increased from 1.0 to 1.5 M, the adsorption site density remains almost unchanged, underscoring that the state of saturation has been reached.

Table 7-3. Adsorption statistics calculated from the atomic density profiles of chloride ions in contact with $[Ca_2Al(OH)_6]^+$ substrate.

		Inner-Sphere			Total Surface-Bound		
	N_t	N_{ad}	X_{ad} (%)	ρ (nm^{-2})	N_{ad}	X_{ad} (%)	ρ (nm^{-2})
0.1 M	6	5.80	96.72	0.32	5.99	99.86	0.33
0.2 M	12	11.55	96.26	0.63	11.98	99.84	0.65
0.5 M	30	21.71	72.35	1.18	25.74	85.80	1.40
1.0 M	61	23.24	38.10	1.26	29.46	48.30	1.60
1.5 M	92	23.21	25.23	1.26	30.43	33.08	1.66

Table 7-4. Adsorption statistics calculated from the atomic density profiles of sodium ions in contact with $[0.5SO_4.3H_2O]^-$ substrate.

		Inner-Sphere			Total Surface-Bound		
	N_t	N_{ad}	X_{ad} (%)	ρ (nm^{-2})	N_{ad}	X_{ad} (%)	ρ (nm^{-2})
0.1 M	6	1.72	28.70	0.09	5.78	96.26	0.31
0.2 M	12	4.36	36.31	0.24	11.11	92.59	0.60
0.5 M	30	6.43	21.43	0.35	21.01	70.03	1.14
1.0 M	61	5.75	9.43	0.31	21.67	35.53	1.18
1.5 M	92	4.84	5.26	0.26	22.46	24.42	1.22

To evaluate the binding capacity of monosulfoaluminate, the binding isotherms for the inner-sphere and total surface-bound chloride ions are determined (Figure 7-4). Binding isotherm is commonly referred to the relationship between the concentration of free and bound ions at a given temperature. The binding isotherms obtained from MD simulations are compared with those determined from experimental tests. Hirao et al. (2005) performed a set of chloride sorption tests on samples with a mixing ratio of 10 cm^3 NaCl solution and 1.0 g of AFm at 20 °C for 2 days. In a separate effort, Yoon (2010) conducted adsorption-reaction tests on a synthesized AFm added to chloride solutions with various concentrations for 10 days at 20 °C. It was found that the Freundlich and Langmuir isotherms fit well the experimental test data obtained from Hirao et al. (2005) and Yoon (2010), respectively. The Langmuir isotherm assumes that all the adsorption sites are occupied at high concentrations (Sergi et al., 1992), while the Freundlich isotherm suggests

that monolayer adsorption occurs at low concentrations (Luping and Nilsson, 1993). While there is an insignificant difference between the two isotherms at low ionic strengths (up to 1.0 M), the Langmuir isotherm matches the trend extracted from the MD simulation results beyond 1.0 M.

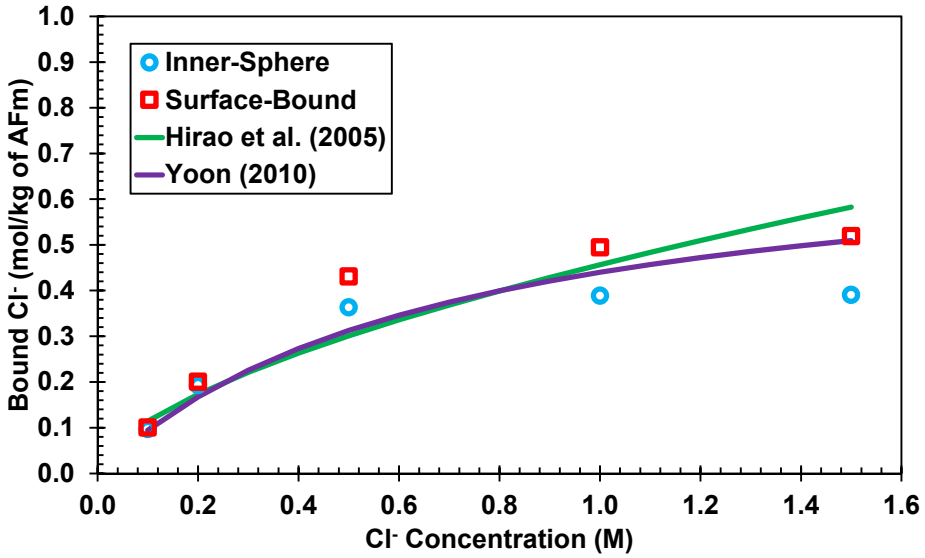

Figure 7-4. Chloride binding isotherm calculated by MD simulations in comparison with the empirical models proposed based on the experimental test results.

7.3.4 Water Orientation Profiles

The angular distributions, θ_d and θ_{hh}, are used to describe the orientation of water molecules with respect to the solid surfaces. The former refers to the angle between the surface's normal direction [001] and the water dipole vector (v_d), while the latter measures the angle between the surface's normal vector and the vector passing from one hydrogen atom to the other in the same water molecule (v_{hh}). These two angles provide detailed information about the structure of water molecules adsorbed to the surfaces of monosulfoaluminate. The angular distributions are calculated for the water molecules at various distances from the $[0.5SO_4.3H_2O]^-$ and $[Ca_2Al(OH)_6]^+$ surfaces (Figures 7-5 and 7-6). Layers 1-4 are each 1 Å thick, corresponding to the first four peaks observed in the density profiles of WatO (shown in Figure 7-2). While the orientation profiles of water molecules for 1.5 M NaCl solution are presented, the angular

distributions extracted for various ionic strengths are found to be similar, indicating that the structure of water molecules is not significantly influenced by the solution's concentration.

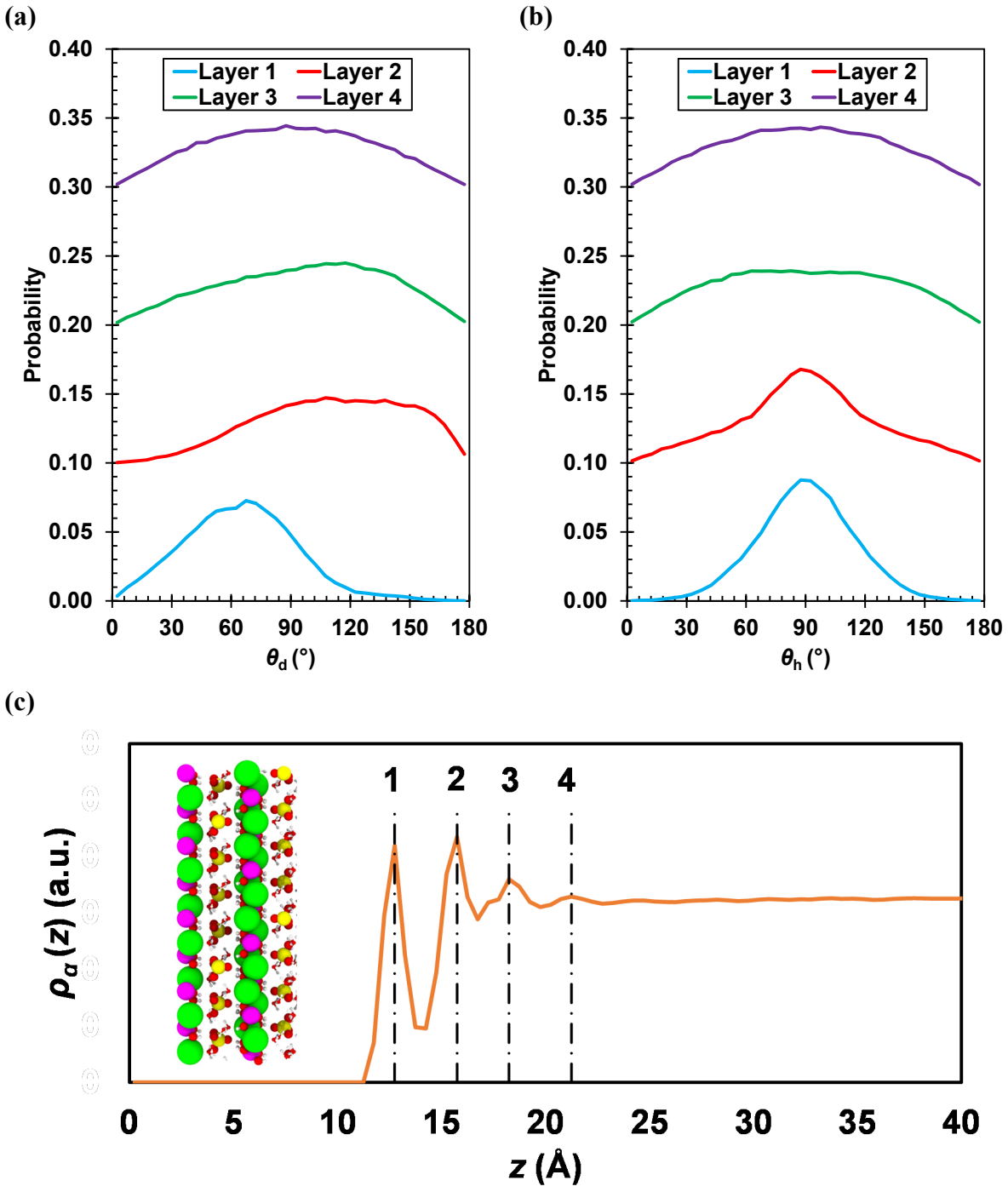

Figure 7-5. Water orientation profiles: (a) dipole and (b) HH angle distribution of water molecules in contact with the $[0.5SO_4.3H_2O]^-$ surface, (c) the atomic density profile of WatO.

At the $[0.5SO_4.3H_2O]^-$ surface, the adsorbed water molecules are observed to have different orientations in the first two layers. The water molecules at the first layer are predominantly oriented with $\theta_d \sim 67.5°$ and $\theta_{hh} \sim 90°$, whereas the water molecules of the second layer are oriented with $\theta_d \sim 107.5\text{-}137.5°$ and $\theta_{hh} \sim 90°$. This highlights that there are two types of water molecules near the negatively-charged surface, depending on the direction of their dipole vectors (i.e., away from and toward the solid surface). For both types of water molecules, the sharp peak in the θ_{hh} distribution indicates that the hydrogen atoms of each water molecule are located almost at the same distance from the surface. The water molecules in the third layer are oriented with $\theta_d \sim 117.5°$ and $\theta_{hh} \sim 52.5\text{-}122.5°$. The dipole angular distributions show that the dipole vectors of water molecules in this layer primarily point toward the surface. However, the broad peak in the HH angular distribution reflects that the H-O bonds are not as ordered as those in the first and second layers. The alternating orientation of water molecules in the first three layers is mainly attributed to the large surface charges. As mentioned earlier, there is a pronounced peak in the density profile of sulfate groups, separating the first two peaks in the density profiles of WatO atoms at the $[0.5SO_4.3H_2O]^-$ surface. The sulfate groups located between the two types of water molecules induce a strong electrostatic field, which aligns the water molecules located in the second and the third layers of water molecules in the orientations with a dipole vector pointing toward the surface. At the fourth layer, the water molecules exhibit a wide dipole and HH angular distributions, suggesting that the water molecules are randomly oriented with respect to the solid surface.

At the $[Ca_2Al(OH)_6]^+$ surface, the water molecules show similar features in the first two layers. The first layer's water molecules exhibit a sharp peak in the θ_d of 27.5°. The dipole distribution of the water molecules in the second layer reflects a reduced intensity with the peak shifted to 57.5°. This indicates that the water molecules in the first two layers are oriented with the dipole vectors

pointing away from the surface. This was expected, as the positive charge of the surface attracts the hydrogen atoms of the adsorbed water molecules.

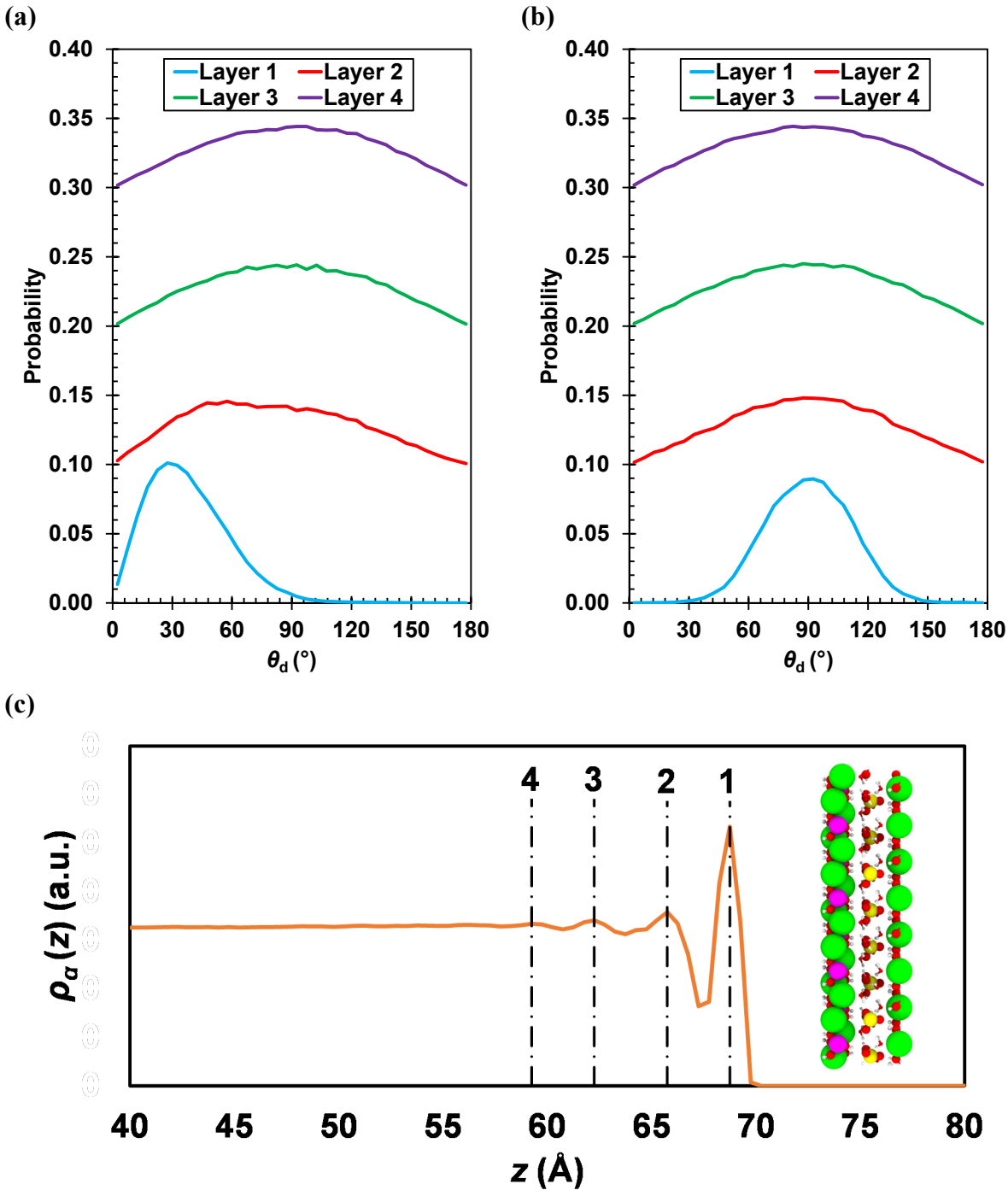

Figure 7-6. Water orientation profiles: (a) dipole and (b) HH angle distribution of water molecules in contact with the $[Ca_2Al(OH)_6]^+$ surface, (c) the atomic density profile of WatO.

It is also observed that there is a sharp peak at 90° in the HH distribution of water molecules in the first layer, while the water molecules of the second layer exhibit a broad HH distribution. This reflects the difference in the orientation of hydroxyl groups in the water molecules of the first two layers. The random orientation of water molecules in the third and fourth layers, which can be confirmed with the wide dipole and HH distributions, indicates that the structure of water molecules is not significantly affected by the solid surface beyond the second layer. This is because the first two water layers shield the electrostatic interactions between the solid surface and water molecules in the upper layers. Thus, a hydrophobic feature is observed in the third and fourth layers, where the water molecules have stronger interactions with each other (through hydrogen bonding) than with the solid surface.

7.3.5 Planar Atomic Density Distributions

To understand the adsorption mechanisms of sodium and chloride ions to the basal surfaces of monosulfoaluminate, the planar atomic density distributions (PADDs) of the Cl^- and Na^+ are extracted from the MD simulations. A PADD is a map of the integrated atomic density of the atom types of interest calculated over the 5.0 ns production time. For various sections selected along the *z* axis of the simulation cell, the atomic trajectories are recorded and then mapped to a grid in the *x*-*y* plane.

Figure 7-7 shows the PADDs of the Cl^- and Na^+ ions that are present within the inner- and outer-sphere distances from the $[Ca_2Al(OH)_6]^+$ surface. For illustration purposes, the PADDs are superimposed on the equilibrium locations of calcium, aluminum, oxygen, and hydrogen atoms that form the calcium aluminate hydrate substrate. The PADD for the 0.1 M NaCl solution indicates that the adsorbed chloride ions are preferentially found in the channels between the calcium atoms and aluminate hydrate hexagons. Consistent with the atomic density profiles, no

sodium ion is found in 0.1 M NaCl solution over the inner- and outer-sphere range distances from the $[Ca_2Al(OH)_6]^+$ surface. At 1.5 M NaCl, however, a few long-lived sodium ions are detected at both inner- and outer-sphere regions. Since the PADD of the sodium ions overlaps with that of the chloride ions, it can be inferred that a few long-lived Na^+-Cl^- clusters are formed on the surface of monosulfoaluminate in equilibration with the 1.5 M NaCl solution.

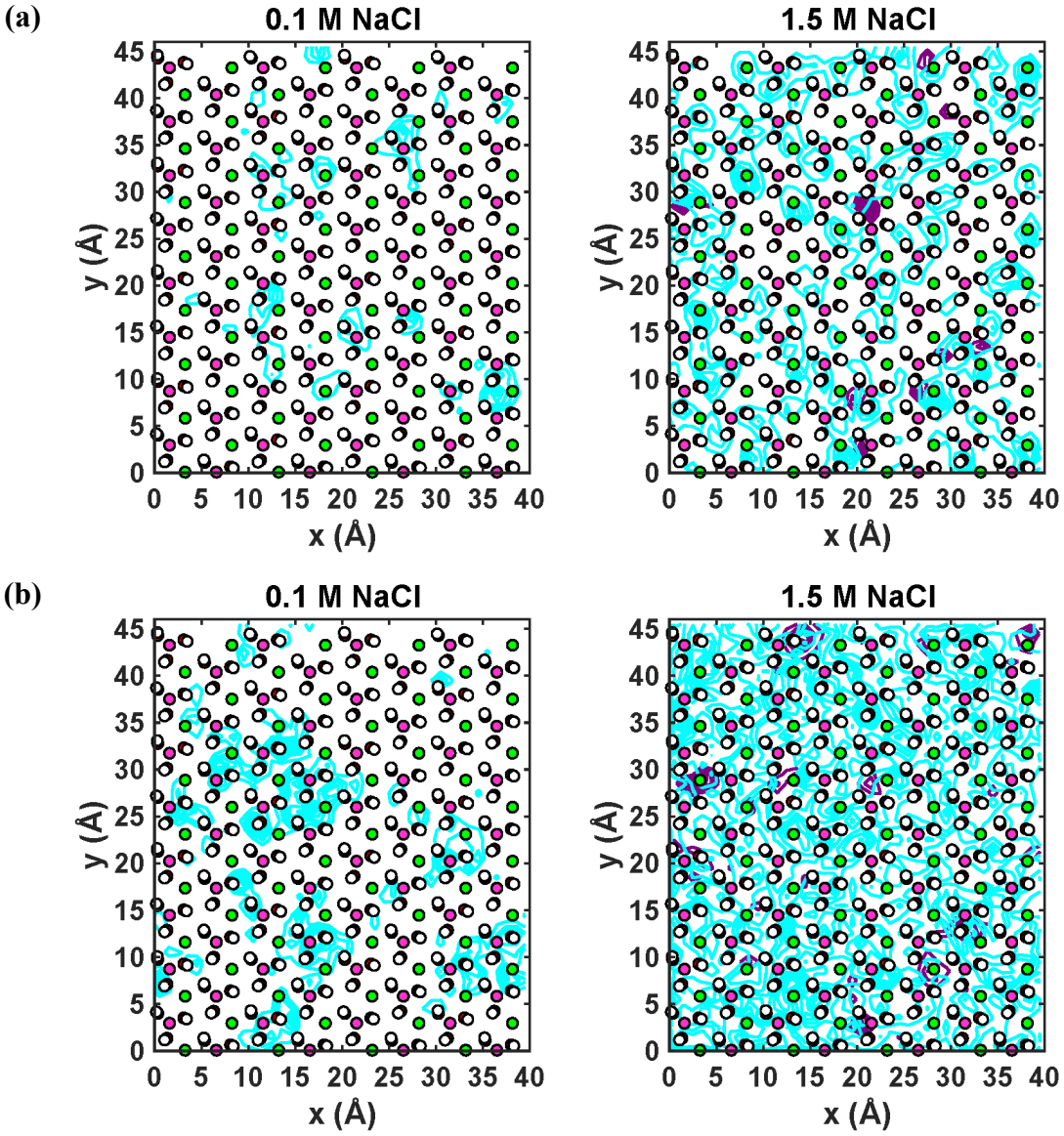

Figure 7-7. Planar atomic density distributions of Cl^- (cyan) and Na^+ (purple) ions within (a) inner-sphere and (b) outer-sphere distances from the $[Ca_2Al(OH)_6]^+$ surface, superimposed on the equilibrium locations of Ca (green), Al (pink), O (red), and H (white) atoms that form the calcium aluminate hydrate substrate.

It is also observed that the PADD of the ions in the outer-sphere range is very scattered, covering almost the entire surface. This indicates that the saturation state is reached. Figure 7-8 shows the PADDs of the Cl^- and Na^+ ions present within the inner- and outer-sphere distances from the $[0.5SO_4.3H_2O]^-$ surface, superimposed on the equilibrium locations of the sulfur and oxygen atoms that are present in the surface layer of sulfate groups. At 0.1 M NaCl, it can be observed that there are a few sodium ions at the inner-sphere distances from the solid surface. These ions are strongly coordinated to either the water molecules between the sulfate groups or to the calcium aluminate hydrates under the sulfate groups. The PADD for the Na^+ ions of the outer-sphere range are found to be more scattered than those of the inner-sphere range. This is expected because of the presence of at least one layer of water molecules between the Na^+ ions and the surface. Nevertheless, it is evident that the outer-sphere Na^+ ions preferentially move over the diagonal sulfate groups with a negligible mobility elsewhere. Such inner- and outer-sphere PADDs confirm that the outer-sphere complex formation is the main adsorption mechanism for the Na^+ ions. Moreover, consistent with the atomic density profiles, no chloride ions are found in the vicinity of the $[0.5SO_4.3H_2O]^-$ surface equilibrated with the 0.1 M NaCl solution. At high ionic strengths, there are a few chloride ions detected in the channels between the sulfate groups. This suggests that the surface-adsorbed ions are strongly coordinated to the surface water molecules and the outmost layer of calcium aluminate hydrates.

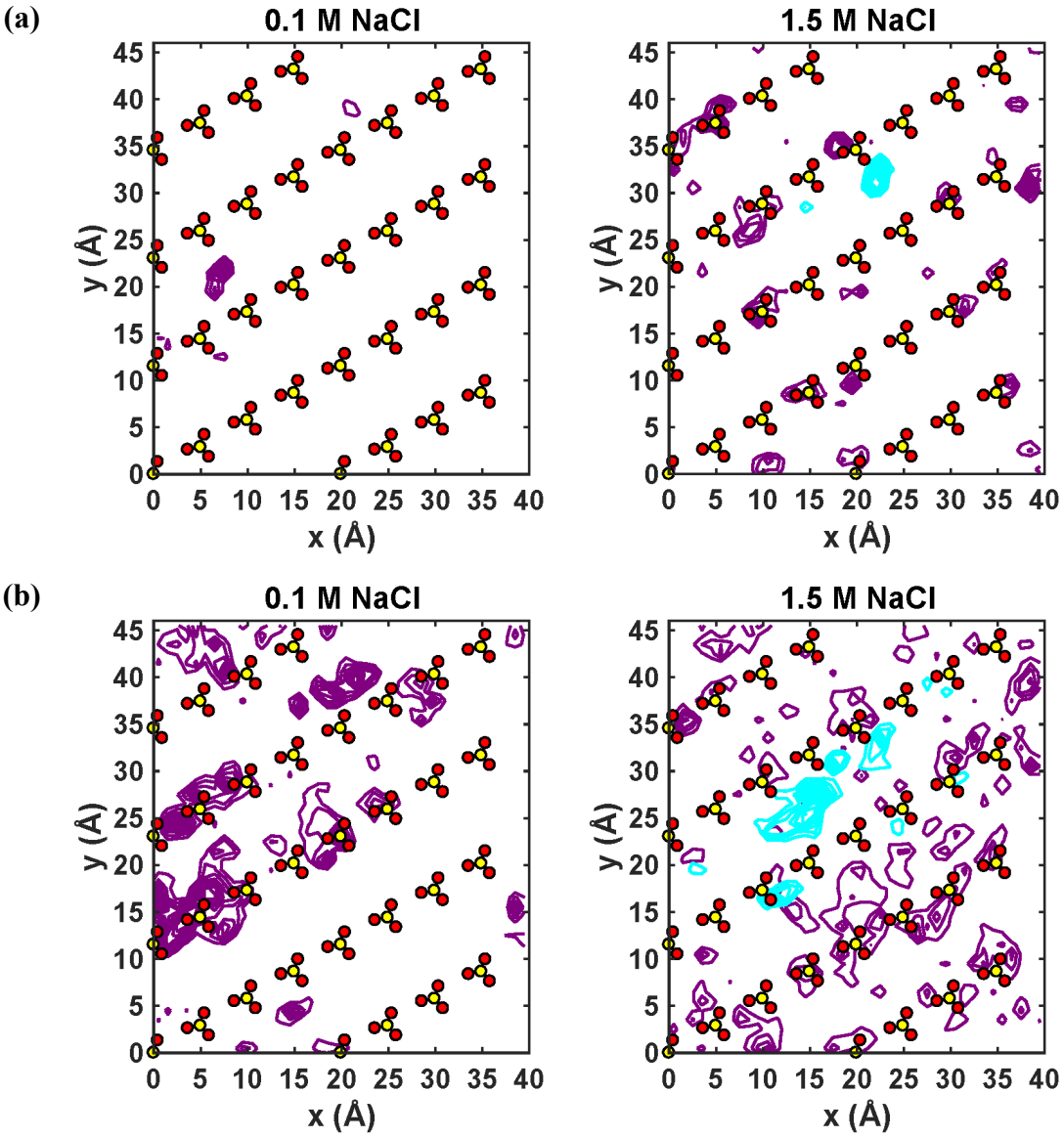

Figure 7-8. Planar atomic density distributions of Cl^- (cyan) and Na^+ (purple) ions within the (a) inner-sphere and (b) outer-sphere distances from the $[0.5SO_4.3H_2O]^-$ surface, superimposed on the equilibrium locations of S (yellow), and O (red) atoms that exist in the surface layer of sulfate groups.

7.3.6 Radial Distribution Functions

Atom-atom radial distribution functions (RDFs) are employed to characterize the structure of adsorption sites in the basal surfaces of monosulfoaluminate. An RDF specifies the probability density function of finding the atoms of type *j* at a distance r_{ij} from the reference atoms of type *i* averaged over time. The number of atoms *j* immediately surrounding a central atom of *i* is often

called coordination number, which is calculated by integrating the RDF function from zero to immediately after the first peak. The plot that presents the coordination numbers with respect to their distance from the central atom of interest is referred to as running coordination number (RCN) plot. Figure 7-9(a) shows the RDFs and RCNs for Cl^- ions with respect to the surrounding WatO atoms obtained from the equilibrated 1.5 M NaCl solution in contact with the basal surfaces of monosulfoaluminate. It is observed that the Cl^--WatO RDFs exhibit a pronounced peak between 2.85 and 3.85 Å centered at 3.25 Å, corresponding to the first hydration shell. While there is a relatively small peak attributed to the second shell for the inner-sphere Cl^--WatO RDF, the intensity of the second peak increases for the outer-sphere and aqueous Cl^--WatO RDFs. This confirms the weak interactions between chloride ions and water molecules in the inner-sphere region. The coordination number of the first hydration shell of Cl^-, determined from the RCNs at a distance of 3.85 Å, is 5.42, 7.48, and 7.50 for the inner-sphere, outer-sphere, and aqueous ions, respectively. This shows that the presence of the $[Ca_2Al(OH)_6]^+$ surface reduces the water molecules of the first hydration shell of the adsorbed chloride ions. The coordination number of chloride ions calculated in this study is comparable with the numbers reported in the previous studies, including 6.0 from the infrared spectroscopic tests (Bergstrom et al., 1991), 5.6 from the Car-Parrinello MD simulations (Bakker, 2008), and 6.9 from the classical MD simulations (Smith and Dang, 1994). It must be noted that the referenced numbers were obtained for the sodium chloride solutions without the presence of monosulfoaluminate. Moreover, it is evident that the coordination numbers, as well as characteristic distances and intensities corresponding to the outer-sphere Cl^--WatO, are very similar to those obtained for the aqueous chloride ions. This highlights the fact that the chloride ions are predominantly adsorbed within the inner-sphere range distances

from the surface of monosulfoaluminate. This is fully supported with the findings from the simulation snapshots, atomic density profiles, and adsorption statistics.

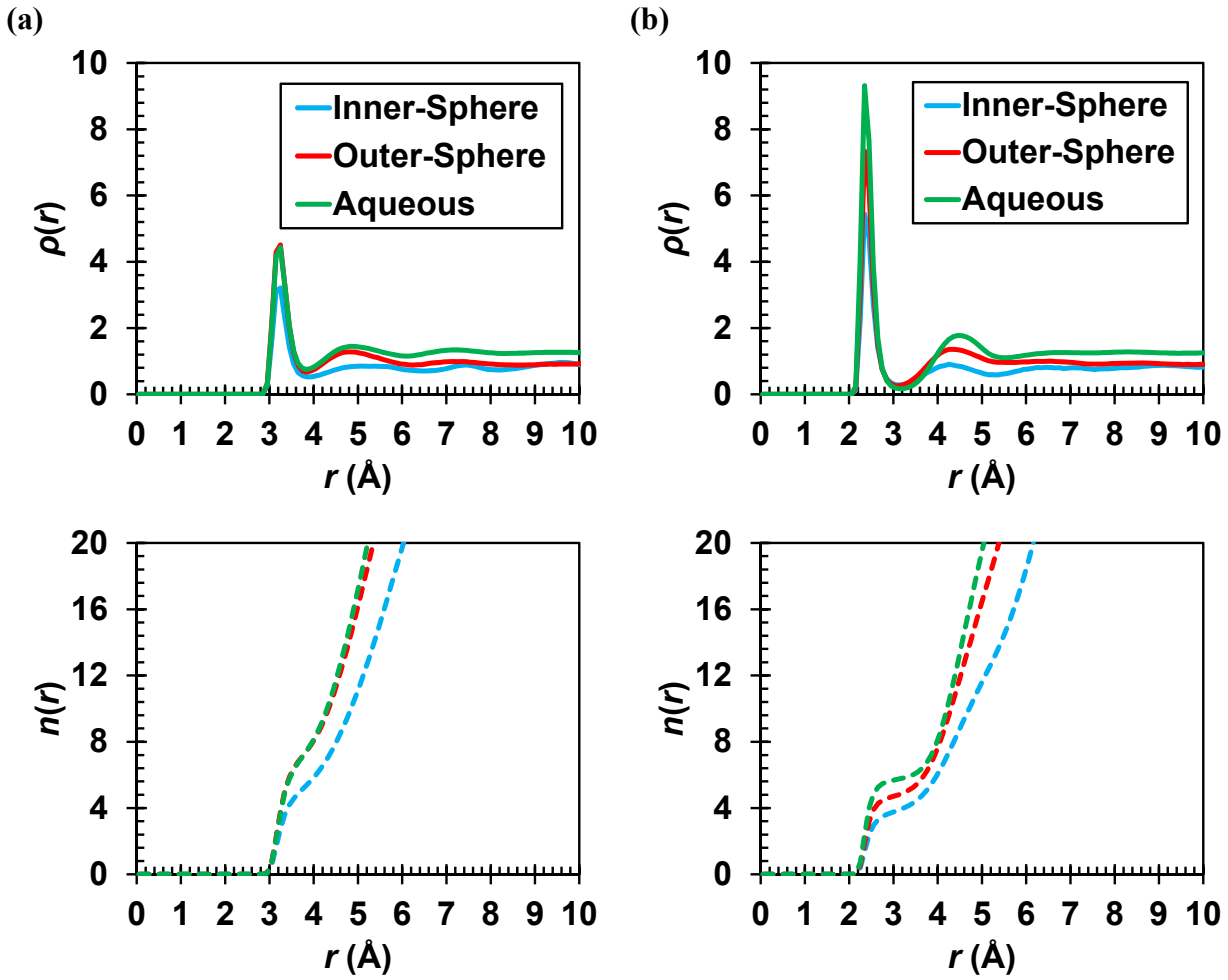

Figure 7-9. Radial distribution functions (solid lines) and running coordination numbers (dash lines) of (a) Cl^--WatO and (b) Na^+-WatO calculated for 1.5 M NaCl solution in equilibrium with the $[Ca_2Al(OH)_6]^+$ and $[0.5SO_4.3H_2O]^-$ surface of monosulfoaluminate, respectively.

In the Na^+-WatO RDFs shown in Figure 7-9(b), the first peak is located at 2.35 Å, consistent for the adsorbed and aqueous ions. This indicates that the interatomic distance between the sodium ions and water molecules is not dependent on their distance to the $[0.5SO_4.3H_2O]^-$ surface. The coordination number associated with the first hydration shell for the inner-sphere, outer-sphere, and aqueous sodium ions is 3.81, 4.75, and 5.71, respectively. There is also a distinct peak located

at 4.30 and 4.45 Å in the RDFs of the adsorbed and aqueous sodium ions, respectively, which correspond to the second hydration shell. The coordination number of 5.71 and the bond length of 2.35 Å for the aqueous sodium ions are in a complete agreement with those predicted by Smith and Dang (1994). Smith and Dang (1994) performed classical MD simulations of NaCl in a polarizable water and found that sodium ions are surrounded by 5.80 water molecules with a Na^+-WatO bond length of 2.33 Å at 25 °C.

Figure 7-10(a) shows the RDFs of the inner-sphere chloride ions and the main structural elements of the $[Ca_2Al(OH)_6]^+$ surface of monosulfoaluminate. As expected, the Cl^--Al, Cl^--Ca, and Cl^--Ho RDFs have several peaks within a large distance from the surface due to the crystalline structure of the solid substrate. The first peaks in the Cl^--Al and Cl^--Ca RDFs correspond to 2.78 aluminum and 0.63 calcium atoms distanced 4.95 and 2.75 Å from the chloride ions, respectively. Furthermore, there are 1.57 and 5.40 hydrogen atoms from the hydroxyl groups captured from the first and second peak in the Cl^--Ho RDF, respectively. This is consistent with the inner-sphere adsorption of chloride ions in the channels between the calcium atoms and the aluminum hexagonal lattices with hydroxyl groups sticking out. Figure 7-10(b) illustrates the RDFs of the outer-sphere sodium ions and the main structural elements of the $[0.5SO_4.3H_2O]^-$ surface of monosulfoaluminate. The first peaks in the Na^+-Os and Na^+-S RDFs correspond to 1.11 oxygen and 0.26 sulfur atoms from the sulfate groups distanced 2.35 and 3.55 Å from the sodium ions, respectively. On the other hand, the Na^+-Oh RDF is almost flat with a low-intensity peak at 4.55 Å from the sodium ions. The coordination number of close to 1.0 captured from the Na^+-Os RDF and the large interatomic distance between the outer-sphere Na^+ and Oh atoms are both consistent with the observation that Na^+ remains directly above the Os atoms of the sulfate groups present in the outer-sphere range (rather than the hydroxyl groups present in the channels between the

calcium aluminate layers). This description confirms the finding that the outer-sphere sodium ions are adsorbed on the negatively-charged sulfate groups of the $[0.5SO_4.3H_2O]^-$ surface.

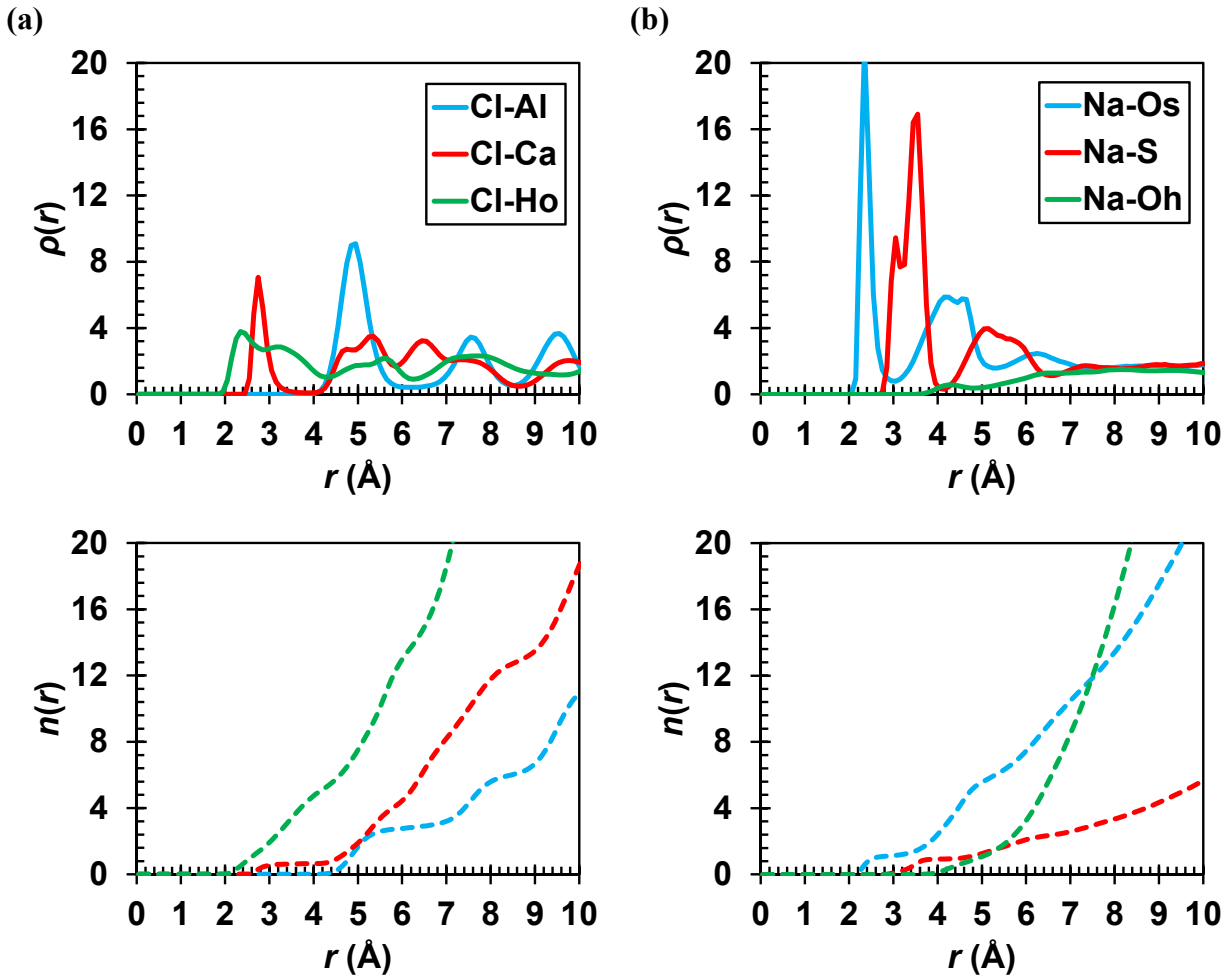

Figure 7-10. Radial distribution functions (solid lines) and running coordination numbers (dash lines) of (a) inner-sphere chloride ions and the elements of the $[Ca_2Al(OH)_6]^+$ surface, and (b) outer-sphere sodium ions and the elements of the $[0.5SO_4.3H_2O]^-$ surface, both calculated for 1.5 M NaCl solution.

7.3.7 Self-Diffusion Coefficients

To characterize the dynamic properties of water molecules, as well as sodium and chloride ions, in contact with the basal surfaces of monosulfoaluminate, their self-diffusion coefficients are determined. The self-diffusion coefficients of various species are estimated following the procedure described in Ngouana and Kalinichev (2014), in which the quasi-linear part of the mean

square displacement (MSD) over time is divided into four segments and the arithmetic average of their slopes is calculated to determine the self-diffusion coefficient.

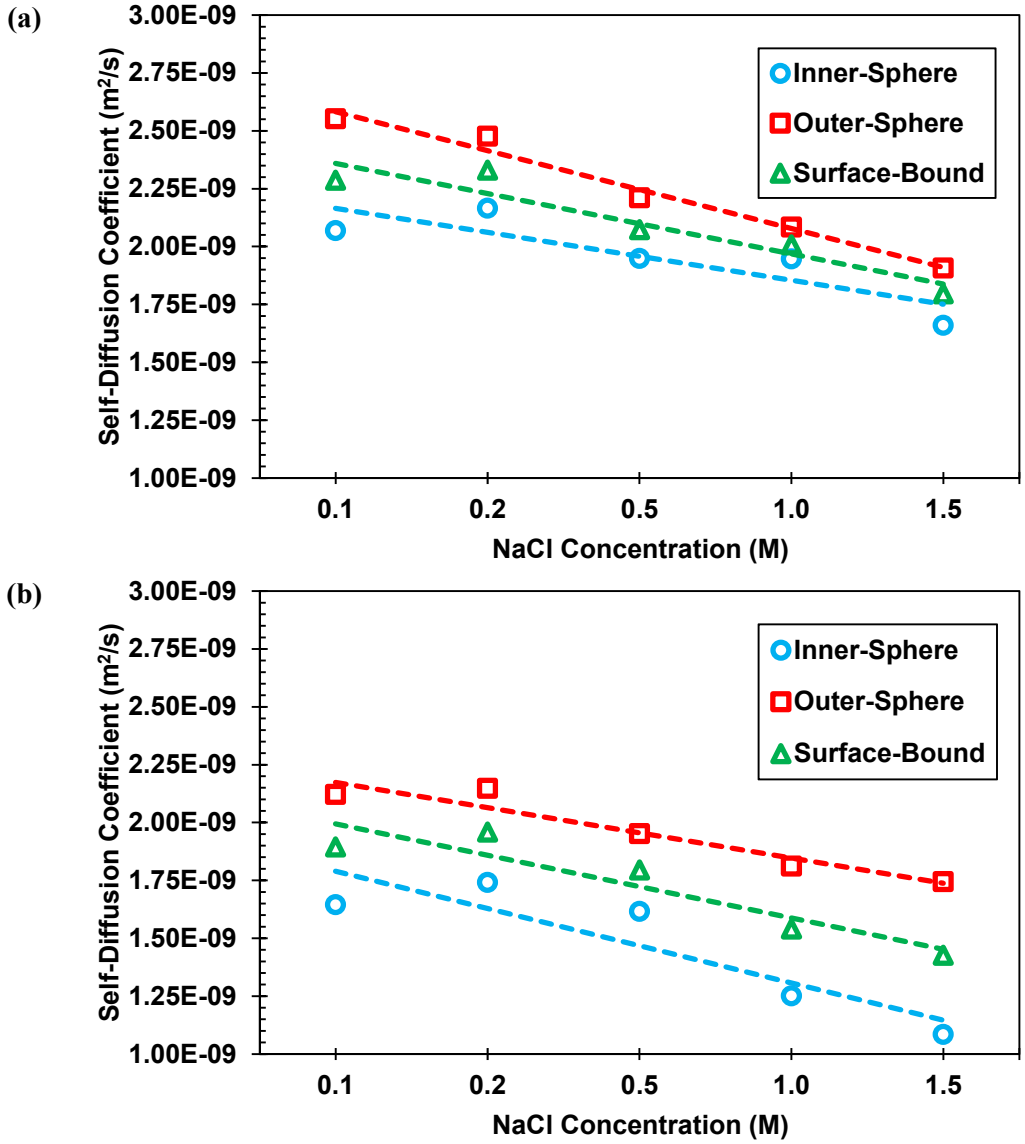

Figure 7-11. Self-diffusion coefficients as a function of NaCl concentration for the inner-sphere, outer-sphere, and total surface-bound water molecules in contact with (a) $[Ca_2Al(OH)_6]^+$ and (b) $[0.5SO_4.3H_2O]^-$ surface.

It is seen in Figure 7-11 that as the NaCl concentration increases from 0.1 to 1.5 M, the self-diffusion coefficients of water molecules decrease. This can be attributed to the low diffusivity of ions in the system, which decelerates the mobility of neighboring water molecules. It can be observed that the water molecules in the inner-sphere range of the $[Ca_2Al(OH)_6]^+$ surface are

almost 1.5 times more mobile than those in the same range of the $[0.5SO_4.3H_2O]^-$ surface. This is due to the formation of additional H-bond interactions, originating from the presence of the sulfate groups, which lower the mobility of the water molecules on the $[0.5SO_4.3H_2O]^-$ surface. Nonetheless, the mobility of water molecules in the outer-sphere range of the negatively-charged surface is approximately similar to that of molecules residing at the same distances from the $[Ca_2Al(OH)_6]^+$ substrate. This is expected, as the water molecules adsorbed to each surface shield the interactions between the water molecules of upper layers and the solid surface. Thus, a substantial increase in the self-diffusion coefficient of the water molecules in the outer-sphere range is recorded.

Table 7-5 summarizes the self-diffusion coefficients calculated for the 1.5 M NaCl solution species adsorbed to the basal surfaces of monosulfoaluminate. The diffusion coefficients are reported for the inner- and outer-sphere, as well as the total surface-bound species. On average, the self-diffusion coefficient for the inner-sphere, outer-sphere, and total surface-bound water molecules fall in the range of 1.09-1.66 $\times 10^{-9}$, 1.75-1.91 $\times 10^{-9}$, and 1.43-1.80 $\times 10^{-9}$ m^2/s, respectively. This is consistent with the range of 0.6-2.0 $\times 10^{-9}$ m^2/s obtained from the QENS experiments on the samples of HCP (Bordallo et al., 2006). It is observed that the self-diffusion coefficients of the chloride and sodium ions that reside in the outer-sphere range are 83% and 47% larger than those of present in the inner-sphere range. While with increasing the distance from the solid surface, an increase in the self-diffusion coefficient is anticipated, a larger increase in the mobility of chloride ions than that of sodium ions can be justified based on the fact that the inner- and outer-sphere complex formation are the governing adsorption mechanisms for the Cl^- and Na^+ ions, respectively.

Table 7-5. Self-diffusion coefficients of 1.5 M NaCl solution species in contact with the basal surfaces of monosulfoaluminate.

Self-diffusion coefficient	$[Ca_2Al(OH)_6]^+$		$[0.5SO_4.3H_2O]^-$	
	H_2O	Cl^-	H_2O	Na^+
Inner-Sphere ($\times 10^{-9}$ m^2/s)	1.66	0.58	1.09	0.39
Outer-Sphere ($\times 10^{-9}$ m^2/s)	1.91	1.06	1.75	0.57
Total Surface-Bound ($\times 10^{-9}$ m^2/s)	1.80	0.69	1.43	0.56

7.4 Conclusions

A set of MD simulations were performed to unravel, for the first time, the atomistic origins of the diffusion of water molecules and aggressive ions at the interfaces of monosulfoaluminate. As for water molecules, it was found that their mobility substantially decreases as the concentration of sodium chloride increases in the solution. In addition, it was observed that water molecules near the basal surfaces of monosulfoaluminate are strongly oriented. This was explored in depth through comprehensive dipole and HH angular distribution analyses, which were performed at different distances from both negatively- and positively-charged surface of monosulfoaluminate. At the $[0.5SO_4.3H_2O]^-$ substrate, the first layer of water molecules closest to the surface were oriented with a dipole vector pointing away from the surface. The orientation of water molecules, however, was found to be reversed in the layers farther from the surface. This was primarily attributed to the presence of a layer of sulfate groups between the first and second layer of water molecules, inducing a strong electrostatic field, which attracts the hydrogen atoms of the water molecules from both sides. In contrast, the layers of water molecules adsorbed to the $[Ca_2Al(OH)_6]^+$ substrate were found to be all oriented with a dipole vector pointing away from the surface as expected. As for chloride and sodium ions, their structures and dynamics were found to be significantly influenced by the concentration of sodium chloride solutions. At low ionic strengths, there is a complete separation between the ions, such that the chloride and sodium ions were mostly adsorbed to the $[0.5SO_4.3H_2O]^-$ and $[Ca_2Al(OH)_6]^+$ surface, respectively. At the high

sodium chloride concentration, however, close to 75% of the ions are located in the bulk solution. Nonetheless, the adsorption statistics obtained from MD simulations was able to confirm and explain the strong chloride binding capacity of monosulfoaluminate reported from the experimental tests. It was inferred that the inner- and outer-sphere complex formation is the main adsorption mechanism for the chloride and sodium ions, respectively. This highlighted the fact that the sodium ions have a weak affinity to the basal surfaces of monosulfoaluminate (compared to the chloride ions). Concerning the dynamics of ions, both sodium and chloride ions were found to have a lower mobility in the inner-sphere range than in the outer-sphere range. It was revealed that the inner-sphere chloride ions were preferentially located in the channels between the calcium and aluminate hydrate groups of the $[Ca_2Al(OH)_6]^+$ surface. The sodium ions, on the other hand, coordinate themselves with one of the oxygen atoms of the sulfate groups.

7.5 Acknowledgments

The feedback and support from Dr. Andrey Kalinichev are gratefully acknowledged. The Extreme Science and Engineering Discovery Environment (XSEDE), which is supported by National Science Foundation grant number ACI-1548562, was used for part of the atomistic simulations conducted in this study.

7.6 References

1- Abdolhosseini Qomi M.J., Bauchy M., Ulm F.-J., and Pellenq R.J.-M., 2014. "*Anomalous composition-dependent dynamics of nanoconfined water in the interlayer of disordered calcium-silicates*". The Journal of Chemical Physics 140: 054515.

2- Alipour A., Shafei B., and Shinozuka M., 2011. "*Performance evaluation of deteriorating highway bridges located in high seismic areas*". Journal of Bridge Engineering 16(5): 597-611.

3- Alipour A., Shafei B., and Shinozuka M., 2013. "*Capacity loss evaluation of reinforced concrete bridges located in extreme chloride-laden environments*". Structure and Infrastructure Engineering 9(1): 8-27.

4- Allen M., and Tildesley D., 1987. "*Computer simulation of liquids*". Oxford University Press, New York.

5- Allmann R., 1997. "*Refinement of the hybrid layer structure* $[Ca_2Al(OH)_6]^+.[1/2SO_4.3H_2O]^-$ ". Neus Jahrbuch fur Mineralogie Monatshefte 4: 136-144.

6- Anderson K., Allard B., Bengtsson M., and Magnusson B., 1989. "*Chemical composition of cement pore solutions*". Cement and Concrete Research 19: 327-332.

7- Arya C., Buenfeld N.R., and Newman J.B., 1990. "*Factors influencing chloride binding in concrete".* Cement and Concrete Research 20(2): 291-300.

8- Bakker H.J., 2008. "*Structural dynamics of aqueous salt solutions*". Chemistry Reviews 108: 1456-1473.

9- Barberon F., Barpghel-Bouny V., Zanni H., and Bresson B., 2005. "*Interactions between chloride and cement-paste materials".* Magnetic Resonance Imaging 23: 267-272.

10- Beaudoin J.J., Ramachandran V.S., and Feldman R.F., 1990. "*Interaction of chloride and C-S-H*". Cement and Concrete Research 20(6): 875-883.

11- Berendsen H.J.C., Postma J.P.M., van Gunsteren W.F. and Hermans J., 1981. "*Interaction models for water in relation to protein hydration*". The Jerusalem Symposia on Quantum Chemistry and Biochemistry 14: 331-342.

12- Berendsen H.J.C., Grigera J.R., and Straatsma T.P., 1987. "The missing term in effective pair potentials". The Journal of Physical Chemistry 91(24): 6269-6271.

13- Bergstrom P.A., Lindgren J., and Kristiansson O., 1991. "*An IR study of the hydration of ClO_4^-, NO_3^-, I^-, Br^-, Cl^-, and SO_4^{2-} anions in aqueous solution*". Journal of Physical Chemistry 95: 8575-8580.

14- Bordallo H.N., Aldridge L.P., and Desmedt A., 2006. "*Water dynamics in hardened ordinary Portland cement paste or concrete: From quasielastic neutron scattering*". Journal of Physical Chemistry B 110: 17966-17976.

15- Cygan R.T., Liang J.J., and Kalinichev A.G., 2004. "*Molecular models of hydroxide, oxyhydroxide, and clay phases and the development of a general force field*". The Journal of Physical Chemistry B 108(4): 1255-1266.

16- Ekolu S.O., Thomas M.D.A., and Hootan R.D., 2006. "*Pessimum effect of externally applied chlorides on expansion due to delayed ettringite formation: Proposed mechanism*". Cement and Concrete Research 36: 688-696.

17- Ewald P.P., 1921. "*Die Berechnung optischer und elektrostatischer Gitterpotentiale"*. Annalen der Physik 64: 253.

18- Florea M.V.A., and Brouwers H.J.H., 2012. "*Chloride binding related to hydration products, Part I: Ordinary Portland Cement*". Cement and Concrete Research 42: 282-290.

19- Glasser F.P., Kindness A., and Stronach S.A., 1999. "*Stability and solubility relationships in AFm phases Part I. Chloride, sulfate and hydroxide*". Cement and Concrete Research 29: 861-866.

20- Greener J., Peemoeller H., Choi C., Holly R., Reardon E.J., Hansson C.M., and Pintar M.M., 2000. "*Monitoring of hydration of white cement paste with proton NMR spin-spin relaxation*". Journal of the American Ceramic Society 83(3): 623-627.

21- Hajilar S., and Shafei B., 2014. "*Nano-scale characterization of elastic properties of AFt and AFm phases of hydrated cement paste*". Proceedings of the European Conference on Computational Modeling of Concrete Structures (EURO-C) 1: 299-306.

22- Hajilar S., and Shafei B., 2015. "*Nano-scale investigation of elastic properties of hydrated cement paste constituents using molecular dynamics simulations*". Computational Materials Science 101: 216-226.

23- Hajilar S., and Shafei B., 2016 (a). "*Mechanical failure mechanisms of hydrated products of tricalcium aluminate: A reactive molecular dynamics study*". Materials and Design 90: 165-176.

24- Hajilar S., and Shafei B., 2016 (b). "*Assessment of structural, thermal, and mechanical properties of portlandite through molecular dynamics simulations*". Journal of Solid State Chemistry 244: 164-174.

25- Hajilar S., Shafei B., Cheng T., and Jaramillo-Botero A., 2017. "*Reactive molecular dynamics simulations to understand mechanical response of thaumasite under temperature and strain rate effects*". Journal of Physical Chemistry A 121(24): 4688-4697.

26- Hajilar S., and Shafei B., 2018. "*Atomic-scale investigation of physical adsorption of water molecules and aggressive ions to ettringite's surfaces*". Journal of Colloid and Interface Science 513: 104-116.

27- Hirao H., Yamada K., Takahashi H., and Zibara H., 2005. "*Chloride binding of cement estimated by binding isotherms of hydrates*". Journal of Advanced Concrete Technology 3(1): 77-84.

28- Hoover W.G., 1985. "*Canonical dynamics: Equilibrium phase-space distributions*". Physical Review A 31(3): 1695-1697.

29- Hou D., and Li Z., 2014 (a). "*Molecular dynamics study of water and ions transported during the nanopore calcium silicate phase: Case study of jennite*". Journal of Materials in Civil Engineering 26(5): 930-940.

30- Hou D., and Li Z., 2014 (b). "*Molecular dynamics study of water and ions transport in nano-pore of layered structure: A case study of tobermorite*". Microporous and Mesoporous Materials 195: 9-20.

31- Hou D., Zeyu L., Peng Z., and Qingjun D., 2016. "*Molecular structure and dynamics of an aqueous sodium chloride solution in nano-pores between portlandite surfaces: A molecular dynamics study*". Physical Chemistry Chemical Physics 18: 2059-2069.

32- Ji Q., Pellenq R.J.-M., and van Vliet K.J., 2012. "*Comparison of computational water models for simulation of calcium-silicate-hydrate*". Computational Materials Science 53: 234-240.

33- Jones M.R., Macphee D.E., Chudek J.A., Hunter G., Lannegrand R., Talero R., and Scrimgeour S.N., 2003. "*Studies using ^{27}Al MAS NMR of AF_m and AF_t phases and the formation of Friedel's salt*". Cement and Concrete Research 33: 177-182.

34- Kalinichev A.G., Kirkpatrick R.J., and Cygan R.T., 2000. "*Molecular modeling of the structure and dynamics of the interlayer and surface species of mixed-metal layered hydroxides: Chloride and water in hydrocalumite (Friedel's salt)*". American Mineralogist 85: 1046-1052.

35- Kalinichev A.G., and Kirkpatrick R.J., 2002. "*Molecular dynamics modeling of chloride binding to the surfaces of calcium hydroxide, hydrated calcium aluminate, and calcium silicate phases*". Chemistry of Materials 14: 3539-3549.

36- Kalinichev A.G., Wang J., and Kirkpatrick R.J., 2007. "*Molecular dynamics modeling of the structure, dynamics and energetics of mineral-water interfaces: Application to cement materials*". Cement and Concrete Research 37: 337-347.

37- Korb J.P., McDonald P.J., Monteilhet L., Kalinichev A.G., and Kirkpatrick R.J., 2007. "*Comparison of proton field-cycling relaxometry and molecular dynamics simulations for proton–water surface dynamics in cement-based materials*". Cement and Concrete Research 37: 348-350.

38- Krishnan N.M.A., Wang B., Falzone, G., Pape Y.L., Neithalath N., Pilon L., Bauchy M., and Sant G., 2016. "*Confined water in layered silicates: The origin of anomalous thermal expansion behavior in calcium-silicate-hydrates*". Applied Materials and Interfaces 8(51): 35621–35627.

39- Luping T., and Nilsson L.O., 1993. "*Chloride binding capacity and binding isotherms of OPC pastes and mortars*". Cement and Concrete Research 23(2): 247-253.

40- Ma H., and Li Z., 2013. "*Realistic pore structure of Portland cement paste: experimental study and numerical simulation*". Computers and Concrete 11(4): 317-336.

41- Manzano H., Durgun E., Lopez-Arbeloa I., and Grossman J.C., 2015. "*Insight on tricalcium silicate hydration and dissolution mechanism from molecular simulations*". Applied Materials and Interfaces 7(27): 14726-14733.

42- Mesbah A., Cau-dit-Coumes C., Renaudin G., Frizon F., and Leroux F., 2012. "*Uptake of chloride and carbonate ions by calcium monosulfoaluminate hydrate*". Cement and Concrete Research 42(8): 1157-1165.

43- Ngouana B.F., and Kalinichev A.G., 2014. "*Structural arrangements of isomorphic substitutions in smectites: Molecular simulation of the swelling properties, interlayer*

structure, and dynamics of hydrated Cs-Montmorillonite revisited with new clay models". The Journal of the Physical Chemistry C 118(24): 12758-12773.

44- Nosé S., 1984. "*A unified formulation of the constant temperature molecular dynamics methods*". The Journal of Chemical Physics 81(1): 511-519.

45- Plimpton S., 1995. "*Fast parallel algorithms for short-range molecular dynamics*". Journal of Computational Physics 117(1): 1-19.

46- Sergi G., Yu S.W., and Page C.L., 1992. "*Diffusion of chloride and hydroxyl ions in cementitious materials exposed to a saline environment*". Magazine of Concrete Research 44(158): 63-69.

47- Shafei B., Alipour A., and Shinozuka M., 2012. "*Prediction of corrosion initiation in reinforced concrete members subjected to environmental stressors: A finite-element framework*". Cement and Concrete Research 42: 365-376.

48- Shafei B., Alipour A., and Shinozuka M., 2013. "*A stochastic computational framework to investigate the initial stage of corrosion in reinforced concrete superstructures*". Computer-Aided Civil and Infrastructure Engineering 28: 482-494.

49- Shafei B., and Alipour A., 2015 (a). "*Application of large-scale non-Gaussian stochastic fields for the study of corrosion-induced structural deterioration*". Journal of Engineering Structures 88: 262-276.

50- Shafei B., and Alipour A., 2015 (b). "*Estimation of corrosion initiation time in reinforced concrete bridge columns: How to incorporate spatial and temporal uncertainties*". ASCE Journal of Engineering Mechanics 141(10): 04015037.

51- Smith D.E., and Haymet A.D.J., 1993. "*Simulations of aqueous solutions: the role of flexibility and the treatment of long-range forces*". Fluid Phase Equilibria 88: 79-87.

52- Smith D.E., and Dang L.X., 1994. "*Computer simulations of NaCl association in polarizable water*". The Journal of Chemical Physics 100(5): 3757-3766.

53- Stukowski A., 2010. "*Visualization and analysis of atomistic simulation data with OVITO- the open visualization tool*". Modeling and Simulation in Materials Science and Engineering 18, 015012.

54- Suryavanshi A.K., Scantlebury J.D., and Lyon S.B., 1996. "*Mechanism of Friedel's salt formation in cements rich in tricalcium aluminate".* Cement and Concrete Research 26(5): 717-727.

55- Taylor, H.F.W., 1997. "*Cement Chemistry*". 2nd Edition, Thomas Telford Publishing, London.

56- Teleman O., Jonsson B., and Engstrom S., 1987. "*A molecular dynamics simulation of a water model with intramolecular degrees of freedom*". Journal of Molecular Physics 60(1): 193-203.

57- Tritthart J., 1989. "*Chloride binding in cement II. The influence of the hydroxide concentration in the pore solution of hardened cement paste on chloride binding*". Cement and Concrete Research 19(5): 683-691.

58- Van der Spoel D., van Maaren P.J., and Berendsen H.J.C., 1998. "*A systematic study of water models for molecular simulation: Derivation of water models optimized for use with a reaction field*". The Journal of Chemical Physics 108(24): 10220-10230.

59- Vasconcelos I.F., Bunker B.A., and Cygan R.T., 2007. "*Molecular dynamics modeling of ion adsorption to the basal surfaces of kaolinite".* The Journal of the Physical Chemistry C 111: 6753-6762.

60- Verlet L., 1967. "*Computer "Experiments" on classical fluids. I. Thermodynamical properties of Lennard-Jones molecules*". Physical Review 159(1): 98-103.

61- Verlet L., 1698. "*Computer "Experiments" on classical fluids. II. Equilibrium correlation functions*". Physical Review 165(1): 201-214.

62- Wallqvist A., and Teleman O., 1991. "*Properties of flexible water models*". Journal of Molecular Physics 74(3): 515-533.

63- Wang P.S., Ferguson M.M., Eng G., Bentz D.P., Ferraris C.F., and Clifton J.R., 1998. "*^{1}H nuclear magnetic resonance characterizations of Portland cement: molecular diffusion of water studied by spin relaxation and relaxation time-weighted imaging*". Journal of Materials Science 33: 3065-3071.

64- Ye H., Jin X., Chen W., Fu C., and Jin N., 2016. "*Prediction of chloride binding isotherms for blended cements*". Computers and Concrete 17(5): 655-672.

65- Yoon S., and Monteiro P., 2013. "*Molecular dynamics study of water molecules in interlayer of 14 Å tobermorite*". Journal of Advanced Concrete Technology 11: 180-188.

66- Yoon I.S., 2010. "*Reaction experimental study on chloride binding behavior in cement composition*". 2nd International Symposium on Service Life Design for Infrastructure, Delft, The Netherlands, October 4-6.

67- Youssef M., Pellenq R.J.-M., and Yildiz B., 2011. "*Glassy nature of water in an ultraconfining disordered material: The case of calcium-silicate-hydrate*". Journal of the American Chemical Society 133: 2499-2510.

68- Yu P., and Kirkpatrick R.J., 2001. "*^{35}Cl NMR relaxation study of cement hydrate suspensions*". Cement and Concrete Research 31(10): 1479-1485.

CHAPTER 8: SUMMARY AND FUTURE WORK

8.1 Summary of Main Contributions

In this work, a bottom-up computational framework supported by experimental test data is established to unravel the atomistic processes underlying the response of cement-based materials subjected to the mechanical and environmental stressors. The main contributions and findings of the current study are summarized below.

The structure of the crystalline HCP phases, such as portlandite and the aluminum-rich species are modeled at the nanoscale. The atomistic models are validated with the experimental test data available in the literature. *The interplay between the structure and the mechanical characteristics of the phases under consideration was fully investigated.* It was determined that the sequential breakage of the Ca-O and Al-O bonds in hydrogarnet results in a significant reduction in the tensile strength after the yield stress is reached. The tricalcium aluminate columns in ettringite and $[Ca_2Al(OH)_6]^+$ layers in monosulfoaluminate were found mainly responsible for resisting tensile strains. The separation and sequential breakage of the tricalcium aluminate columns are the main causes of failure identified for ettringite in the *x*/*y* and *z* directions, respectively. As for monosulfoaluminate, the sequential breakage of the Ca-O and Al-O bonds of the $[Ca_2Al(OH)_6]^+$ layers results in the failure of the atomic structure in the *x* and *y* directions. In the *z* direction, however, the segregation of the positively charged layers was identified as the main cause of failure under large strains. It was shown that the mechanical properties of the aluminum-rich species improve with the increase in the ratio of the number of aluminum to calcium atoms. As for portlandite, the presence of strong [CaO_6] layers running in the [001] direction resulted in the enhanced strength and stiffness in the *x* and *y* directions. In the *z* direction, however, the breakage of weak dispersive forces causes the segregation of the layers resulting in a mechanical failure.

Furthermore, it was observed that the tensile strength, Young's modulus, and fracture strain of portlandite decrease with temperature (temperature softening) and increase with strain rate (strain rate hardening). Lastly, a constitutive relationship was derived to describe the tensile strain of portlandite at various temperature and strain rate conditions.

The mechanical properties of the secondary sulfate-bearing phases formed as a result of the chemical attack reactions, i.e. ettringite and thaumasite, were characterized in this study for the first time using RMD simulations. It was observed that ettringite and thaumasite are about three times stronger in the *z* direction compared to the *y* direction, reflecting a strength anisotropy. While the tensile and compressive strengths are virtually identical, both ettringite and thaumasite in the *y* direction are stronger in the net compressive state than in the net tensile state. It was revealed that the breakage of Ca-O, Al-O, and Si-O interactions in the tricalcium aluminate and tricalcium silicate columns of ettringite and thaumasite, respectively, are mainly responsible for the strength anisotropy captured from the stress-strain relationships. The stress asymmetry in the tension and compression was attributed to the breakage and densification of the hydrogen bond network between the tricalcium aluminate and tricalcium silicate columns of ettringite and thaumasite, respectively. A yield criterion was identified to capture the strength anisotropy and stress asymmetry in the flow surfaces of ettringite and thaumasite. The effects of temperature change and strain rate on the mechanical properties were also investigated in detail. As the temperature increases, the rate of chemical bond dissociation increases, which in turn results in a substantial reduction in the mechanical properties, while a decrease in the strain rate favors larger atomic fluctuations accompanied by temperature-induced rearrangements, which caused a noticeable reduction in the mechanical properties.

The structure, orientation, and dynamics of water molecules and aggressive ions at the basal surfaces of the main aluminum-rich species in HCP, namely ettringite and monosulfoaluminate, was studied in detail. It was observed that the structure, orientation, and distribution of water molecules are fairly independent of the concentration of sodium chloride solutions. It was found that the orientation of water molecules are affected up to ~10 Å from the surfaces beyond which the molecules were randomly oriented. The alternating orientation of water molecules at different distances from the solid surfaces was attributed to the complexities involved in the surface charges. Unlike water molecules, the structure and dynamics of chloride and sodium ions were significantly affected by the concentration of sodium chloride solutions. At higher ionic strengths, the Na^+-Cl^- pair formation was observed due to the coadsorption of the ions to the solid surfaces. It was found that ettringite and monosulfoaluminate have low and high chloride binding capacity, respectively. In the inner-sphere distances from the ettringite's surfaces, the chloride ions were mostly found on the tricalcium aluminate columns, while the sodium ions were located on the top of the oxygen atoms of sulfate groups. For monosulfoaluminate, it was also observed that the chloride and sodium ions are mostly adsorbed to the $[0.5SO_4.3H_2O]^-$ and $[Ca_2Al(OH)_6]^+$ surface, respectively. It was shown that the chloride and sodium ions were present at both the inner- and outer-sphere distances from the ettringite's surfaces. For monosulfoaluminate, however, the inner- and outer-sphere complex formation is the main adsorption mechanism for the chloride and sodium ions, respectively. This highlighted the fact that the sodium ions have a weaker affinity to the basal surfaces of monosulfoaluminate compared to the chloride ions. Nonetheless, for both types of solid surfaces, the mobility of the sodium and chloride ions was lower at the inner-sphere regions compared to that of the ions at the outer-sphere distances to the surfaces. Also, the diffusion rate of the Na^+ and Cl^- ions were found to be several times smaller than that of the water molecules.

8.2 Perspective for Future Work

The atomistic computational framework developed in this dissertation can be directly employed in follow-up research studies to further improve the state of knowledge on the response of cement-based materials under the mechanical and environmental stressors.

The atomic-scale models developed in this study provide a robust foundation to incorporate elemental substitutions (e.g., Fe, Hg, Mg, Mn, and Zn, to name a few) in the structure of the HCP phases. Depending on the type, concentration, and distribution of the elemental substitutions, the physical and chemical characteristics of the HCP phases might be aggravated or enhanced. The current literature falls short in providing the necessary forcefield parameters to accurately model the chemical interactions between the substituted elements and elements of the host HCP phase. Characterization of the accurate forcefield parameters to perform such atomistic simulations remains to be explored in future. It is expected that the future studies in this area of research can shed light on the role of elemental inclusions in modulating the structure of the HCP phases with the aim of enhancing their physical and chemical properties.

The atomic-scale processes underlying the mechanical and thermal characteristics of the sulfate-bearing crystals formed as a result of chemical sulfate attack reactions (i.e., ettringite and thaumasite) are determined in this study. It was shown that thaumasite is mechanically weaker than the C-S-H gel, which is an important step forward to justify the macro-level loss of strength caused by the formation of thaumasite at the expense of the C-S-H gel, a.k.a thaumasite attack. Nonetheless, follow-up research studies are required to bridge the direction-dependent tensile strength of ettringite, estimated in this study, to the expansive stresses induced to the capillary pore walls in the cement paste as a result of the formation of ettringite. Given the size of the capillary pores ($\sim 10^{-8}$- 10^{-7} m), millions of atoms are necessary to be modeled to capture the atomistic origin

of the tensile stresses. While such simulations are not feasible by the current computational speed, with the possible advancement of computer technology in near future it will become computationally more tractable to fill in this research gap.

In this study, a nonreactive forcefield was used to investigate the diffusion of water molecules and aggressive ions in contact with the basal surfaces of the aluminum-rich species of HCP. Although the classical MD simulations provided invaluable knowledge about the structure and dynamics of the adsorbed water and ions, characterization of the chemical reactions that may occur during adsorption processes has remained unresolved. For example, the transfer of a proton from a strongly adsorbed water molecule to a neighboring hydroxyl group in the surface of the HCP phases cannot be captured in the MD simulations. This can be addressed by performing RDM simulations that will help shed light on the chemical reactions that may take place in solid-aqueous environments.

REFERENCES

1- ACI 562-16, 2016. "*Code requirements for assessment, repair, and rehabilitation of existing concrete structures and commentary*". American Concrete Institute.

2- Ali M.M., Gopal S., and Handoo S.K., 1994. "*Studies on the formation kinetics of calcium sulphoaluminate*", Cement and Concrete Research 24 (4): 715-720.

3- Alipour A., Shafei B., and Shinozuka M., 2011. "*Performance evaluation of deteriorating highway bridges located in high seismic areas*". Journal of Bridge Engineering 16(5): 597-611.

4- Alipour A., Shafei B., and Shinozuka M., 2013. "*Capacity loss evaluation of reinforced concrete bridges located in extreme chloride-laden environments*". Structure and Infrastructure Engineering 9(1): 8-27.

5- Allen A.J., Thomas J.J., and Jennings H.M., 2007. "*Composition and density of nanoscale calcium-silicate-hydrate in cement*". Nature Materials 6: 311-316.

6- Andrade C., Alonso C., and Molina F.J., 1993. "*Cover cracking as a function of rebar corrosion: Part I: Experimental test*". Materials and Structures 26(3): 345–353.

7- Batilov I., 2016. "*Sulfate resistance of nanosilica contained Portland cement mortars".* Master's Thesis, University of Nevada, Las Vegas, Nevada, U.S.A.

8- Chabrelie A., 2010. "*Mechanisms of degradation of concrete by external sulfate ions under laboratory and field conditions*". Ph.D. Dissertation, Ecole Polytechnique Federale De Lausanne, Lausanne, Switzerland.

9- Collepardi M., 2003. "*A state-of-the-art review on delayed ettringite attack on concrete*". Cement and Concrete Composites 25: 401-407.

10- Dolado J.S., Griebel M., Hamaekers J., and Heber F., 2011. "*The nano-branched structure of cementitious calcium–silicate–hydrate gel*". Journal of Materials Chemistry 21: 4445-4449.

11- Du Y.G., Clark L.A., and Chan A.H.C., 2005. "*Residual capacity of corroded reinforcing bars*". Magazine of Concrete Research 57(3): 135–147.

12- Fang C., Lundgern K., Plos M., and Gylltoft K., 2006. "*Bond behavior of corroded reinforcing steel bars in concrete*". Cement and Concrete Composites 36(10): 1931–1938.

13- Garboczi E.J., and Bentz D.P., 1996. "*Multi-scale picture of concrete and its transport properties: Introduction for non-cement researchers*". National Institute of Standards and Technology Internal Report 5900.

14- Jennings H.M., 2008. "*Refinements to colloidal model of C-S-H in cement: CM-II*". Cement and Concrete Research 38(3): 275-289.

15- Mehta P., and Monteiro P., 1993. "*Concrete: Structure, properties, and materials*". Englewood Cliffs, N.J.: Prentice Hall.

16- NRMCA, National Ready Mixed Concrete Association, 2017. "*U.S. ready mixed concrete production through June 2017*". Retrieved on September 19th, 2017.

17- Neville A., 2004. "*The confused world of sulfate attack on concrete*". Cement and Concrete Research 34: 1275-1296.

18- Pellenq R.J.M., Kushima A., Shahsavari R., Van Vliet K.J., Buehler M.J., Yip S., and Ulm F.J., 2009. "*A realistic molecular model of cement hydrates*". Proceedings of the National Academy of Sciences of the United States of America 106(38): 16102-16107.

19- Qomi M.J.A., Krakowiak K.J., Bauchy M., Stewart K.L., Shahsavari R., Jagannathan D., Brommer D.B., Baronnet A., Buehler M.J., Yip S., Ulm F.J., van Vilet K.J., and Pellenq

R.J.M., 2014. "*Combinatorial molecular optimization of cement hydrates*". Nature Communications 4960.

20- Richardson I.G., 2008. "*The calcium silicate hydrates*". Cement and Concrete Research 38(2): 137-158.

21- Santhanam M., Cohen M., and Olek J., 2002. "*Mechanism of sulfate attack: A fresh look, Part 1: Summary of experimental results*". Cement and Concrete Research 32: 915-921.

22- Santhanam M., Cohen M., and Olek J., 2003. "*Mechanism of sulfate attack: a fresh look, Part 2. Proposed mechanisms*". Cement and Concrete Research 33: 341-346.

23- Shafei B., Alipour A., and Shinozuka M., 2012. "*Prediction of corrosion initiation in reinforced concrete members subjected to environmental stressors: A finite-element framework*". Cement and Concrete Research 42: 365-376.

24- Shafei B., Alipour A., and Shinozuka M., 2013. "*A stochastic computational framework to investigate the initial stage of corrosion in reinforced concrete superstructures*". Computer-Aided Civil and Infrastructure Engineering 28: 482-494.

25- Shafei B., and Alipour A., 2015 (a). "*Application of large-scale non-Gaussian stochastic fields for the study of corrosion-induced structural deterioration*". Journal of Engineering Structures 88: 262-276.

26- Shafei B., and Alipour A., 2015 (b). "*Estimation of corrosion initiation time in reinforced concrete bridge columns: How to incorporate spatial and temporal uncertainties*". ASCE Journal of Engineering Mechanics 141(10): 04015037.

27- Stutzman P.E., 2001. "Scanning Electron Microscopy in Concrete Petrography". Proceedings of Materials Science of Concrete Special Volume: Calcium Hydroxide in Concrete, April 2001, Wiley-Blackwell.

28- Suleiman A.R., 2014. "*Physical sulfate attack on concrete*". Master's Thesis, The University of Western Ontario, London, Ontario, Canada.

29- Taylor H., Famy C. and Scrivener K., 2001. "*Delayed ettringite formation*". Cement and Concrete Research 31(5): 683-693.

30- Taylor R., Sakdinawat A., Chae S.R., Wenk H.R., Levitz P., Sougrat R., and Monteiro P.J.M., 2015. "*Developments in TEM nanotomography of calcium silicate hydrate*". Journal of American Ceramic Society 98(7): 2307-2312.

31- Telesca A., Marroccoli M., Pace M.L., Tomasulo M., Valenti G.L., and Monteiro P.J.M., 2014. "A hydration study of various calcium sulfoaluminate cements". Cement and Concrete Composites 53: 224-232.

32- Vidal T., Castel A., Francois R., 2004. "*Analyzing crack width to predict corrosion in reinforced concrete*". Cement Concrete Research 34(1): 165–174.

33- Whittaker M., and Black L., 2015. "*Current knowledge of external sulfate attack"*. ICE Advances in Cement Research 27(9): 532-545.

34- Winnefeld F., and Lothenbach B., 2010. "*Hydration of calcium sulfoaluminate cements - Experimental findings and thermodynamic modelling*". Cement and Concrete Research 40: 1239-1247.